ST. LOUIS
JUN 6
PUBLIC LIBRARY

JOURNAL OF THE AERONAUTICAL SCIENCES

VOLUME 24 JUNE, 1957 NUMBER 6

CONTENTS

Vortex Interference Effects on the Aerodynamics of Slender Airplanes and Missiles ..... ALVIN H. SACKS 393

Experimental Study of the Stagnation Temperature in a Free Molecular Flow ..... F. M. DEVIENNE 403

Bending and Buckling of Clamped Sandwich Plates ..... G. A. THURSTON 407

Circumferential Inlet Distortions in Axial Flow Turbomachinery ... FREDRIC EHRICH 413

Influence of Thermal Stresses on the Aeroelastic Stability of Supersonic Wings ..... M. A. BIOT 418

On Magnus Effects Caused by the Boundary-Layer Displacement Thickness on Bodies of Revolution at Small Angles of Attack ..... JOHN C. MARTIN 421

Laminar Boundary Layer on a Spinning Cone at Small Angles of Attack in a Supersonic Flow ..... R. SEDNEY 430

Buckling Under External Pressure of Cylindrical Shells Evenly Stiffened by Rings Only ..... P. P. BIJLAARD 437

Newtonian Flow Theory for Slender Bodies ..... J. D. COLE 448

Readers' Forum 456

Published by
INSTITUTE OF THE AERONAUTICAL SCIENCES, INC.

JOURNAL OF THE AERONAUTICAL SCIENCES

Editor: W. R. SEARS
Director, Graduate School of Aeronautical Engineering, Cornell University

Associate Editor: ROBERT R. DEXTER *Managing Editor:* RITA J. TURINO
Editorial Assistant: CAROLINE TAYLOR

Editorial Committee

Aerodynamics and Fluid Mechanics
Holt Ashley
H. Julian Allen
Dean R. Chapman
Francis H. Clauser
Hugh L. Dryden
John C. Evvard
Antonio Ferri
Alexander Flax
Wallace D. Hayes
R. T. Jones
Carl Kaplan
H. W. Liepmann
C. C. Lin
H. F. Ludloff
Harold Luskin
Clark B. Millikan
C. D. Perkins
H. J. E. Reid
George S. Schairer
G. B. Schubauer
John Stack
Theodore Theodorsen
Arthur N. Tifford
Th. von Kármán

Flight Testing
R. R. Gilruth
Melvin N. Gough
W. L. Howland
W. F. Milliken, Jr.

Rotating Wing Aircraft
F. B. Gustafson
K. H. Hohenemser
Bartram Kelley
R. B. Maloy
Ralph McClarren
R. H. Miller
R. H. Prewitt
Igor I. Sikorsky

Structures
John E. Duberg
N. J. Hoff
Samuel Levy
J. F. McBrearty
W. Ramberg
E. E. Sechler
F. R. Shanley
C. R. Strang
S. Timoshenko

Meteorology
C. F. Brooks
D. M. Little
F. W. Reichelderfer
K. C. Spengler

Vibration and Flutter
Lee Arnold
M. A. Biot
R. L. Bisplinghoff
Harold A. Cheilek
I. E. Garrick
Martin Goland

Aircraft Design
W. E. Beall
E. H. Heinemann
Hall L. Hibbard
Richard Hutton
C. L. Johnson
A. A. Kartveli
E. G. Stout
F. K. Teichmann

Electronics
Welcome W. Bender
K. C. Black
M. V. Kiebert, Jr.
David S. Little
S. B. Rogers
Paul Rosenberg
L. M. Sherer

Physiologic Problems
H. G. Armstrong
Louis H. Bauer
Robert J. Benford
W. Randolph Lovelace, II
Ross A. MacFarland

Flight Propulsion
William Bollay
George W. Brady
R. P. Kroon
Frank E. Marble
Abe Silverstein
Martin Summerfield
E. S. Taylor

Instruments
Alan G. Binnie
Charles H. Colvin
Frank R. Cook
C. S. Draper
S. G. Eskin
C. F. Savage
R. C. Sylvander

SUBSCRIPTION RATES

JOURNAL OF THE AERONAUTICAL SCIENCES, Published Monthly. United States and Possessions: 1 Year, $15.00; Single Copies, $1.50. Foreign Countries Including Canada (American Currency Rates): 1 Year, $16.00; Single Copies, $1.50.

AERONAUTICAL ENGINEERING REVIEW, Published Monthly. United States and Possessions: 1 Year, $3.00; Single Copies, $0.50. Foreign Countries Including Canada (American Currency Rates): 1 Year, $3.50; Single Copies, $0.50.

Notices of change of address should be sent to the Institute at least 30 days prior to actual change of address.

Manuscripts for publication, proofs, and all correspondence should be addressed to the Editorial Office of the JOURNAL.

Publication Office, 20th and Northampton Sts., Easton, Pa. Correspondence regarding subscriptions may be addressed to the Editorial Office of the JOURNAL OF THE AERONAUTICAL SCIENCES, 2 East 64th Street, New York 21, N.Y.

© Copyright, 1957, by the Institute of the Aeronautical Sciences, Inc.

Entered as Second-Class Matter at the Post Office, Easton, Pa., May 1, 1937. Acceptance for mailing at a special rate of Postage provided for in the Act of August 24, 1912. Authorized April 29, 1937.

JOURNAL OF THE AERONAUTICAL SCIENCES

VOLUME 24 JUNE, 1957 NUMBER 6

Vortex Interference Effects on the Aerodynamics of Slender Airplanes and Missiles

ALVIN H. SACKS*

Ames Aeronautical Laboratory, NACA

SUMMARY

Numerous examples of wing-tail and wing-body-tail interference have been calculated within the framework of slender-body theory. The resulting variations of total forces and moments are found to be highly nonlinear. These variations and particularly their nonlinearities are discussed from the standpoint of stability. Significant changes in longitudinal stability with angle of attack are predicted for high tails, and large losses in directional stability are found at moderate angles of attack for a conventional slender wing-tail arrangement. The calculated variation of pitching moment with angle of attack is compared with experiment for a banked cruciform missile arrangement. Results of a water-tank experiment are presented, showing the influence of the tail on the positions of the vortices shed by the wing.

SYMBOLS

A = aspect ratio

$C_{L_\alpha} = \left.\frac{\partial C_L}{\partial \alpha}\right]_{\dot{\alpha}=q=0}$

$C_{L_{\dot\alpha}} = \left.\frac{\partial C_L}{\partial(\dot\alpha c/U_\infty)}\right]_{\dot\alpha=q=0}$

$C_{L_q} = \left.\frac{\partial C_L}{\partial(qc/U_\infty)}\right]_{\dot\alpha=q=0}$

$C_{n_\beta} = \left.\frac{\partial C_n}{\partial \beta}\right]_{\beta=0}$

c = maximum chord of wing

c_1 = distance from airplane nose to pivot point [$c_1 = (2/3)c$ for all results presented]

h_T = height of horizontal tail trailing edge above wing chord plane

i_T = incidence of horizontal tail relative to wing chord plane, rad.

L = force in the z direction (approximately lift)

L' = rolling moment about the x axis

M = pitching moment about the pivot point $x = c_1$

N = yawing moment about the pivot point $x = c_1$

p = rate of roll about the x axis, rad./sec.

q = angular pitching velocity about the pivot point $x = c_1$, rad./sec.

$R = U_\infty(\beta - i\alpha) - (r + iq)(x - c_1)$

r = angular yawing velocity about the pivot point $x = c_1$, rad./sec.

s = local semispan of wing or tail

t = time, sec.

t_1 = local span of upper vertical tail panel

t_0 = maximum span of vertical tail panel

U_∞ = free-stream velocity, ft./sec.

xyz = Cartesian coordinates fixed in the tail

Y = force in the y direction (side force)

α = angle of attack, rad.

α_{cr} = angle of attack at which rolled-up wing vortices intersect line containing trailing edge of horizontal tail

$\dot\alpha$ = time rate of change of angle of attack, rad./sec.

β = angle of sideslip, rad.

$\zeta = y + iz$

ζ_1 = lateral position of starboard rolled-up vortex, $y_1 + iz_1$

ρ = fluid mass density

$\oint$ = contour integral taken once round the cross section of the airplane and vortex wake in the positive (counter-clockwise) sense

$\Re$ = real part

$\Im$ = imaginary part

$(\bar{\ })$ = complex conjugate of ( )

Subscripts

I = due to vortex interference

l = tail trailing edge

TE = wing trailing edge

$TE+$ = immediately behind wing trailing edge

w = wing (forward lifting surface)

All coefficients based on wing area and wing chord

INTRODUCTION

OVER the past several years, a considerable amount of research has been concerned with the distortion of the vortex sheets shed from wings and with the downwash fields associated with those vortex sheets. The final objective of such studies is, of course, the predic-

Presented at the Aerodynamics—II Session, Twenty-Fifth Annual Meeting, IAS, New York, January 28–31, 1957.

* Formerly, Aeronautical Research Engineer. Now, Head, Theoretical Aerodynamics, Advanced Research Division, Hiller Helicopters, Palo Alto, Calif.

tion of the aerodynamics of a tail placed in such a downwash field. Figs. 1 and 2, taken from reference 1 and 2, respectively, show the vortex sheets behind a plane and cruciform wing of aspect ratio 2, and it can be seen that for such cases the flat vortex sheet approximation is not a useful one, particularly at large distances behind the wing. On the other hand, it is now generally recognized that for many practical slender configurations the wake can be satisfactorily approximated by assuming that the vortex sheet shed from each wing panel is fully rolled up into a single line vortex at the tail. Certain special cases of wing-tail interference have been calculated with this assumption[3] and limiting cases of wing-body-tail interference have likewise been treated (without regard to the influence of the body on the vortex paths.) This is certainly a great simplification, although even the paths of the rolled-up vortices with no body may be quite complicated, as in the case of the cruciform wing (see Fig. 2). The situation is, of course, further complicated by the presence of a body and some such cases of wing-body-tail interference have been treated by calculating the vortex paths numerically.[5]

Once the vortex strengths and positions are determined, there remains the problem of calculating the forces on the body and tail due to the vortex wake. The forces acting on a tail surface placed in a known arbitrary downwash field have recently been calculated successfully by the method of reverse flow[6, 7] for many cases. However, this method was developed within the framework of linear theory and is based on a linear dependence of the pressure on the perturbation velocities. For slender wings and tails, such a relationship is often inadequate and the pressure depends also upon the squares of the perturbation velocities. Therefore, some other technique seems in order for handling these cases. Such a technique is described briefly in the present paper, which is concerned with the calculation of the vortex strengths and positions at the tail and particularly of the corresponding forces and moments due to vortex interference. The emphasis will be placed on the results obtained and on their implications with regard to stability.

Outline of Analysis

The method developed in references 8 and 9 is an extension of the classical formulas of Blasius[10] presented in 1910 for the calculation of the force and moment exerted on an arbitrary two-dimensional body immersed in a steady incompressible stream. There are several aspects of the Blasius problem which make it particularly attractive for extension to the slender airplane maneuvering in a compressible fluid. First of all, the differential equation is in both cases Laplace's equation in two dimensions.* That is,

$$\varphi_{vv} + \varphi_{zz} = 0 \tag{1}$$

This was first shown by R. T. Jones[12] in 1946 for steady flow, and it is known to be true also for unsteady flow of sufficiently small frequencies. Second, the pressure relation employed takes proper account of the quadratic terms required in the slender-body problem. And finally, the form of the contour integrals obtained permits integration by the method of residues.

Now if the airplane cross section in the physical z plane is mapped onto a circle in the σ plane (Fig. 3) with center at the origin, by means of the transformation

$$\zeta = y + iz = f(\sigma) = \sigma + \sum_{n=0}^{\infty} (b_n/\sigma^n) \tag{2}$$

then the distance between the kth shed vortex and its image is represented by $\sigma_k - (r_0^2/\bar{\sigma}_k)$. Therefore, the impulse of all of the shed vortices and their images is proportional to the quantity

$$I = \sum_{k=1}^{m} \Gamma_k \left[\sigma_k - (r_0^2/\bar{\sigma}_k)\right] \tag{3}$$

where m is the number of shed vortices. The quantity I is found to enter into the expressions for the interference forces and moments, which, according to reference 9, are given by

$$\left.\begin{aligned}
Y_I - iL_I &= -i\rho U_\infty(\bar{I}_l - \bar{I}_{TE+}) - \\
&\quad i\rho \int_{TE}^{l} (\partial\bar{I}/\partial t)\, dx + \rho p \int_{TE}^{l} \bar{I}\, dx \\
N_I - iM_I &= i\rho U_\infty \int_{TE}^{l} (x - c_1)\, (\partial\bar{I}/\partial x)\, dx + \\
&\quad i\rho \int_{TE}^{l} (x - c_1)\, (\partial\bar{I}/\partial t)\, dx - \\
&\quad \rho p \int_{TE}^{l} (x - c_1)\, \bar{I}\, dx \\
L_I' &= (1/2)\, \rho U_\infty \Re \oint_{x=l} F' d(\zeta\bar{\zeta}) - \\
&\quad (1/2)\, \rho U_\infty \Re \oint_{x=x_{TE+}} (F' d(\zeta\bar{\zeta}) + \\
&\quad (1/2)\, \rho \Re \int_{TE}^{l} dx\, (\partial/\partial t) \times \\
&\quad \oint F' d(\zeta\bar{\zeta}) - \rho \Re \int_{TE}^{l} \bar{R} I\, dx
\end{aligned}\right\} \tag{4}$$

Here the bar indicates the complex conjugate, p is the rate of roll about the x axis, and F' is the part of the complex potential due to the shed vortices and their images. These expressions are applicable to the type of aircraft illustrated in Fig. 3, which also shows the locations indicated by the symbols TE and l.

Some of the features of the configuration shown in Fig. 3 should be pointed out since they highlight the assumptions made in obtaining Eqs. (4). Specifically, it can be seen that the wing trailing edges are assumed to lie in a single plane ($x = x_{TE}$) normal to the x axis. Similarly, the tail trailing edges and the base (if any) of the body are taken to lie in a common plane ($x = l$) normal to the x axis. The formulas of Eqs. (4) could

* The complete determination of the potential φ for problems involving thickness actually involves an undetermined function of x to be found from the wave equation, as first pointed out by Ward.[11] However, this function is not required for the calculation of the integrated forces and moments to be considered here.

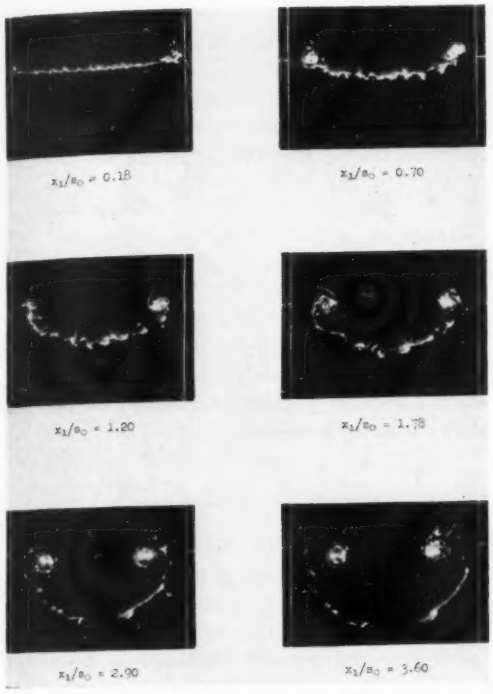

FIG. 1. Wake behind a plane triangular wing of aspect ratio 2; $C_L = 0.93$.

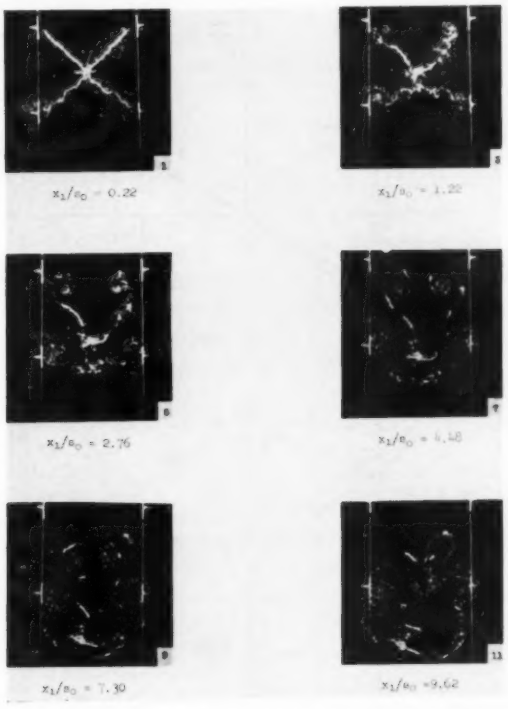

FIG. 2. Wake behind a cruciform triangular wing of aspect ratio 2; $C_L = 0.66$.

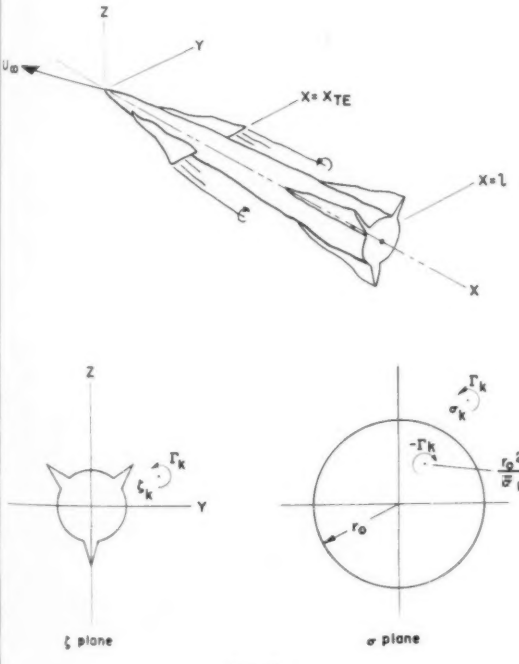

FIG. 3.

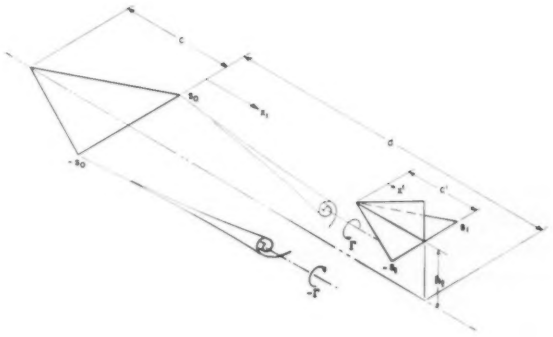

FIG. 4.

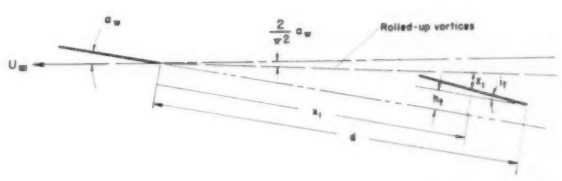

FIG. 5.

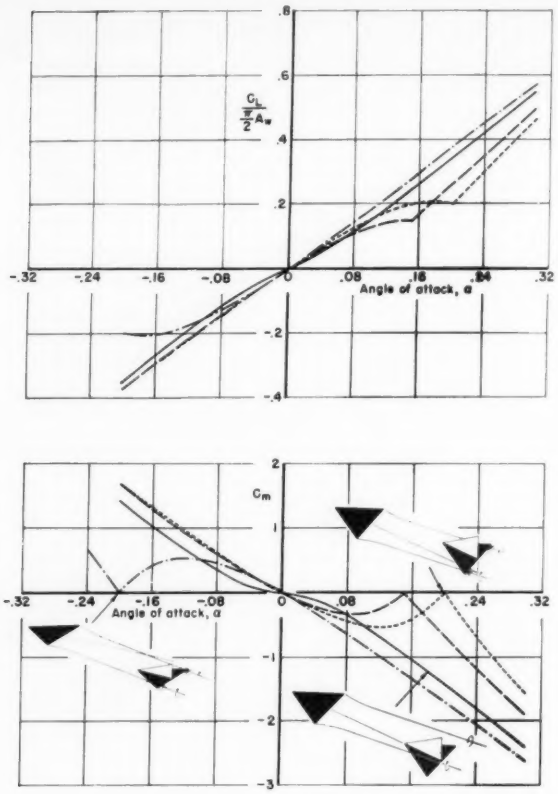

FIG. 6.

easily be extended to configurations involving additional surfaces with trailing edges lying at other x locations, but not to wings with sweptback trailing edges. The airplane is, of course, assumed to be slender and the frequencies of its motions to be small so that the perturbation potential satisfies Laplace's equation in planes normal to the x axis.

It can be seen from Eqs. (3) and (4) that the determination of the interference forces and moments requires a knowledge of the strengths and positions of all of the shed vortices. This is a major difficulty in any such calculation, and it severely restricts the classes of problems which can be handled analytically. First let us consider the simplest type of combination which encounters problems of vortex interference—namely, a wing-tail combination with no body. Fig. 4 shows such a combination with the appropriate vortex sheet shed from the wing. The tail is assumed rigidly attached to the wing and, as shown in the Figure, the vortex sheet is assumed to leave the wing as a flat sheet and become fully rolled up ahead of the tail. It is further assumed that the tail has no influence on the paths of the vortices shed by the wing.* The downward drift of the rolled-up vortices is predicted very well by the velocity induced on a two-dimensional vortex pair and is, according to slender-body theory, equal to $(2/\pi^2)\alpha$ so that the vortex cores are inclined below the flight direction at about one fifth of the angle of attack (see Fig. 1 and reference 1). This drift is accounted for in the calculations.

As for the actual calculations of the aerodynamic characteristics of the wing-tail arrangement shown in Fig. 4, it was shown in reference 13 that for steady straight flight ($p = \partial/\partial t = 0$) the interference lift and pitching moment of Eqs. (4) are given by

$$\left.\begin{aligned} L_I &= 4\rho U_\infty{}^2 \alpha_w s_0 \left[\Re \sqrt{\zeta_{1_t}{}^2 - s_1{}^2} - (\pi/4)s_0\right] \\ M_I &= 4\rho U_\infty{}^2 \alpha_w s_0 \times \\ &\quad \left[(l - c_1)\Re \sqrt{\zeta_{1_t}{}^2 - s_1{}^2} - (\pi/4)s_0 \times \right. \\ &\quad \left. (l - c_1 - c') - \int_0^{c'} R \sqrt{\zeta_1{}^2 - s^2}\, dx' \right] \end{aligned}\right\} \quad (5)$$

where the position ζ_1 of the starboard rolled-up vortex relative to the tail is (see Fig. 5)

$$\zeta_1 = y_1 + iz_1 = (\pi/4)s_0 + i\left\{\alpha_w[1 - (2/\pi^2)]\, x_1 - h_T - (d - x_1)i_T\right\} \quad (6)$$

and ζ_{1_t} is found by setting $x_1 = d$. The lateral position $y_1 = (\pi/4)s_0$ is dictated by slender-body theory which predicts an elliptic spanwise distribution of circulation. Thus, by adding to Eq. (5) the well-known expressions for the lift of the isolated slender wing and tail (see, e.g., reference 12), we can easily calculate the total lift and pitching moment as a function of the angle

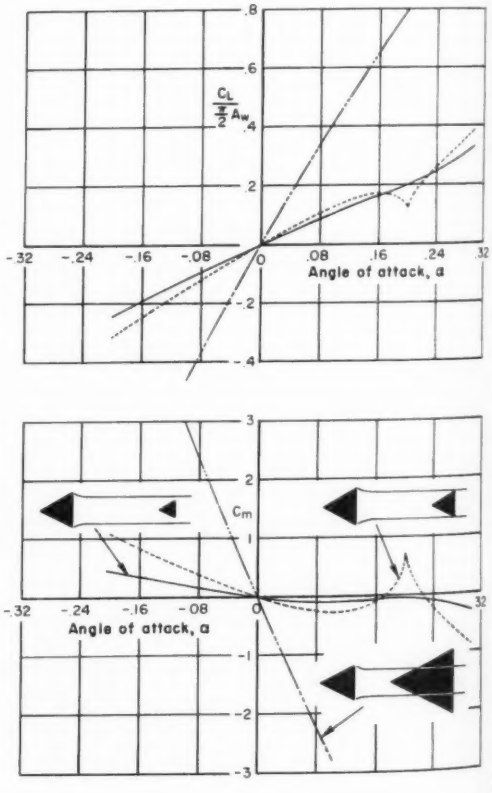

FIG. 7.

* This assumption has been investigated experimentally and will be discussed in a later section of this article.

of attack of the combination for various geometric arrangements.*

Discussion of Results

Fig. 6 shows the calculated lift and pitching-moment curves for several horizontal-tail heights with the wing and tail of equal span ($s_1/s_0 = 1.0$). Now, if it is recalled that the rolled-up vortices are inclined to the flight direction at about one-fifth of the angle of attack, it becomes clear that if the wing and tail lie in the same plane, the vortices cannot strike the tail at any angle of attack. Thus for zero tail height the lift and moment curves are smooth, although nonlinear. But if the tail is raised above the plane of the wing, then there is some positive angle of attack at which the wing vortices are expected (under the present assumptions) to strike the tail trailing edge, as shown in the upper sketch on Fig. 6. At that angle of attack, since the tail span is greater than the vortex span—i.e., $s_1 > y_{1l}$—then the vortices strike the tail. Since z_1 is then zero it can be seen that $\theta\sqrt{\zeta_{1l}^2 - s_1^2} = 0$ so that the interference lift of Eq. (5) becomes equal and opposite to the lift of the wing. Now it may be seen from Eq. (5) that this value is a maximum negative value for L_l and therefore we can expect a dip in the lift curve and the associated peak in the pitching moment curve as shown in Fig. 6. It will be noted that the pitching moment at this particular angle of attack (hereinafter called the "critical" angle of attack) is exactly zero in Fig. 6, but this is because the tail span was taken equal to the wing span, which makes the sum of the interference lift and the tail-alone lift just cancel. The long-dashed curve shows the same phenomenon for a smaller positive tail height. Now, if the tail is placed below the plane of the wing, the critical angle of attack is negative and the peaks in the curves are reversed, as shown. We find a severe instability just below the critical angle and abrupt changes of slope at the critical. Of course if the tail is placed very high this phenomenon will occur outside the operating range of angle of attack. However, such a shift of the horizontal tail will reduce the supersonic speeds at which other longitudinal problems arise due to wave interference from the wing.

From the sketches on Fig. 6, it is clear that the parameter determining the critical angle of attack is actually the angle included between the plane of the wing and the plane containing the trailing edges of the wing and tail. Therefore, the critical angle of attack is increased either by raising the tail or by reducing the tail length d. In fact, it can be seen from Eq. (6) that

$$\alpha_{cr} = (h_T/s_0)/\{(d/s_0)[1 - (2/\pi^2)]\} \qquad (7)$$

However, the magnitudes of the pitching moments involved are affected more strongly by changing the tail length than by changing the height of the horizontal tail. For all of the calculated results presented herein,

* Note that Eqs. (5) and (6) show the lift and pitching moment to be nonlinear with respect to the individual geometric parameters. The calculated effects of the various parameters are therefore not additive.

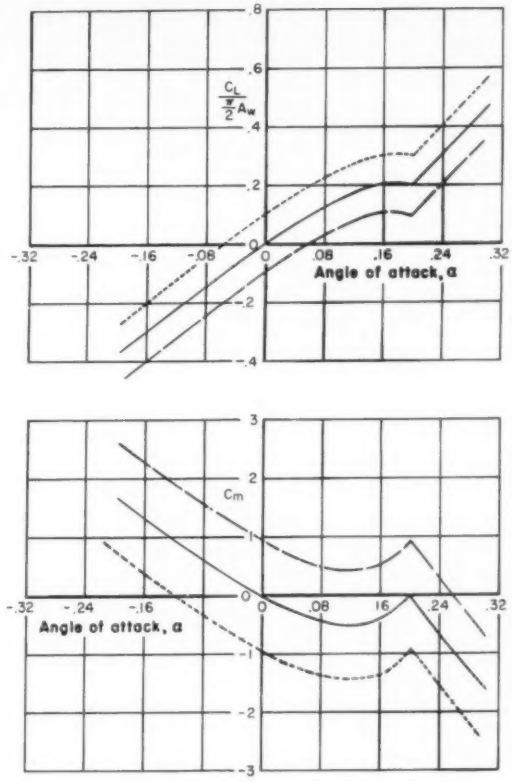

Fig. 8.

the tail length ratio d/s_0 was taken as 6 and the aspect ratio of wing and tail was taken as 2. The tail height ratios h_T/s_0 corresponding to the curves presented in Fig. 6 are thus easily obtained from Eq. (7).

Another important factor affecting the longitudinal stability of the wing-tail combination is the ratio of tail span to wing span, s_1/s_0. Fig. 7 shows, for example, the calculated lift and pitching-moment curves for several span ratios with a fixed tail height. It can be seen that if the tail span is less than the vortex span [in this case $(\pi/4)s_0$] then the abrupt changes in slope at the critical angle do not appear since the vortices do not strike the tail. On the other hand, if the tail span is very large, then the slopes change abruptly but the magnitude of the change is so small compared with the lift of the tail as to be insignificant. A maximum interference effect is observed when the tail span is equal to the vortex span since the tail is then in a maximum downwash field.

Fig. 8 shows the effect of tail incidence for an all-movable rear control surface at a fixed positive tail height. It will be observed that the curves are shifted linearly up and down with tail incidence, but due to the nonlinearity with angle of attack, we find a nonlinear control effectiveness. For example, the change in trim angle of attack from a tail incidence of 0 (solid curve) to 6° (dotted curve) is about one third the change from 0 to −6° (dashed curve). Furthermore,

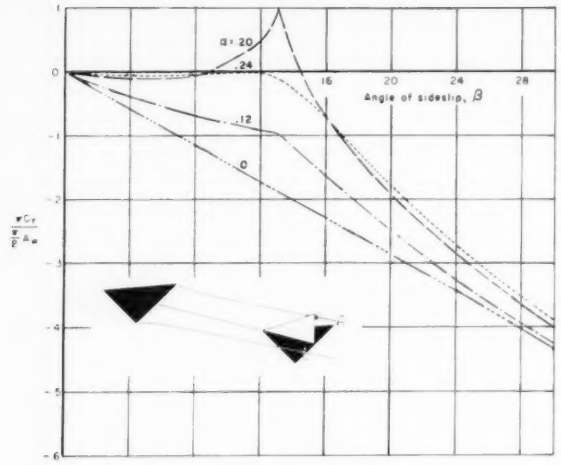

FIG. 9.

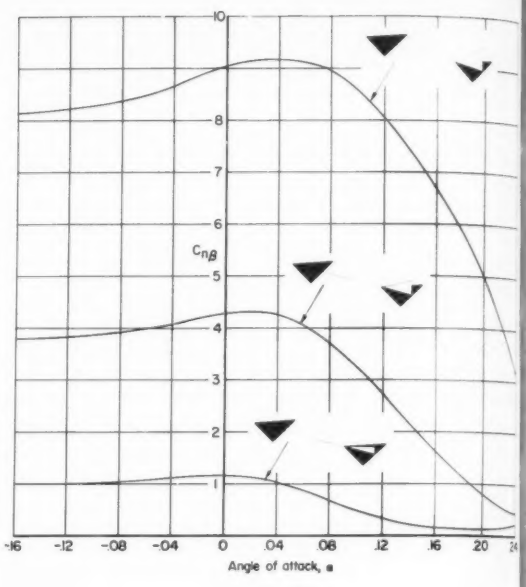

FIG. 10.

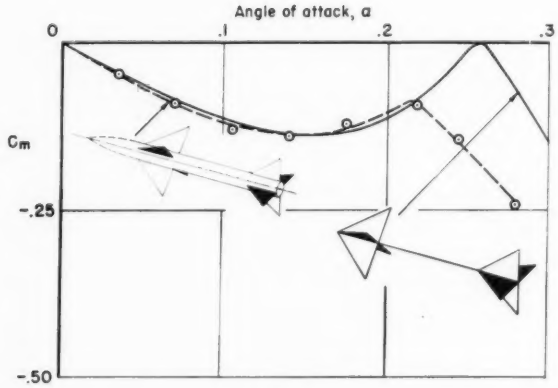

FIG. 11.

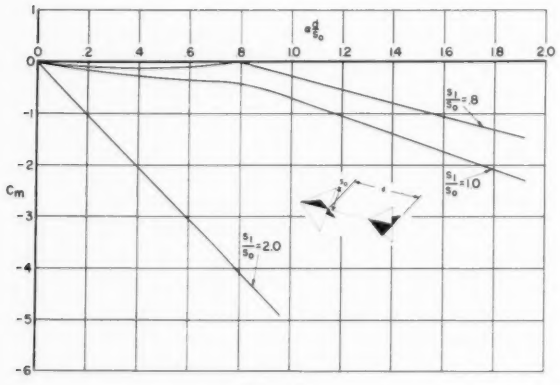

FIG. 12.

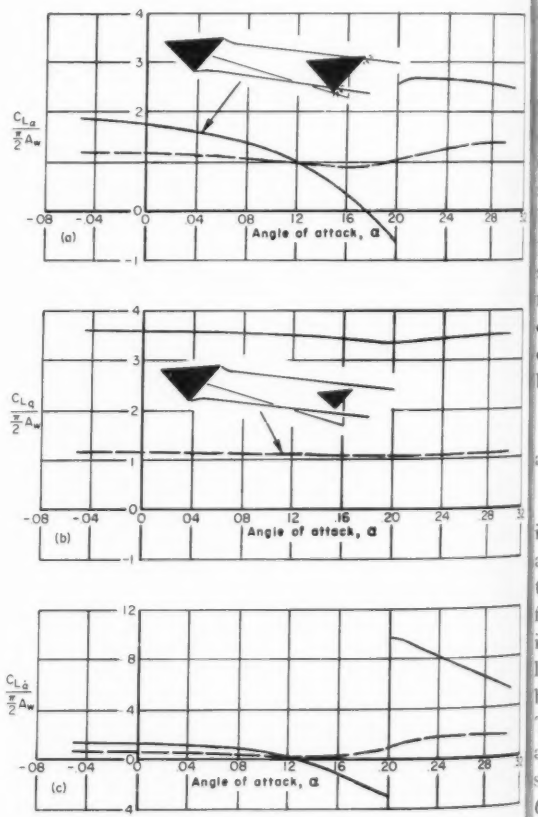

FIG. 13.

It is evident that at an incidence of about $-3°$ (not shown) there will be three possible trim angles of attack. It should be mentioned that for a tail height of zero such extreme effects do not occur, but the control effectiveness is still nonlinear.

So far only longitudinal stability has been considered, but very similar behavior is observed in connection with directional stability. Here, even with the horizontal tail lying in the plane of the wing, we find similar nonlinearities due to vortex interference with the vertical tail. Fig. 9 shows a more or less conventional wing-tail arrangement and the calculated variation of total side force with angle of sideslip at several angles of attack. The interference side force is calculated directly from Eqs. (3) and (4) by using the relationship

$$\vartheta[\sigma_k - (r_0^2/\bar{\sigma}_k)] = -(1/2)\vartheta \times \sqrt{[i(\sqrt{s^2 + t_1^2} - s) - 2\sqrt{\zeta_k^2 - s^2}]^2 + [\sqrt{s^2 + t_1^2} + s]^2} \tag{8}$$

developed in reference 13 for this configuration and by noting that the lateral positions of the rolled-up vortices relative to the vertical tail are

$$y_1 = (\pi/4)s_0 - \beta x_1 \qquad y_2 = -(\pi/4)s_0 - \beta x_1 \tag{9}$$

where β is the angle of sideslip. The additional side force carried by the isolated tail (with no vortices) is given by (see reference 8)

$$Y_T = (\pi/2)\rho U_\infty^2 \beta\,[s_1^2 - (t_0^2/2) - s_1\sqrt{s_1^2 + t_0^2}] \tag{10}$$

In Fig. 9, the span ratio s_1/s_0 is taken as unity and the span of the vertical fin is equal to the span of one panel of the horizontal tail. Here we find a critical angle of sideslip at which a wing vortex strikes the vertical tail, but if the angle of attack is large enough the vortex passes above the vertical tail and the nonlinearities are smoothed out. A maximum interference effect is found when a vortex from the wing just strikes the tip of the vertical tail. The angles of attack and sideslip corresponding to this condition are found from Eq. (6) by setting $\zeta_1 = it_0$ at $x_1 = d$. Thus,

$$\alpha = [(t_0/s_0) + (h_T/s_0)]/(d/s_0)\,[1 - (2/\pi^2)] \qquad \text{and} \qquad \beta = (\pi/4)/(d/s_0) \tag{11}$$

Perhaps a more significant effect to be noted in Fig. 9 is the variation of the slope $(\partial C_Y/\partial\beta)_{\beta=0}$ with angle of attack, since this derivative gives a direct measure of the directional stability. That is, since all of the side force is carried on the vertical tail, the yawing moment is simply equal to minus the side force times the tail length. It will be noted in Fig. 9 that the slope $C_{Y\beta}$ becomes less negative as the angle of attack is increased. The values of the directional stability derivative $C_{n\beta}$, as calculated from these slopes for several vertical tail sizes, are shown in Fig. 10. Since a positive value of $C_{n\beta}$ indicates stability, it is clear that increasing the angle of attack causes considerable loss in directional stability. Such losses are not indicated for negative angles of attack, which might suggest an inversion of the tail assembly or, more practically, the addition of a ventral fin.

Having worked out some of the simpler vortex interference problems, we shall now consider a cruciform missile arrangement and see how well the theory can predict the variation of pitching moment with angle of attack. With the cruciform wing at 45° bank and the tail at zero bank (the so-called "interdigitated" arrangement), it was shown in reference 13 that the interference lift is given by

$$L_I = 2\sqrt{2}\rho U_\infty^2 \alpha_w s_0[\Re\sqrt{\zeta_{1l}^2 - s_1^2} + \Re\sqrt{\zeta_{3l}^2 - s_1^2} - (\pi/2\sqrt{2})s_0] \tag{12}$$

where ζ_{1l} and ζ_{3l} are the positions of the upper and lower starboard vortices at the tail trailing edge. These positions correspond to the case shown in Fig. 2 and have been determined analytically in reference 14. The interference pitching moment is taken as minus L_I times the tail length and the lift of the isolated cruciform wing is known to be the same as that of a plane wing of equal span, according to slender-body theory.

Fig. 11 shows experimental data obtained in the Ames 6- by 6-ft. supersonic wind tunnel for an air-to-air missile with the wing at 45° bank and the tail at zero bank.[15] Here we have a phenomenon similar to the longitudinal behavior of the plane wing-tail combinations with raised tail. At a critical angle of attack, the vortices shed from the lower panels of the cruciform wing strike the trailing edge of the horizontal tail. It is difficult to compare the theory with the experiment since the theoretical model used here has no body. In addition to increasing the pitching moments, the presence of a body affects the vortex paths and raises some question about what wing dimensions to use for the calculations. However, by substracting the experimental pitching moment contributed by the body nose (as indicated schematically in the Figure), and using the ratio of exposed spans with the corresponding theoretical vortex paths in the absence of the body, we obtain the comparison shown in Fig. 11. The main discrepancy between the theory and the experiment seems to be in the predicted and observed values of the critical angle of attack. The reason for this discrepancy is evidently that the body upwash brings the vortices up from the lower wing panels at a faster rate and thereby reduces the critical angle of attack below that predicted by the theory. At angles of attack below the experimental critical angle, the agreement is quite good, and above that angle, the slopes seem to be in approximate agreement.

It might be mentioned, before leaving the symmetrically banked cruciform, that the pitching moment of such a wing-tail combination for given values of s_1/s_0, h_T/s_0, and i_T is actually a function of $\alpha(d/s_0)$ only. Fig. 12 shows such curves for several span ratios with zero tail height and zero tail incidence.

Although the results presented so far have been confined to steady straight flight, Eqs. (3) and (4) are directly applicable to quasi-stationary motions—i.e., to unsteady motions whose frequencies are small com-

pared with the flight velocity divided by the length of the body and also small compared with the velocity of sound divided by the body diameter. In reference 13 it was shown, by using the familiar lag-in-downwash concept, that for a plane triangular wing-tail combination (Fig. 4) performing two-degree-of-freedom longitudinal oscillations about the point $x = c_1$ the interference lift is

$$L_I = 4\rho U_\infty^2 s_0[\alpha_w + (q/U_\infty)(c - c_1) - (\dot{\alpha}d/U_\infty)] \Re\sqrt{\zeta_{1l}^2 - s_1^2} - \pi\rho U_\infty^2 s_0^2[\alpha_w + (q/U_\infty)(c - c_1)] - \pi\rho U_\infty \dot{\alpha} s_0^2(d - c') - 4\rho\dot{\alpha}U_\infty s_0[1 - (2/\pi^2)] \int_{d-c'}^{d} x_1[\alpha_w + (q/U_\infty) \times (c - c_1) - (\dot{\alpha}x_1/U_\infty)]\vartheta[\zeta_1/\sqrt{\zeta_1^2 - s^2}]dx_1 + 4\rho U_\infty \dot{\alpha} s_0 \int_{d-c'}^{d} \Re\sqrt{\zeta_1^2 - s^2}\, dx_1 \quad (13)$$

which for steady straight flight ($\dot{\alpha} = q = 0$) reduces to Eq. (5).

Now, by adding the known slender-body expressions for the lift of the isolated wing and tail and carrying out the appropriate partial differentials (see reference 13), one can easily obtain formulas for the stability derivatives $C_{L\alpha}$, C_{Lq}, and $C_{L\dot{\alpha}}$. Fig. 13 shows the calculated variations of these derivatives with angle of attack for two ratios of tail span to wing span with a given positive tail height. It can be seen that for the case in which the tail span is greater than the vortex span ($s_1/s_0 = 1$) both $C_{L\alpha}$ and $C_{L\dot{\alpha}}$ show large decreases as the angle of attack is increased up to the critical angle of attack and discontinuous increases at the critical angle. On the other hand, if the tail span is less than the vortex span ($s_1/s_0 = 0.5$), the variations with angle of attack are considerably smaller and show no discontinuities since the vortices do not strike the tail. The variation of C_{Lq} appears to be small in both cases but shows a minimum value at the critical angle of attack.

Up to this point, the calculations have been restricted to wing-tail combinations in order to circumvent the complication of calculating the vortex paths in the presence of a body or fuselage. The complications are, in fact, so great that in the past the vortex paths for such cases have been determined only by numerical methods—see, e.g., reference 5. There is, however, a very special class of wing-body-tail problems for which the vortex paths can be determined analytically—namely, a plane wing and tail mounted at incidence on a cylindrical body at zero angle of attack. The solution of this problem has been given in reference 16 in which the interference lift was determined by means of Eqs. (3) and (4). The resulting expression for a body of radius a is

$$L_I = 2\rho U_\infty \Gamma \Re\sqrt{[\zeta_{1l} + (a^2/\zeta_{1l})]^2 - [s_1 + (a^2/s_1)]^2} - L_{wB} \quad (14)$$

where

$$\Gamma = \frac{2U_\infty \delta_w s_0}{\pi}\left(1 - \frac{a^2}{s_0^2}\right)\left\{\frac{\pi}{2} + \cos^{-1}\left[\frac{2(a/s_0)}{1 + (a^2/s_0^2)}\right]\right\}$$

Γ is the circulation of one rolled-up vortex, δ_w is the wing incidence, and the lift L_{WB} of the isolated wing-body combination and that of the isolated body-tail combination in the absence of vortex interference are given according to slender-body theory in reference 17.

Fig. 14 shows curves of total lift obtained by using the vortex paths calculated in reference 16. The combinations shown have a tail span to wing span ratio s_1/s_0 of 1.5, the tail is at zero incidence, and the lift curves have been calculated for two wing spans and several tail lengths. The curves are of course nonlinear in all cases, but particularly so for the smaller wing span ($a/s_0 = 0.8$). For the larger wing span ($a/s_0 = 0.2$), the lift is consistently increased as the tail length d is increased. For the smaller wing span, however, above about 10° incidence, an increase in tail length results in a reduction of lift.

Limitations of the Theory

In view of the rather drastic effects predicted in some of the calculated curves presented herein, it might be well to look a little more closely at some of the assumptions made in the theory. First, the rolled-up vortices were assumed to be potential line vortices with no viscous cores. This assumption will have no effect so long as the cores do not touch the tail. However, when the distance from the tail to the center of the vortex is smaller than the radius of the core, the viscous core will change the downwash distribution at the tail location and affect the calculated lift on the tail. In order to get some idea of the magnitude of this effect, a calculation was made by the method of reverse flow to determine the lift on a plane tail which bisects two viscous cores of diameter equal to one-quarter of the tail span. The results showed that these relatively large viscous cores reduced the negative interference lift on the tail by 12 per cent at the critical angle of attack. Now since the viscous cores have no effect unless they touch the tail, the only effect is to round off the sharp peak at the critical angle.

Another important assumption of the theory is that the tail does not influence the paths of the vortices shed by the wing. This assumption is commonly made in calculations of the forces on the tail, but it means that the vortices do not follow the actual streamlines. Instead, they follow the streamlines in the absence of the tail. Thus, while the condition of no flow through the tail is satisfied, the vortices are nevertheless permitted to penetrate the tail. In fact, the most drastic effects on stability are predicted when the wing vortices touch or pass through the tail surface.

Water-Tank Experiment

In view of the implications just mentioned, the above assumption regarding the secondary influence of the tail would seem to warrant investigation. For this pur-

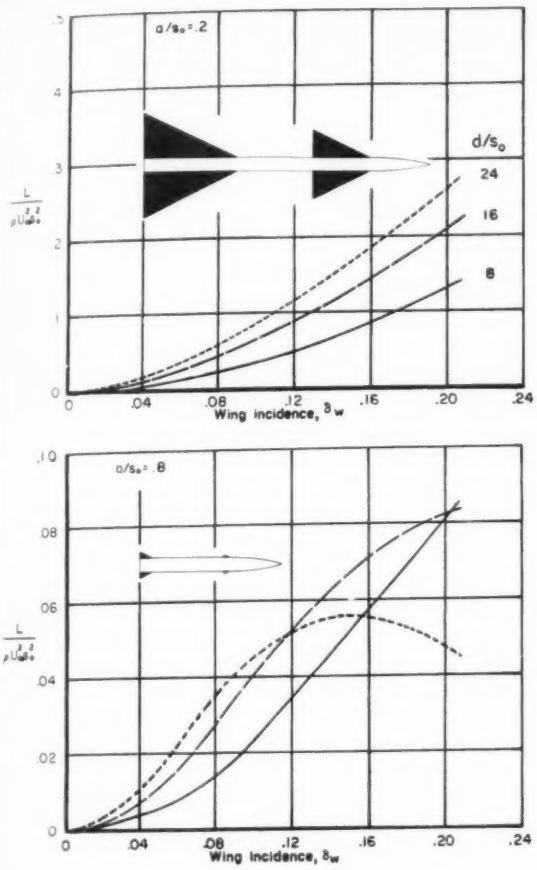

FIG. 14.

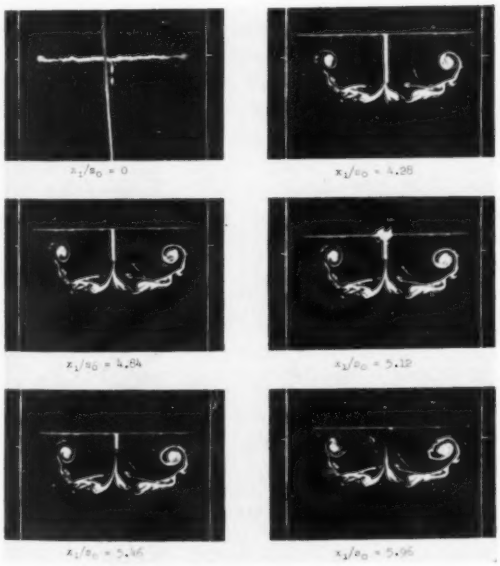

FIG. 15.

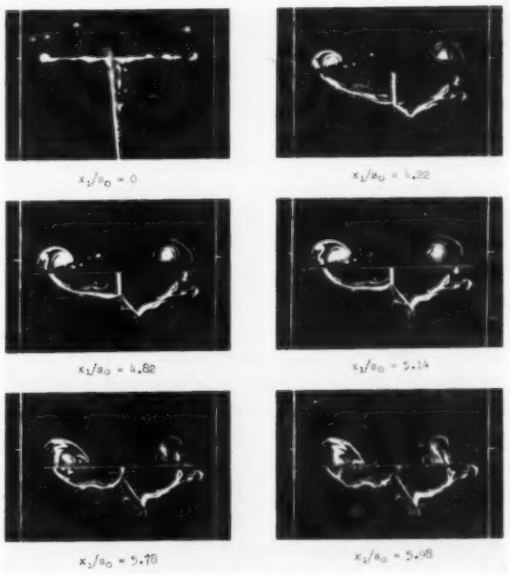

FIG. 16.

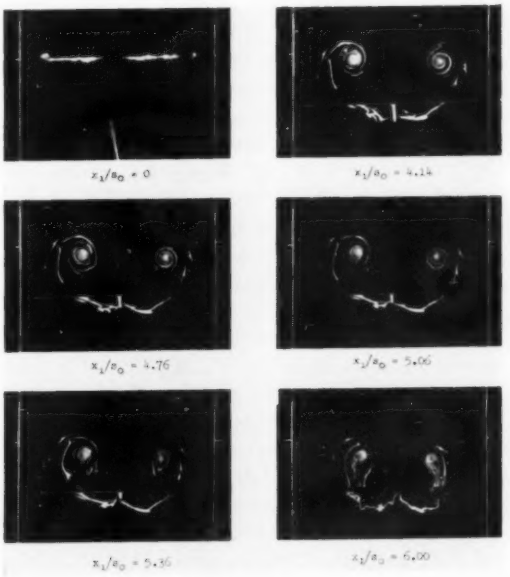

FIG. 17.

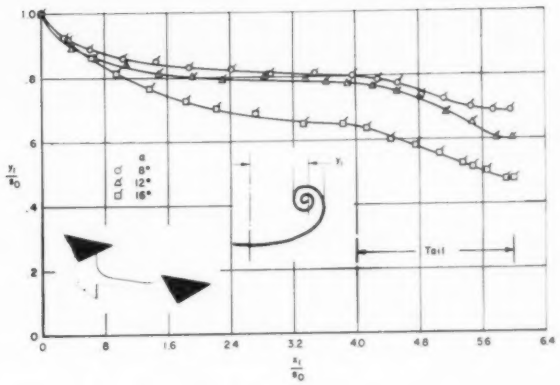

FIG. 18.

pose, an experiment was performed in a water tank in which the surface trace of the wake of a plane wing was photographed in the presence of a raised horizontal tail.* Selected frames of the motion pictures taken at three angles of attack are shown in Figs. 15, 16, and 17. In all of these Figures, the first picture shows the vortex sheet just behind the wing trailing edge. The strut connecting the wing and tail can be seen above the water surface. The second frame shows the apex of the tail just entering the water surface, and the succeeding frames show the development of the wake in the presence of the tail. In all cases, the supporting strut is observed to alter the center of the vortex sheet but it is believed that the effect on the positions of the rolled-up vortices is negligible. Fig. 15 shows no obvious effects attributable to the tail at the lowest angle of attack, which is below the critical angle. At the calculated critical angle of attack, Fig. 16 shows that, although the vortices are quite distorted at the trailing edge of the tail, the centers of the vortices do very nearly coincide with the tail trailing edge. At a still higher angle of attack, Fig. 17 indicates that the tail severs the vortex sheet and produces considerable distortions above the surface of the tail.

Now in interpreting these pictures quantitatively, one must bear in mind that after sufficient rolling up, the positions of the theoretical vortices should correspond to the positions of the centroids of vorticity of each half of the vortex sheet. It does not seem feasible to try to define the vertical location of the centroid of vorticity because of the unrolled portion of the sheet. However, the lateral position can reasonably be taken as midway between the innermost and outermost winds of the vortex sheet. Fig. 18 shows a plan view of the path of one vortex as determined in this manner from pictures similar to Figs. 15, 16, and 17. The vortex sheet starts to roll up at the tip and seems to approach very well the theoretical position of $(\pi/4)\ s_0$ ahead of the tail, at least at the lower angles of attack.

At the higher angles, a shift toward a triangular span loading causes the inboard shift ahead of the tail. But right at the apex of the tail $(x_1/s_0 = 4)$ another inboard shift starts at all three angles of attack, and this shift is appreciable.† However, it will be recalled from Eq. (5) and the ensuing discussion that at the critical angle of attack (12° here), since $\Re\sqrt{\zeta_{1l}^2 - s_1^2} = 0$, the lift on the tail is independent of the lateral positions of the vortices so long as they intersect the tail trailing edge, which they did (see Fig. 16). Hence we have the curious result that the predicted lateral positions of the vortices are in error but the predicted lift and pitching moment appear to be correct. At the other angles of attack above and below the critical, the calculated force and moment will be affected by amounts depending on both the lateral and vertical positio This problem is as yet unsolved and would seem to wa- rant some investigation.

Concluding Remarks

Although the present calculations have been re- stricted to slender configurations for which the vorte sheet leaves the wing as a flat sheet, it should be noted that the origin of the vortices is immaterial to the method of calculation. If, for example, the wing is a delta wing with sharp leading edges, there may be separation vortices above the wing. These can be handled by the present method, provided that their positions and strengths over the wing are known. Similarly, if the wing is a sweptback wing (not necessarily slender), the vortices from the wing may be caused to roll up quickly because of tip stalling or other viscous phenomena. Nevertheless, if the tail is slender and the vortices are rolled up ahead of the tail, the techniques of the present calculations are still applicable for the determination of the interference forces and moments. As a matter of fact, pitching-moment curves having the same general nonlinear character as those of Figs. 6 and 7 have been measured on swept-wing airplane models having high tails—see, e.g., reference 18.

From the results presented here, it would seem that there are several possibilities for avoiding the most drastic effects on stability caused by vortex interference. For longitudinal stability, either a low horizontal tail or a very high T tail is often effective, although if the interfering vortices arise from sources ahead of the wing—e.g., from the body or from air inlets—the tail height required to move α_{cr} out of the operating range may be prohibitive. A canard arrangement $(s_1/s_0 \gg 1)$ also seems to have possibilities for giving reasonably linear characteristics. It should be noted, however, that if the span of the tail is restricted by other considerations, a horizontal tail of span slightly less than the vortex span would be expected to give smoother longitudinal characteristics than one having a span slightly greater than the vortex span. For directional stability, a ventral fin appears to be beneficial in alleviating vortex interference effects. However, all in all, the most efficient practice may be simply to fill in the gaps between the wing and tail surfaces and thereby eliminate wing-tail interference.

References

[1] Spreiter, John R., and Sacks, Alvin H., *The Rolling up of the Trailing Vortex Sheet and its Effects on the Downwash Behind Wings*, Journal of the Aeronautical Sciences, Vol. 18, No. 1, pp. 21–32, 72, January 1951.

[2] Sacks, Alvin H., *Behavior of Vortex System Behind Cruciform Wings—Motions of Fully Rolled-up Vortices*, NACA TN 2605, 1952.

[3] Graham, Martha E., *Some Linearized Computations of Supersonic Wing-Tail Interference*, Rep. SM-13430, Douglas Aircraft Co., Inc., December 23, 1948

[4] Morikawa, George, *Supersonic Wing-Body-Tail Interference*, Journal of the Aeronautical Sciences, Vol. 19, No. 5, pp. 333–340, May, 1952.

(*Continued on page 412*)

* The model has an identical triangular wing and tail of aspect ratio 2 with $d/s_0 = 6$ and $\alpha_{cr} = 12°$.

† The nature of the water-tank experiment precluded any influence of the tail ahead of the apex of the tail, but this is in keeping with the basic assumption of slender-body theory.

Experimental Study of the Stagnation Temperature in a Free Molecular Flow†

F. M. DEVIENNE*

Laboratoire Méditerranéen de Recherches Thermodynamiques, Nice, France

SUMMARY

The purpose of the experimental work described in this paper was the measurement of the temperature of a small thermally insulated flat plate in motion at high speed in a free molecular flow. The plate was oriented perpendicular to the direction of motion, and was fixed at the extremity of an arm which revolved at high speed in a vacuum chamber.

The experimental results indicate that the temperature increase of the plate is a function of the speed of the plate, the pressure in the chamber and the surface condition of the plate. The results were compared with values calculated from the theory for free molecular flow, which gives the temperature increase of the plate as a function of the molecular speed ratio, the total emissivity and the thermal accommodation coefficients of the surface. In general, the experimental values for the temperature increase were less than those predicted by theory, when values for ϵ and a taken from tables of constants were used in the theoretical formulas. The theory, which assumes a Maxwellian distribution of molecular velocities, can be brought into accord with the experimental findings only if it is assumed that the accommodation coefficient is a function of pressure and speed.

SYMBOLS

a = accommodation coefficient
k = Boltzmann constant
K = Knudsen Number (ratio of mean free molecular path to the length of the plate)
m = mass of a gas molecule
n = number of molecules per unit volume
p = pressure in microns of mercury
T = free-stream static temperature, °K.
T_p = stagnation temperature of the plate, °K.
U = plate velocity
s = molecular speed ratio U/v_s
v_s = most probable molecular speed
W = energy received by the plate per unit of time per unit area
W_1 = energy received by the plate per unit of time per unit area at a pressure of 1 micron of mercury if $a = 1$
ϵ = total emissivity factor
$\Delta\theta$ = $T_p - T$ (rise in temperature of the plate)
ν' = number of molecules impinging on the unit area of the front surface
ν'' = number of molecules impinging on the unit area of the rear surface
$\Phi(s)$ = error function $2/\sqrt{\pi} \int_0^s e^{-x^2}\,dx$
ρ_1 = gas density at a pressure of 1 micron of mercury
ρ = density (mass per unit volume)
σ = Stefan constant
$\mathfrak{N}$ = a/ϵ, dimensionless

Received December 4, 1956.

† This work has been carried out under the support and sponsorship of the European Office of the Air Research and Development Command, United States Air Force.

* Director.

INTRODUCTION

FREE MOLECULAR FLOW is characterized by the fact that the mean molecular path of the gas is great when compared to the size of the moving body it surrounds. In other words, the Knudsen Number, equal to the ratio of the mean free molecular path to the specific size of the body, in a free molecular flow, is several times greater than unity. It is generally assumed that in most cases the flow regime is a free molecular flow if the Knudsen Number is greater than 10. However, Stalder and his coworkers found that in the case of experiments made with a transverse circular cylinder, free molecular flow exists with a Knudsen Number equal to 2.

The pressure at which we conducted the tests described in this paper were such that the Knudsen Number was generally above 5. We shall discuss later on the influence exerted by the pressure and, in so doing, the influence of the Knudsen Number on the phenomena observed.

Although a continuous flow no longer exists in the free molecular flow regime, we shall continue to use the words stagnation temperature to designate the temperature of the small plate oriented perpendicular to the direction of motion, when it is moving at high speed in a rarefied gas. In this case the plate moves through an isothermal gas at rest and at the same temperature as the walls bounding it. Experiments show that, as the plate moves in the motionless gas, it accumulates heat until a permanent temperature difference is reached between the plate and the surrounding medium.

THEORY

We shall not repeat the theory of energy exchange between a plane plate and the molecules of a rarefied gas in which the movement takes place. We shall only give the main results of this theory.

When a plane plate moves perpendicularly to the direction of the speed in a rarefied gas, the number of molecules impinging on its front surface is greater per unit of time than that of the molecules striking the same surface when it is at rest; their number is smaller when they strike the rear surface. The kinetic energy of the molecules in relation to the plate when the plate is in motion is greater for the front surface and smaller for the rear surface than when the plate is at rest.

The kinetic energy can only be calculated if the distribution function for molecular velocities is known.

The assumption made here is that the distribution is Maxwellian. In this case, the number of molecules impinging on the unit area of the front and rear surfaces per unit of time is, respectively,

$$\nu' = (nv_s/2\sqrt{\pi})\{e^{-s^2} + \sqrt{\pi}\, s[1 + \Phi(s)]\} \quad (1)$$

$$\nu'' = (nv_s/2\sqrt{\pi})\{e^{-s^2} - \sqrt{\pi}\, s[1 - \Phi(s)]\} \quad (2)$$

The mean kinetic energies of the molecules in relation to the plate during the relative movement are given for the front and rear surfaces by

$$E' = m\left\{\frac{U^2}{2} + v_s^2\left[1 + \frac{1 + 3/2\sqrt{\pi}\, s[1 + \Phi(s)]e^{s^2}}{1 + \sqrt{\pi}\, s[1 + \Phi(s)]e^{s^2}}\right]\right\} \quad (3)$$

$$E'' = m\left\{\frac{U^2}{2} + v_s^2\left[1 + \frac{1 - 3/2\sqrt{\pi}\, s[1 - \Phi(s)]e^{s^2}}{1 - \sqrt{\pi}\, s[1 - \Phi(s)]e^{s^2}}\right]\right\} \quad (4)$$

These formulas only concern monatomic gases. In the case of a diatomic gas, it is necessary to add the rotational energy of the molecules—i.e., about kT.

Lastly, if the rise in temperature of the plate is relatively small, the energy received by the unit area of the plate per unit of time is

$$W = (a\rho v_s^3/2)[(s/2)\Phi(s) + (s^2e^{-s^2}/\sqrt{\pi}) + s^3\Phi(s)] \quad (5)$$

We have assumed that the accommodation coefficient has the same value for the front and rear surfaces. This is presumably inaccurate. However, lacking any further data, we are obliged to make this hypothesis.

The preceding formula can also be written as follows:

$$W = apW_1 \quad (6)$$

Therefore we have

$$W_1 = (\rho_1 v_s^3/2)[(s/2)\Phi(s) + (s^2e^{-s^2}/\sqrt{\pi}) + s^3\Phi(s)] \quad (6a)$$

We can calculate the value of W_1 when the speed U and the temperature of the rarefied gas are known.

To determine the increase in temperature when the small plate is insulated, it will suffice to write down that the energy due to the impact of the molecules striking the small plate is equal to its emissive power. If the rise in temperature $\Delta\theta$ is small, the following equation is obtained:

$$W = 2\epsilon \cdot 4\sigma T_p^3 \cdot \Delta\theta \quad (7)$$

If we compare the W of Eqs. (5) and (7), we have

$$\mathfrak{N} = a/\epsilon = 8\sigma T^3{}_p \Delta\theta/pW_1 \quad (8)$$

We shall see that this way of expressing the result of the analysis offers a certain number of advantages.

Description of the Apparatus

A revolving arm made of duralumin, the extremity of which describes a circle 1.25 m. in diameter, is placed in a vacuum tank (1.50 m. inside diameter) and is driven by a shaft passing through a rotary seal of a special type. The small measuring plates are symmetrically arranged at the extremity of the arm and are fixed to Plexiglas supports. The plates have the dimensions 6 by 6 by 0.1 mm. Thermocouples are welded to the rear surfaces of the plates.

The temperature difference of the small measuring plate is measured by comparison with a similar reference plate placed on the arm and shielded from the flow. We have checked that the measurements can be reproduced and that at the lower pressures—i.e. under 10^{-5} mm.—the rise in temperature of the small measuring plates was practically null at the speeds up to 200 m./sec. and it was very small for speeds around 300 m./sec.

We shall not give a full description of the experimental device, but shall merely state that the rise in temperature is measured, after calibration, by deflection of a galvanometer, which indicates the output of the constantan-copper thermocouple. The copper wires of the thermocouple pass through capillary tubes placed inside the axis of the rotary seal which has previously been drilled and filled with Piceine.

The temperature difference measured does not correspond to a completely insulated plate, but to a small plate placed on a Plexiglas support. Although the support has been perforated and every precaution has been taken to minimize thermal conduction, the temperature difference observed is less than that obtained with a completely insulated small plate. We were consequently led to make a correction which allowed us to determine the heat exchange with the support. It is impossible to calculate such exchanges, and hence an experiment was devised for their evaluation. For this purpose, a small lamp with a rectilinear filament is placed at a certain distance in front of the small plate. The different pressures used and the rise in temperature of the small plate with and without its support are then measured. The thermal conduction, in the second case, is very low since the thermocouple wires are spiral-wound over a fairly large length and their diameter is small.

Tests conducted with this technique show that with a perfectly thermally insulated plate the temperature difference would be about 1.47 times that experimentally observed when the small plate is on its support. This factor, measured with sufficient precision, varies slightly with the support of the small plate, but only very slightly with the pressure, at least in the range of pressures used.

Experimental Results

The rise in temperature is dependent on (1) the speed of the plate moving in the rarefied atmosphere, (2) the pressure of the atmosphere, and (3) the nature and surface conditions of the small plate.

(1) *Influence of the Speed*

All other experimental conditions being identical, the rise in temperature increases with the speed U. It can be stated that it generally varies more rapidly

than the square of the speed and less rapidly than the cube.

Table 1 gives the value of $\Delta\theta$ as a function of U, using a small nickel-plated copper plate moving in a freon 12 atmosphere at a pressure of 0.5 micron of mercury.

Fig. 1 shows in logarithmic coordinates the values of $\Delta\theta$ expressed in terms of s for various gases under different pressures, using small plates of different materials and surface conditions. In this connection, it is advisable to point out that we have been obliged to change the plates from time to time, on account of accidents or of distortions due to the centrifugal force. Results obtained with plates of a similar nature are not absolutely the same. The straight lines show the mean variation rate for a given gas at a given pressure, and, of course, with the same small plate.

2) *Influence of the Pressure*

In the range of pressures used, the temperature rises as the pressure increases, though the increase in temperature is less than linearly proportional to the pressure increase. The variation of $\Delta\theta$ in terms of p at a speed of 298 m./sec. in dry air are given in Table 2.

3) *Influence of the Nature of the Gas*

The rise in temperature depends on the nature of the gas. It is generally greater at a given speed and pressure when the molecular mass of the gas is higher. The rise in temperature of a few gases corresponding to a pressure of 0.5 micron at a speed very near to 205 m./sec. are shown in Table 3.

(4) *Influence of the Nature and Surface Conditions of the Small Plate*

The rise in temperature is dependent on the surface condition of the plate. Examination of Fig. 2 reveals in particular that—all other experimental conditions being identical—the rise in temperature of a small blackened plate moving in freon 12 at 0.5 micron is about 3/5 of that observed with a small plate made of nickel-plated copper.

Comparison of Theory and Experiments

We have seen that the rise in temperature can be expressed in a dimensionless form

Table 1

U in m./sec.	50.7	101.7	152.2	203.3	253.7	303.8
$\Delta\theta$ in °K.	0.161	0.58	1.41	2.70	4.48	6.72

Table 2

p	0.25	0.50	1.00
$\Delta\theta$ in °K.	1.46	2.48	4.10

Table 3

Gas	Argon	Air	CO_2	Freon 12
$\Delta\theta$ in °K.	1.33	1.26	1.57	2.67

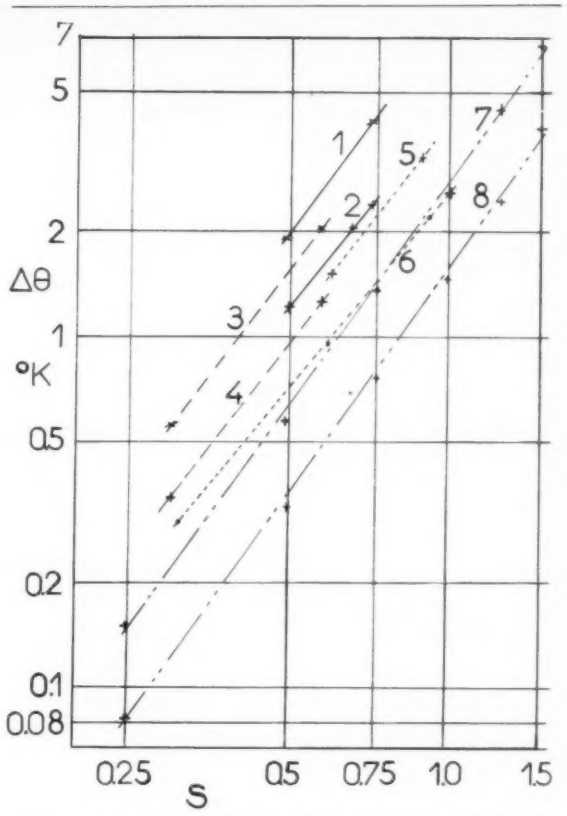

Fig. 1. *Nickel-plated copper plate:* Air (1: $p = 1\mu$; 2: $p = 0.50\mu$), Argon (3: $p = 1\mu$; 4: $p = 0.50\mu$), Carbon Dioxide (5: $p = 0.50\mu$; 6: $p = 0.30\mu$), Freon 12 (7: $p = 0.50\mu$). *Blackened-copper plate:* Freon 12 (8: $p = 0.50\mu$).

$$\mathfrak{N} = 8\sigma T^3 \Delta\theta / \rho W_1 = a / \epsilon$$

If theory is correct—i.e., if the speed distribution is really Maxwellian—and if, on the other hand, a free molecular flow is obtained and finally, if the emission factor ϵ and the accommodation coefficient a are constant, then the ratio calculated from the increase in temperature must remain constant.

Inasmuch as results show that the ratio a/ϵ varies with the speed and the pressure for a given gas, with a given plate, we shall discuss the validity of the different hypotheses which we assumed were exact when we established the theory.

(1) *Influence of Speed Distribution*

Fig. 3 shows that in the case of different gases at the same pressure, the ratio a/ϵ is a function of a and decreases as the parameter increases. The results show that this variation is not the same for all gases and that it varies, moreover, according to the surface conditions of the plate; this is why the variation in a/ϵ is generally less great with a blackened plate than with a polished one. Variation of the ratio a/ϵ must therefore be ascribed, at least in part, to other causes than the departure of the molecular speed distribution from the Maxwellian distribution.

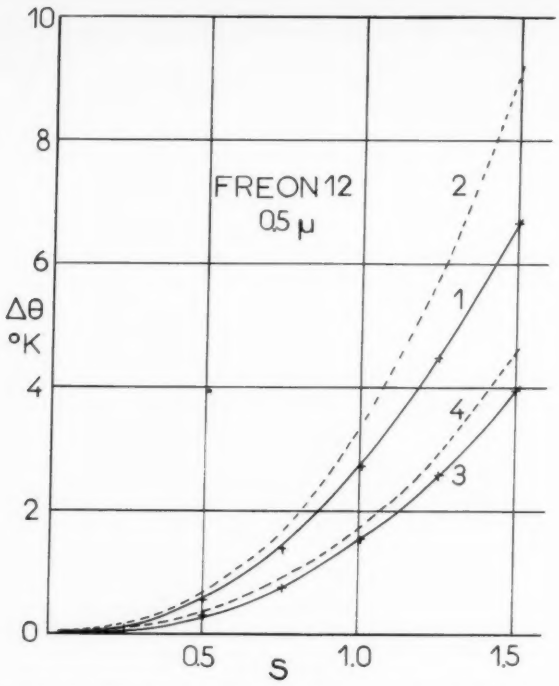

FIG. 2. *Nickel-plated copper plate:* 1—experimental values, 2—theoretical values for $a/\epsilon = 1.962$. *Blackened-copper plate:* 3—experimental values, 4—theoretical values for $a/\epsilon = 0.995$.

(2) *Influence of the Nature of the Flow Regime*

Tests conducted with Knudsen Numbers near to unity show that at these pressures the ratio a/ϵ rapidly decreases as the pressure increases—i.e., when the Knudsen Number is smaller. This result allows us to explain the observed decrease in the ratio a/ϵ in relation to the pressure. It can be assumed that the free molecular flow is only established for K values well above 10. In the case of lower values, a transition flow is established between the free molecular flow and the slip flow.

It is also to be remarked that the measurement of the accommodation coefficient by using a new method when the plates are at rest shows that it generally decreases as the pressure increases. These two phenomena are probably added to one another and explain therefore the variation of the ratio a/ϵ.

(3) *Influence of the Variation of the Accommodation Coefficient*

We have already shown that the accommodation coefficient generally decreases with the pressure. On the other hand, we have seen that a probable departure in the law of molecular speed distribution in relation to the Maxwellian distribution is not sufficient to explain the difference in the calculated ratio a/ϵ. Considering that ϵ certainly remains constant, we must admit that the accommodation coefficient decreases as the speed increases. The variation observed therefore depend on those of the accommodation coefficient. Lastly, we would like to recall that the accommodation coefficient varied in a large measure with the nature and surface conditions of the small plate. Experiments further show that the law of variations in accordance with the speed is not the same for two different small plates.

CONCLUSIONS

Experimental data show that the increases in temperature of the small plate are fairly large, even under very low pressures around 0.5 micron of mercury. The results are not quantitatively far from those given by free molecular flow theory but, in order to justify this theory, it must be assumed that the accommodation coefficient varies not only according to the nature of the gas and to the surface conditions of the solid body, which is to be expected, but also with the speed and with the pressure. An important research work on the accommodation coefficient conducted in our laboratory will shortly allow us to draw from it some laws concerning this variation.

REFERENCES

[1] Stalder, J. R., Goodwin, G., and Creager, M. O., *A Comparison of Theory and Experiments for High-Speed Free-Molecule Flow*, NACA Report 1032, 1951.

[2] Stalder, J. R., Goodwin, G., and Creager, M. O., *Heat Transfer to Bodies in a High-Speed Rarefied-Gas Stream*, NACA TN 2.438, 1951.

[3] Devienne, F. Marcel, *Etude Thermique des Ecoulements d'Air Raréfié en Régime Moléculaire Libre*, Publications Scientifiques et Techniques du Ministère de l'Air, Note technique 55, 1955.

(*Continued on page 412*)

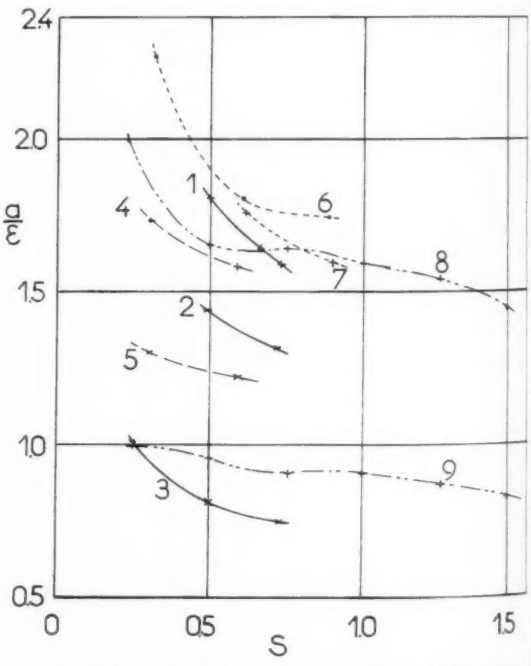

FIG. 3. *Nickel-plated copper plate:* Air ($1: p = 0.50\mu$; $2: p = 1\mu$), Argon ($4: p = 0.50\mu$; $5: p = 1\mu$), Carbon Dioxide ($6: p = 0.30\mu$; $7: p = 0.50\mu$), Freon 12($8: p = 0.50\mu$). *Blackened-copper plate:* Air ($3: p = 1\mu$), Freon 12($9: p = 0.50\mu$).

Bending and Buckling of Clamped Sandwich Plates

G. A. THURSTON*

General Electric Company

SUMMARY

The Lagrangian multiplier method is applied to Hoff's energy expressions for sandwich plates to derive equations for finding the deflections and buckling loads of rectangular plates clamped on all four edges.

Numerical calculations have been performed to find the buckling coefficients. These are plotted for use as design curves and show the reduction of buckling load due to shear in the core.

Although the method is approximate in theory, the convergence is rapid. The calculations were carried out on an IBM 704 computer which made it possible to obtain essentially an exact solution.

SYMBOLS

a, b	= edge lengths of sandwich panel
a_{mn}, b_{mn}, c_{mn}	= coefficients in Fourier expansions of w, u, and v, respectively
A_{mn}	= a parameter
c	= core thickness
E	= Young's modulus of face plates
G	= shear modulus of core
i, j, m, n, r, s	= integers
K	= buckling coefficient
P	= compressive edge load, lbs. per in.
q	= distributed transverse load on plate
S	= sandwich buckling parameter $D_0\pi^2/a^2Gc$
t	= face thickness
u, v, w	= sandwich plate displacements
U	= strain energy
V	= potential energy of external loads
x, y, z	= coordinate system
β	= ratio (a/b)
λ, μ	= Lagrange multipliers
δ_{mn}	= Kronecker delta
ν	= Poisson's ratio for the face plates

Subscripts

b = bending
c = core
f = face
q = transverse load
s = shear

PREVIOUS STUDIES

THE STRAIN-ENERGY EXPRESSION for sandwich plates used in this paper is due to Hoff.[1] He also applied the principle of virtual displacements to obtain the equations of equilibrium as three partial differential equations and solved these for the buckling loads of simply supported rectangular plates.

In another report, Hoff, Yen, and Salerno[2] obtained the buckling loads for the case of a rectangular plate with the loaded edges simply supported and the unloaded edges clamped. Nardo[3] solved Hoff's equations for a plate with the same boundary conditions as above, with the buckling load applied along either the clamped or simply supported edges.

Using a theory similar to Hoff's, March and Ericksen[4] applied the Rayleigh-Ritz energy method to calculate approximate buckling loads for a clamped rectangular plate. Their results, which are reproduced in reference 8, are from 5 to 10 per cent higher than the results presented in this paper.

The Lagrangian multiplier method used in the present paper was developed by Budiansky and Hu[5] in order to find buckling loads for clamped rectangular solid plates.

ENERGY EXPRESSIONS

Deformations are described by the functions u, v, and w of the coordinates x and y (see Fig. 1). Note that u is a displacement in the positive x-direction of the middle surface of the upper plate and an equal but opposite displacement in the lower plate. v corresponds to u with x replaced by y. The plate becomes curved only during the w displacements.

The parts of the strain energy considered essential are as follows: (1) $2U_f$, energy due to strains in the face plates in their own plane; (2) $2U_b$, strain energy of bending of the faces; and (3) U_s, strain energy of shear in the core.

$$2U_f = [Et/(1-\nu_2)] \iint \{[(\partial u/\partial x)^2 + 2\nu\,(\partial u/\partial x) \times (\partial v/\partial y) + (\partial v/\partial y)^2] + [(1-\nu)/2]\,[(\partial u/\partial y) + (\partial v/\partial x)]^2\}\,dxdy \quad (1)$$

$$2U_b = D_f \iint \{[(\partial^2 w/\partial x^2) + (\partial^2 w/\partial y^2)]^2 - 2(1-\nu)[(\partial^2 w/\partial x^2)\,(\partial^2 w/\partial y^2) - (\partial^2 w/\partial x \partial y)^2]\}\,dxdy \quad (2)$$

where D_f is the bending rigidity of one face plate.

$$D_f = Et^2/12(1-\nu^2)$$

$$U_s = (Gc/2) \iint (\{[2u/(c+t)] - (\partial w/\partial x)\}^2 + \{[2v/(c+t)] - (\partial w/\partial y)\}^2)\,dxdy \quad (3)$$

Strain energy due to transverse shearing in the faces and normal strains in the core is considered negligible.

The potential energy of the distributed transverse load q is

$$V_q = -\iint qw\,dxdy \quad (4)$$

The potential of the distributed compressive load

Presented at the Structures Session, Twenty-Fifth Annual Meeting, IAS, New York, January 28–31, 1957.

* Technical Engineer.

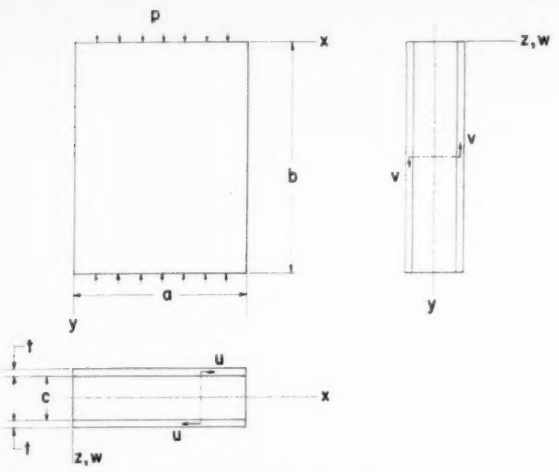

FIG. 1. Sketch of sandwich plate with thickness exaggerated.

P is

$$V_e = -(P/2) \iint (\partial w/\partial y)^2 \, dxdy \tag{5}$$

Boundary Conditions

The boundary conditions for the clamped plate are

$$w = 0 \quad \text{when } x = 0, a \text{ and when } y = 0, b \tag{6a}$$

$$\partial w/\partial x = 0 \quad \text{when } x = 0, a \tag{6b}$$

$$\partial w/\partial y = 0 \quad \text{when } y = 0, b \tag{6c}$$

$$u = 0 \quad \text{when } x = 0, a \tag{6d}$$

$$v = 0 \quad \text{when } y = 0, b \tag{6e}$$

$$(\partial u/\partial y) + (\partial v/\partial x) = 0 \quad \text{when } x = 0, a \text{ and } y = 0, b \tag{6f}$$

Eq. (6f), which sets the shear strain in the faces equal to zero along their edges, is the natural boundary condition which is obtained by applying the principle of virtual displacements to the potential energy. It assumes that v-displacements are possible along the edges parallel to the y-axis and that u-displacements are possible along the edges parallel to the x-axis.

SOLUTIONS

For loadings which are symmetrical about the axes $x = a/2$ and $y = b/2$, the displacement functions can be represented by

$$w = \sum_{m=0,2,4}^{\infty} \sum_{n=0,2,4}^{\infty} a_{mn} \cos(m\pi x/a) \cos(n\pi y/b) \tag{7}$$

$$u = \sum_{m=2,4}^{\infty} \sum_{n=0,2,4}^{\infty} b_{mn} \sin(m\pi x/a) \cos(n\pi y/b) \tag{8}$$

$$v = \sum_{m=0,2,4}^{\infty} \sum_{n=2,4}^{\infty} c_{mn} \cos(m\pi x/a) \sin(n\pi y/b) \tag{9}$$

The expansions for u and v satisfy their boundary conditions, Eqs. (6d), (6e), and (6f), term by term. The expansion for w satisfies the slope conditions Eqs. (6b) and (6c) term by term, but not the conditions on deflection Eqs. (6a).

These latter conditions will be satisfied by the expression for w as a whole. Along two edges

$$w(x, 0) = w(x, b) = \sum_{m=0,2,4}^{\infty} \sum_{n=0,2,4}^{\infty} a_{mn} \cos(m\pi x/a) \tag{10}$$

Each coefficient of $\cos(m\pi x/a)$ must be zero in order to satisfy Eq. (10), so that

$$\sum_{n=0,2,4}^{\infty} a_{in} = 0 \qquad (i = 0, 2, 4 \ldots) \tag{11}$$

For the other two edges,

$$w(0, y) = w(a, y) = \sum_{m=0,2,4}^{\infty} \sum_{n=0,2,4}^{\infty} a_{mn} \cos(n\pi y/b) \tag{12}$$

To satisfy Eq. (12), it is necessary that

$$\sum_{m=0,2,4}^{\infty} a_{mj} = 0 \qquad (j = 0, 2, 4 \ldots) \tag{13}$$

Therefore, all the boundary conditions are satisfied if Eqs. (11) and (13) are satisfied.

If the expressions for u, v, and w are substituted in the integrals for potential energy, Eqs. (1), (2), (3), (4), and (5), the following equation is obtained:

$$U + V = 2U_f + 2U_b + U_s + V_q + V_e = \frac{ab}{4} \sum_{m=0,2,4}^{\infty} \sum_{n=0,2,4}^{\infty} \left\{ \left[\frac{\pi^4}{a^4} D_f (m^2 + n^2\beta^2)^2 - \frac{Pn^2\beta^2\pi^2}{2a^2} \right] a_{mn}^2 + \frac{\pi^2}{a^2} \frac{Et}{1-\nu^2} \left[m^2 b_{mn}^2 + 2\nu mn\beta b_{mn} c_{mn} + n^2\beta^2 c_{mn} + \frac{1-\nu}{2} (n\beta b_{mn} + m c_{mn})^2 \right] + \frac{Gc}{2} \left[\left(\frac{2b_{mn}}{c+t} + \frac{m\pi}{a} a_{mn} \right)^2 + \left(\frac{2c_{mn}}{c+t} + \frac{n\beta\pi}{a} a_{mn} \right)^2 \right] \right\} \{1 + \delta_{m0} + \delta_{0n}\} - \sum_{m=0,2,4}^{\infty} \sum_{n=0,2,4}^{\infty} q_{mn} a_{mn} \tag{14}$$

where

$$q_{mn} = \int_0^a \int_0^b q \cos(m\pi x/a) \cos(n\pi y/b) \, dxdy$$

and δ_{m0}, δ_{0n} are Kronecker deltas defined by

$$\delta_{mn} = 1 \qquad m = n$$
$$\delta_{mn} = 0 \qquad m \neq n$$

It should be remembered that b_{0n} and c_{m0} do not exist.

Using the Rayleigh-Ritz method, the problem is to determine the a_{mn}'s, b_{mn}'s, and c_{mn}'s such that the expression $U + V$ is a minimum. However, the a_{mn}'s are not all independent since, in order to satisfy the boundary conditions, they are bound by the sets of Eqs. (11) and (13).

Minimizing the energy expression Eq. (14) and satisfying all the constraint Eqs. (11) and (13) would lead to an infinite determinant which theoretically would yield an exact solution for the buckling load or the static deflection. To obtain approximate results with a finite determinant, there are two alternate procedures. One method yields an upper bound for the buckling load while the other gives a lower bound. Bounds can also be obtained for the mean static deflection.

An upper bound is obtained by the usual Ritz procedure of satisfying all the boundary conditions, but setting some of the undetermined coefficients equal to zero. Using the incomplete set of functions in the Ritz method has the effect of stiffening the plate and raising the buckling load.

A lower bound is obtained using the complete set of coefficients but not satisfying all the constraining relations Eqs. (11) and (13). This method is based on a principle from the calculus of variations due to Courant:[6] "By strengthening the conditions in a minimum problem we do not diminish the value of the minimum; conversely, by weakening the conditions the minimum decreases, or at any rate does not increase."

From an engineering viewpoint, relaxing the condition that $w = 0$ on the boundary has the effect of making the plate more flexible, hence decreasing the buckling load.

Lower Bound Solution

In the lower bound solution the constraining relationships Eqs. (11) and (13) will be satisfied up to $i = r$ and $j = s$. Using Lagrange multipliers, the function to be minimized is

$$H = U + V - \sum_{j=0,2,4}^{s} \lambda_j \sum_{m=0,2,4}^{\infty} a_{mj} - \sum_{i=0,2,4}^{r} \mu_i \sum_{n=0,2,4}^{\infty} a_{in} \quad (15)$$

where the λ's and the μ's are the Lagrange multipliers and $U + V$ is given in terms of the unknown coefficients in Eq. (14).

$$\partial H/\partial a_{mn} = \partial H/\partial b_{mn} = \partial H/\partial c_{mn} = 0 \qquad (m, n = 0, 2, 4) \quad (16)$$

Performing the differentiation and arranging terms obtains

$$q_{00} = -\lambda_0 - \mu_0 \quad (17a)$$

$$(\pi^4 b D_0/4a^3)\,[(2D_f/D_0)(m_2 + n^2\beta^2)^2 + (1 - S)(m^2 + n^2\beta^2) - Kn^2\beta^2]a_{mn} + (Gc/2\beta) \times [m\pi a(c + t)]b_{mn} + (Gc/2)[n\pi a/(c + t)]c_{mn} = (\mu_m + \lambda_n + q_{mn})(1 + \delta_{m0} + \delta_{0n}) \quad (17b)$$

$$m\pi[(c + t)/a]a_{mn} + [2m^2S + (1 - \nu)n^2\beta^2S + 2]b_{mn} + (1 + \nu)mn\beta S\, c_{mn} = 0 \quad (17c)$$

$$n\beta\pi[(c + t)/a]a_{mn} + (1 + \nu)mn\beta S b_{mn} + [2n^2\beta^2S + (1 - \nu)m^2S + 2]c_{mn} = 0 \quad (17d)$$

where

$$D_0 = Et(c + t)^2/2(1 - \nu^2), \qquad S = D_0\pi^2/a^2Gc, \qquad K = Pa^2/\pi^2D_0$$

λ_n appears in Eq. (17b) only if $n \leqq s$ and μ_m appears only if $m \leqq r$. Solving the above equations obtains

$$a_{mn} = A_{mn}(\mu_m + \lambda_n + q_{mn}) \qquad m \text{ or } n \neq 0 \quad (18a)$$

$$b_{mn} = -\{m\pi(c + t)/2a[1 + S(m^2 + n^2\beta^2)]\}a_{mn} \quad (18b)$$

$$c_{mn} = -\{n\beta\pi(c + t)/2a[1 + S(m^2 + n^2\beta^2)]\}a_{mn} \quad (18c)$$

where

$$\frac{1}{A_{mn}} = \frac{\pi^4 b\, D_0}{4a^3}\left\{\left[\frac{2D_f}{D_0} + \frac{1}{1 + S(m^2 + n^2\beta^2)}\right] \times [m^2 + n^2\beta^2]^2 - Kn^2\beta^2\right\}\{1 + \delta_{m0} + \delta_{0n}\} \quad (19)$$

Substituting the a_{mn}'s given in Eq. (18a) back into the constraint Eqs. (11) and (13) up to $i = r$ and $j = s$ yields

$$a_{00} + \mu_0 \sum_{n=2,4}^{\infty} A_{0n} + \sum_{n=2,4}^{s} A_{0n}\lambda_n = \sum_{n=2,4}^{\infty} A_{0n}q_{0n} \quad (20a)$$

$$\mu_i \sum_{n=0,2,4}^{\infty} A_{in} + \sum_{n=0,2,4}^{s} A_{in}\lambda_n = -\sum_{n=0,2,4}^{\infty} A_{in}\, q_{in} \qquad (i = 2, 4 \ldots r) \quad (20b)$$

$$a_{00} + \sum_{m=2,4}^{r} \mu_m A_{m0} + \lambda_0 \sum_{m=2,4}^{\infty} A_{m0} = -\sum_{m=2,4}^{\infty} A_{m0}q_{m0} \quad (20c)$$

$$\sum_{m=0,2,4}^{r} \mu_m A_{mj} + \lambda_j \sum_{m=0,2,4}^{\infty} A_{mj} = -\sum_{m=0,2,4}^{\infty} A_{mj}\, q_{mj} \qquad (j = 2, 4 \ldots s) \quad (20d)$$

The set of Eqs. (20) and (17a) contains $[(r + s)/2] + 3$ linear nonhomogeneous equations in $[(r + s)/2] + 2$ Lagrange multipliers and a_{00}. After solving for the multipliers, it is possible to determine the a_{mn}'s, b_{mn}'s, and c_{mn}'s from Eqs. (18). These coefficients determine u, v, and w from Eqs. (7), (8), and (9). For the case of a uniformly distributed load, all the Fourier coefficients q_{mn} vanish except q_{00}, which simplifies Eqs. (20).

If the transverse load q is zero ($q_{mn} = 0$), the set of Eqs. (20) and (17a) reduces to a set of $[(r + s)/2] + 1$ homogeneous equations in the same number of Lagrange multipliers. For a solution different from zero, the determinant of the coefficients of the unknown λ's and μ's in these equations must vanish. The smallest value of K for given values of $2D_f/D_0$ and S which makes the determinant vanish determines a lower bound to the lowest buckling load.

Upper Bound Solution

In the solution for an upper bound, some of the a_{mn}'s are set equal to zero but all the constraints are satisfied. Arbitrarily let

$$a_{r+d,\,s+e} = 0 \qquad (d, e = 2, 4, 6 \ldots)$$

If all of the boundary conditions are satisfied, it can be shown that one of the constraining relations, Eqs. (11) or (13), is redundant. Omitting the first of Eqs. (11), the constraining relations become

$$\sum_{n=0,2,4}^{\infty} a_{in} = 0 \qquad (i = 2, 4 \ldots r) \tag{21}$$

$$\sum_{n=0,2,4}^{s} a_{in} = 0 \qquad (i = r+2, r+4, \ldots) \tag{22}$$

$$\sum_{m=0,2,4}^{\infty} a_{mj} = 0 \qquad (j = 0, 2, 4 \ldots s) \tag{23}$$

$$\sum_{m=0,2,4}^{r} a_{mj} = 0 \qquad (j = s+2, s+4 \ldots) \tag{24}$$

The function to be minimized becomes

$$H = U + V - \sum_{j=0,2,4}^{s} \lambda_j \sum_{m=0,2,4}^{\infty} a_{mj} - \sum_{j=s+2,s+4}^{\infty} \lambda_j \sum_{m=0,2,4}^{r} a_{mj} - \sum_{i=2,4}^{r} \mu_i \sum_{n=0,2,4}^{\infty} a_{in} - \sum_{r+2,r+4}^{\infty} \mu_i \sum_{n=0,2,4}^{s} a_{in}$$

The expression for $U + V$ is in the same form as in Eq. (14) except that some of the a_{mn}'s are now zero.

Evaluating $\partial H/\partial a_{mn} = 0$, $\partial H/\partial b_{mn} = 0$, and $\partial H/\partial c_{mn} = 0$ for the a_{mn}'s which exist gives

$$a_{mn} = A_{mn}(\mu_m + \lambda_n + q_{mn}) \qquad m \text{ or } n \neq 0$$

where μ_0 does not exist, and

$$\lambda_0 = -q_{00}$$

Substituting back into the constraint equations—Eqs. (21), (22), (23), and (24)—obtains

$$\sum_{n=0,2,4}^{\infty} A_{in}\lambda_n + \mu_i \sum_{n=0,2,4}^{\infty} A_{in} = -\sum_{n=0,2,4}^{\infty} A_{in}q_{in} \qquad (i = 2, 4, \ldots r) \tag{25}$$

$$\sum_{n=0,2,4}^{s} A_{in}\lambda_n + u_i \sum_{n=0,2,4}^{s} A_{in} = -\sum_{n=0,2,4}^{s} A_{in}q_{in} \qquad (i = r+2, r+4 \ldots) \tag{26}$$

$$a_{00} + \lambda_0 \sum_{m=2,4}^{\infty} A_{m0} + \sum_{m=2,4}^{\infty} A_{m0}\mu_m = -\sum_{m=2,4}^{\infty} A_{m0}q_{m0} \tag{27}$$

$$\lambda_j \sum_{m=0,2,4}^{\infty} A_{mj} + \sum_{m=2,4}^{\infty} A_{mj}\mu_m = -\sum_{m=0,2,4}^{\infty} A_{mj}q_{mj} \qquad (j = 2, 4 \ldots s) \tag{28}$$

$$\lambda_j \sum_{m=0,2,4}^{r} A_{mj} + \sum_{m=2,4}^{r} A_{mj}\mu_m = -\sum_{m=0,2,4}^{r} A_{mj}q_{mj} \qquad (j = s+2, s+2, s+4 \ldots) \tag{29}$$

The solutions of Eqs. (26) for μ_i and Eqs. (29) for λ_j are

$$\mu_i = -\left[\sum_{n=0,2,4}^{s} A_{in}(\lambda_n + q_{in}) \Big/ \sum_{n=0,2,4}^{s} A_{in}\right] \qquad (i = r+2, r+4 \ldots) \tag{30}$$

$$\lambda_j = -\left[\sum_{m=0,2,4}^{r} A_{mj}(\mu_m + q_{mj}) \Big/ \sum_{m=0,2,4}^{r} A_{mj}\right] \qquad (j = s+2, s+4 \ldots) \tag{31}$$

Substituting Eq. (31) into Eq. (25) and Eq. (30) into Eqs. (27) and (28), respectively, gives

$$\sum_{n=0,2,4}^{s} A_{in}\lambda_n - \sum_{n=s+2,s+4}^{\infty} A_{in}\left[\sum_{m=0,2,4}^{r} A_{mn}(\mu_m + q_{mn}) \Big/ \sum_{m=0,2,4}^{r} A_{mn}\right] + \mu_i \sum_{n=0,2,4}^{\infty} A_{in} = -\sum_{n=0,2,4}^{\infty} A_{in}q_{in} \qquad (i = 2, 4, \ldots r) \tag{32a}$$

$$a_{00} + \lambda_0 \sum_{m=2,4}^{\infty} A_{m0} + \sum_{m=2,4}^{r} A_{m0}\mu_m - \sum_{m=r+2,r+4}^{\infty} A_{m0}\left[\sum_{n=0,2,4}^{s} A_{mn}(\lambda_n + q_{mn}) \Big/ \sum_{n=0,2,4}^{s} A_{mn}\right] = -\sum_{m=2,4}^{\infty} A_{m0}q_{m0} \tag{32b}$$

$$\lambda_j \sum_{m=0,2,4}^{\infty} A_{mj} + \sum_{m-2,4}^{r} A_{mj}\mu_m - \sum_{m=r+2,r+4}^{\infty} A_{mj}\left[\sum_{n=0,2,4}^{s} A_{mn}(\lambda_n + q_{mn}) \Big/ \sum_{n=0,2,4}^{s} A_{mn}\right] = -\sum_{m=0,2,4}^{\infty} A_{mj}q_{mj} \qquad (j = 2, 4, \ldots s) \tag{32c}$$

The set of Eqs. (32) contains $[(r + s)/2] + 1$ equations in the same number of unknowns. If q is zero, the smallest value of K which makes the determinant of the coefficients of the unknowns vanish for given values of $2D_f/D_0$ and S gives an upper bound to the lowest buckling load.

For limiting values of the parameter S, which depends on the stiffness of the sandwich plate in bending compared to the shear rigidity of its core, the sandwich plate can be compared directly to a solid plate.

Equations similar to Eqs. (20) and Eqs. (32) can be derived for a solid isotropic plate where the term corresponding to $1/A_{mn}$ in Eq. (19) of this paper is derived in reference 5 as

$$1/A_{mn} = (\pi^4 bD/4a^3)\left\{[m^2 + n^2\beta^2]^2 - Kn^2\beta^2\right\} \times \left\{1 + \delta_{m0} + \delta_{0n}\right\}$$

where D is the plate bending rigidity and replaces D_0 in K.

When the core is infinitely rigid in shear, $S = 0$, and by comparing the $1/A_{mn}$ terms it can be seen that the sandwich plate has the same buckling load as a solid plate with bending rigidity

$$D = D_0 + 2D_f \tag{25}$$

If the core is so weak in shear that S approaches infinity, the sandwich plate has an effective stiffness of

$$D = 2\,D_f \tag{26}$$

which says the two face plates act independently.

Results

The solution for the buckling loads was programed for an IBM 704 computer. The equations for a lower bound were used with $r = s = 6$. This results in a seven by seven determinant which vanishes at the critical values of K. The value of K which makes the determinant vanish must be determined by trial and error. In each case four trial values were assumed for K, the corresponding values of the determinant computed, and the critical value of K calculated using the Lagrange interpolation formula.

Some of the coefficients of the determinant are infinite series. The first 25 terms were summed for each series.

An "exact" solution for the solid isotropic plate is due to Levy.[7] This solution corresponds to the sandwich plate with $S = 0$. The exact value of K was checked by the lower bound solution to five significant figures for the case of the square plate ($K = 10.074$). As S increases the infinite series in the determinant converge more slowly, but the values of K plotted in Fig. 2 should be very near the exact solution for Hoff's equations. In view of the good accuracy obtained with the lower bound solution, the numerically more complex upper bound solution was not programed.

Results (not shown) were obtained for a few cases with $2\,D_f/D_0 = 0.01$. Values of K ranged from one per cent higher for $S = 0$ to approximately four per cent for $S = 0.15$. The ratio of $2\,D_f/D_0 = 0.01$ corresponds to a ratio of $c/t = 4.76$ which is a plate with relatively thick face plates. These results indicate that the usual practice of neglecting $2D_f$ compared to D_0 is justified for most sandwich plates.

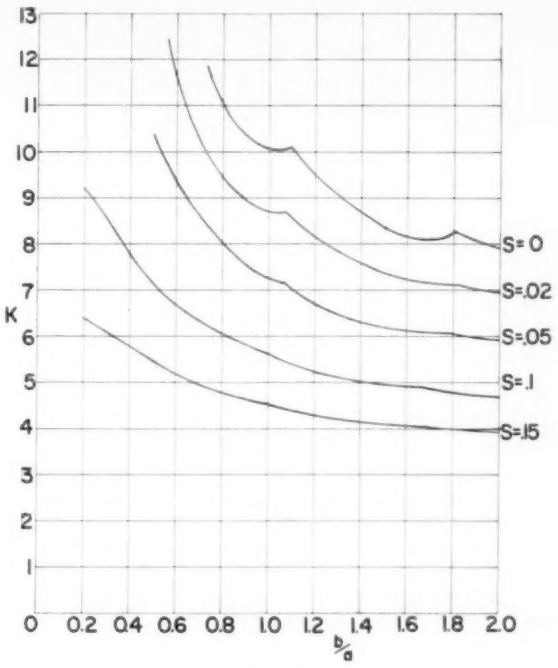

Fig. 2.

Numerical Example

As an example of the use of the curves in Fig. 2, the buckling load of an Alclad-cellulose acetate sandwich plate will now be computed. The plate has the following dimensions and elastic properties:

$a = b = 37.27$ in.
$t = 0.012$ in.
$c = 0.244$ in.
$E = 9.9 \times 10^6$ psi for facings
$\nu = 0.3$
$G = 3{,}500$ psi for the core material

$$D_0 = \frac{Et(c+t)^2}{2(1-\nu^2)} = \frac{(9.9)\ (10^6)\ (0.012)\ (0.256)^2}{2\ (0.91)}$$

$D_0 = 4{,}278$ in.-lb.

$$S = \frac{D_0\pi^2}{a^2Gc} = \frac{(4{,}278)\,\pi^2}{(37.27)^2\ (3{,}500)\ (0.244)} = 0.0355$$

$$D_f = \frac{Et^3}{12(1-\nu^2)} = \frac{(9.9)\ (10^6)\ (0.012)^3}{12(0.91)} =$$

1.57 in.-lb.

It can be seen that $2D_f/D_0$ is negligible in this case.

Interpolating between the curves in Fig. 2 gives $K = 7.94$ when $S = 0.0355$ and $b/a = 1$.

$$P = \frac{K\pi^2 D_0}{a^2} = \frac{(7.94)\pi^2(4{,}278)}{(37.27)^2} = 242 \text{ lbs. per in.}$$

The results of experiments conducted at the Forest Products Laboratory on four specimens of this type and reported in Table 19 of reference 9 had observed buckling loads ranging from 223 to 242 lbs. per in.

On this basis of this and other results reported in reference 9, there appears to be good agreement between Hoff's theory and experiment.

Concluding Remarks

A method of solution has been presented for bending and buckling of sandwich plates.

Curves are obtained for buckling loads which are suitable for use in design. Comparison of the theory with published test data indicates good agreement between theory and experiment.

Equations are also obtained which are suitable for obtaining stresses and deflections in clamped sandwich plates under transverse loads.

References

[1] Hoff, N. J., *Bending and Buckling of Rectangular Sandwich Plates*, NACA TN 2225, 1950.

[2] Yen, Kuo Tai, Salerno, V. L., and Hoff, N. J., *Buckling of Rectangular Sandwich Plates Subjected to Edgewise Compression with Loaded Edges Simply Supported and Unloaded Edges Clamped*, NACA TN 2556, January, 1952.

[3] Nardo, S. V., *An Exact Solution for the Buckling Load of Flat Sandwich Panels with Loaded Edges Clamped*, Journal of the Aeronautical Sciences, Vol. 20, No. 9, pp. 605–612, September 1953.

[4] March, H. W., and Ericksen, W. S., *Compressive Buckling of Sandwich Panels Having Facings of Unequal Thickness*, Forest Product Laboratory Report No. 1583-B, November, 1950.

[5] Budiansky, B., and Hu, Pai C., *The Lagrangian Multiplier Method of Finding Upper and Lower Limits to the Critical Stresses of Clamped Plates*, NACA TN 1103, 1946.

[6] Courant, R., and Hilbert D., *Methods of Mathematical Physics*, Vol. 1, p. 407, Interscience Publishers, Inc., New York, 1953.

[7] Levy, S., *Buckling of Rectangular Plates with Built-in Edges*, Trans ASME, Vol. 64, p. A171, 1942.

[8] *Sandwich Construction for Aircraft*, ANC-23 Bulletin, Second Ed., 1955.

[9] Boller, K. H., "Buckling Loads of Flat Sandwich Panels in Compression," *The Buckling of Flat Sandwich Panels with All Edges Clamped*, Forest Products Laboratory Report No. 1525-D, September, 1947.

Vortex Interference Effects...(*Continued from page 402*)

[5] Lagerstrom, P. A., and Graham, M. E., *Aerodynamic Interference in Supersonic Missiles*, Rep. SM-13743, Douglas Aircraft Co., Inc., July, 1950.

[6] Heaslet, Max. A., and Spreiter, John R., *Reciprocity Relations in Aerodynamics*, NACA Rep. 1119, 1953 (Formerly NACA TN 2700).

[7] Flax, A. H., *General Reverse Flow and Variational Theorems in Lifting-Surface Theory*, Journal of the Aeronautical Sciences, Vol. 19, No. 6, pp. 361–374, June, 1952.

[8] Sacks, Alvin H., *Aerodynamic Forces, Moments, and Stability Derivatives for Slender Bodies of General Cross Section*, NACA TN 3283, 1954.

[9] Sacks, Alvin, H., *Vortex Interference on Slender Airplanes*, NACA TN 3525, 1955.

[10] Blasius, H., *Funktiontheoretische Methoden in der Hydrodynamik*, Zeitschr. für Math. und phys, Bd 58, S. 90–110, 1910.

[11] Ward, G. N., *Supersonic Flow Past Slender Pointed Bodies*, Quart. Jour. Mech. and Appl. Math., Vol. 2, pt. 1, pp. 75–97, 1949.

[12] Jones, Robert T., *Properties of Low-Aspect-Ratio Pointed Wings at Speeds Below and Above the Speed of Sound*, NACA Rep. 835, 1946 (Formerly NACA TN 1032).

[13] Sacks, Alvin H., *Aerodynamic Interference of Slender Wing-Tail Combinations*, NACA TN 3725, 1956.

[14] Spreiter, John R., and Sacks, Alvin H., *A Theoretical Study of the Aerodynamics of Slender Cruciform-Wing Arrangements and their Wakes*, NACA TN 3528, 1956.

[15] Edwards, S. Sherman, *Experimental and Theoretical Study of Factors Influencing the Longitudinal Stability of an Air-to-Air Missile at a Mach Number of 1.4*, NACA RM A51J19, 1952.

[16] Sacks, Alvin H., *Theoretical Lift Due to Wing Incidence of Slender Wing-Body-Tail Combinations at Zero Angle of Attack*, NACA TN 3796, 1956.

[17] Dugan, Duane W., and Hikido, Katsumi, *Theoretical Investigation of the Effects Upon Lift of a Gap Between Wing and Body of a Slender Wing-Body Combination*, NACA TN 3224, 1954.

[18] Lichtenstein, Jacob H., *Experimental Determination of the Effect of Horizontal-Tail Size, Tail Length, and Vertical Location on Low-Speed Static Longitudinal Stability and Damping in Pitch of a Model Having 45° Sweptback Wing and Tail Surfaces*, NACA Rep. 1096, 1952.

Experimental Study of the Stagnation Temperature...

(*Continued from page 406*)

[4] Devienne, F. Marcel, *Research on the Study of the Conditions Surrounding a Body Moving at High Speeds in the Ionosphere*, Technical Report AF 61 (514)-818.

[5] Devienne, F. Marcel, *Etude Expérimentale de la Pression et de la Température d'Arret en Régime Moléculaire Libre*, Séminaire d'Aérothermique, Institut H. Poincaré, May, 1956.

[6] Devienne, F. Marcel, and Crave, B., *Appareil Destiné à la Mesure des Témperatures et de la Pression d'Arret sur un Corps en Mouvement à Trés Grande Vitesse dans un Gaz Raréfié*, Le Vide, No. 64, pp. 163–171, July, 1956.

[7] Brun, Edmond A., and Devienne, F. Marcel, *Etude Expérimentale de la Température d'Arret en Régime Moléculaire Libre*, Communication to the Ninth Congress of Applied Mechanics, Brussels, Belgium, September, 1956

Circumferential Inlet Distortions in Axial Flow Turbomachinery

FREDRIC EHRICH*

Westinghouse Electric Corporation

SUMMARY

An actuator disc type of analysis is carried out to determine the effect of a nonuniformity in the circumferential velocity profile entering an axial flow stage of turbomachinery. The analysis is restricted to study of incompressible, inviscid flow with the assumption of hub/tip ratios close to unity reducing the problem to two dimensions.

Expressions are derived giving the attenuation of the velocity distortion through the stage, the circumferential shift in the profile, and the fluctuation in load felt by the rotor blades passing through the nonuniform velocity field, all as a function of stage geometry.

Results are given for compressor, turbine, and free wheeling stages as a function of wheel speed, stage loading, and mean stagger angle. General conclusions and design recommendations are made with respect to minimizing blade load fluctuation and optimizing distortion attenuation.

SYMBOLS

a	= tan α = tangent of absolute flow angle
b	= tan β = tangent of relative flow angle
n	= order of distortion harmonic component
p	= static pressure
r	= mean radius of passage
U	= wheel speed
$\bar{u}$	= mean axial gas velocity
u	= axial gas velocity
v	= tangential gas velocity
Δv	= change in tangential gas velocity
$\delta\Delta(v)$	= fluctuation amplitude of Δv
W	= loading
x	= axial direction
y	= tangential direction
α	= absolute flow angle
β	= relative flow angle
γ	= "fluid" stagger angle
ϵ	= amplitude of velocity distortion
ζ	= vorticity vector in radial direction
ρ	= fluid density
φ	= circumferential phase orientation of distortion

Station Subscripts

1	= some distance upstream of the blade row
2	= immediately in front of the blade row
3	= immediately after the blade row
4	= some distance downstream of the blade row

GENERAL EQUATIONS

WE CONSIDER first the action of an isolated rotor in an annular passage of uniform height with hub/tip ratio near unity as in Fig. 1, permitting us to neglect variations in the radial direction. The circumferential inlet velocity distortion far upstream of the rotor will be assumed to be a sinusoidal variation of velocity superimposed on a mean velocity with a uniform swirl angle indicated by a slope a_1

$$u_1 = \bar{u} + \epsilon_1 \sin [n(y - a_1x)/r] \tag{1a}$$

$$v_1 = a_1\bar{u} + a_1\epsilon_1 \sin [n(y - a_1x)/r] \tag{1b}$$

The outlet velocity pattern far downstream of the rotor will have, superimposed on the mean velocity, a sinusoidal variation of velocity of a different amplitude and shifted in circumferential orientation with respect to a reference mean flow streamline. The gas will have a uniform swirl angle indicated by a slope a_4

$$u_4 = \bar{u} + \epsilon_4 \sin [n(y - a_4x)/r + \varphi_4] \tag{2a}$$

$$v_4 = a_4\bar{u} + a_4\epsilon_4 \sin [n(y - a_4x)/r + \varphi_4] \tag{2b}$$

Since we have restricted our attention to the situation where variations of parameters in the radial direction may be neglected, the continuity equation is

$$(\partial u/\partial x) + (\partial v/\partial y) = 0 \tag{3}$$

The radial component of vorticity has the magnitude

$$(\partial v/\partial x) - (\partial u/\partial y) = \zeta(x, y) \tag{4}$$

In order to linearize the problem, we assume that vorticity, instead of being transported by the streamlines, is transported along the lines of mean swirl. We therefore neglect the second-order effect of vorticity transport induced by perturbation velocities.

In the region upstream of the rotor (from station 1 to station 2)

$$(\partial v/\partial x) - (\partial u/\partial y) = \zeta(y - a_1x) \tag{5a}$$

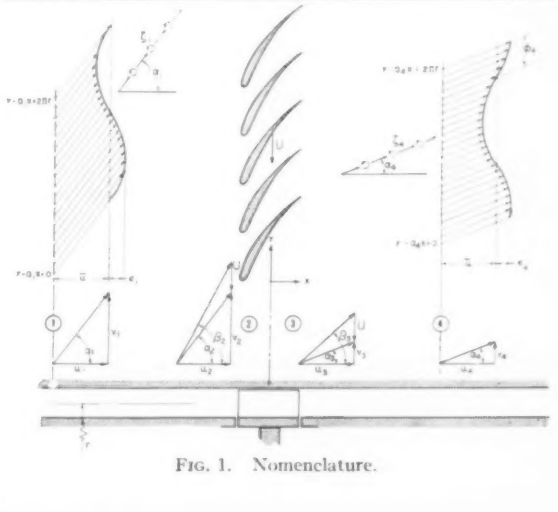

FIG. 1. Nomenclature.

Received January 14, 1957.

* Advisory Engineer, Aviation Gas Turbine Division.

In the region downstream of the rotor (from station 3 to station 4)

$$(\partial v/\partial x) - (\partial u/\partial y) = \zeta(y - a_4 x) \tag{5b}$$

The general expressions for the velocity components which satisfy the foregoing equations and the foregoing boundary conditions are found to be (a) In the upstream region from stations 1 to 2 where $-\infty < x < 0$

$$u = \bar{u} + \epsilon_1 \sin [n(y - a_1 x)/r] + \epsilon_2 \sin [ny/r + \varphi_2] e^{nx/r} \tag{6a}$$

$$v = a_1\bar{u} + a_1\epsilon_1 \sin [n(y - a_1 x)/r] + \epsilon_2 \cos [ny/r + \varphi_2] e^{nx/r} \tag{6b}$$

and (b) in the downstream region from stations 3 to 4 where $0 < x < \infty$

$$u = \bar{u} + \epsilon_4 \sin [n(y - a_4 x)/r + \varphi_4] + \epsilon_3 \sin [ny/r + \varphi_3] e^{-nx/r} \tag{7a}$$

$$v = a_4\bar{u} + a_4\epsilon_4 \sin [n(y - a_4 x)/r + \varphi_4] - \epsilon_3 \cos [ny/r + \varphi_3] e^{-nx/r} \tag{7b}$$

An immediate conclusion to be derived from the above expression is that any circumferential distortion of width $(2\pi r/n)$ will induce local disturbances at the rotor. But these disturbances will die away (to a value of exp $-\pi$) upstream and downstream of the rotor in an axial distance equal to the width of the distortion.

Axial Velocity Match Condition

Since we are neglecting any change in density through the rotating row, and the annulus area is constant, the axial velocity entering the blade row must equal the axial velocity leaving the blade row

$$u_2 = u(0-, y) = u_3 = u(0+, y) \tag{8}$$

Using the general expressions for the velocity components, we find

$$\bar{u} + \epsilon_1 \sin [ny/r] + \epsilon_2 \sin [ny/r + \varphi_2] = \bar{u} + \epsilon_4 \sin [ny/r + \varphi_4] + \epsilon_3 \sin [ny/r + \varphi_3] \tag{9}$$

Matching phase components of sin (ny/r) and cos (ny/r) in the latter equation we derive the two conditions

$$1 + (\epsilon_2/\epsilon_1) \cos \varphi_2 = (\epsilon_4/\epsilon_1) \cos \varphi_4 + (\epsilon_3/\epsilon_1) \cos \varphi_3 \tag{10a}$$

$$(\epsilon_2/\epsilon_1) \sin \varphi_2 = (\epsilon_4/\epsilon_1) \sin \varphi_4 + (\epsilon_3/\epsilon_1) \sin \varphi_3 \tag{10b}$$

Rotor Exit Angle Condition

If we assume that the mixer is heavily bladed, the relative exit angle of the fluid leaving the rotor will coincide with the geometric exit blade angle irrespective of the relative incidence angle

$$u_3 b_3 = v_3 + U \tag{11}$$

Again inserting the general expressions for the velocity components, we find

$$\bar{u}b_3 + b_3\epsilon_4 \sin [ny/r + \varphi_4] + b_3\epsilon_3 \sin [ny/r + \varphi_3] = U + a_4\bar{u} + a_4\epsilon_4 \sin [ny/r + \varphi_4] - \epsilon_3 \cos [ny/r + \varphi_3] \tag{12}$$

Matching the phase components of sin (ny/r) and cos (ny/r), and also the constant mean value elements of the equation, gives

$$b_3(\epsilon_4/\epsilon_1) \cos \varphi_4 + b_3(\epsilon_3/\epsilon_1) \cos \varphi_3 = a_4(\epsilon_4/\epsilon_1) \cos \varphi_4 + (\epsilon_3/\epsilon_1) \sin \varphi_3 \tag{13a}$$

$$b_3(\epsilon_4/\epsilon_1) \sin \varphi_4 + b_3(\epsilon_3/\epsilon_1) \sin \varphi_3 = a_4(\epsilon_4/\epsilon_1) \sin \varphi_4 - (\epsilon_3/\epsilon_1) \cos \varphi_3 \tag{13b}$$

$$U/\bar{u} = b_3 - a_4 \tag{13c}$$

No Loss Condition

For our last condition we assume that there are no losses along any streamline in the upstream region,

$$p_1/\rho + (u_1^2 + v_1^2)/2 = p_2/\rho + (u_2^2 + v_2^2)/2 \tag{14a}$$

no losses in the flow relative to the rotor,

$$p_2/\rho + [u_2^2 + (v_2 + U)^2]/2 = p_3/\rho + [u_3^2 + (v_3 + U)^2]/2 \tag{14b}$$

and no losses in the downstream region.

$$p_3/\rho + (u_3^2 + v_3^2)/2 = p_4/\rho + (u_4^2 + v_4^2)/2 \tag{14c}$$

Combination of these three Bernoulli equations gives

$$2(p_1 - p_4)/\rho + u_1^2(1 + a_1^2) - u_4^2(1 + a_4^2) = 2U(v_3 - v_2) \tag{15}$$

which can also be inferred from the Euler pump and turbine equation.

Consistent with our assumption of vorticity transport along the lines of mean swirl angle, we also identify variations of parameters on a streamline along these lines of mean swirl angle.

Inserting the general expressions for the velocity components and eliminating terms of order (ϵ^2) we find our last requirement

$$2(p_1 - p_4)/\rho + (1 + a_1^2)\{\bar{u}^2 + 2\bar{u}\epsilon_1 \sin [ny/r]\} - (1 + a_4^2)\{\bar{u}^2 + 2\bar{u}\epsilon_4 \sin [ny/r + \varphi_4]\} = 2U\{a_4\bar{u} + a_4\epsilon_4 \sin [ny/r + \varphi_4] - \epsilon_3 \cos [ny/r + \varphi_3]\} - 2U\{a_1\bar{u} + a_1\epsilon_1 \sin [ny/r] + \epsilon_2 \cos [ny/r + \varphi_2]\} \tag{16}$$

Finally, matching phase components of sin (ny/r) and cos (ny/r) in the latter equation and, in addition, the mean value elements of the equation, we derive the last set of conditions

$$(1 + a_1^2)[1 - (\epsilon_4/\epsilon_1) \cos \varphi_4] = (U/\bar{u})[a_4(\epsilon_4/\epsilon_1) \cos \varphi_4 + (\epsilon_3/\epsilon_1) \sin \varphi_3 - a_1 + (\epsilon_2/\epsilon_1) \sin \varphi_2] \tag{17a}$$

$$-(1 + a_4^2)(\epsilon_4/\epsilon_1) \sin \varphi_4 = (U/\bar{u})[a_4(\epsilon_4/\epsilon_1) \sin \varphi_4 - (\epsilon_3/\epsilon_1) \cos \varphi_3 - (\epsilon_2/\epsilon_1) \cos \varphi_2] \tag{17b}$$

$$(p_1 - p_4)/\rho + (a_1^2 - a_4^2)\bar{u}^2/2 = U\bar{u}(a_4 - a_1) \tag{17c}$$

Solution

The three match conditions (giving six component equations) permit solution for the six unknown quantities (amplitude and phase at stations 2, 3, and 4) as a function of the inlet distortion amplitude and the rotor geometry. The six simultaneous equations, (10a), (10b), (13a), (13b), (17a), and (17b), may be written in matrix form as

$$\begin{bmatrix} 1 & 0 & -1 & 0 & -1 & 0 \\ 0 & 1 & 0 & -1 & 0 & -1 \\ 0 & 0 & 1 & -b_3 & 0 & -(b_3 - a_4) \\ 0 & 0 & b_3 & 1 & (b_3 - a_4) & 0 \\ 0 & -(b_3 - a_4) & 0 & -(b_3 - a_4) & (1 + b_3a_4) & 0 \\ (b_3 - a_4) & 0 & (b_3 - a_4) & 0 & 0 & (1 + b_3a_4) \end{bmatrix} \begin{Bmatrix} (\epsilon_2/\epsilon_1) \sin \varphi_2 \\ (\epsilon_2/\epsilon_1) \cos \varphi_2 \\ (\epsilon_3/\epsilon_1) \sin \varphi_3 \\ (\epsilon_3/\epsilon_1) \cos \varphi_3 \\ (\epsilon_4/\epsilon_1) \sin \varphi_4 \\ (\epsilon_4/\epsilon_1) \cos \varphi_4 \end{Bmatrix} = \begin{Bmatrix} 0 \\ -1 \\ 0 \\ 0 \\ 0 \\ (1 + a_1^2) + a_1(b_3 - a_4) \end{Bmatrix} \tag{18}$$

The solution is somewhat simplified if the mean flow angle relative to the rotor (based on the uniform value of inlet swirl for upstream of the rotor) is introduced as an intermediate variable

$$b_2 = (U + v_1)/u_1 = b_3 - a_4 + a_1 \tag{19}$$

The set of six equations implied by Eq. (18) may be solved, first for $(\epsilon_4/\epsilon_1) \sin \varphi_4$ and then for $(\epsilon_4/\epsilon_1) \cos \varphi_4$. The amplitude and phase of these two components in combination is then

$$(\epsilon_4/\epsilon_1) = \left\{ \frac{(1 + a_1^2)(1 + b_2^2)(1 + b_3^2)}{(1 + a_4^2)[4(b_3 - a_4)^2 + (1 + b_3^2)^2]} \right\}^{1/2} \tag{20}$$

$$\tan \varphi_4 = \frac{(b_3 - a_4)\{(1 + b_2^2)[(1 + a_4b_3) + (1 + a_1b_2)] + 2(b_3 - a_4)^2 - 2(1 + a_4b_3)(1 + a_1b_2)\}}{(b_3 - a_4)^2\{-2[(1 + a_4b_3) + (1 + a_1b_2)] + (1 + b_3^2)\} - (1 + b_2^2)(1 + a_4b_3)(1 + a_1b_2)} \tag{21}$$

Stage Attenuation

The latter result gives the attenuation and phase shift of a distortion through an isolated rotor. The effect of a stationary row of blades is deduced from this result by letting the wheel speed, or $(b_3 - a_4)$, go to zero, giving

$$(\epsilon_4/\epsilon_1)_{stator} = (1 + a_1^2)/(1 + a_4^2) \tag{22}$$

$$\tan \varphi_4 = 0 \tag{23}$$

We may study the net cumulative effect of a complete turbomachinery stage (axial inlet flow, inlet guide vanes, rotor and outlet guide vanes returning the flow to the axial direction) by neglecting interblade-row interference effects and correcting the attenuation of the rotor for the acceleration and deceleration effects of the stationary rows. In this way, we isolate the primary quantity of interest, the effect of the rotor on the profile attributable only to the differential work on the distorted inlet profile. The stage attenuation is then

$$(\epsilon_4/\epsilon_1)_{stage} = \left\{ \frac{(1 + a_4^2)(1 + b_2^2)(1 + b_3^2)}{(1 + a_1^2)[4(b_3 - a_4)^2 + (1 + b_3^2)^2]} \right\}^{1/2} \tag{24}$$

The phase shift is given by Eq. (21) since it is unaffected by stationary rows, Eq. (23).

Fluctuating Blade Load

An additional parameter of significance is the fluctuation in load felt by the rotating blading as it passes through the velocity distortion field which is stationary in space. The tangential component of the blade loading (or circulation) is proportional to the change in tangential velocity across the row, either in the stationary or rotational sense.

The fluctuation in this value is indicative of the amplitude of oscillatory forces that the blading will feel,

$$\delta(\Delta v) = |(v_3 - v_2) - (\bar{v}_3 - \bar{v}_2)| \tag{25}$$

Manipulation of the equation involving the total fluctuating load, Eq. (15), and the mean value, Eq. (17c) leads to the result

$$\delta(\Delta v)/\epsilon_1 = \{1 - 2(\epsilon_4/\epsilon_1)_{stage} \cos \varphi_4 + (\epsilon_4/\epsilon_1)^2_{stage}\}^{1/2}(1 + a_1^2)/(b_3 - a_4) \tag{26}$$

It will be seen that the blade load fluctuation is approximately equal to

$$\delta(\Delta v)/\epsilon_1 \approx \{1 - (\epsilon_4/\epsilon_1)_{stage}\}(1 + a_1^2)/(b_3 - a_4) \tag{27}$$

when the phase shift φ_4 is small. Thus, the design criteria of best attenuation and small load fluctuation are generally incompatible, and design compromises are necessary.

Results

The independent parameters chosen to study behavior of the derived equations are (1) the rotor's "fluid" stagger angle defined by the mean tangent of the relative gas inlet and outlet angles

$$\tan \gamma = (b_2 + b_3)/2 \tag{28}$$

(2) the rotor velocity ratio

$$U/\bar{u} = b_3 - a_4 \tag{29}$$

and (3) the stage loading coefficient

$$W/U^2 = \Delta v/U = (a_4 - a_1)/(b_3 - a_4) \tag{30}$$

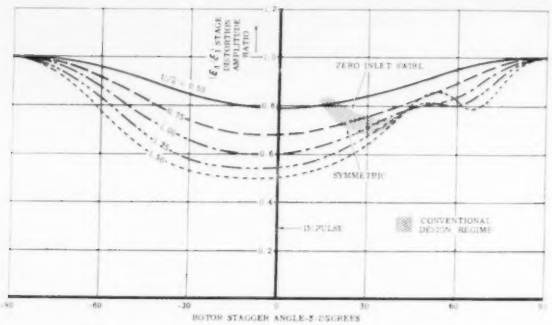

FIG. 2. Effect of wheel speed on velocity distortion amplitude ratio through compressor stages ($W/U^2 = -0.50$).

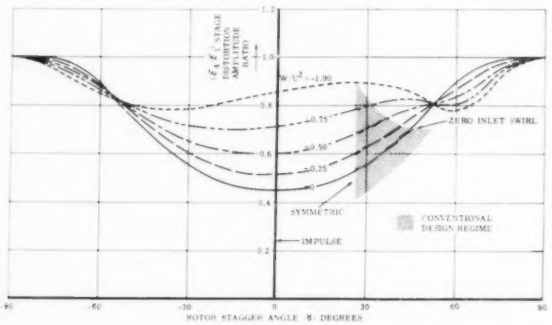

FIG. 3. Effect of stage loading on velocity distortion amplitude ratio through compressor stages ($U/\bar{u} = 1.00$).

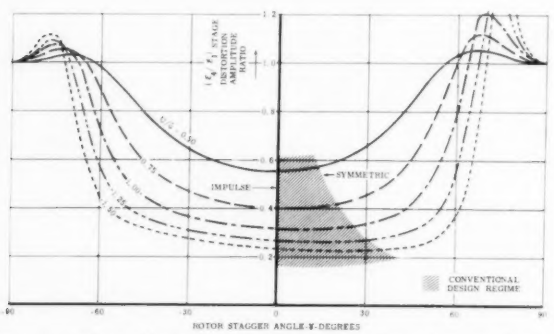

FIG. 4. Effect of wheel speed on velocity distortion amplitude ratio through turbine stages ($W/U^2 = 2.00$).

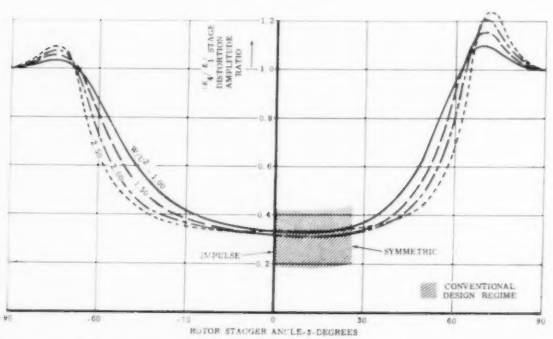

FIG. 5. Effect of stage loading on velocity distortion amplitude ratio through turbine stages ($U/\bar{u} = 1.00$).

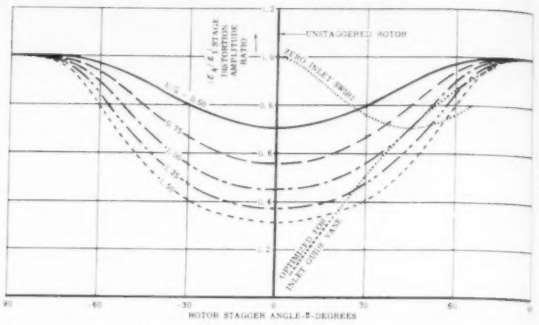

FIG. 6. Effect of wheel speed on velocity distortion amplitude ratio through freewheeling stages ($W/U^2 = 0$).

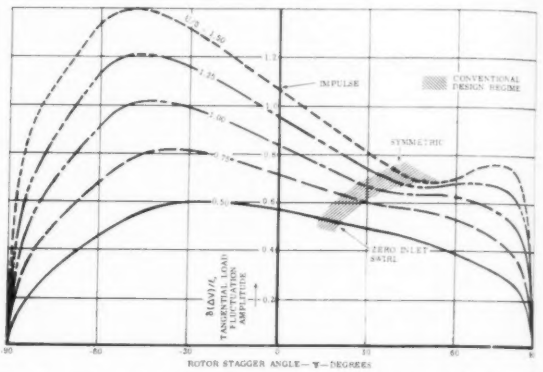

FIG. 7. Effect of wheel speed on tangential blade load fluctuation in compressor stages ($W/U^2 = -0.50$).

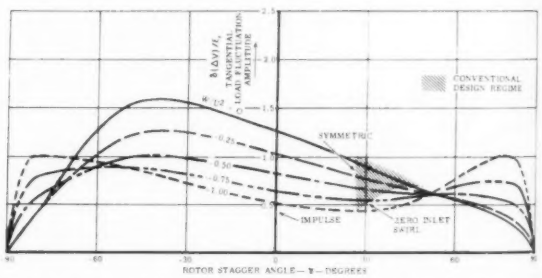

FIG. 8. Effect of stage loading on tangential blade load fluctuation in compressor stages ($U/\bar{u} = 1.00$).

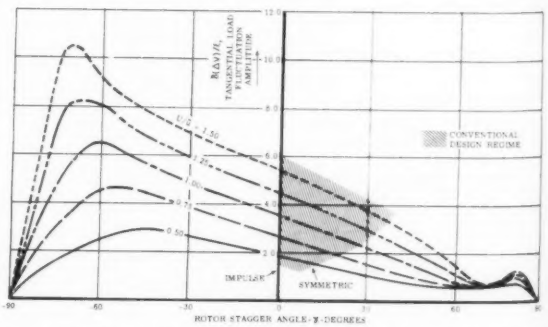

FIG. 9. Effect of wheel speed on tangential blade load fluctuation in turbine stages ($W/U^2 = 2.00$).

Figs. 2 through 11 summarize some typical results obtained from the foregoing analysis for turbines, compressors, and freewheeling (or very lightly loaded) stages. Stage velocity distortion amplitude ratio and tangential blade load fluctuation are shown as they are affected by stage loading and wheel speed over the range of blade stagger angles for representative values of these various parameters.

Conventional design regimes are indicated on these diagrams by shaded areas with the representative limits of: (1) compressors—design regime defined by locus of symmetric staging ($b_3 = -a_1$) and the locus of stages designed for zero inlet swirl ($a_1 = 0$); (2) turbines—design regime defined by locus of symmetric staging ($b_3 = -a_1$) and the locus of impulse stages ($\gamma = 0$); and (3) freewheeling stages—design criterion of zero inlet swirl ($a = 0$), or zero blade stagger ($\gamma = 0$), or the locus, derived from the attenuation equation, which gives the optimum attenuation for a given inlet swirl angle

$$b = a \pm (1 + a^2)^{1/2} \tag{31}$$

Arbitrary Inlet Profiles

The analysis has been carried out for a pure harmonic velocity distortion. But, because of the linearized nature of the solution, any arbitrary inlet distortion profile may be handled as the summation of its harmonic components. For an inlet profile defined by

$$u_1 = \bar{u} + \sum_n (\epsilon_1)_n \sin [ny/r + (\varphi_1)_n] \tag{32}$$

the velocity at exit (referred to the same mean streamline) will be given by

$$u_4 = \bar{u} + (\epsilon_4/\epsilon_1)_{stage} \sum_n (\epsilon_1)_n \sin [ny/r + (\varphi_1)_n + \varphi_4] \tag{33}$$

which is equivalent to

$$u_4 = \bar{u} + (\epsilon_4/\epsilon_1)_{stage}[(u_1 - \bar{u}) \cos \varphi_4 + (u_1^* - \bar{u}) \sin \varphi_4] \tag{34}$$

The function u_1^* is the complementary function of u_1 and is defined by

$$u_1^* = \bar{u} + \sum_n (\epsilon_1)_n \cos [ny/r + (\varphi_1)_n] \tag{35}$$

with $(\epsilon_4/\epsilon_1)_{stage}$ and (φ_4) given by Eqs. (24) and (21). Fig. 12 shows the effect of a compressor stage on a typical inlet distortion.

Conclusions

The foregoing analysis indicates the following general conclusions.

(1) *Compressors*

Conventional design practice lies in regime for minimizing the load fluctuation felt by the rotor blades. Attenuations of 0.7 to 0.8 are probable for typical stages. Better attenuation is achievable if designs could incorporate lower reaction staging.

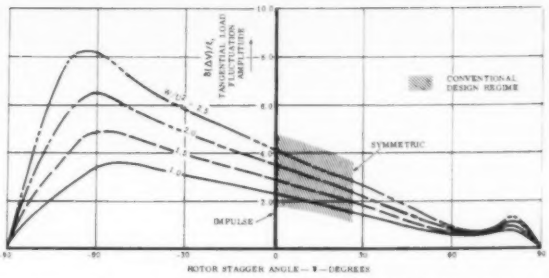

FIG. 10. Effect of stage loading on tangential blade load fluctuation in turbine stages ($U/\bar{u} = 1.00$).

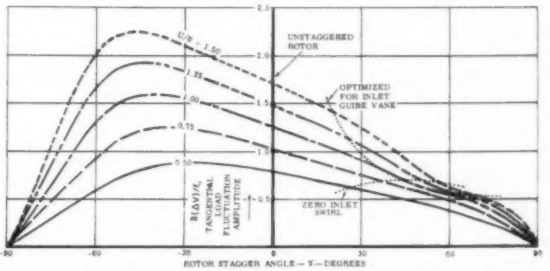
UNSTAGGERED ROTOR
OPTIMIZED FOR INLET GUIDE VANE
ZERO INLET SWIRL
BLADE TANGENTIAL LOAD FLUCTUATION AMPLITUDE
ROTOR STAGGER ANGLE — γ — DEGREES

FIG. 11. Effect of wheel speed on tangential blade load fluctuation in freewheeling stages ($W/U^2 = 0$).

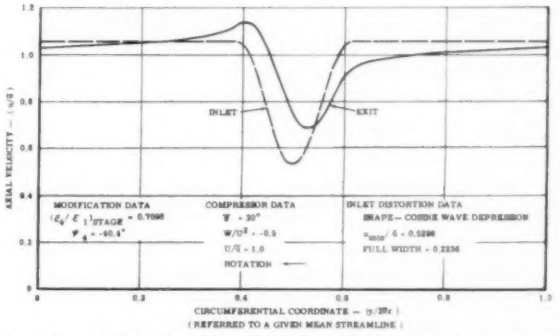

FIG. 12. Modification of a distortion profile through a typical compressor stage.

(2) *Turbines*

Conventional design practice lies in the regime for best attenuation of distortions. Attenuations of 0.3 to 0.4 are probable for typical stages. The attenuation is insensitive to stage loading. Higher reaction stage design would result in lower blade load fluctuation.

(3) *Freewheeling (or Lightly Loaded) Stages*

Design without inlet swirl is relatively ineffective, giving, at best, an attenuation of 0.71 when the rotor blades are staggered at 45°. For a given wheel speed, optimum attenuation is achieved with unstaggered rotor blading and appropriate inlet guide vane swirl to induce design wheel speed. For a given inlet swirl, and no wheel speed limitation, optimum attenuation is achieved by staggering the rotor at an angle given by Eq. (31).

In all cases, higher design speed results in better attenuation and higher load fluctuations.

Influence of Thermal Stresses on the Aeroelastic Stability of Supersonic Wings

M. A. BIOT*

Cornell Aeronautical Laboratory, Inc.

SUMMARY

The theory of static aeroelastic stability of supersonic wings including chordwise bending, as developed in reference 1, is further extended to include the influence of stresses arising from thermal gradients. The wing spanwise twist distribution is found to obey an ordinary differential equation of the fourth order whose coefficients depend on the thermal gradients. The influence of finite deformation is taken into account by the fact that the coefficients of the differential equation also depend on the amplitude of the deformation. The thermal stresses affect the stability in two distinct and independent ways, through its influence on the effective torsional stiffness and on the anticlastic effect. These factors act in opposite directions in such a way that if the thermal stress produces an increase in torsional stability it decreases the anticlastic stability, and vice versa. It is possible to embody the effect of the thermal stresses in a single parameter. Stability curves constitute a single family in this thermal parameter and plots are shown for three numerical values of the parameter.

EVALUATION OF THE MEMBRANE STRESS

IN REFERENCE 1 we have investigated the aeroelastic stability of supersonic wings including chordwise bending. It was found that the stability is extremely sensitive to the anticlastic effect—i.e., the tendency of the wing to acquire a saddle shape as it deflects. It must be expected that thermal stresses have a strong influence on the anticlastic effect and therefore also on the aeroelastic stability. Our purpose here is to give a simplified treatment, leading to an evaluation of the influence of thermal stresses on the wing stability, including the chordwise bending, the anticlastic effects, the change in effective torsional stiffness, and the nonlinear aspects due to finite deformation.

We follow the procedure developed in Section 7 of reference 1. This is a modified strip method which takes into account the influence of Poisson's ratio along with the membrane stresses. We consider a cantilever wing of rectangular plan form and double-wedge airfoil section (see Fig. 1). The method, however, is not restricted to this particular configuration. For simplicity, we shall assume the temperature distribution to be parabolic along the chord and independent of the spanwise coordinate. As is pointed out below, this is an approximation which embodies the essential temperature parameter. The present treatment is easily extended to cases of nonuniform distribution along the span by introducing a spanwise variation of this parameter. Also, as is pointed out below, the equivalent parameter for a nonparabolic distribution may be introduced by an averaging method.

We represent the chordwise temperature distribution by

$$\theta = \{[(\theta_1 + \theta_2)/2] - \theta_0\}\ (x^2/l^2) + [(\theta_2 - \theta_1)/2]\ (x/l) + \theta_0 \quad (1)$$

where θ_0 is the temperature at the midchord ($x = 0$) while θ_1, θ_2 are temperatures, respectively, at the leading edge ($x = -l$) and the trailing edge ($x = l$). These temperatures are taken to be average temperatures across the thickness.

We denote by σ_{xx} and σ_{yy} the two stress components in the plane of the wing. It is easily shown by proceeding as in the theory of plates for large deformation[1] that they satisfy the equation

$$\nabla^2(\sigma_{xx} + \sigma_{yy} + \alpha_t E\theta) = -E\gamma \quad (2)$$

where α_t (assumed constant) is the coefficient of thermal expansion and γ is the Gaussian curvature of the deflected wing surface,

$$\gamma = w_{yy}\, w_{xx} - w_{xy}^2 \quad (3)$$

The subscripts indicate partial derivatives $\partial^2/\partial x^2$, $\partial^2/\partial y^2$, $\partial^2/\partial x\,\partial y$ of the deflection w taken positive upward in Fig. 1. We may assume the membrane stress to be only spanwise—i.e., $\sigma_{xx} = 0$. Moreover, we may put

$$\alpha_t \nabla^2\theta = (\alpha_t/l^2)\ [\theta_1 + \theta_2 - 2\theta_0] = \delta \quad (4)$$

This is a quantity proportional to the chordwise curvature of the temperature distribution. It is the significant temperature parameter. Since we take $\sigma_{xx} = 0$, we write Eq. (2) as

$$\partial^2\sigma_{yy}/\partial x^2 = -E(\gamma + \delta) \quad (5)$$

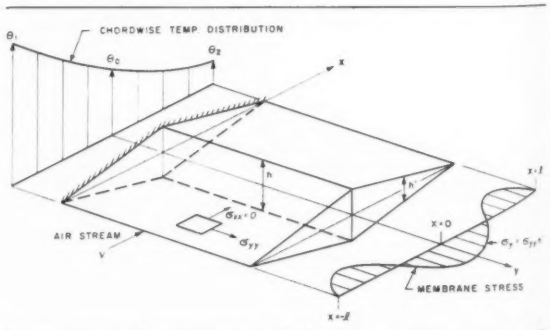

FIG. 1. General configuration of the wing, temperatures, and stresses.

Received September 5, 1956.

* Research Consultant.

In first approximation we may assume the curvature γ to be constant along the chord. We see immediately the reason for which we have assumed a parabolic variation of the temperature since this yields a constant value for δ. The effect of the temperature then plays the same role as the curvature γ, and we may therefore proceed exactly as Section 7 of reference 1. There is one difference, however, which constitutes an improvement. In the previous work we considered the total membrane stress—i.e., the stress σ_{yy} integrated across the local thickness h'.

$$\sigma_y = \sigma_{yy} h'$$

and we assumed that it satisfied the approximate equation, Eq. (7.1) of reference 1,

$$\partial^2 \sigma_y / \partial x^2 = -Eh'\gamma \tag{6}$$

Actually it is more correct to use Eq. (5), and we shall rederive the theory on the basis of Eq. (5) instead of Eq. (6).

The distribution of the stress along the chord is obtained by integrating Eq. (5) and choosing the constants of integration in such a way that the total stress is self-equilibrating—i.e.,

$$\int_{-l}^{+l} h'\sigma_{yy}\, dx = 0 \qquad \text{and} \qquad \int_{-l}^{+l} h'\sigma_{yy} x\, dx = 0 \tag{7}$$

The wing has a double-wedge cross section of maximum thickness h. Hence,

$$h' = h\left[1 - \frac{|x|}{l}\right] \tag{8}$$

This yields

$$\sigma_{yy} = (1/2)E(\gamma + \delta)\,[(l^2/6) - x^2] \tag{9}$$

The chordwise distribution of the total membrane stress is

$$\sigma_y = \frac{1}{2} E(\gamma + \delta) hl^2 \left(1 - \frac{|x|}{l}\right)\left(\frac{1}{6} - \frac{x^2}{l^2}\right) \tag{10}$$

Differential Equation for the Wing Twist

We now evaluate the torque, acting on a strip of spanwise coordinate y. The local wing deflection is approximately

$$w' = w - \alpha x$$

where w and α are, respectively, the deflection and angle of attack at the midchord.* The local spanwise curvature is

$$w_{yy}' = w_{yy} - x\alpha_{yy} \tag{11}$$

where α_{yy} is the second spanwise derivative of α. The wing considered as a thin plate deflects under an equivalent load per unit area equal to

$$q' = \sigma_y w_{yy}' - q \tag{12}$$

* Note that w is used for w' in the previous section. In the equations below, w_{yy}, w_{xx}, and w_{xy} designate the second derivatives at the midchord.

where q is the aerodynamic load [see Eq. (1.1), reference 1]. Hence, from Eq. (11),

$$q' = \sigma_y w_{yy} - \alpha_{yy}\sigma_y x + q \tag{13}$$

This load produces a torque, made up of two terms. One term T' is due to the load $-\alpha_{yy}\sigma_y x$, the other T is an aerodynamic torque, originating with the chordwise curvature, which itself is caused by the load q'. We shall first evaluate T'. We find

$$T' = 2\alpha_{yy}\int_0^l \sigma_y x^2\, dx = \frac{-7}{360} E(\gamma + \delta) hl^3 \alpha_{yy} \tag{14}$$

The torque is positive in the stalling direction.

The chordwise curvature w_{xx} produced by the load q' is obtained as in reference 1 by a method of virtual work, and by assuming that w_{xx} is constant along the chord. We derive

$$w_{xx} + \nu w_{yy} = -(7/30)(1 - \nu^2) w_{yy}(\gamma + \delta) \times (l^4/h^2) + (2/3)(k/l)\alpha \tag{15}$$

In this expression, ν is Poisson's ratio and k is the stability parameter defined in reference 1 as

$$k = 24(M^2/\sqrt{M^2 - 1})\,[\rho c^2(1 - \nu^2)/E]\,(l/h)^2 \tag{16}$$

Eq. (15) is the same as Eq. (7.8) of reference 1, except for the addition of a temperature parameter δ and the numerical coefficient 7/30 instead of 11/15. The latter difference is due to our use of Eq. (5) instead of Eq. (6) for the membrane stress distribution. We must remember that γ contains w_{xx}, hence, solving Eq. (15) for w_{xx}, we obtain

$$w_{xx} = -\nu_1' f w_{yy} + (2/3) f (k/l)\alpha \tag{17}$$

$$\text{with } \nu_1' = \nu - (7/30)(1 - \nu^2)(l^4/h^2)(w_{xy}^2 - \delta) \tag{18}$$

$$f = 1/[1 + (7/30)(1 - \nu^2)(l^4/h^2) w_{yy}^2] \tag{19}$$

The coefficient $\nu_1' f$ is an "effective" Poisson's ratio which gives an immediate evaluation of the magnitude of the anticlastic effect associated with a spanwise bending w_{yy}. The effective Poisson's ratio is increased if δ is positive—i.e., if the temperature at the midchord is lower than the average of the leading- and trailing-edge temperatures. We shall discuss the magnitude of this effect later.

The chordwise curvature w_{xx} produces an aerodynamic torque which is easily evaluated. Its value (positive in the stalling direction) is

$$T = (4/3)(M^2/\sqrt{M^2 - 1})\rho c^2 l^2 [(2/3) fk\alpha - \nu_1' f l w_{yy}] \tag{20}$$

The total torque being $T' + T$, we may write a differential equation for the spanwise distribution of the wing twist

$$-Q(d^2\alpha/dy^2) = T' + T \tag{21}$$

where Q is the wing torsional stiffness. Substituting the value of T' from Eq. (14), we may write

$$-Q_1(d^2\alpha/dy^2) = T \tag{22}$$

with an "effective" torsional stiffness

$$Q_1 = Q - (7/360)\, E(\gamma + \delta)hl^5 \qquad (23)$$

We see immediately that if δ is positive—i.e., if the distribution of temperature is concave upward—its effect is to lower the effective torsional rigidity. The effect of the twist w_{xy} alone appears through $\gamma = -w_{xy}^2$ which gives a measure of the increase of torsional rigidity due to finite twist. Torsional instability occurs for $Q_1 = 0$. For infinitesimal deformation, $\gamma = 0$, and this gives the stability criterion in twist,

$$\delta = (360/7)\,(Q/Ehl^5) \qquad (24)$$

When δ exceeds this value a finite γ appears, the magnitude of which is again derived from the condition $Q_1 = 0$—i.e.,

$$-\gamma = \delta - (360/7)\,(Q/Ehl^5) \qquad (25)$$

As mentioned above, the effect of the temperature on the aeroelastic stability appears, not only through a change in effective torsional rigidity, but also through the anticlastic effect. To evaluate the combined effect, we may proceed entirely as in Section 7 of reference 1, provided we replace Q by Q_1, and ν' by ν_1'. We write

$$P_1 = h^3lE/24(1 - \nu^2)Q_1 \qquad (26)$$

$$R = h^3l/6(1 - \nu^2)I_1 \qquad (27)$$

where I_1 is the wing cross section moment of inertia about the chord. Furthermore, we put

$$\left.\begin{aligned} H_1 &= (8/9)k^2P_1(b^2/l^2) \\ S_1 &= (3/2)\,\nu_1'R(b^2/l^2) \end{aligned}\right\} \qquad (28)$$

where b is the wing span.

The differential equation for the wing twist in terms of a nondimensional spanwise coordinate $\eta = y/b$ is then identical with Eq. (7.17) of reference 1, except that H and S are replaced by H_1 and S_1—i.e.,

$$(d^4\alpha/d\eta^4) + H_1f(d^2\alpha/d\eta^2) - fH_1S_1\alpha = 0 \qquad (29)$$

Discussion

The stability diagram in the $\sqrt{H_1}$, S_1 plane is the same as that given by Fig. 19 in the above reference. In order to discuss the effect of the temperature it is convenient to separate the parameter δ in the expressions of H_1 and S_1,

$$H_1 = H(Q/Q_1) \qquad S_1 = S(\nu_1'/\nu') \qquad (30)$$

H and S are defined as in reference 1:

$$\left.\begin{aligned} H &= (8/9)k^2P(b^2/l^2) \\ S &= (3/2)\nu'R\,(b^2/l^2) \\ P &= h^3lE/24(1 - \nu^2)Q \\ \nu' &= \nu - (7/30)\,(1 - \nu^2)\,(l^4/h^2)w_{xy}^2 \end{aligned}\right\} \qquad (31)$$

Because we have used Eq. (5) instead of Eq. (6) expressions for ν' and f are different from those of reference 1. The temperature parameter is contained only in the factors Q/Q_1 and ν_1'/ν'. The influence of the temperature on the $\sqrt{H}$, S stability diagram is therefore obtained by a change of scale of the coordinate axes. Consider, for instance, the case of incipient instability—i.e., small deformation—then $f = 1$, $\nu' = \nu$, $\gamma = 0$. The torsional rigidity of the thin double wedge is

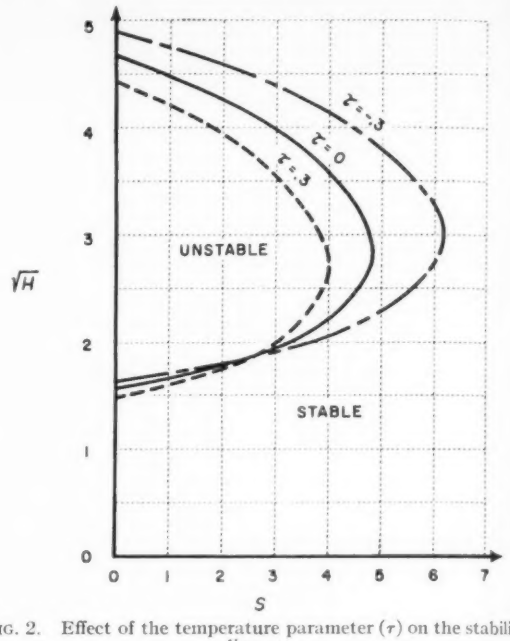

FIG. 2. Effect of the temperature parameter (τ) on the stability diagram.

$$Q = (1/6)lh^3G = (1/12)\,[lh^3E/(1 + \nu)] \qquad (32)$$

hence (with $\nu = \nu'$ and $w_{xy} = 0$)

$$\left.\begin{aligned} Q_1/Q &= 1 - (7/30)\,(1 + \nu)\,(l^4\delta/h^2) \\ \nu_1'/\nu' &= 1 + (7/30)\,[(1 - \nu^2)/\nu]\,(l^4\delta/h^2) \end{aligned}\right\} \qquad (33)$$

The influence of the temperature is contained in the nondimensional parameter

$$\tau = l^4\delta/h^2 = \alpha_t[\theta_1 + \theta_2 - 2\theta_0]\,(l^2/h^2) \qquad (34)$$

For steel we put $\alpha_t = 7.22 \times 10^{-6}/°\text{F.}$ and $\nu = 0.3$. If we assume $(1/2)\,(\theta_1 + \theta_2) - \theta_0 = 208°\text{F.}$ and $l/h = 10$, this case corresponds to $\tau = 0.3$. Fig. 2 shows a plot of the diagram for three values $\tau = 0.3$, $\tau = 0$, and $\tau = -0.3$. The value of $\tau = -0.3$ corresponds to a mid-chord temperature in excess of the average temperatures of leading and trailing edge. This can happen during a cooling period of a heated wing.

Fig. 2 indicates that for positive τ the effect of the temperature is destabilizing with regard to torsional rigidity and stabilizing with regard to the anticlastic effect. An interesting result is that for negative τ (cooling phase) the influence of the temperature on the stability is reversed.

The present treatment can easily be extended to include spanwise variations of temperature and the effect of the wing tip and aspect ratio on the structural

(*Continued on page 429*)

On Magnus Effects Caused by the Boundary-Layer Displacement Thickness on Bodies of Revolution at Small Angles of Attack

JOHN C. MARTIN*

Ballistic Research Laboratories, Aberdeen Proving Ground

SUMMARY

The effect of the boundary-layer displacement thickness on Magnus effects is investigated by analyzing the laminar boundary layer on a cylindrical portion of a slender body of revolution. A solution of the three-dimensional boundary-layer equations is obtained. The displacement thickness is found and then is used to calculate the Magnus force and center of pressure by slender body theory.

The Magnus effects caused by turbulent boundary layers are investigated under certain assumptions, and values from the resulting expression for the center of pressure are compared with data obtained from range firings.

SYMBOLS

a	= radius of cylindrical portion of body
C_p	= pressure coefficient {pressure/[(1/2) ρ V^2]}
d	= diameter of cylindrical portion of body
F_m	= Magnus force
F	= Magnus force per unit length
$f_0, f_1, \ldots f_5$ g_0, g_1, g_2, g_3 h_0, h_1	= functions describing boundary-layer velocity components
K_F	= Magnus force coefficient $[F_m/2\rho V^2 \alpha d^2 (V_r/V)]$
l	= length of cylindrical portion of body
P	= pressure
q_0	= dynamic pressure [(1/2) ρ V^2]
R, ϑ	= polar coordinates
Re	= Reynolds Number based on cylindrical portion of body
u, v, w	= boundary-layer velocity components in the x, y, z directions
u_0, v_0	= nondimensional boundary-layer velocity components for zero spin and zero yaw (velocity/V)
u_1, u_2 v_1, v_2 w_1, w_2	= first- and second-order perturbations of the nondimensional boundary-layer velocity components in α and/or V_r/V
V	= free-stream velocity
V_r	= surface velocity of cylindrical portion of body
x, y, z	= rectangular coordinates (see Fig. 4)
$\bar{x}$	= distance from the nose to the center of pressure of the Magnus force
α	= angle of attack or yaw
Δ	= boundary-layer displacement thickness
Δ_0	= boundary-layer displacement thickness for $\alpha = 0$ and $V_r = 0$
Δ_1, Δ_2	= first- and second-order perturbations of the displacement thickness with α and/or V_r/V
ρ	= density
δ	= boundary-layer thickness
δ_0^*	= boundary-layer displacement thickness at the body base
η	= $y\sqrt{V/\nu x}$
ν	= kinematic viscosity
Φ	= potential function
ϕ	= perturbation potential function

Received September 18, 1956.

* Aerodynamicist, Airflow Branch, Exterior Ballistics Laboratory.

The author wishes to acknowledge the contribution of Mr. Nathan Gerber of the Airflow Branch, who checked the many mathematical operations performed in the analysis and aided in preparing the paper for publication.

INTRODUCTION

THE TERM "Magnus effect" was originally used to refer to the lift produced by a rotating two-dimensional cylinder in a steady stream. This led to the use of the term to refer to the force and moment on spinning projectiles which are perpendicular to the plane of yaw. In this paper we shall use the term "Magnus effect" to refer to the force, together with its moment, acting perpendicular to the plane of yaw on a body of revolution which is spinning about its axis at a constant angle of yaw.

Up to the present no satisfactory explanation has been presented which explains the observed Magnus effects at small angles of yaw. It is the purpose of this paper to explain the production of the Magnus effects at small angles of yaw on certain types of bodies, to calculate the Magnus force and center of pressure under certain conditions, and to indicate some possible future investigations. The results of this paper show that the boundary layer can cause Magnus effects of the proper sign and magnitude at small angles of yaw even without separating ahead of the base.

To investigate the effect of the boundary-layer displacement thickness on the Magnus effect we shall analyze the laminar boundary layer on a cylindrical portion of a slender body of revolution. The three-dimensional boundary-layer equations for a cylindrical portion of a body of revolution are solved for small angles of attack and small rates of spin. The boundary-layer velocity components are used to calculate the boundary-layer displacement thickness, and this is used to compute the Magnus force and center of pressure by slender body theory.

The effects of the boundary layer ahead of the cylindrical portion of the body are assumed to have very little effect on the velocity profile of the boundary layer

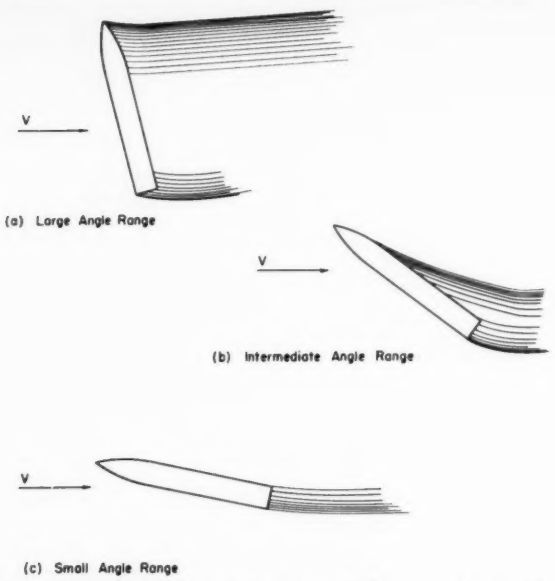

FIG. 1. An illustration of the types of flow associated with various angles of yaw.

on the cylindrical portion. This assumption simplifies the analysis considerably. Unfortunately, the validity of the assumption is not well established. For this reason it is felt that the results should be considered as being only rough approximations to the flow around a slender body such as is shown in Fig. 1. The results should correspond much more closely to the flow around this body if the boundary layer on the nose is removed at the base of the nose by suction. The results should also represent an approximation to the flow around an open end spinning cylinder at very small angles of yaw.

ANALYSIS

General Considerations

The flow around a slender spinning body of revolution at large angles of yaw is quite similar to the flow around a two-dimensional spinning circular cylinder [Fig. 1(a)]. In the large angle of attack range it seems logical that one could estimate the Magnus force and moment on the basis of experimental data obtained from a two-dimensional spinning cylinder in a steady flow.

As the angle of yaw is decreased the vortex filaments shed from the body approach the axis of the body [Fig. 1(b)]. In this region the author believes that experimental data obtained from a two-dimensional spinning cylinder in a steady flow would be of little value in estimating the Magnus effects; for the vorticity shed lies close to the body, and this is not the case for the analysis using the two-dimensional spinning cylinder concept. It is felt that two-dimensional considerations can be of value in studying the Magnus effects in this region, provided the presence of the vortex filaments which are shed from the body is given proper consideration. Therefore, as long as vorticity is shed from the body ahead of the base, at least part of the cause for the Magnus effects appears fairly clear.

At small angles of yaw there is no vorticity shed ahead of the base. On the basis of perfect fluid theory one would expect that there would be no Magnus effects since in the absence of viscosity the flow should be symmetrical with respect to the plane of yaw. It is helpful to consider a closed loop which travels with the fluid and encircles a spinning body of revolution as shown in Fig. 2. When the loop is well upstream of the body as in Fig. 2(a), it does not encircle any vorticity; therefore, the circulation around the loop is zero. For an ideal frictionless fluid the circulation around the loop will remain zero regardless of the path of the loop since the circulation around any closed curve moving with the fluid is constant (see, for example, page 203 of reference 1). It follows that, if one uses slender body theory, the cross flow would be the potential flow around a circular cylinder with zero circulation; and without considering the effects of the boundary layer the Magnus effects would be zero.†

Experiments indicate that in the small angle of yaw range Magnus effects do exist, and that they are strong enough to have a strong effect on the dynamic stability of spinning projectiles. Since perfect fluid theory predicts no Magnus effects in this range of yaw, we are led to suspect that it may be caused by the boundary layer. An explanation of the Magnus effect in this

† The loop argument can be applied to the cases where vortex filaments are shed from the body ahead of the base. In these cases the application of potential flow will yield finite values for the Magnus force and moment.

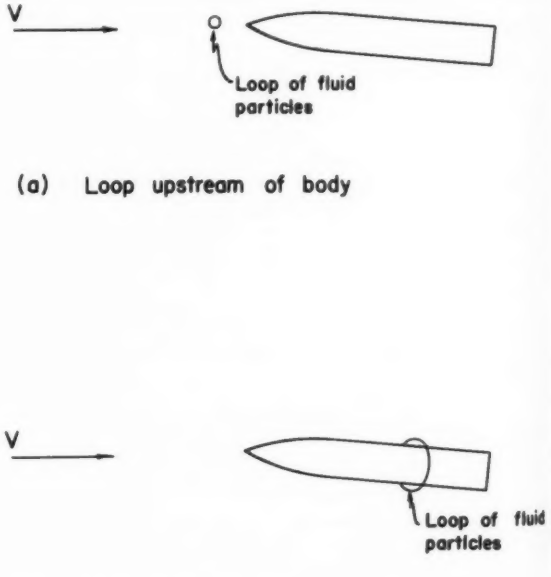

FIG. 2. Instantaneous positions of a closed loop of fluid particles which travels with the fluid and encircles a spinning body of revolution.

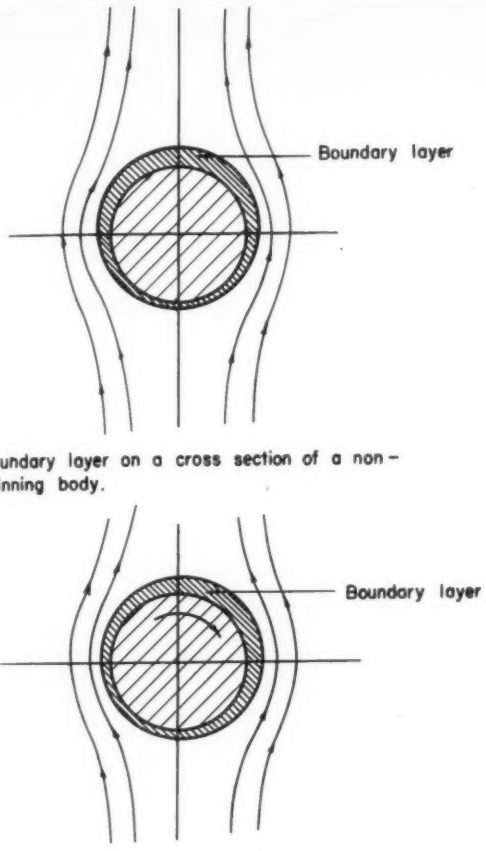

(a) Boundary layer on a cross section of a non-spinning body.

(b) Boundary layer on a cross section of a spinning body.

FIG. 3. An illustration of the effect of spin on the boundary layer on a body of revolution.

range was suggested to the author by Charles L. Poor of the Exterior Ballistics Laboratory.

This explanation is as follows. For zero spin, the cross flow causes the boundary layer to be thicker on the leeward side of the body than on the windward side [see Fig. 3(a)]. For the spinning body the moving surface tends to displace the thickened portion of the boundary layer [see Fig. 3(b)]. The reason for this is that in rotation the retreating surface will delay the thickening due to angle of yaw, whereas the advancing surface will advance the thickening due to angle of yaw. Thus the thick part of the boundary layer may be expected to be displaced in the direction of rotation. This produces an asymmetric boundary-layer displacement thickness. Since the boundary layer thickens in the downstream direction, the surface defined by the displacement surface on the cylindrical portion of the body resembles a slightly bent cylinder. For zero spin this slightly distorted cylinder bends toward the leeward and the bending is confined to the plane of yaw. When spin is present the direction of the bending has a component perpendicular to the plane of yaw, due to the shifting of the boundary layer [see Fig. 3(b)]. Thus, as far as the flow outside the boundary layer is concerned, the cylindrical portion of the body and its boundary layer can be replaced by a bent cylinder which has part of its bending perpendicular to the plane of yaw. It is the component of the bending which is perpendicular to the plane of yaw that causes the Magnus effect at small angles of yaw.

The effect of the boundary-layer displacement thickness on the Magnus effect will be investigated by analyzing the laminar boundary layer on a cylindrical portion of slender body of revolution (see Fig. 4). The "slender body" potential flow will be used for the flow outside the boundary layer. It will be assumed that the nose effects can be neglected when considering the boundary layer some distance down the body. The coordinate axes are chosen so that the x-axis is parallel to the axis of the body, the y-axis is normal to the body surface, and the z-axis is the distance along the surface of the body on the plane perpendicular to the axis of the body (see Fig. 4). The angle α and the ratio V_r/V are assumed to be small. All flows considered are assumed to be incompressible.

Boundary-Layer Equations

The differential equations of an incompressible viscous fluid are

$$\left.\begin{aligned} u\frac{\partial u}{\partial x} + v\frac{\partial u}{\partial y} + w\frac{\partial u}{\partial z} &= \frac{-1}{\rho}\frac{\partial P}{\partial x} + \nu\nabla^2 u \\ u\frac{\partial v}{\partial x} + v\frac{\partial v}{\partial y} + w\frac{\partial v}{\partial z} &= \frac{-1}{\rho}\frac{\partial P}{\partial y} + \nu\nabla^2 v \\ u\frac{\partial w}{\partial x} + v\frac{\partial w}{\partial y} + w\frac{\partial w}{\partial z} &= \frac{-1}{\rho}\frac{\partial P}{\partial z} + \nu\nabla^2 w \\ \frac{\partial u}{\partial x} + \frac{\partial v}{\partial y} + \frac{\partial w}{\partial z} &= 0 \end{aligned}\right\} \quad (1)$$

Under the usual boundary-layer assumptions, Eqs. (1) become[2]

$$u(\partial u/\partial x) + v(\partial u/\partial y) + w(\partial u/\partial z) = (-1/\rho)(\partial P/\partial x) + \nu(\partial^2 u/\partial y^2) \quad (2a)$$

$$u(\partial w/\partial x) + v(\partial w/\partial y) + w(\partial w/\partial z) = (-1/\rho)(\partial P/\partial z) + \nu(\partial^2 w/\partial y^2) \quad (2b)$$

$$(\partial u/\partial x) + (\partial v/\partial y) + (\partial w/\partial z) = 0 \quad (2c)$$

We shall assume that the pressure gradient along the body axis is zero, and that the pressure gradient in the z direction is given by slender body theory.[3] Thus,

$$\partial P/\partial x = 0$$

and

$$\partial P/\partial z = -\rho(4\alpha^2/a)V^2 \sin(z/a)\cos(z/a)$$

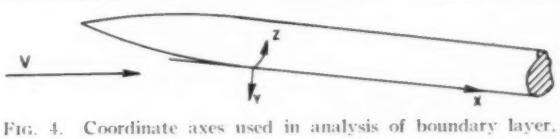

FIG. 4. Coordinate axes used in analysis of boundary layer.

Eqs. (2) now reduce to

$$u(\partial u/\partial x) + v(\partial u/\partial y) + w(\partial u/\partial z) = \nu(\partial^2 u/\partial y^2) \quad (3a)$$

$$u(\partial w/\partial x) + v(\partial w/\partial y) + w(\partial w/\partial z) = (4/a)\alpha^2 V^2 \sin(z/a)\cos(z/a) + \nu(\partial^2 w/\partial y^2) \quad (3b)$$

$$(\partial u/\partial x) + (\partial v/\partial y) + (\partial w/\partial z) = 0 \quad (3c)$$

Note that for zero angle of attack and no rotation the preceding equations reduce to the equations for the boundary layer on a flat plate with no pressure gradient.

The boundary conditions are (to the second power in α):

$$u/V]_{y=0} = 0; \qquad u/V]_{y=\infty} = 1 - (\alpha^2/2)$$

$$v/V]_{y=0} = 0; \qquad w/V]_{y=0} = V_r/V$$

$$w/V]_{y=\infty} = 2\alpha \sin(z/a)$$

Solution of Boundary-Layer Equations

We shall assume that the velocity components can be expressed in the form

$$u/V = u_0 + u_1 + u_2 \quad (4a)$$

$$v/V = v_0 + v_1 + v_2 \quad (4b)$$

$$w/V = w_1 + w_2 \quad (4c)$$

where u_0 and v_0 are nondimensional velocity components for zero spin and zero angle of yaw; (u_1, v_1, w_1) are perturbations of the first order in α or V_r/V; and (u_2, v_2, w_2) are of the order α^2, $\alpha V_r/V$, or $(V_r/V)^2$.

Substituting Eqs. (4) into Eqs. (3) yields the following system of partial differential equations:

(Equations independent of α and V_r/V)

$$u_0(\partial u_0/\partial x) + v_0(\partial u_0/\partial y) = (\nu/V)(\partial^2 u_0/\partial y^2) \quad (5a)$$

$$(\partial u_0/\partial x) + (\partial v_0/\partial y) = 0 \quad (5b)$$

(Equations of the first order in α and V_r/V)

$$u_0(\partial u_1/\partial x) + u_1(\partial u_0/\partial x) + v_0(\partial u_1/\partial y) + v_1(\partial u_0/\partial y) = (\nu/V)(\partial^2 u_1/\partial y^2) \quad (6a)$$

$$u_0(\partial w_1/\partial x) + v_0(\partial w_1/\partial y) = (\nu/V)(\partial^2 w_1/\partial y^2) \quad (6b)$$

$$(\partial u_1/\partial x) + (\partial v_1/\partial y) + (\partial w_1/\partial z) = 0 \quad (6c)$$

(Equations of the second order in α and V_r/V)

$$u_0(\partial u_2/\partial x) + u_1(\partial u_1/\partial x) + u_2(\partial u_0/\partial x) + v_0(\partial u_2/\partial y) + v_1(\partial u_1/\partial y) + v_2(\partial u_0/\partial y) + w_1(\partial u_1/\partial z) = (\nu/V)(\partial^2 u_2/\partial y^2) \quad (7a)$$

$$u_0(\partial w_2/\partial x) + u_1(\partial w_1/\partial x) + v_0(\partial w_2/\partial y) + v_1(\partial w_1/\partial y) + w_1(\partial w_1/\partial z) = 4(\alpha^2/a)\sin(z/a)\cos(z/a) + (\nu/V)(\partial^2 w_2/\partial y^2) \quad (7b)$$

$$(\partial u_2/\partial x) + (\partial v_2/\partial y) + (\partial w_2/\partial z) = 0 \quad (7c)$$

The boundary conditions are

for $y = 0$:

$$u_0 = 0 \quad v_0 = 0$$
$$u_1 = 0 \quad v_1 = 0 \quad w_1 = V_r/V$$
$$u_2 = 0 \quad v_2 = 0 \quad w_2 = 0$$

for $y = \infty$:

$$u_0 = 1$$
$$u_1 = 0 \quad w_1 = 2\alpha \sin(z/a)$$
$$u_2 = -\alpha^2/2 \quad w_2 = 0$$

Eqs. (5) and their boundary conditions are satisfied by the well-known Blasius solution for the flat plate This solution is

$$u_0 = f_0'(\eta) \quad (8a)$$

$$v_0 = (1/2)\sqrt{\nu/xV}\,[\eta f_0'(\eta) - f_0(\eta)] \quad (8b)$$

where $\eta = y\sqrt{V/\nu x}$, and the function f_0 satisfies the ordinary differential equation

$$f_0(\eta)f_0''(\eta) + 2f_0'''(\eta) = 0 \quad (9)$$

with the conditions that

$$f_0'(0) = f_0(0) = 0 \quad \text{and} \quad f_0'(\infty) = 1$$

The function f_0 and its first two derivatives are tabulated in a number of publications.[4, 5]

In the case of an open-end cylinder, the variable, x, is measured from the leading edge of the cylinder. In the case of a body such as is illustrated in Fig. 1, the variable, x, is measured from the base of the nose if the boundary layer on the nose is removed. In case the boundary layer on the nose is not removed, x is measured from some fictitious point ahead of the nose. This point is determined by the following considerations: The length of cylinder is determined which has the same boundary layer at its base that the nose has at its base. This length of cylinder is assumed to replace the nose. The variable, x, is measured from the leading edge of the equivalent cylinder which is made up of the original cylinder plus the length of cylinder which represents the nose.

The next step is the solution of Eqs. (6). Eq. (6b) is of the same form as Eq. (5a); thus it has a solution of the form

$$w_1 = C(z) + K(z)\,f_0'(\eta)$$

where $C(z)$ and $K(z)$ can be chosen so that the boundary conditions are satisfied. The resulting expression for w_1 is

$$w_1 = (V_r/V) + [2\alpha \sin(z/a) - (V_r/V)]\,f_0'(\eta) \quad (10)$$

For the special case of zero angle of attack, Eq. (10) agrees with a result obtained by Howarth[6] for the boundary layer on an open-end rotating cylinder. The solutions for u_0, v_0, and w_1 suggest that u_1 and v_1 may be of the form

$$u_1 = 2\alpha(x/a)\,f_1(\eta)\cos(z/a) \quad (11a)$$

$$v_1 = (\alpha/a)\sqrt{x\nu/V}\,g_0(\eta)\cos(z/a) \quad (11b)$$

where f_1 and g_0 are functions of η only. Substituting Eqs. (11) into Eqs. (6a) and (6c) leads to the following ordinary differential equations:

$$2 f_0' f_1 - \eta f_1 f_0'' - f_0 f_1' + g_0 f_0'' = 2 f_1'' \quad (12a)$$

$$g_0' = \eta f_1' - 2 f_1 - 2 f_0' \quad (12b)$$

and the conditions that

$$f_1(0) = g_0(0) = f_1(\infty) = 0$$

The final step is the solution of Eqs. (7); w_2 can be found from Eq. (7b) and its values used in determining u_2 and v_2 from Eqs. (7a) and (7c). Writing w_2 in the form

$$w_2 = \alpha(V_r/V)(x/a) h_0(\eta) \cos(z/a) + \alpha^2 (x/a) h_1(\eta) \sin(z/a) \cos(z/a) \quad (13)$$

where h_0 and h_1 are functions of η only, and substituting it into Eq. (7b), it is found that h_0 and h_1 must satisfy the ordinary differential equations:

$$f_0' h_0 - (1/2) f_0 h_0' + \eta f_1 f_0'' - g_0 f_0'' + 2(1 - f_0') f_0' = h_0'' \quad (14a)$$

$$f_0' h_1 - (1/2) f_0 h_1' - 2\eta f_1 f_0'' + 2 g_0 f_0'' + (2 f_0')^2 - 4 = h_1'' \quad (14b)$$

and the conditions that

$$h_0(0) = h_1(0) = h_0(\infty) = h_1(\infty) = 0$$

The forms of u_0, v_0, u_1, and v_1, and Eqs. (7a) and (7c) suggest that u_2 and v_2 are of the forms:

$$u_2 = \alpha (V_r/V)(x/a)^2 f_2(\eta) \sin(z/a) + (\alpha x/a)^2 [f_3(\eta) + f_4(\eta) \cos(2z/a)] - (\alpha^2/2) f_5'(\eta) \quad (15a)$$

$$v_2 = \sqrt{x\nu/V} \{(\alpha x/a^2)(V_r/V) g_1(\eta) \sin(z/a) + (\alpha^2 x/a^2)[g_2(\eta) + g_3(\eta) \cos(2z/a)]\} - (\alpha^2/4) \sqrt{\nu/(Vx)} [\eta f_5'(\eta) - f_5(\eta)] \quad (15b)$$

Substituting Eqs. (15) into Eqs. (7a) and (7c), it is found that f_2, f_3, f_4, f_5, g_1, g_2, and g_3 must satisfy the following ordinary differential equations and conditions:

$$2 f_2 - (\eta/2) f_2' + g_1' - h_0 = 0 \quad (16a)$$

$$2 f_0' f_2 - (1/2) f_0 f_2' + g_1 f_0'' - 2 f_1 + 2 f_1 f_0' - (\eta/2) f_2 f_0'' = f_2'' \quad (16b)$$

where $f_2(0) = g_1(0) = f_2(\infty) = 0$,

$$2 f_3 - (\eta/2) f_3' + g_2' = 0 \quad (17a)$$

$$2 f_3 f_0' - (1/2) f_0 f_3' + 2(f_1)^2 - \eta f_1 f_1' + g_0 f_1' - (\eta/2) f_3 f_0'' + f_0'' g_2 - 2 f_0' f_1 = f_3'' \quad (17b)$$

where $f_3(0) = g_2(0) = f_3(\infty) = 0$,

$$2 f_4 - (\eta/2) f_4' + g_3' + h_1 = 0 \quad (18a)$$

$$2 f_0' f_4 - (1/2) f_0 f_4' + 2(f_1)^2 - \eta f_1 f_1' - (\eta/2) f_4 f_0'' + g_0 f_1' + f_0'' g_3 + 2 f_0' f_1 = f_4'' \quad (18b)$$

where $f_4(0) = g_3(0) = f_4(\infty) = 0$, and

$$f_0 f_5'' + f_5 f_0'' = -2 f_5''' \quad (19)$$

where $f_5(0) = f_5'(0) = 0$ and $f_5'(\infty) = 1$.

The velocity components in the boundary layer are then given by†

$$u/V = f_0'(\eta) + 2(\alpha x/a) f_1(\eta) \cos(z/a) + \alpha (V_r/V)(x/a)^2 f_2(\eta) \sin(z/a) + (\alpha x/a)^2 \times [f_3(\eta) + f_4(\eta) \cos(2z/a)] - (\alpha^2/2) f_5'(\eta) \quad (20a)$$

$$v/V = \sqrt{\nu/Vx} \{(1/2)[\eta f_0'(\eta) - f_0(\eta)] + (\alpha x/a) g_0(\eta) \cos(z/a) + \alpha (V_r/V) \times (x/a)^2 g_1(\eta) \sin(z/a) + (\alpha x/a)^2 [g_2(\eta) + g_3(\eta) \cos(2z/a)] - (\alpha^2/4)[\eta f_5'(\eta) - f_5(\eta)]\} \quad (20b)$$

$$w/V = (V_r/V) + [2\alpha \sin(z/a) - (V_r/V)] f_0'(\eta) + (V_r/V)(\alpha x/a) h_0(\eta) \cos(z/a) + \alpha^2 (x/a) h_1(\eta) \sin(z/a) \cos(z/a) \quad (20c)$$

Since the product $(\alpha x/a)$ appears in some of the terms, the solution is limited in x as well as in α.

Fig. 5 presents the variation of u/V and w/V with η for $\alpha = 0, 1°$; $x/a = 20$; and $V_r/V = 0, 1/10$.

Eqs. (20) permit the calculation of the normal force and drag due to small angles of attack and spin; however, these changes appear to be quite small for the range of α for which Eqs. (20) are valid.

Displacement Thickness

Eqs. (20) allow the calculation of the boundary-layer displacement thickness. Franklin Moore[7] derived an expression for the boundary-layer displacement thickness on nonmoving three-dimensional surfaces. An examination of his analysis indicates that his expression is also valid for moving surfaces. For the boundary layer considered here, the displacement thickness, Δ, is determined by the equation [see Eq. (8a) of reference 7]

$$(\partial/\partial x)(\Delta - \delta_x) + 2\alpha(\partial/\partial z) \sin(z/a)(\Delta - \delta_z) = 0 \quad (21)$$

where

$$\delta_x = \int_0^\delta \{1 - [u/V(1 - \alpha^2/2)]\} dy \approx \int_0^\delta [1 - (u/V) - \alpha^2 u/2V] dy$$

$$\delta_z = \int_0^\delta \{1 - [w/2\alpha V \sin(z/a)]\} dy$$

† The profile functions f_0, f_1, f_2, f_3, f_4, f_5, g_0, g_1, g_2, g_3, h_0, and h_1, together with their derivatives, are tabulated in reference 9, pp. 35–48.

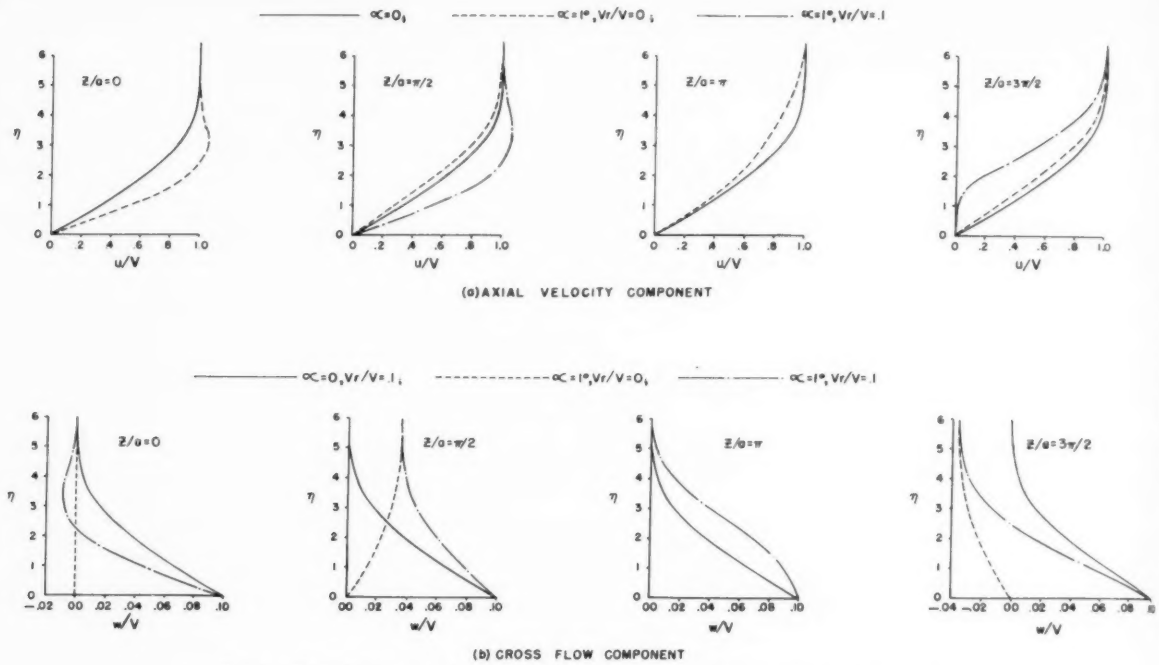

FIG. 5. Boundary-layer velocity profiles for $\alpha = 0, 1°$; $x/a = 20$, and $V_r/V = 0$ 0.1.

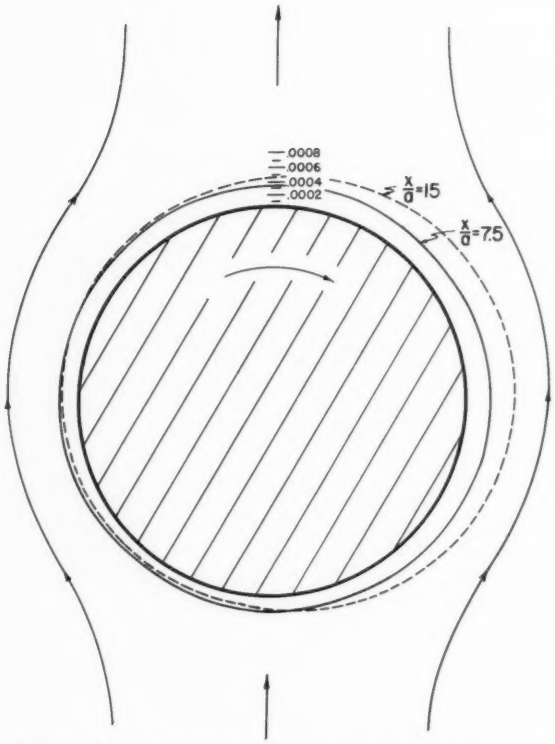

FIG. 6. Cross sections of Δ, the boundary-layer displacement thickness, for $x/a = 7.5$ and $x/a = 15$ for $V = 30$ ft./sec., $V_r/V = 1/10$, and $a = 1$ in. at sea level pressure.

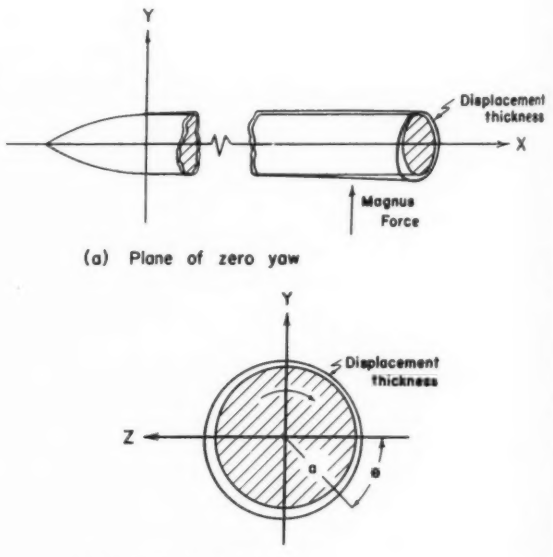

FIG. 7. An illustration of the change in effective body shape due to spin. (Note that $\theta = z/a$.)

From Eqs. (20) the quantities δ_r and δ_z are

$$\delta_r = \left\{ \int_0^\infty (1 - f_0')\, d\eta - (2\alpha x/a) \cos(z/a) \times \right.$$
$$\int_0^\infty f_1\, d\eta - \alpha(V_r/V)(x/a)^2 \sin(z/a) \int_0^\infty f_2\, d\eta -$$
$$\alpha^2 (x/a)^2 \left[\int_0^\infty f_3\, d\eta + \cos(2z/a) \int_0^\infty f_4\, d\eta \right] +$$
$$\left. (\alpha^2/2) \int_0^\infty (f_5' - f_0')\, d\eta \right\} \sqrt{\nu x/V}$$

$$\delta_z = \left[\left\{ 1 - [V_r/2\alpha V \sin(z/a)] \right\} \int_0^\infty (1 - f_0')\, d\eta - \right.$$
$$(1/2)(V_r/V)(x/a) \cot(z/a) \int_0^\infty h_0 d\eta -$$
$$\left. (\alpha/2)(x/a) \cos(z/a) \int_0^\infty h_1 d\eta \right] \sqrt{\nu x/V}$$

After the indicated integrations the preceding expressions reduce to

$$\delta_r = \left\{ 1.721 - 1.721 (\alpha x/a) \cos(z/a) - \right.$$
$$1.526 (\alpha V_r/V)(x/a)^2 \sin(z/a) -$$
$$\alpha^2 (x/a)^2 [-0.1434 + 1.667 \cos(2z/a)] +$$
$$\left. 0.4240\, \alpha^2 \right\} \sqrt{\nu x/V} \quad (22a)$$

$$\delta_z = (1.721 \left\{ 1 - [V_r/2\alpha V \sin(z/a)] \right\} +$$
$$1.380 (V_r/V)(x/a) \cot(z/a) -$$
$$4.943 (\alpha x/a) \cos(z/a)) \sqrt{\nu x/V} \quad (22b)$$

We shall assume that the displacement thickness can be expressed in the form

$$\Delta = \Delta_0 + \Delta_1 + \Delta_2 \quad (23)$$

where Δ_0 is the displacement thickness for zero spin and zero yaw, and Δ_1 and Δ_2 are the first- and second-order perturbations in α and/or V_r/V.

Substituting Eqs. (22) and (23) into Eq. (21) yields the following system of partial differential equations:

$$(\partial/\partial x)(\Delta_0 - 1.721 \sqrt{\nu x/V}) = 0 \quad (24a)$$

$$(\partial/\partial x)[\Delta_1 + 1.721 (\alpha x/a) \sqrt{\nu x/V} \cos(z/a)] +$$
$$2\alpha(\partial/\partial z)[\sin(z/a)(\Delta_0 - 1.721 \sqrt{\nu x/V})] = 0 \quad (24b)$$

$$(\partial/\partial x) \left\{ \Delta_2 + 1.526 (\alpha V_r/V) \times \right.$$
$$(x/a)^2 \sqrt{\nu x/V} \sin(z/a) + (\alpha x/a)^2 \sqrt{\nu x/V}$$
$$[-0.1434 + 1.667 \cos(2z/a)] - 0.4240 \times$$
$$\left. \alpha^2 \sqrt{\nu x/V} \right\} + 2\alpha (\partial/\partial z) \left\{ \sin(z/a) [\Delta_1 - \right.$$
$$1.380 (V_r/V)(x/a) \sqrt{\nu x/V} \cot(z/a) +$$
$$\left. 4.943 (\alpha x/a) \sqrt{\nu x/V} \cos(z/a)] \right\} = 0 \quad (24c)$$

Eq. (24a) can be integrated to yield

$$\Delta_0 = 1.721 \sqrt{\nu x/V} \quad (25)$$

The constant of integration is zero since we have neglected the boundary layer on the nose.

Substituting Eq. (25) into Eq. (24b), and integrating, yields

$$\Delta_1 = -1.721 (\alpha x/a) \sqrt{\nu x/V} \cos(z/a) \quad (26)$$

Again the constant of integration is zero.

Eq. (24c) can be integrated by using Eq. (26). It follows that

$$\Delta_2 = \left\{ -2.630\, \alpha(V_r/V)(x/a)^2 \sin(z/a) - \right.$$
$$(\alpha x/a)^2 [-0.1434 + 4.245 \cos(2z/a)] +$$
$$\left. 0.4240\, \alpha^2 \right\} \sqrt{\nu x/V} \quad (27)$$

Thus the boundary-layer displacement thickness is given by

$$\Delta = 1.721 \sqrt{\nu x/V} - 1.721 (\alpha x/a) \sqrt{\nu x/V} \times$$
$$\cos(z/a) - 2.630 (\alpha V_r/V)(x/a)^2 \sqrt{\nu x/V} \times$$
$$\sin(z/a) - (\alpha x/a)^2 [-0.1434 + 4.245 \times$$
$$\cos(2z/a)] \sqrt{\nu x/V} + 0.4240\, \alpha^2 \sqrt{\nu x/V} \quad (28)$$

Fig. 6 presents cross sections of the boundary-layer displacement thickness at sea level pressure for $x/a = 7.5$ and $x/a = 15$, and for $V = 30$ ft./sec. and $a = 1$ in.

Eq. (28) indicates that the boundary-layer displacement thickness is not symmetrical with respect to z when the body is spinning. The asymmetrical term

$$\Delta' = -2.630 (\alpha V_r/V)(x/a)^2 \sqrt{\nu x/V} \sin(z/a)$$

will produce a Magnus effect which will be calculated in the next section.

Magnus Force and Center of Pressure

The asymmetrical boundary-layer displacement thickness will produce an effective body shape which bends away from the original body axis. This is illustrated in Fig. 7. The Magnus effects produced by the displacement thickness will be investigated by the use of slender body theory.

The bending of the effective body shape will cause a cross flow in the plane of zero yaw. The velocity potential for this cross flow at any station along the body axis is given by (in polar coordinates)

$$\Phi = Vx - V(\partial\Delta'/\partial x)]_{\theta=\pi/2} (a^2/R) \sin(z/a)$$

where Δ' is the part of the displacement thickness which contributes to the Magnus effects. Thus,

$$\partial\Delta'/\partial x]_{\theta=\pi/2} = 6.575 (\alpha V_r/V)(x/a) (\sqrt{x\nu/V}/a)$$

It follows that the perturbation potential function is

$$\phi = -6.575\, \alpha V_r (x/a) (\sqrt{x\nu/V}/a) (a^2/R) \sin(z/a) \quad (29)$$

The pressure coefficient is

$$C_p = -(2\phi_x/V) - (\phi_x^2/V^2) - (\phi_y^2/V^2) - (\phi_z^2/V^2)$$

In this case the pressure is (to the first power in $\alpha V_r/V$)

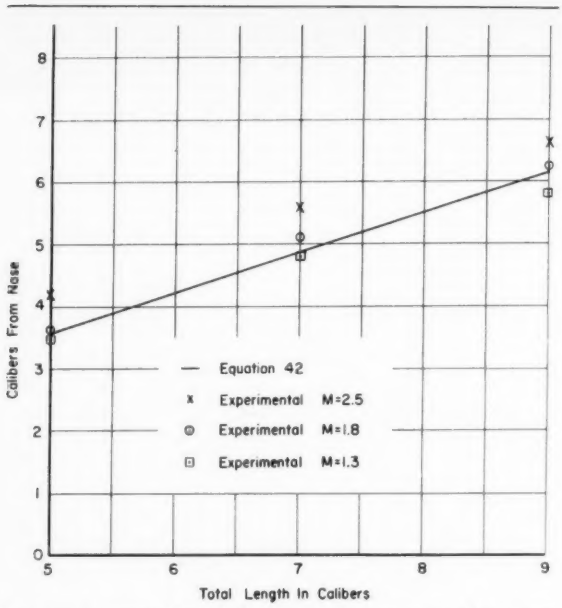

FIG. 8. A comparison of the center of pressure obtained from range firings with values calculated from Eq. (42).

$$C_p = 19.725\ (\alpha\ V_r/V)\ (\sqrt{\nu x/V}/a)\ (a/R) \times \sin\ (z/a) \quad (30)$$

Assuming a thin boundary layer, the pressure on the body can be found by evaluating Eq. (30) on the surface of the body. On the surface of the body Eq. (30) reduces to

$$C_p = 19.725\ (\alpha/a)\ (V_r/V)\ \sqrt{x\nu/V}\ \sin\ (z/a) \quad (31)$$

The Magnus force per unit length can be expressed as

$$F = 2\ q_0 \int_0^\pi C_p a\ \sin\ (z/a)\ d(z/a) \quad (32)$$

Substituting Eq. (31) into Eq. (32) and performing the indicated integration yields

$$F = 19.725\ \pi\ q_0(\alpha V_r/V)\ \sqrt{x\nu/V} \quad (33)$$

The total Magnus force is

$$F_m = \int_0^l F\,dx = 13.15\pi\ q_0(\alpha V_r/V) l\ \sqrt{l\nu/V} \quad (34)$$

Since the displacement thickness at zero yaw is

$$\Delta_0 = 1.721\ \sqrt{x\nu/V}$$

Eq. (34) can be written as

$$F_m = 7.641\ \pi\ q_0(\alpha\ V_r/V)\ l\ \delta_0^* \quad (35)$$

where δ_0^* is the displacement thickness at the base for zero yaw. Eq. (35) indicates that the Magnus force is a linear function of the displacement thickness at the base for zero yaw.

The Magnus force expressed in coefficient form is

$$K_F = 6.001\ (l/d)\ (\delta_0^*/d) \quad (36)$$

or

$$K_F = 10.33\ (l/d)^2/(Re)^{1/2} \quad (37)$$

where Re represents the Reynolds Number at the base.

The center of pressure of the Magnus force is located at

$$\bar{x} = \int_0^l xF dx \Big/ \int_0^l F dx = (3/5)l \quad (38)$$

The preceding equations for the Magnus force yield results which are of the same order of magnitude as observed experimentally. Unfortunately, the author has been unable to find any experimental data for the Magnus force on long slender bodies at small angles of attack in incompressible flow with laminar boundary layers.

Since the publication of the original BRL Report No. 870 in 1953, extensive work has been done by Howard R. Kelly on the determination of Magnus forces using the same general method developed here. In reference 10 he obtains the above result for K_F for "thin" boundary layers (small δ/a), and he indicates a method for obtaining Magnus forces for thicker boundary layers.

Turbulent Boundary Layers

The preceding analysis applies only to laminar boundary layers. Eqs. (35) and (36) indicate that the Magnus force for laminar boundary layers is a function of the displacement thickness at the base for zero yaw. We shall investigate the result of assuming that the expression for the Magnus force on bodies with turbulent boundary layers has the same form as Eq. (35). We have no justification for making this assumption other than an intuitive feeling that the perturbations caused by small angles of yaw and small rates of spin in a turbulent boundary layer may be similar in many respects to the perturbations in the laminar boundary layer considered in the preceding analysis.

Based on the assumption set forth above, the Magnus force coefficient on a body with a turbulent boundary layer can be expressed as

$$K_F = C_1\ (l/d)\ (\delta_0^*/d) \quad (39)$$

where C_1 is an unknown constant. The boundary-layer displacement thickness at the base can be expressed approximately by

$$\delta_0^* = C_2\ l/\sqrt[5]{Re} \quad (40)$$

where C_2 is a function of the Mach Number, the velocity profile, and the temperature distribution in the boundary layer. Thus, the Magnus force coefficient can be expressed as

$$K_F = C_3\ [(l/d)^2\sqrt[5]{Re}] \quad (41)$$

where C_3 is a function of the Mach Number, the velocity profile, and the temperature distribution in the boundary layer.

The center of pressure of the Magnus force for turbulent boundary layers is located at

$$\bar{x} = (9/14)l \quad (42)$$

Fig. (8) presents a comparison of Eq. (42) with experimental data obtained by the Free-Flight Aerodynamics Branch of the Exterior Ballistics Laboratory from range firings. The agreement between Eq. (42) and the experimental data is quite good considering the manner in which Eq. (42) was obtained. In using Eq. (42) the two caliber nose was assumed to be equivalent to adding one caliber to the cylinder.

Concluding Remarks

The preceding analysis is limited to very small angles of yaw, and applies to bodies with long cylindrical portions, such as the body illustrated in Fig. 1. Much work remains to be done before the Magnus effects can be predicted accurately even for slender bodies. The present analysis could probably be easily extended to the compressible case by using the equations given by Moore in reference 8. It also seems likely that one could obtain the boundary-layer solution on a body of rather general shape on which the axial pressure distribution can be expanded in a power series about some point on the nose. Some interesting results would undoubtedly be obtained if the analysis were to be extended so as to relax the limitations on x/a, α, and V_r/V.

Much experimental data is needed on the Magnus force and moment, the boundary-layer vector profiles, and the boundary-layer separation. A knowledge of the turbulent boundary-layer velocity vector profiles on given bodies could probably be used to calculate the displacement thickness and separation on other bodies of the same type by the use of momentum integrals.

References

[1] Lamb, Horace, *Hydrodynamics*; Dover Publications, New York.

[2] Howarth, L., *The Boundary Layer in Three Dimensional Flow—Part I*, Phil. Mag., Vol. XLII—Seventh Series, pp. 239–244, March, 1951.

[3] Allen, Julian H., *Pressure Distribution and Some Effects of Viscosity on Slender Inclined Bodies of Revolution*, NACA TN 2044, 1950.

[4] Schlichting, H., *Boundary Layer Theory—Part I—Laminar Flows*, NACA TM 1217, 1949.

[5] Moore, Franklin K., *Laminar Boundary Layer on a Circular Cone in Supersonic Flow at a Small Angle of Attack*, NACA TN 2521, 1951.

[6] Howarth, L., *Note on the Boundary Layer on a Rotating Sphere*, Phil. Mag., Vol. XLII—Seventh Series, pp. 1308—1315, November, 1951.

[7] Moore, Franklin K., *Displacement Effect of a Three-Dimensional Boundary Layer*, NACA TN 2722, 1952.

[8] Moore, Franklin K., *Three-Dimensional Compressible Laminar Boundary-Layer Flow*, NACA TN 2279, 1951.

[9] Martin, John C., *On Magnus Effects Caused by the Boundary Layer Displacement Thickness on Bodies of Revolution at Small Angles of Attack*, BRL Report No. 870 (Revised), Aberdeen Proving Ground, 1955.

[10] Kelly, Howard R., *An Analytical Method for Predicting the Magnus Forces and Moments on Spinning Projectiles*, TM-1634, U.S. Naval Ordnance Test Station, Inyokern, China Lake, California, 1954.

Influence of Thermal Stresses . . .

(*Continued from page 420*)

properties. Variational methods are suggested as a practical approach.

We note that in evaluating the effect of the temperature on the torsional rigidity, it is not necessary to assume a parabolic distribution of the temperature along the chord. A refinement in the present treatment is to introduce the equivalent value of δ giving the same torsional rigidity. Referring to Eqs. (14) and (21), we may define Q_1 as*

$$Q_1 = Q + 2\int_0^l \sigma_y x^2\, dx \tag{35}$$

The stress σ_y is the total membrane stress across the thickness.

* The influence of axial stress on torsional stiffness was previously investigated by Wagner,[2] Biot,[3] and Goodier.[4] Simplified expressions were also derived by Budiansky and Mayers[5] and by Hoff.[7]

References

[1] Biot, M. A., *The Divergence of Supersonic Wings Including Chordwise Bending*, Journal of the Aeronautical Sciences, Vol 23, No. 3, pp. 237–251, March, 1956.

[2] Wagner, H., *Tension and Buckling of Open Sections*, NACA TM 807, October, 1936.

[3] Biot, M. A., *Increase of Torsional Stiffness of a Prismatical Bar Due to Axial Tension*, Journal of Applied Physics, Vol. 10, No. 12, pp. 860–864, December, 1939.

[4] Goodier, J. N., *Elastic Torsion in the Presence of Initial Axial Stress*, Journal of Applied Mechanics, Vol. 17, No. 4, p. 383, 1950.

[5] Budiansky, B., and Mayers, J., *Influence of Aerodynamic Heating on the Effective Torsional Stiffness of Thin Wings*, Journal of the Aeronautical Sciences, Vol. 23, No. 12, p. 1081, December, 1956.

[6] Love, A. E. H., *The Mathematical Theory of Elasticity*, p. 558; Dover Publications, New York.

[7] Hoff, N. J., *Approximate Analysis of the Reduction in Torsional Rigidity and of the Torsional Buckling of Solid Wings Under Thermal Stresses*, Readers' Forum, Journal of the Aeronautical Sciences, Vol. 23, No. 6, p. 603, June, 1956.

Laminar Boundary Layer on a Spinning Cone at Small Angles of Attack in a Supersonic Flow

R. SEDNEY*

Ballistic Research Laboratories, Aberdeen Proving Grouna

SUMMARY

The problem of finding the laminar, compressible boundary-layer flow over a rotating cone at small angles of attack is considered. The cone angle and free-stream Mach Number are such that the nonviscous flow is conical. A Prandtl Number unity and a linear viscosity-temperature relation are also assumed. The "exact" solution for small angle of attack and small spin is obtained by a perturbation method including the first-order interaction effects. For a slender cone the results are used to calculate the Magnus effects due to displacement thickness. As yet, there are no experimental measurements which yield a conclusive test of the analytical results for Magnus force given here.

SYMBOLS

A_i	= coefficients in angle of attack expansion of nonviscous flow
C	= proportionality factor in $\mu - T$ relation
C_{fx}, $C_{f\phi}$	= dimensionless skin friction in x and ϕ directions
$C.P.$	= center of pressure of Magnus force
$C.M.$	= center of mass of cone
d	= diameter of cone
F, G	= generalized stream functions
F_{ij}, G_{ij}	= coefficients in expansion of F and G in α and κ
K_1, J_1, J_2	= coefficients in expression for Δ
K_T, K_F	= Magnus moment and force coefficients (ballistic notation)
l	= length of cone
L	= reference length, $C\bar{\mu}/\bar{\rho}\bar{u}$
M	= Mach Number
p	= pressure
q	= $1 + [(\gamma - 1)\bar{M}^2/2]$
r	= radius of cross section
$\bar{R}$	= Reynolds Number with fluid properties at reference condition and length indicated by subscript
s	= coordinate along free-stream velocity direction
S	= base area of cone
T	= temperature
u, v, w	= velocities along x, y, ϕ coordinate lines
U	= free-stream velocity
x	= coordinate along cone generators
y	= coordinate normal to cone surface
α	= angle of attack
γ	= ratio of specific heats
Δ	= displacement surface
η	= dimensionless coordinate
Θ	= cone half-angle
θ	= sin Θ
κ	= dimensionless coordinate $\omega r/\bar{u}'$
λ	= dimensionless coordinate $\eta/2\xi^{1/2}$
μ	= coefficient of viscosity
ν	= $\omega d/U$
ξ	= $x^3/3$
ρ	= density
ϕ	= coordinate angle around circumference of cone
ω	= angular velocity of cone about axis
Ω	= $\omega l\Theta/\bar{u}'$
$\bar{\ }$	indicates reference condition taken as conditions on surface of cone for zero angle of attack
0	= subscript indicating free-stream value
1	= subscript indicating outer edge of boundary layer
$'$	indicates quantity with dimensions, except in Eqs. (1) and Eqs. (6)–(19)

Received August 8, 1956.

* Aeronautical Research Engineer, Exterior Ballistics Laboratory.

INTRODUCTION

THE STUDY of three-dimensional boundary-layer flows is becoming increasingly important. The class of flows for which "exact" solutions can be obtained is limited to flat plate and yawed cylinder problems.[1] However, if one considers flows for which the departure from a basic two-dimensional flow is small, then by application of small perturbation methods a much wider class of flows becomes amenable to calculation.[1, 2] It is interesting to note that the bound ry-layer flow over a rotating body of revolution at zero angle of attack can be classed roughly between the two- and three-dimensional problems. For small relative spin, however, this problem is fairly easy to solve.[3] A body of revolution with nonzero angle of attack which is also rotating is a rather intricate three-dimensional problem but one which is of basic importance in ballistics.

To the author's knowledge, only one example of this type of flow has been considered. Martin[4] has solved the case of a semi-infinite open-ended cylinder in incompressible flow. The main purpose of his work was to test a hypothesis that Magnus effects on slender bodies at small angles of attack are caused by the displacement effect of the boundary layer. Since the prediction of Magnus effects has remained rather elusive, the fact that Martin obtained some meaningful results was encouraging. However, because of the model chosen, experimental verification could not be conclusive. Thus, it was decided to try a similar analysis for a more easily realizable model. Since it is desirable to take into account compressibility for ballistic applications, the cone in supersonic flow seems to be the obvious choice for an analytical solution including angle of attack and spin effects. This is, of course, because when the external flow is conical there is no pressure gradient along generators, and this allows

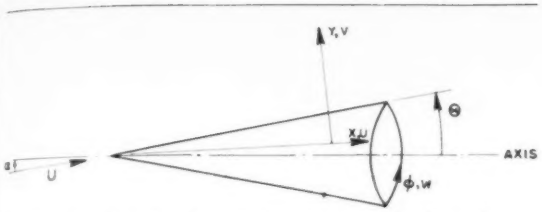

FIG. 1. Notation for spinning cone at angle of attack.

a boundary-layer solution to be obtained by introducing similarity variables.

The three special cases of the above problem have been worked out: for zero angle of attack and zero spin by Hantzsche and Wendt;[5] for zero spin by Moore;[6] and for zero angle of attack by Illingworth.[3] Moore's analysis is restricted to the first power in angle of attack, and Illingworth considers up to cubic terms in the spin. If one is interested in only first-order effects of both angle of attack and spin, these two results can be superposed, since the perturbations enter linearly. However, to obtain the interaction effects, which are necessary for Magnus effects, additional analysis must be made. This is what has been done here. The basic assumption is that the solution to the boundary-layer equations can be expanded in power series in the two (small) parameters angle of attack, α, and a spin parameter, κ. The lowest order interaction term is the coefficient of $\alpha\kappa$. From symmetry, no Magnus effects can be obtained when either α or κ is zero. Only the lowest order interaction term is calculated here; the higher order interaction terms—e.g., coefficients of $\alpha^2\kappa$ and $\alpha\kappa^2$—would presumably give a more accurate estimate of Magnus effects.

Only laminar flow is considered; compressibility is, of course, not neglected; heat conduction is allowed for with the assumptions of Prandtl Number unity and a linear viscosity–temperature relationship. In the solution to the boundary-layer problem the only other assumption (aside from the representation in terms of small perturbations) is that the external flow Mach Number and the cone angle are such that the flow is conical. When the results are applied to Magnus force calculations slender-body theory is used so that the restrictions to small cone angles and Mach Numbers which are not too large are necessary.

Aside from the interest in Magnus effects, the three dimensional problem considered here has some intrinsic interest, so that additional results are given—e.g., velocity profiles and skin friction. In particular, the following should be noted. To obtain generally useful results for three-dimensional flows approximate (momentum-integral) methods must be developed; this is especially true if the turbulent case it is to be considered. Reliability of these methods cannot be based alone on experience in two-dimensional flows since there are fundamental differences in the two cases. Thus exact solutions are necessary to test proposed approximate methods.

The Magnus effects to be considered here are those commonly observed in ballistics. In the terminology of airplane dynamics the Magnus effects are a side force and yawing moment due to angle of attack which implies that the body must be spinning for nonzero Magnus effects. It is clear that nonviscous flow could not allow Magnus effects (this is discussed more fully in reference 4); thus, one is forced to investigate the boundary-layer flow.

Assume a Prandtl Number equal to one; then a linear viscosity-temperature relation gives the boundary-layer solution for no heat transfer at the surface only if the surface is stationary. For a spinning body this is not the case, as Illingworth has noted.[3] For the cone one finds that, exactly, the solution is for a surface temperature which varies as the square of the distance along a generator. An alternate interpretation is that the heat transfer at the surface is zero, neglecting quadratic terms in α and κ. (Martin Fiebig called to the author's attention an error in the original manuscript concerning this point.)

Equations of Motion

The form of the equations of motion used here is taken from the work by Moore[7, 8] and will only be summarized. A two-component vector potential is introduced to satisfy the continuity equation exactly (generalization of stream function). Prandtl Number unity and the viscosity temperature relation

$$\mu/\bar{\mu} = CT/\bar{T}$$

are assumed, where the bar refers to the reference condition taken as the nonviscous flow at zero angle of attack evaluated at the surface and C is a suitably chosen constant. Two transformations are introduced; one like that of Howarth to try to remove compressibility effects and another like that of Mangler to try to remove curvature effects. Nondimensional dependent variables are used with the reference condition denoted by a bar with the same meaning as above, and lengths are made dimensionless with the length $L = (C\bar{\mu})/(\bar{\rho}\bar{u})$. Let u and w denote (nondimensional) velocities along generators (x-coordinate) and around the circumference (ϕ-coordinate); see Fig. 1. If F and G denote the two components of the vector potential mentioned above, then

$$u = F_\eta, \qquad w = G_\eta$$

where the subscript denotes differentiation and

$$\eta = x(\bar{\rho}/\rho)^{1/2} \int_0^y \rho \, dy$$

Let Θ be the half-angle of the cone

$$\theta = \sin \Theta, \qquad \xi = x^3/3$$

then the equations of motion are (see Eq. 42, reference 7):

$$F_\eta F_{\eta\xi} - [F_\xi + G_\phi/(3\theta\xi)]F_{\eta\eta} + G_\eta F_{\eta\phi}/(3\theta\xi) - (G_\eta)^2/(3\xi) = p'(\phi)\, GF_{\eta\eta}/(6\theta\xi p) + F_{\eta\eta\eta} \quad (1a)$$

$$F_\eta G_{\eta\xi} - [F_\xi + G_\phi/(3\theta\xi)]G_{\eta\eta} + G_\eta G_{\eta\phi}/(3\theta\xi) + G_\eta F_\eta/(3\xi) = -p'(\phi)/(3\theta\xi\rho) + p'(\phi)GG_{\eta\eta}/(6\theta\xi p) + G_{\eta\eta\eta} \quad (1b)$$

$$T + (F_\eta)^2 + (G_\eta)^2 = T_1 + u_1^2 + w_1^2 \quad (1c)$$

where p, ρ, and T are (nondimensional) pressure, density, and temperature; $p'(\phi)$ is the derivative of p; and the subscript 1 denotes conditions at the outer edge of the boundary layer. The form of the variables η and ξ comes from the Howarth and Mangler transformations. For the boundary conditions at the outer edge of the boundary layer ($y = \eta = \infty$),

$$\left.\begin{aligned} u &= u_1 = 1 - \alpha A_1 \cos\phi \\ w &= w_1 = \alpha A_2 \sin\phi \\ p/\bar{p} &= 1 + \alpha A_3 \cos\phi \\ \rho_1 &= 1 + \alpha A_4 \cos\phi \end{aligned}\right\} \quad (2)$$

since the flow is conical. The A_i are tabulated,[9] see reference 6 for further discussion. It is assumed that the rotation of the cone does not alter the external flow, so that the pressure is given by the expression in Eqs. (2). For the boundary conditions on the body surface ($y = \eta = 0$),

$$u = v = 0 \qquad w = \omega r/\bar{u}' \qquad r = xL\theta \quad (3)$$

where ω is the angular velocity of the cone about its axis, r is the local radius, and L is reference length defined above.

Since the pressure gradient is zero along the generators of the cone, a Blasius-type similarity variable is introduced:

$$\lambda = \eta/2\xi^{1/2}$$

(This differs by a factor of one half from the λ used by Moore.) However, because of the spin of the body there is no longer similarity in terms of λ. Thus variation with x must be allowed, and for this it is convenient to introduce a new variable κ,

$$\kappa = \omega r/\bar{u}' = \omega L\theta\,(3\xi)^{1/3}/\bar{u}'$$

Furthermore, the following forms for F and G are assumed:

$$F = \xi^{1/2} f(\kappa, \lambda, \phi)$$
$$G = \xi^{1/2} g(\kappa, \lambda, \phi)$$

For most ballistic applications the maximum value of κ will be less than 0.5, but it is assumed here that κ remains small enough so that f and g can be expanded in power series in κ. Hence, for this analysis, both the length of the cone and the angular velocity are limited. Thus, we write

$$\left.\begin{aligned} f &= f_0(\lambda, \phi) + \kappa f_1(\lambda, \phi) + \ldots \\ g &= g_0(\lambda, \phi) + \kappa g_1(\lambda, \phi) + \ldots \\ T &= t_0(\lambda, \phi) + \kappa t_1(\lambda, \phi) + \ldots \end{aligned}\right\} \quad (4)$$

For $\omega = 0$, f_0 and g_0 are the same as the f and g defined by Moore.[6] For $\alpha = 0$ all quantities are independent of ϕ, and we obtain essentially Illingworth's first-order spin effect terms;[3] the correspondence is

$$(f_0)_I = f_0, \qquad (g_0)_I = (1/2)g_{1\lambda}$$

where the I indicates Illingworth's functions (f_1 would be identically zero for $\alpha = 0$).

The partial differential equations satisfied by the coefficients of κ in Eqs. (4) will not be written down. In order to reduce the integration problem to one amenable to numerical processes the dependence of the coefficients on ϕ is assumed as follows [the form can be deduced from the appropriate boundary conditions and Eqs. (1a) and (1b)]:

$$\left.\begin{aligned} f_0 &= F_{00}(\lambda) - \alpha A_1 \cos\phi F_{01}(\lambda) + \ldots \\ g_0 &= \alpha A_2 \sin\phi G_{01}(\lambda) + \ldots \\ f_1 &= \alpha A_1 \sin\phi F_{11}(\lambda) + \ldots \\ g_1 &= G_{10}(\lambda) - \alpha A_2 \cos\phi G_{11}(\lambda) + \ldots \end{aligned}\right\} \quad (5)$$

Only the functions of λ explicitly given in the expansions (5) will be obtained. If the assumed form of the solution be regarded as a power series expansion in the two small parameters α and κ, it is evident that only one second-order term is included—i.e., the product (interaction) term $\alpha\kappa$. The α^2 and κ^2 terms could be included at the expense of more numerical integrations. This may seem inconsistent, but, at least for Magnus effects, the second-order terms contribute nothing. The functions of λ indicated in Eqs. (5) can be identified as follows: F_{00} governs the pure axial flow, F_{01} and G_{01} the angle of attack effects, G_{10} the spin effect, and F_{11} and G_{11} the interaction effects.

As expected, F_{00} satisfies the Blasius equation. The remaining functions satisfy linear third-order ordinary differential equations with boundary conditions at $\lambda = 0$ and $\lambda = \infty$. These were not the equations that were integrated, however, and therefore will not be written down for the following reason. These differential equations contain, through the A_i, the two parameters cone angle Θ and free-stream Mach Number M_0. But, since they are linear, it is an easy matter to rewrite the equations in a form which contains universal functions—i.e., independent of any parameters. Thus, the following sequence of equations was obtained (the Blasius equation and that for G_{10}, which is related to Illingworth's g_0, require no change but are rewritten in a different notation):

$$\left.\begin{aligned} &h_1''' + h_1 h_1 = 0'' \\ &h_1(0) = h_1'(0) = 0, \qquad h_1'(\infty) = 2 \\ &F_{00} = h_1 \end{aligned}\right\} \quad (6)$$

$$\left.\begin{aligned} k_1''' + h_1 k_1'' - (2/3)h_1' k_1' &= \\ -(8/3)\,[1 - (h_1'^2/4)]& \\ k_1(0) = k_1'(0) = 0, \qquad k_1'(\infty) &= 0 \end{aligned}\right\} \quad (7)$$

Then $G_{01} = h_1 + q\,k_1, \qquad q = 1 + (\gamma - 1)\bar{M}^2/2$

Define

$$L_1(f) = f''' + h_1 f'' + h_1'' f$$

$$\left.\begin{aligned} L_1(h_2) = 0, \qquad h_2(0) = h_2'(0) = 0 \\ h_2'(\infty) = 1 \end{aligned}\right\} \quad (8)$$

$$\left.\begin{aligned} L_1(h_3) - h_1'' k_1 = 0, \qquad h_3(0) = h_3'(0) = 0 \\ h_3'(\infty) = 0 \end{aligned}\right\} \quad (9)$$

then

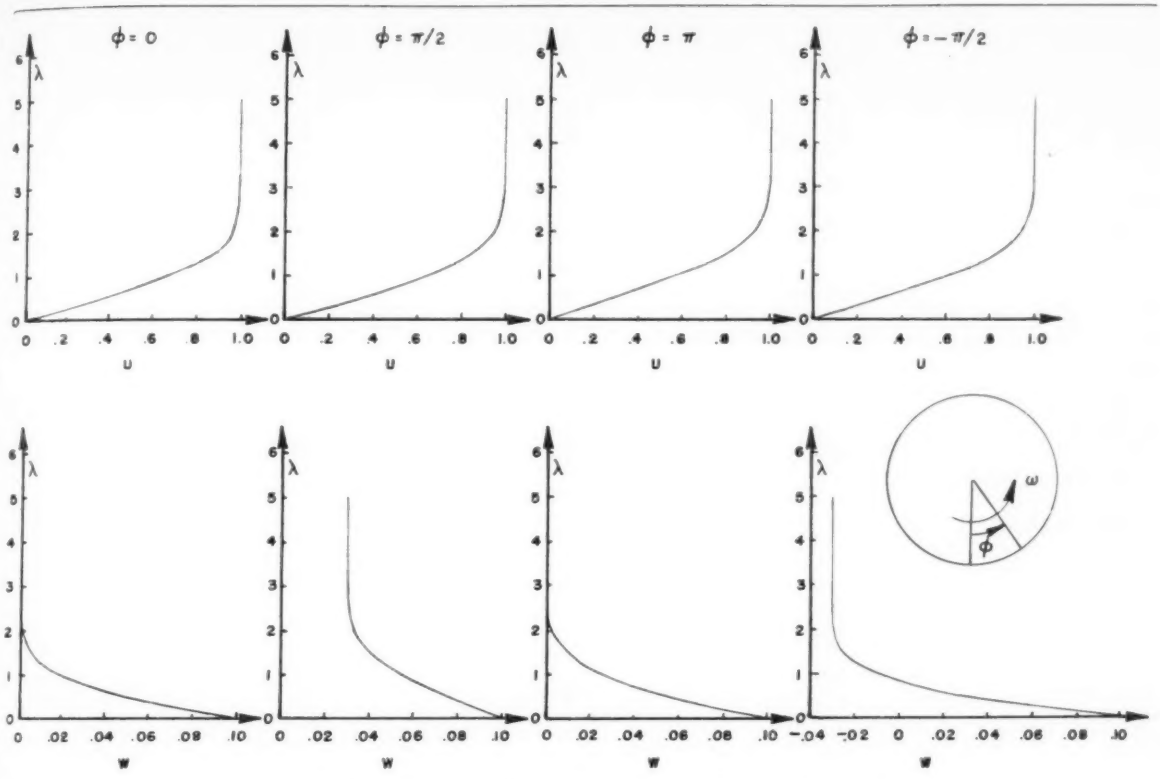

FIG. 2. Nondimensional velocity components u, w for $M = 1.82$, $\theta = 10°$, $\alpha = 1°$, $\kappa = 0.1$.

$$F_{01} = [2A_2/(3\theta A_1)]h_1 + 2[1 - (2A_2/3\theta A_1)]h_2 + [2A_2\, q/(3\theta A_1)]h_3$$

Define

$$L_2(f) = f''' + h_1 f'' - (4/3)h_1' f'$$

$$L_2(k_2) = 0,\ k_2(0) = 0,\ k_2'(0) = 2,\ k_2'(\infty) = 0 \quad (10)$$

then $$G_{10} = k_2$$

Also,

$$L_2(k_3) + k_2''\, h_2 - (4/3)k_2'\, h_2' = 0 \quad (11)$$

$$L_2(k_4) + k_2''(h_3 - k_1) + k_2'[k_1' - (4/3)h_3'] = 0 \quad (12)$$

$$L_2(k_5) - (1/3)h_1'\, k_2' = 0 \quad (13)$$

$$k_i(0) = k_i'(0) = k_i'(\infty) = 0, \qquad i = 3, 4, 5$$

Then

$$G_{11} = [2/(3\theta)]\,\{[2(3\theta A_1/2A_2) - 1]k_3 + qk_4 + k_5\}$$

Define

$$L_3(f) = f''' + h_1 f'' - (2/3)h_1' f' + (5/3)\, h_1'' f$$

$$L_3(h_4) + (4/3)k_2' h_1' = 0 \quad (14)$$

$$L_3(h_5) + (4/3)k_2' k_1' = 0 \quad (15)$$

$$L_3(h_6) - h_1' k_2' + h_1'' k_5 = 0 \quad (16)$$

$$L_3(h_7) - k_2' h_3' + h_1'' k_4 = 0 \quad (17)$$

$$L_3(h_8) - k_2' h_2' + h_1'' k_3 = 0 \quad (18)$$

$$L_3(h_9) - k_2 h_1'' = 0 \quad (19)$$

$$h_i(0) = h_i'(0) = h_i'(\infty) = 0, \qquad i = 4, 5, \ldots, 9$$

then

$$F_{11} = (A_2/A_1)\,(h_4 + qh_5) + (2/3\theta)^2\,(A_2/A_1)\,(h_6 + qh_7) + (4/3\theta)\,(1 - 2A_2/3\theta A_1)h_8 + (A_2/3\theta A_1)h_9$$

Eqs. (6)–(19) were integrated numerically on the ORDVAC and are tabulated in BRL Report No. 991. The functions were obtained to an accuracy of at least five significant figures. More accuracy was needed in the first few equations because of accumulation of errors. Eqs. (7), (8), and (9) are essentially the same as those integrated by Moore[6] (the numerical results agreed except that for the larger values of λ the agreement was only in the second or third significant figure). Eq. (10) is essentially the same as one of Illingworth's (results agree to as many places as given). The remaining equations give the interaction effects.

RESULTS

After numerical integration of the sequence of ordinary differential equations it is possible to compute a number of quantities of interest.

(a) Velocity Profiles

The nondimensional velocity components u and w are obtained from

$$u = F_\eta = (1/2)f_\lambda, \qquad w = G_\eta = (1/2)g_\lambda$$

and making use of Eqs. (4) and (5). For given free-stream Mach Number, M, and cone angle, Θ, the velocities are functions of α, κ, λ, and ϕ. In Fig. 2, u and w are plotted for the case $M = 1.82$, $\Theta = 10°$, $\alpha = 1°$, $\kappa = 0.1$ as functions of λ for $\phi = -\pi/2$, 0, $\pi/2$, and π.

As expected, there is a reversal in the w component for $\phi < 0$—i.e., where the rotational velocity opposes the direction of the flow outside the boundary layer. For the values of parameters chosen the u component does not change drastically around the circumference. There is no indication of separation type profiles. Note that it has not been necessary to compute the temperature variations. However this would have to be done if the velocity profiles were derived as functions of the physical coordinate y.

(b) Skin Friction

The two components of skin friction, expressed in dimensionless form, are

$$C_{fx} = 2[\mu' \partial u' / \partial y']_{y'=0} \bar{\rho}' \bar{u}'^2$$

$$C_{f\phi} = 2[\mu' \partial w' / \partial y']_{y'=0} \bar{\rho}' \bar{u}'^2$$

where the prime indicates that a quantity has dimensions. To the same order of approximation that has been carried throughout, the following expressions are obtained:

$$2C_{fx} = (3C/\bar{R}_x)^{1/2} [F_{00}''(0) - \alpha\{A_1 F_{01}''(0) - (1/2)A_3 F_{00}''(0)\} \cos\phi + \kappa\alpha A_1 F_{11}''(0) \sin\phi] \quad (20)$$

$$2C_{f\phi} = (3C/\bar{R}_x)^{1/2} [\kappa G_{10}''(0) + \alpha A_2 G_{01}''(0) \sin\phi + \kappa\alpha\{A_3 G_{10}''(0)/2 - A_2 G_{11}''(0)\} \cos\phi] \quad (21)$$

where $\bar{R}_x = x'\bar{\rho}'\bar{u}'/\bar{\mu}'$. The terms in Eqs. (20) and (21) which are independent of or linear in α and κ can be obtained from references 6 and 3, respectively. The interaction terms ($\alpha\kappa$) are

$$\partial^2 C_{fx}(\bar{R}_x/3C)^{1/2}/\partial\kappa\partial\alpha \sin\phi = A_1 F_{11}''(0)/2 = A_2[0.6145 + 0.2522\bar{T}^{-1} + (2/3\theta)^2 (0.3592 + 0.1325\bar{T}^{-1})] - (2/3\theta)[0.5109 A_1 + 0.2395 A_3] \quad (22)$$

$$\partial^2 C_{f\phi}(\bar{R}_x/3C)^{1/2}/\partial\kappa\partial\alpha \cos\phi = [A_3 G_{10}''(0) - 2A_2 G_{11}''(0)]/4 = 0.4896A_1 - 0.4898A_3 - (A_2/3\theta)[1.4496 + 0.5868\bar{T}^{-1}] \quad (23)$$

where $\bar{T}^{-1} = (\gamma - 1)\bar{M}^2/2$. The right-hand sides of Eqs. (22) and (23) are plotted in Figs. 3 and 4, respectively, for cone angles of 10°, 12.5°, and 15°. According to the expression (20) for C_{fx}, the effect of the $\alpha\kappa$ term, for negative ϕ, is to reduce the skin friction. This reduction is a maximum at $\phi = -\pi/2$. However, for reasonably small values of α and κ the reduction is not enough to indicate component separation. For example, to reduce C_{fx} to zero for $\Theta = 10°$ at $\phi = -\pi/2$ it would be necessary to have $\alpha\kappa = 0.06$. For such values of α and κ the higher order terms would no longer be negligible. Since this is a three-dimensional flow it is by no means clear that component separation is pertinent to the general question of separation.

In Fig. 5 a sketch of $C_{f\phi}(\bar{R}_x/3C)^{1/2}$ is presented for $M = 1.82$ and $\Theta = 10°$. It is seen that the variation

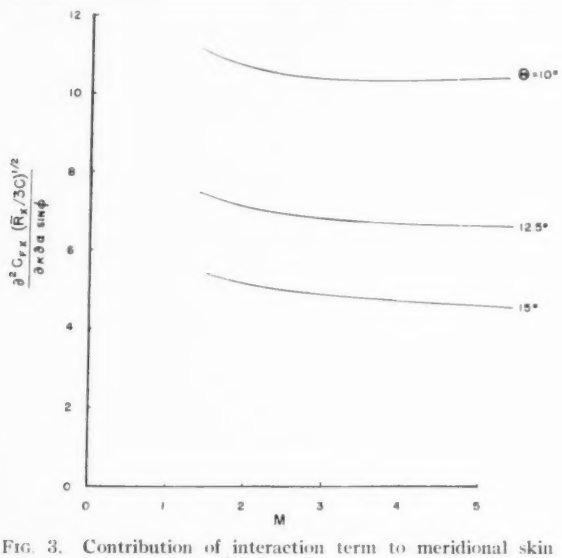

FIG. 3. Contribution of interaction term to meridional skin friction, C_{fx}.

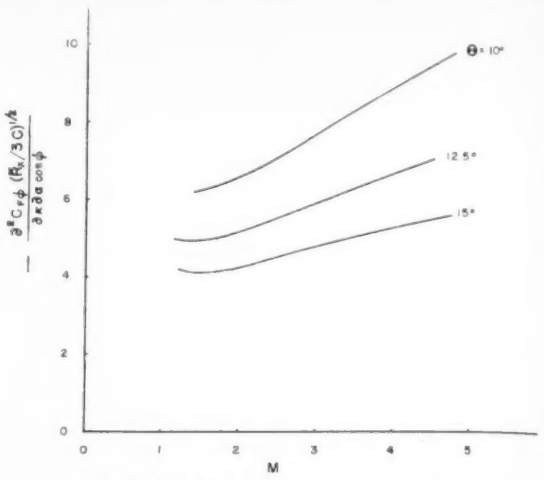

FIG. 4. Contribution of interaction term to circumferential skin friction, $C_{f\phi}$.

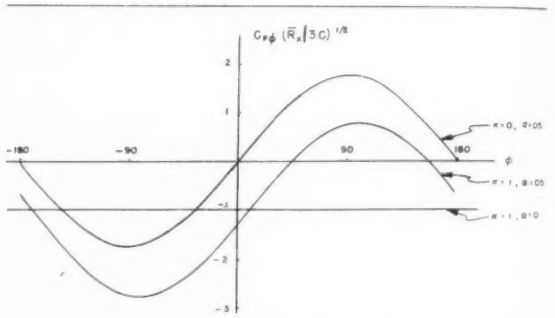

FIG. 5. Variation of $C_{f\phi}(R_x/3C)^{1/2}$ around circumference for $M = 1.82$ and $\theta = 10°$.

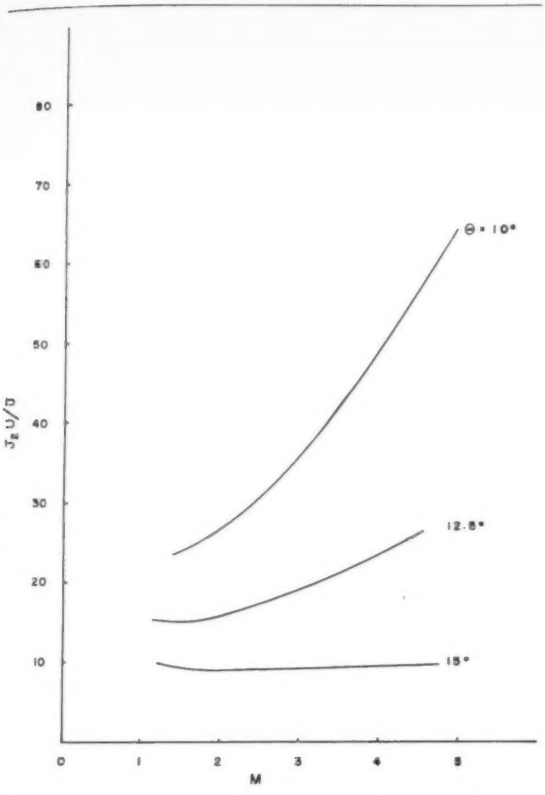

FIG. 6. Contribution of interaction term to displacement thickness Δ.

of the skin friction is affected significantly by the interaction terms. However, the integrated value, which gives the spin reducing torque, is unaffected in the present approximation. (See reference 3 for a discussion of the effect of the second-order term in the spin on this torque.)

(c) *Displacement Thickness*

To find the displacement thickness for a three-dimensional boundary-layer flow it is necessary to solve a first-order partial differential equation.[10,11] For the cone problem, if Δ is the displacement thickness,

$$\partial[\rho_1 u_1 x(\Delta - \delta_x)]/\partial x + \partial[\rho_1 w_1(\Delta - \delta_\phi)]/\theta\partial\phi = 0 \quad (24)$$

where

$$\delta_x = L\int_0^\infty [1 - (\rho u/\rho_1 u_1)]\, dy$$

$$\delta_\phi = L\int_0^\infty [1 - (\rho w/\rho_1 w_1)]\, dy$$

$$L = C\bar{\mu}/\bar{\rho}\bar{u}$$

Integrating Eq. (24) and introducing a displacement thickness Reynolds Number

$$R_\Delta = \bar{\rho}'\bar{u}'\Delta/\bar{\mu}'$$

the following is obtained:

$$R_\Delta = 2C[K_1 + \alpha J_1 \cos\phi - \alpha\kappa J_2 \sin\phi]\,(x/3)^{1/2} \quad (25)$$

where K_1, J_1, and J_2 are functions of free-stream Mach Number and cone angle. From references 10 and 6, J_1 and K_1 can be obtained and

$$J_2 = K_4 + K_5 + (K_6/5\theta)$$

where

$$K_4 = (2/3\theta)\,[A_1(0.4142 - 0.5198\bar{T}^{-1}) - A_3(0.2158 + 0.2771\bar{T}^{-1})] + A_2\,[0.4106 + 0.6396\bar{T}^{-1} + 0.1697\bar{T}^{-2} + (2/3\theta)^2(0.3186 + 0.5247\bar{T}^{-1} + 0.1495\bar{T}^{-2})]$$

$$K_5 = A_2\bar{T}^{-1}(0.6692 + 0.2493\bar{T}^{-1})$$

$$K_6 = A_2(2/3\theta)(0.9207 + 0.3289\bar{T}^{-1}) - 0.6546A_1 - 0.6538A_3$$

The $\alpha\kappa$ term in Eq. (25) makes the displacement thickness unsymmetrical with respect to the plane of yaw and is indicative of Magnus effects. For these effects, which will be considered in the next section, it is convenient to have $J_2 U/\bar{u}$ which is plotted in Fig. 6 where U is the free-stream velocity. This velocity ratio is introduced because the dimensionless force and moment coefficients are conventionally based on free-stream velocity. In Fig. 7 the variation of Δ around the circumference is shown for $M = 1.82$, $\Theta = 10°$. The effect of the spin on displacement thickness is to rotate it in the direction of the spin. For the values of α and κ of Fig. 7 the maximum and minimum are rotated through 15° from the plane of yaw.

MAGNUS EFFECTS

The concept that the unsymmetrical displacement thickness on a rotating body at angle of attack causes Magnus effects was used by Martin[4] for the case of a semi-infinite cylinder. Basically the same idea will be used here. The potential flow over the distorted body—i.e., body plus displacement thickness—is calculated by means of slender-body theory. Thus, we now assume that the cone angle is small. The displacement thickness as given by Eq. (25) is measured normal to the body surface, but for the approximation of slender-body theory this thickness can be added to the cross section of the body normal to its axis. Then the cross section of the body can be expressed in polar coordinates as

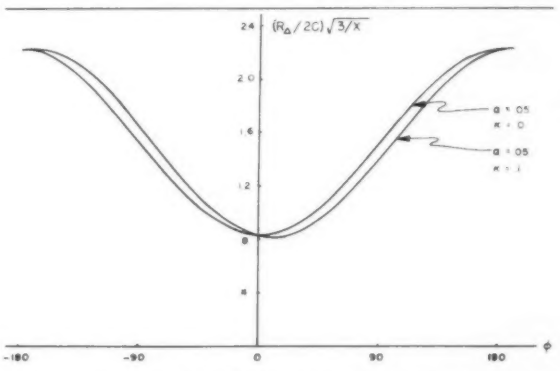

FIG. 7. Variation of $(R_\Delta/2C)(x/3)^{1/2}$ around circumference for $M = 1.82$ and $\theta = 10°$.

$$r'/l = a + b\cos\phi + c\sin\phi \qquad (26)$$

where

$$a = (x'\Theta/l) + 2K_1(Cx'/3R_l)^{1/2}$$
$$b = 2\alpha\, J_1(Cx'/3R_l)^{1/2}$$
$$c = -2\alpha\, J_2\Omega(x'/l)\,(Cx'/3R_l)^{1/2}$$
$$\Omega = \omega\Theta l/\tilde{u}'$$

with l the length of the cone, R_l the Reynolds Number based on l and the surface quantities at zero angle of attack, and the prime indicates a quantity with dimensions. To the first order in α the expression (26) for the cross section is a circle of radius a and center (b, c).

The details of the slender-body calculation need not be given since Ward[12] has presented all the necessary formulas for the cross force and moments. Ward uses, instead of the axis of the body, the s-axis parallel to the direction of the free stream. With respect to the s-axis the center of the circle (26) is (b^*, c) where

$$b^* = b + \alpha s$$

and for the approximation made here $x = s$. Then the complex transverse force, F, is given by

$$2F/\rho_0 U^2 S = -2(db^*/ds + idc/ds)_{s=1} \qquad (27)$$

where S is the base area and ρ_0 the free-stream density. The real and imaginary parts give the lift and cross force, respectively. The negative sign in Eq. (27) results from the choice of axes in the cross section. Thus the displacement thickness causes a decrease in the lift coefficient from the value 2α by an amount

$$2\cdot\alpha J_1(C/3R_l)^{1/2}$$

(J_1 is negative). The Magnus force coefficient (in aerodynamic notation) is

$$\text{Im}\,[2F/\rho_0 U^2 S] = 6\alpha J_2\Omega(C/3R_l)^{1/2} \qquad (28)$$

The ratio of the Magnus force to lift force due to displacement thickness is

$$3\Omega\, J_2/J_1$$

which for $\Theta = 10°$ is of the order of magnitude 10Ω which is less than one for the small spin contemplated here. Such a small Magnus force would be difficult to measure.

The center of pressure of the Magnus force is found to be

$$1 - \int_0^1 s^{1/2}[s\Theta + 2K_1(Cs/3R_l)^{1/2}]^2 \times ds/[\Theta + 2K_1(C/3R_s)^{1/2}]^2$$

in units of the length of the cone. To within a few per cent at most this result shows that the center of pressure is independent of Mach Number and Reynolds Number and is given by

$$C.P. = (5/7)l$$

In ballistic notation the Magnus force and moment coefficients, K_F and K_T, respectively, are found to be

$$K_F = F/\rho_0 U^2 d^2 \nu\alpha = (\pi/8)\,(J_2 U/\tilde{u}')\,(3C/R_l)^{1/2}$$
$$K_T = T/\rho_0 U^2 d^3 \nu\alpha = -(C.P._F - C.M.)K_F$$

where d is the diameter of the base, $\nu = \omega d/U$, $C.P._F$ is the center of pressure, and $C.M.$ is the center of mass both measured in calibers (diameters). The moment is taken about the center of mass. In Fig. 6, $J_2 U/\tilde{u}'$ is plotted.

As yet there appear to be no experimental measurements which provide a conclusive test of these analytical results. There is some work in progress at the Ballistic Research Laboratories which may yield such a test. Some measurements have been reported[13] giving only the Magnus moment on a slender cone. However, the boundary layer was definitely turbulent over most of the cone. Moreover, it is felt that the predicted moment will be more in error than the force. When the above result for K_T was compared with the results of reference 13 it was found to disagree considerably, but in view of the above statements this is not regarded as conclusive.

Finally the contribution to the Magnus force of the meridional skin friction will be discussed. This was done for Martin's cylinder problem by Kelly[14] who found that skin friction contributed a negative Magnus force about 7 per cent of displacement thickness contribution. Integrating Eq. (21) it is found that for the cone the $\alpha\kappa$ term gives a negative Magnus force which for $\Theta = 10°$ is about 20 per cent of that due to displacement thickness.

Martin[4] has attempted to extend his analysis of the laminar flow over a cylinder to the turbulent case by assuming that the Magnus force coefficient depends on the product of displacement thickness at the base for zero angle of attack and the length of the cylinder as in the laminar case. Aside from the fact that an empirical constant is left to be determined, it is not clear that the above assumption is valid. Thus the important matter of treating the turbulent boundary layer remains to be solved as well as the extension to more general bodies. This will necessitate the development of approximate methods for three-dimensional boundary-layer flows.

References

[1] Sears, W. R., *Boundary Layers in Three-Dimensional Flows*, Appl. Mech. Revs., Vol. 7, No. 7, p. 281, July, 1954.

[2] Moore, F. K., *Advances in Applied Mechanics*, "Three-Dimensional Boundary Layer Theory," Vol. 4, p. 160; Academic Press, New York, 1956.

[3] Illingworth, C. R., *The Laminar Boundary Layer of a Rotating Body of Revolution*, Phil. Mag., Vol. 44, Series 7, p. 389, April, 1953.

[4] Martin, J. C., *On Magnus Effects Caused by the Boundary Layer Displacement Thickness on Bodies of Revolution at Small Angles of Attack*, BRL Report No. 870, June, 1955.

[5] Hantzsche, W., and Wendt, H., *The Laminar Boundary Layer on a Circular Cone at Zero Incidence in a Supersonic Stream*, Rep. and Trans. No. 276, British M. A. P., August, 1946.

[6] Moore, F. K., *Laminar Boundary Layer on a Circular Cone in Supersonic Flow at a Small Angle of Attack*, NACA TN 2521, October, 1951.

(*Continued on page 455*)

Buckling Under External Pressure of Cylindrical Shells Evenly Stiffened by Rings Only†

P. P. BIJLAARD*

Bell Aircraft Corporation

SUMMARY

Calculations are given for determining the critical pressure for panel buckling as well as general instability of shells evenly stiffened by rings with equal spacings. The panel buckling stress is calculated by determining the length of the equivalent simply supported shell, taking account of the rotational restraints offered by the rings. The limited applicability of small deflection theory is accounted for by partially neglecting the curvature of short shells. Rotational spring constants are calculated for rings with plate and box sections.

Critical pressures from general instability are calculated by the method of split rigidities. Reduction factors for plasticity and eccentricity are discussed. An example of the calculation is given and is compared with the experimental result.

SYMBOLS

a	= radius of shell
b	= width of stiffening ring with plate section (Fig. 4)
b	= dimension, in the axial direction of the shell, of stiffening ring with box section (Fig. 5)
c	= $L/2$
e	= eccentricity
g	= $a + b$ for ring with plate section (Fig. 4)
h	= radial dimension of stiffening ring with box section (Fig. 5)
k	= ratio given by Eq. (46)
k_c	= core radius
k_{1m} k_{2m} ...	= coefficients in Eq. (15)
l	= effective simply supported length of shell
$(l/a)_c$	= ratios given by Eqs. (18) or (19)
n	= number of circumferential lobes
p	= external pressure
p, q	= loads per unit length on wall of ring with box section
q_b, q_h	= loads carried by walls of box section with widths b and h, respectively
r	= distance of ring element to axis of shell; also, radius of gyration
s	= slenderness ratio; also, ratio defined in reference 10, p. 480
t	= thickness of shell
t'	= thickness of flat ring and wall thickness of ring with box section
u_m	= normal function
w	= deflection
x, y, z	= coordinates
A, B, C	= constants
C_1 to C_5	= coefficients in Eq. (75)
D	= deflecting force
E	= modulus of elasticity
G	= modulus of rigidity in calculation of ring with box section
G, H	= ratios given by Eqs. (25)
H	= extra load carried by wall of box section with width b, due to distortion of cross section (Fig. 6)
I	= moment of inertia
L	= spacing of rings
L_t	= total length of shell
M	= moment
N	= flexural rigidity
N_r	= flexural rigidity of flat ring and of wall of box section
P	= force
P, Q, R	= parameters given by Eqs. (66)
R	= restraining force
S	= shear force
S^{III}	= quarter spring constant
V	= extra load carried by wall of box section with width h (Fig. 6)
V_R, V_D	= work done by restraining and deflecting forces, respectively
∇^4	= $(\partial^2/\partial x^2 + \partial^2/\partial y^2)^2$
∇^8	= $(\nabla^4)^2$
α_m	= coefficient in Eq. (11)
β	= spring constant
γ	= interaction coefficient in method of split rigidities; also, division factor for eccentricity in column buckling
ϵ	= l/λ; also, means strain
λ	= $\pi a/n$ = half wave length of lobes in the circumferential direction
μ	= reduction factor for eccentricity in shell
ν	= Poisson's ratio
ρ	= ratio given by Eq. (13); also, radius of curvature
σ	= normal stress
τ	= shear stress
φ	= cylindrical coordinate; also, interaction coefficient in method of split rigidities
φ_b, φ_h	= rotations of walls of box section with width b and h, respectively
Φ	= $1 + \epsilon^2 = 1 + (l/\lambda)^2$
ψ	= angle of distortion of box section
ω	= slope of flat ring

INTRODUCTION

BUCKLING OF A RING stiffened cylindrical shell under external pressure can occur in various modes. The individual panels may buckle between the rings, whereby the rings are situated on nodal lines, but are twisted. In this mode, denoted as Mode A (panel

Received October 5, 1956.

† This is part of a study undertaken by the author at the request of Bell Aircraft Corporation. The author wishes to thank the Bell Aircraft Corporation for permission to publish these results and Arthur Schnitt, Chief Structures Engineer of that company, for clearly defining the problem and for his helpful advice and guidance.

* Consultant. Also, Professor of Structural Engineering, Cornell University.

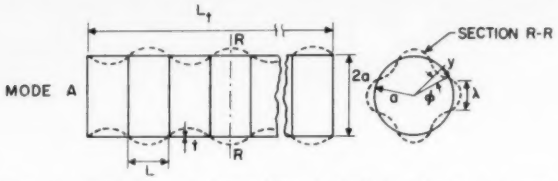

FIG. 1. Buckling of ring stiffened shell in Mode A (panel buckling).

buckling) and illustrated by the dashed deflections in Fig. 1, the panels of length L behave as isotropic cylindrical shells that are rotationally elastically restrained by the rings. Each panel can be considered as symmetrically elastically restrained if the rings at the ends have a rotational spring constant that is half the spring constant of the intermediate rings. If the ends act as a simple support, the end panels can be made 20 per cent shorter than the intermediate ones, in order to have the same critical stress as the latter. This mode involves the determination of the critical stress of symmetrically elastically rotationally restrained shells and the calculation of the rotational spring constants of various types of rings, as carried out in the next two sections.

The other mode, Mode B, is that from buckling due to general instability, where both rings and shell buckle [see Fig. 2(a)]. The buckling stress for this mode can be calculated by the method of split rigidities, by splitting the actual mode into Cases 1 and 2, as sketched in Fig. 2(b) and 2(c). It should be noted that here the deflecting forces caused by the buckling of the rings in all panels for equal ordinates y or φ [see Fig. 2(a)] have the same direction, so that the buckles of the shell between the rings are as shown in Fig. 2(c), the interior panels behaving as fully clamped.

In Case 1, the shell is assumed to be infinitely rigid against a deformation according to Case 2, so that it buckles as a shell of length L_t [see Fig. 2(b)], together with the rings. This has the same effect as assuming that, in Case 1, the rigidity of the rings is distributed continuously along the length of the shell, so that buckling between the rings, as in Case 2, does not occur. On the other hand, in Case 2, the structure is assumed to be infinitely rigid against a deformation according to Case 1, so that only buckling between infinitely rigid rings can occur. After determining the critical stresses or the critical pressures p_1 and p_2, for Cases 1 and 2, respectively, the actual critical pressure for Mode B is calculated by the method of split rigidities. It appears that, practically, the critical pressure for Mode B can be assumed to be equal to p_1.

Also, reduction factors for plasticity and crookedness are discussed. An example of calculation is used for comparing theoretical and experimental results. With the exception of these discussions on plasticity and eccentricity, this paper is essentially a summary of reference 1.

BUCKLING IN MODE A, PANEL BUCKLING

Critical Stress of Symmetrically Rotationally Restrained Shell Panels

As shown in references 1 and 2, for shells where the ratio of the half wave lengths of buckles in the axial and circumferential directions is sufficiently great (more than about 4), the differential equation for a strip, running in the X-direction (see Fig. 3) is

$$Nd^4w/dx^4 = (\pi/l)^4 w \tag{1}$$

where N is the flexural rigidity of the shell wall and l is the length of the simply supported shell that buckles at the same critical pressure as the elastically restrained shell. For buckling in Mode A, as stated in the Introduction, the panels can be considered as symmetrically restrained. Hence, the general solution of Eq. (1) is reduced to

$$w = A \cosh(\pi x/l) + B \cos(\pi x/l) \tag{2}$$

The boundary conditions are (see Fig. 3)

$$\text{for } x = c \begin{cases} w = 0 & (3) \\ -dw/dx = -M_{xe}/\beta & (4) \end{cases}$$

where β is the spring constant due to the rotational restraint of the rings. From reference 3

$$M_x = -N\{(\partial^2 w/\partial x^2) + \nu[(w/a^2) + (\partial^2 w/\partial y^2)]\} \tag{5}$$

so that from Eq. (4), at $x = c$,

$$dw/dx = -(N/\beta)(d^2w/dx^2) \tag{6}$$

Inserting Eq. (2) into the boundary conditions (3) and (6) at $x = c$ leads to two linear homogeneous equations, which for deflections different from zero are satisfied if the determinant of the system is zero, giving the buckling condition

$$\tanh(\pi c/l) + \tan(\pi c/l) + 2\pi N/(\beta l) = 0 \tag{7}$$

from which the length l of the simply supported shell with the same critical pressure can be calculated. From references 2 and 4, the critical pressure is then

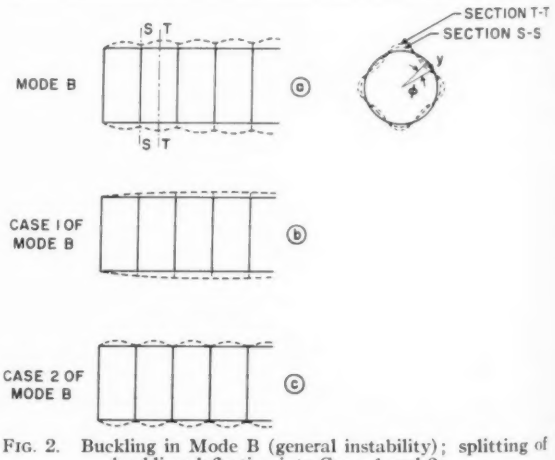

FIG. 2. Buckling in Mode B (general instability); splitting of buckling deflection into Cases 1 and 2.

found as

$$p_{cr} = \frac{0.92\,E(t/a)^2}{(l/a)(a/t)^{1/2} - 0.636} \tag{8}$$

In a way similar to that shown in reference 2, this method of calculation was checked by using Donnell's equation,[5] with $\sigma_x = (1/2)\sigma_y$,

$$N\nabla^8 w + (Et/a^2)(\partial^4 w/\partial x^4) + t\sigma_y\nabla^4[(\partial^2 w/\partial y^2) + (1/2)(\partial^2 w/\partial x^2)] = 0 \tag{9}$$

and assuming[2, 6]

$$w = (\cos ny/a)\Sigma w_m u_m \tag{10}$$

where u_m are the normal functions

$$u_m = (\cosh \alpha_m x/\cosh \alpha_m c) + (\cos \alpha_m x/\cos \alpha_m c) \tag{11}$$

With the same boundary conditions as expressed by Eqs. (3) and (6), one now obtains the buckling condition

$$\tanh \alpha_m c + \tan \alpha_m c + \rho\alpha_m c = 0 \tag{12}$$

where

$$\rho = 2N/(\beta c) \tag{13}$$

This condition is identical to Eq. (7), if $\alpha_m = \pi/l$.

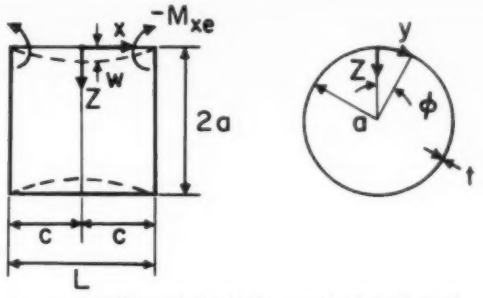

FIG. 3. Buckling of elastically restrained shell panel.

The functions u_m are orthogonal. Further, $\partial^4 u_m/\partial x^4 = \alpha_m{}^4 u_m$ and $\partial^2 u_m/\partial x^2 = \alpha_m{}^2 \bar{u}_m$, where

$$\bar{u}_m = (\cosh \alpha_m x/\cosh \alpha_m c) - (\cos \alpha_m x/\cos \alpha_m c) \tag{14}$$

and can be developed in a series of u_m,

$$\bar{u}_m = k_{1m}u_1 + k_{2m}u_2 + k_{3m}u_3 + \ldots \tag{15}$$

Since the solution converges rapidly, it is sufficient to use only the first terms in Eqs. (10) and (15). Inserting Eq. (10) into Eq. (9), one thus obtains

$$p_{cr} = \frac{t\sigma_x}{a} = \frac{N[\alpha_1{}^8 + (6n^4\alpha_1{}^4/a^4) + (n^8/a^8) - 4(n^2\alpha_1{}^2/a^2)(\alpha_1{}^4 + n^4/a^4)k_{11}] + Et\alpha_1{}^4/a^2}{(n^2/a)(2\alpha_1{}^4 + n^4/a^4) - (1/2)\alpha_1{}^2(\alpha_1{}^4 + 5n^4/\alpha^4)k_{11}/a} \tag{16}$$

From Eq. (15), by integration, for $m = 1$,

$$k_{11} = \frac{\int_{-a}^{a} \bar{u}_1 u_1 dx}{\int_{-a}^{a} u_1{}^2 dx} = \frac{\operatorname{sech}^2 \alpha_1 c - \sec^2 \alpha_1 c + (\tanh \alpha_1 c - \tan \alpha_1 c)/(\alpha_1 c)}{\operatorname{sech}^2 \alpha_1 c + \sec^2 \alpha_1 c + \rho} \tag{17}$$

where α_1 is determined by Eq. (12).

With $t = 0.15$ in., $E = 30(10)^6$ psi, and $\nu = 0.3$, $N = Et^3/[12(1 - \nu^2)] = 9270$ lb.in. If, further, $a = 25$ in., $c = 25$ in., $L = 50$ in. and $\beta = 410$ lb.in./in., Eq. (7) yields $l = 43.5$ in. $= 0.87\,L$, so that from Eq. (8) $p_{cr} = 45.8$ psi, against 39.6 psi for a simply supported shell, with $l = L = 50$ in. On the other hand, from Eq. (13), $\rho = 1.806$, so that Eq. (12) gives $\alpha_1 c = 1.81$ and $\alpha_1 = 0.0724$. Then Eq. (17) yields $k_{11} = -0.758$. From Eq. (16), using only the major terms in numerator and denominator, as was done in reference 2, it follows by differentiation that for a minimum value of p_{cr} the number of lobes n in the circumferential direction is between 7 and 8. With these values of n, Eq. (16) yields $p_{cr} = 45.8$ and 47.0 psi, respectively, confirming the accuracy of the simple method based on Eqs. (7) and (8). As shown earlier in references 1 and 2, a fully clamped shell, where β is infinite, has an effective length $l = 0.665\,L$.

It was stated in the beginning of this section that the condition for the applicability of Eq. (7) is that the ratio between the longitudinal and circumferential half wave lengths is more than about 4. This makes Eq. (7) sufficiently accurate for steel shells with external pressures of 15 to 150 psi if l/a is more than 1 to 2, respectively, and for aluminum shells under 15 to 150 psi if l/a is more than 1.5 to 3, respectively, as shown in reference 1 by comparison of its results for fully clamped shells with graphs in reference 7.

On the other hand, for very short shells, say for $l/a = 0.1$, the pre-existing bending moments from the external pressure, which are not taken into account in the usual computation of the critical pressure, will begin to play a role. Moreover, for such shells the half wave lengths λ of the buckling lobes in the circumferential direction will be so small, as compared to the shell radius, that unavoidable eccentricities may reduce the actual initial curvature in some lobes to zero. However, tests seem to indicate that the number of circumferential half waves is in good agreement with that from classical theory.[4] This is in agreement with the influence of eccentricity on the buckling of flat plates, where it decreases the critical stress, but practically does not affect the half wave length of buckling.[8]

Furthermore, for small ratios L/a, the effect of clamping will be increased, because in that case the actual tangential stresses in the shell close to the rings will be more relieved by the restraining action of the rings than in the case of simply supported edges. It should be noted that this favorable effect, which becomes important for smaller ratios L/a, is not taken into account in calculating the critical stresses for

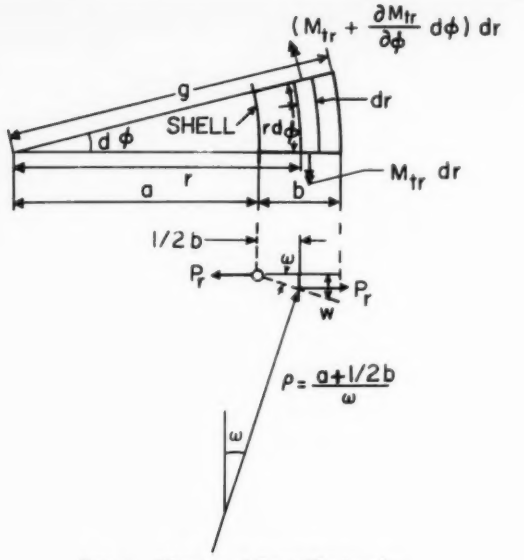

FIG. 4. Element of flat stiffening ring.

any kind of boundary conditions. Nevertheless, the fact of the greater relief of stress for clamped edges will tend to decrease the pertinent effective length l, thus counteracting the relative smaller effect of clamping for shorter shells as shown in Tables A1 and A2 of reference 1.

Consequently, for very short shells it seems to be appropriate to neglect the curvature and to take account of the critical pressure $(p_{cr})_b$ due to bending rigidity alone, but to calculate $(p_{cr})_b$ for a number of lobes according to classical shell theory, as determined by the effective length l from Eq. (7). Denoting p_{cr} from Eqs. (7) and (8) as $(p_{cr})_{sh}$ (from shell theory), one then may assume the actual critical pressure p_{cr} to increase linearly from $(p_{cr})_b$ to $(p_{cr})_{sh}$ for ratios l/a varying from zero to $(l/a)_c$, where from the foregoing for steel shells

$$(l/a)_c = 1 + [(p_{cr})_{sh} - 15]/135 \tag{18}$$

and for aluminum shells

$$(l/a)_c = 1.5 + [(p_{cr})_{sh} - 15]/90 \tag{19}$$

By neglecting the curvature of the shell $(p_{cr})_b$ takes account of the limited applicability of small deflection theory. Taking account of the bending rigidity alone, the differential equation of the shell reduces to

$$N[(\partial^4 w/\partial x^4) + 2(\partial^4 w/\partial x^2 \partial y^2) + (\partial^4 w/\partial y^4)] + t\sigma_y[(1/2)(\partial^2 w/\partial x^2) + (\partial^2 w/\partial y^2)] = 0 \tag{20}$$

Considering a shell with effective length l, with

$$w = w_0 \cos(\pi x/l) \cos(\pi y/\lambda) \tag{21}$$

Eq. (20) yields

$$\sigma_y = \{(1 + \epsilon^2)^2/[(1/2) + \epsilon^2]\}(\pi^2 N/l^2 t)$$

where

$$\epsilon^2 = l^2/\lambda^2 = (n^2 l^2)/(\pi^2 a^2) \tag{22}$$

so that

$$(p_{cr})_b = (t\sigma_y/a) = \{(1 + \epsilon^2)^2/[(1/2) + \epsilon^2]\}(\pi^2 N/l^2 a) \tag{23}$$

From the preceding, ϵ is determined by the optimum number of lobes from small deflection theory. From reference 9, the critical pressure for simply supported cylindrical shells [Eq. (287) of reference 10] reduces to

$$p = G\{(1 + H\Phi^4)/[\Phi - (1/2)]\Phi^2\} \tag{24}$$

where

$$G = Etl^2/\pi^2 a^3; \quad H = \pi^4 a^2 t^2/12(1 - \nu^2) l^4; \quad \Phi = 1 + \epsilon^2 \tag{25}$$

To make p a minimum, Φ has to satisfy the equation

$$(3\Phi - 1)/\Phi^4(\Phi - 1) = H$$

In order to obtain an explicit expression for Φ, it may be observed that, since $\Phi \gg 1$, approximately

$$\Phi = (3/H)^{1/4} \tag{26}$$

Inserting this into Eq. (24), one gets

$$(p_{cr})_{sh} = \frac{0.92(t/a)^2 E}{(l/a)(a/t)^{1/2} - 0.655} \tag{27}$$

which is practically identical to Eq. (8), although the approximations involved in the derivations differ. From Eqs. (22), (25), and (26),

$$\epsilon^2 = \{[36(1 - \nu^2)]^{1/4}/\pi\}[l/(at)^{1/2}] - 1 \tag{28}$$

$$n = (\pi a/l)\{0.763[l/(at)^{1/2}] - 1\}^{1/2} \tag{29}$$

Using Eq. (28) in Eq. (23) gives

$$(p_{cr})_b = \frac{0.69(t/a)^2 E}{(l/a)(a/t)^{1/2} - 0.655} \tag{30}$$

or exactly 75 per cent of Eq. (27). Hence, from the foregoing, if $l/a < (l/a)_c$,

$$p_{cr} = [0.75 + 0.25(l/a)/(l/a)_c](p_{cr})_{sh} \tag{31}$$

where $(p_{cr})_{sh}$ is given by Eq. (27), and $(l/a)_c$ by Eqs. (18) or (19).

Spring Constants of Stiffening Rings

Flat Ring—If the shell buckles in Mode A (Fig. 1), it will exert moments upon the stiffening rings that vary sinusoidally in the circumferential direction. For a flat ring (Fig. 4), the influence of the curvature $1/r$ upon the spring constant is small, so that first a straight flange is considered and the influence of the curvature is subsequently taken into account. The spring constant of a simply supported flange under compression and subjected to a sinusoidally varying moment at its supported edge may be calculated directly from Eq. (56) of reference 11, where $\psi_e = \theta_e/(EID)$ is the angle rotation per unit moment and in the elastic range EID reduces to the flexural rigidity N_r of the flange. Hence, the spring constant of the flange is $\beta_f = 1/\psi_e = N_r/\theta_e$, where θ_e is given by Eq. (56) of reference 11. This same spring constant can

be read from the tables of reference 12, where S^{III} is calculated from the same formula and is given as a function of the compressive stress in the flange and the half wave length λ. Since S^{III} refers to a quarter radian, the spring constant is

$$\beta_f = 4S^{III} \tag{32}$$

In order to take account of the curvature of the flange (ring), it is observed that its rotational stiffness is mainly dependent on its torsional rigidity and its compressive stress. Let the deflection of the ring be (Fig. 4)

$$w = C(r - a)\cos n\varphi \tag{33}$$

so that the torsional moment M_{tr} (Fig. 4) is

$$M_{tr} = N_r(1 - \nu)[(1/r)(\partial^2 w/\partial r\partial\varphi) - (1/r^2)(\partial w/\partial\varphi)] = -N_r(1 - \nu)C(a/r^2)n \sin n\varphi \tag{34}$$

The total restraining moment exerted by the torsional moments upon a ring per unit length at $r = a$ is

$$(M)_r = -(1/a)\int_a^g (\partial M_{tr}/\partial\varphi)dr = N_r(1 - \nu)C(b/ga)n^2 \cos n\varphi \tag{35}$$

where $b = g - a$. On the other hand, for a straight flange, where $r - a = -z$, and $rd\varphi = y$, with a deflection

$$w = -Cz\cos(\pi y/\lambda) \tag{36}$$

one obtains for the same restraining moment

$$(M)_f = \int_{-b}^{0} (\partial M_{yz}/\partial y)dz = N_r(1 - \nu)\int_{-b}^{0} (\partial^3 w/\partial y^2\partial z)dz = N_r(1 - \nu)Cb(\pi^2/\lambda^2)\cos(\pi/\lambda)y \tag{37}$$

From comparison of Eqs. (35) and (37), since for a straight flange $\pi a/\lambda$ and y/a are equivalent to n and φ for a ring—the restraining moment $(M)_r$, for a ring, is (a/g) times $(M)_f$ for a straight flange. Similarly, it is easily shown[1] that the moment exerted about the line $r = a$ by the deflecting forces $t'\sigma_r\partial^2 w/r^2\partial\varphi^2$ due to the compressive stresses σ_r in the ring is (a/g) times that for a straight flange. Hence, the spring constant β_f from Eq. (32) for a ring is reduced to

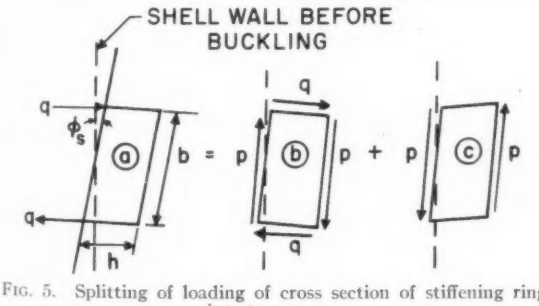

FIG. 5. Splitting of loading of cross section of stiffening ring into two cases.

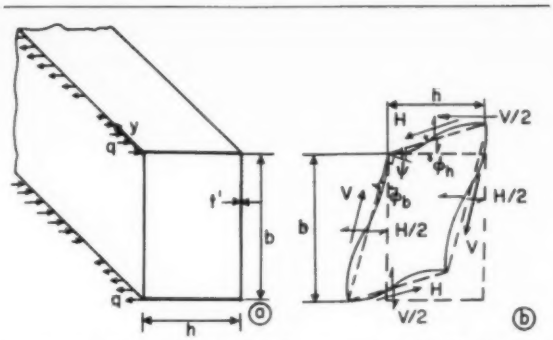

FIG. 6. Loading and distortion of cross section of stiffening ring with box section.

$$\beta_r = (a/g)\beta_f = [4a/(a + b)]S^{III} \tag{38}$$

Further, the radial cross sections of the ring element shown in Fig. 4 are subjected to bending moments $\int_a^g M_t dr$, where

$$M_t = -N_r[(1/r)(\partial w/\partial r) + (1/r^2)(\partial^2 w/\partial\varphi^2) + \nu(\partial^2 w/\partial r^2)]$$

Since these cross sections embrace an angle $d\varphi$, these moments combine to a restraining moment $-\left(\int_a^g M_t dr\right)d\varphi$, preventing the rotation ω of the element about its intersection with the shell, where from Eq. (33) $\omega = C\cos n\varphi$. Inserting Eq. (33) into the above equation for M_t, this leads to an extra restraint

$$\beta_t = -(1/a\omega)\int_a^g M_t dr = -(N_r/a)\{(n^2 - 1) \times \ln[(a + b)/a] - n^2[b/(a + b)]\} \tag{39}$$

The other additional restraint is caused by the fact that after tilting over an angle ω the forces P_r exerted by the shell upon the ring form a restoring couple with the resultant in the radial direction of the tangential forces in the ring (see Fig. 4). Assuming the tangential stresses in the ring to be constant, this restoring moment is $M_\sigma = P_r\omega b/2$ giving an extra spring constant

$$\beta_\sigma = M_\sigma/\omega = P_r b/2 \tag{40}$$

Actually, from Eq. (202) of reference 13, the tangential forces in a ring under internal pressure vary with r. This can be taken into account[1] but, since β_σ is small as compared to β_r, it appears that Eq. (40) is sufficiently accurate. P_r in Eq. (40) can be calculated from Eq. (247) of reference 14. Hence, the spring constant for a flat ring is

$$\beta_R = \beta_r + \beta_t + \beta_\sigma \tag{41}$$

where β_r, β_t, and β_σ are given by Eqs. (38), (39), and (40).

Ring with Box Section—The buckling shell will exert moments on the ring, that consist of sinusoidally varying loads q [Figs. 5(a) and 6(a)]. Assuming in

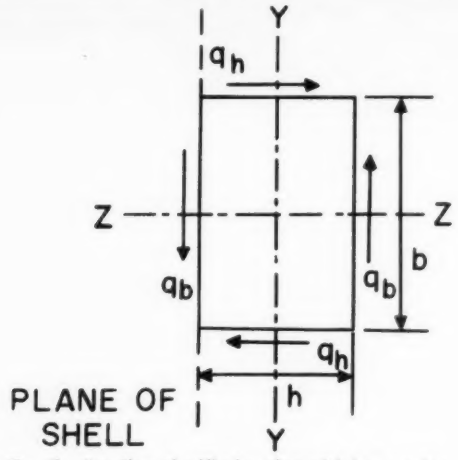

FIG. 7. Loading of stiffening ring with box section.

the following discussion the shell axis to be vertical, these loads may be thought to be composed of (1) pure torsional moments, formed by the loads q in combination with vertical forces p [Fig. 5(b)], and (2) superimposed vertical loads p of opposite sign [Fig. 5(c)]. The latter will distort the cross section of the ring. This distortion will substantially decrease its spring constant.

First, a straight beam is considered, of which the cross section is a rectangular tube with wall thickness t'. The forces [Fig. 6(a)]

$$q = q_0 \cos(\pi y/\lambda) \tag{42}$$

will cause a distortion of the tube [Fig. 6(b)]. With an angle of distortion ψ, extra loads V and H are transferred to the walls. Equilibrium requires [Fig. 6(b)]

$$V = (b/h)H \tag{43}$$

From Fig. 6(b), assuming no rotation of the top left corner,

$$\left.\begin{aligned} \varphi_h &= (V/2)(h/2)^3/3N_r(h/2) = Vh^2/24N_r \\ \varphi_b &= (H/2)(b/2)^3/3N_r(b/2) = Hb^2/24N_r \end{aligned}\right\} \tag{44}$$

where N_r is the flexural rigidity of the walls of the tube. From Eqs. (43) and (44) and from Fig. 6(b), the total angular distortion is

$$\psi = \varphi_h + \varphi_b = Hb(b + h)/24N_r$$

or, using Eq. (43),

$$H = k\psi/b; \qquad V = k\psi/h \tag{45}$$

where

$$k = 24N_r/(b + h) \tag{46}$$

From Fig. 6 and Eqs. (45), this causes total loads (Fig. 7)

$$q_h = q - k\psi/b; \qquad q_b = -k\psi/h \tag{47}$$

These loads cause deflections of the tube walls in their plane from bending and shear. First bending is considered. If only the loads q_b would be present, they would cause tensile and compressive stresses σ in the corners of the tube as indicated in Fig. 8(a) by positive and negative signs. The vertical walls will transfer shear forces S to the horizontal walls, as indicated in Fig. 8(b), for the upper web. This will cause moments Sh in the horizontal webs and edge stresses.

$$\sigma = 6Sh/(t'h^2) = 6S/(t'h) \tag{48}$$

Hence, the stresses and strains caused by the forces S in the horizontal walls are the same as in a centrically loaded plate of width $h/6$, so that the deflection of the vertical walls will be the same as that of beams with a cross section as shown in Fig. 8(c), with a moment of inertia

$$I_b = (1/12)t'b^3 + (1/2)[(1/6)t'h]b^2 = (1/12)b^2(b + h)t' \tag{49}$$

Similarly, the horizontal webs in Fig. 8 have a moment of inertia

$$I_h = (1/12)h^2(b + h)t' \tag{50}$$

From Fig. 8(a), the loads q_b cause stresses σ and strains $\epsilon = \sigma/E$ of equal absolute value in all corners. Hence, the specific angle rotations of the horizontal and vertical walls are $2\epsilon/h$ and $2\epsilon/b$, respectively. Consequently, the angle rotations of the horizontal walls are (b/h) times those of the vertical walls, and the same ratio holds for the bending deflections $\bar{w}_{hb}$ and w_{bb} of horizontal and vertical walls, respectively (Fig. 9). These deflections cause rotations of the webs out of their planes of

$$\varphi_{hb} = 2w_{bb}/h; \quad \varphi_{bb} = 2\bar{w}_{hb}/b = 2w_{bb}/h = \varphi_{hb} \tag{51}$$

A similar distortion occurs in a truss bridge with upper and lower lateral bracing if only one of the main trusses is loaded.[15] The total angle of distortion is (Fig. 9)

$$\psi_{bb} = \varphi_{hb} + \varphi_{bb} = 4w_{bb}/h \tag{52}$$

where w_{bb} is the bending deflection of a beam with a moment of inertia I_b from Eq. (49) from a load q_b. Hence,

$$w_{bb}^{IV} = q_b/(EI_b) \tag{53}$$

where primes indicate differentiation with respect to y (in the present case, 4 times). Similarly, the loads q_h in Fig. 7 cause an angle of distortion

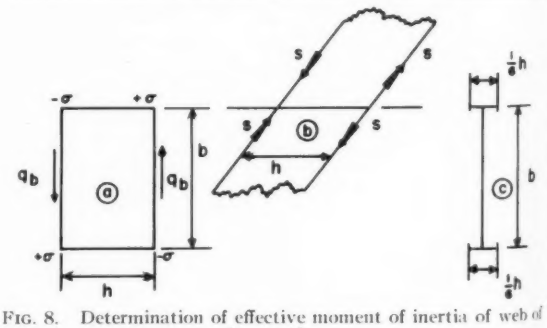

FIG. 8. Determination of effective moment of inertia of web of box section.

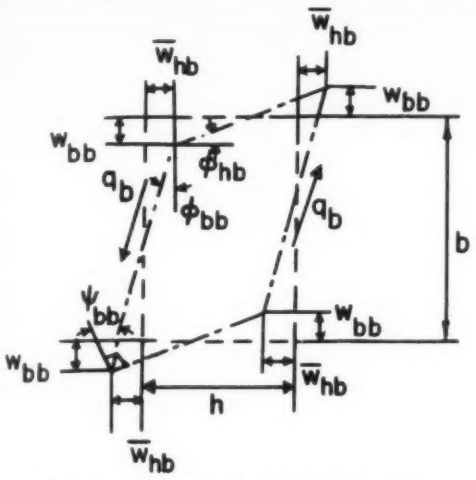

FIG. 9. Deflections of webs of box section.

$$\psi_{hb} = 4w_{hb}/b \tag{54}$$

where w_{hb} is the bending deflection of a beam with a moment of inertia I_h from Eq. (50) from a load q_h, so that

$$w_{hb}^{IV} = q_h/(EI_h) \tag{55}$$

The bending deflections from the loads q_b and q_h cause a total angle of distortion

$$\psi_b = \psi_{bb} + \psi_{hb} = 4[(w_{bb}/h) + (w_{hb}/b)] \tag{56}$$

From Eqs. (53) and (55)

$$\psi_b^{IV} = 4[(w_{bb}^{IV}/h) + (w_{hb}^{IV}/b)] = 4[q_b/(EI_bh) + q_h/(EI_hb)] \tag{57}$$

Deformation by shear can be assumed to cause angle rotations in the plane of a vertical wall of

$$w_{bs}' = \gamma = \tau/G = S/(bt'G) \tag{58}$$

where the second subscript s refers to shear and S is the transverse shear from the loads q_b (Fig. 7), so that $S' = dS/dy = -q_b$ and

$$w_{bs}'' = -q_b/(bt'G) \tag{59}$$

Similarly, for the horizontal walls

$$w_{hs}'' = -q_h/(ht'G) \tag{60}$$

Shear deflections w_{bs} and w_{hs} of vertical and horizontal walls in their own planes cause angles of distortion of the cross section

$$\psi_{bs} = 2w_{bs}/h; \quad \psi_{hs} = 2w_{hs}/b \tag{61}$$

respectively, giving a total distortion by shear deflections of the walls of

$$\psi_s = \psi_{bs} + \psi_{hs} = 2[(w_{bs}/h) + (w_{hs}/b)] \tag{62}$$

and, using Eqs. (59) and (60),

$$\psi_s^{IV} = -(2/bht'G)(q_b'' + q_h'') \tag{63}$$

Hence, from Eqs. (57) and (63), and using Eqs. (47), the fourth derivative of the total angle of distortion is

$$\psi^{IV} = \psi_b^{IV} + \psi_s^{IV} = -(4/EI_bh)(k/h)\psi + (4/EI_hb)[q - (k/b)\psi] - (2/bht'G) \times [-(k/h)\psi'' + q - (k/b)\psi''] \tag{64}$$

Insertion of I_b and I_h from Eqs. (49) and (50) and use of Eq. (42) leads to the differential equation

$$\psi^{IV} - P\psi'' + Q\psi = R \cos(\pi y/\lambda) \tag{65}$$

where

$$\begin{aligned} P &= [2(b+h)k/b^2h^2t'G] \\ Q &= [96k/b^2h^2(b+h)t'E] \\ R &= \{[48/bh^2(b+h)t'E] + (2\pi^2/bht'\lambda^2G)\}q_0 \end{aligned} \tag{66}$$

A somewhat similar differential equation is obtained for a bridge with upper and lower lateral bracings, end and intermediate cross bracings.[15] With

$$\psi = \psi_0 \cos(\pi y/\lambda) \tag{67}$$

Eq. (65) yields

$$\psi = \{R/[(\pi^4/\lambda^4) + (\pi^2/\lambda^2)P + Q]\} \cos(\pi y/\lambda) \tag{68}$$

From Eqs. (51) and (52), the bending deflection of the walls in their plane causes angle rotations φ_s (Fig. 5) of the wall in the plane of the shell of

$$\varphi_{sb} = \varphi_{bb} = \varphi_{hb} = (1/2)\psi_b$$

Shear deflections in their planes of the horizontal walls cause angle rotations out of its plane of the wall in the plane of the shell of

$$\varphi_{ss} = 2w_{hs}/b$$

so that the total angle rotation in the plane of the shell, out of that plane, is

$$\varphi_s = \varphi_{sb} + \varphi_{ss} = (1/2)\psi_b + 2w_{hs}/b$$

or, from Eq. (56),

$$\varphi_s = 2[(w_{bb}/h) + (w_{hb}/b)] + 2w_{hs}/b \tag{69}$$

Hence, from Eqs. (53), (55), and (60)

$$\varphi_s^{IV} = 2[q_b/(EI_bh) + q_h/(EI_hb) - q_h''/(bht'G)] \tag{70}$$

Using Eqs. (47), (49), (50), and also (42), (66), (67), and (68), this yields

$$\varphi_s = \left[\frac{24}{bh^2(b+h)t'E}\left(1 + \frac{\lambda^2}{\pi^2}\frac{b-h}{b+h}P\right) + \frac{2\pi^2}{\lambda^2bht'G}\left(1 + \frac{\lambda^2}{\pi^2}\frac{b}{b+h}P + \frac{\lambda^4}{2\pi^4}Q\right)\right] \times \frac{q_0\cos(\pi y/\lambda)}{(\pi^4/\lambda^4) + (\pi^2/\lambda^2)P + Q} \tag{71}$$

Hence, the spring constant is (Fig. 5)

$$\beta_s = M/\varphi_s = (bq_0/\varphi_s)\cos(\pi y/\lambda) \tag{72}$$

or

$$\beta_s = b\left(\frac{\pi^4}{\lambda^4} + \frac{\pi^2}{\lambda^2}P + Q\right)\Big/\left[\frac{24}{bh^2(b+h)t'E}\left(1 + \frac{\lambda^2}{\pi^2}\frac{b-h}{b+h}P\right) + \frac{2\pi^2}{\lambda^2 bht'G}\left(1 + \frac{\lambda^2}{\pi^2}\frac{b}{b+h}P + \frac{\lambda^4}{2\pi^4}Q\right)\right] \quad (73)$$

This spring constant applies to a straight tube. Analogous to Eq. (38), for a tubular ring the spring constant is

$$\beta_R = \beta_r = [a/(a+h)]\beta_s \quad (74)$$

Owing to the high critical stress of such a ring section (hat section), the influence of the compressive stresses in the ring upon the spring constant may be neglected. Also, the term corresponding to Eq. (39) can usually be neglected.

Buckling in Mode B, General Instability

As explained in the Introduction, this mode is split into Cases 1 and 2. Case 1 is that of a simply supported orthotropic shell where the stiffness of the rings is uniformly distributed along the shell length L_1 and Case 2 is that of fully clamped shell panels with lengths L (Fig. 2).

The critical pressure p_1 for Case 1 may be calculated from Eq. (g) on page 480 of reference 10, from which for the present case, with $\sigma_x = (1/2)\sigma_y$, and $\phi_2 = (1/2)\phi_1$, the critical pressure is

$$p_1 = [Et/(1-\nu^2)a]\phi_1 = [Et/(1-\nu^2)a] \times \{(C_1 + C_2\alpha + C_3\alpha_1)/[C_4 + (1/2)C_5]\} \quad (75)$$

Here the symbol t has been substituted for h, denoting the shell thickness in reference 10. All other symbols are explained in that reference. The calculation of α_1 requires the moment of inertia I_y (Fig. 7) of the rings for bending in their planes, for which it is necessary to know the effective width of the shell that acts together with the rings. The effective width can practically always be assumed as that for an infinitely long shell that was calculated in reference 16 for a Poisson's ratio $\nu = 0$. With $\nu = 0.3$, this effective width can be assumed as

$$b_e = \frac{0.78(at)^{1/2}}{\{[1 + (1/2)n^4(t/a)^2]^{1/2} + (1/\sqrt{3})n^2t/a\}^{1/2}} \quad (76)$$

at each side of the stiffener. To find the minimum value p_{1min} of p_1, the number of lobes in the circumferential direction has to be chosen such that p_1 becomes as small as possible.

For Case 2, that of a clamped shell panel, the minimum critical pressure p_{2min} is given by Eq. (31), where from Eq. (7), with $\beta = \infty$, $l = 0.665\,L$, $(p_{cr})_{sh}$ is given by Eq. (9) of reference 2, or by the present Eq. (27), with $l = 0.665\,L$.

To find the actual critical pressure for Mode B resulting as the interaction between Cases 1 and 2, as will be shown later on, one has also to calculate p_1 and p_2 for a number of lobes for which they are not minimum. In that event, p_1 follows directly from Eq. (75), and p_2 about from Eq. (31), where $l = 0.665\,L$ and $(p_{cr})_{sh}$ is given by Eq. (24). The interaction between Cases 1 and 2 is similar to that between column and plate buckling in I-shaped columns, as calculated by the method of split rigidities in reference 17. This method, on which a comprehensive treatise is given in reference 18, will also be used here. For both Cases 1 and 2, the deflection w can be represented as (Fig. 2)

$$w = X\cos(ny/a) \quad (77)$$

where X is a function of x alone. The compressive stresses σ_y and $\sigma_x = (1/2)\sigma_y$ in the shell cause deflecting forces

$$D = -t\sigma_y\{[(\partial^2 w/\partial y^2) + (w/a^2)] + (1/2)\partial^2 w/\partial x^2\} \quad (78)$$

per unit surface of the shell. Since shells under external pressure buckle in circumferential lobes that are short as compared to the panel length L, $(1/2)\partial^2 w \div \partial x^2$ is neglected with respect to the other terms, so that from Eq. (77)

$$D = t\sigma_y(n^2 - 1)w/a^2 \quad (79)$$

and thus is proportional to σ_y and w. Since σ_y is proportional to the external pressure p, D is also proportional to p and w. Considering a panel (shell plus two half rings) near to the center of the shell, the deflection w_1 for Case 1 can be considered as not to vary with x (Figs. 2 and 10). In Case 1, the total deflecting force acting on a longitudinal strip, running in the axial direction on the crest of a circumferential lobe and with a length L, can be written as

$$D_1 = CLp_1w_1 \quad (80)$$

where C is a constant and p_1 is the critical external pressure for Case 1. Hence, also the restraining force acting on that strip is

$$R_1 = CLp_1w_1 \quad (81)$$

The deflection w_2 from Case 2 causes mainly internal moments M_y in the shell alone, which may be neglected in comparison to those in the rings in Case 1, so that R_1 represents the total restraining force in the combined case. Hence, the equilibrium between deflecting and restraining forces in the combined case, with critical pressure p_{cr}, can be written as $D_1 + D_2 = R_1$, or, using the same constant C (Fig. 10), as

$$CLp_{cr}w_1 + Cp_{cr}\int_{-(L/2)}^{L/2} w_2\,dx = CLp_1w_1$$

or

$$p_{cr}(w_1 + \varphi w_{2m}) = p_1w_1 \quad (82)$$

where

$$\varphi = \left(2\int_0^{L/2} w_2\,dx\right)\Big/(Lw_{2m}) \quad (83)$$

In obtaining Eq. (82), it was sufficient to consider the deflecting and restraining forces themselves only, and not the work they perform. Since these forces exert work on the deflection w_1 only, which does not vary with x, their work is proportional to these forces

themselves. To obtain a second equation, only the shell between two rings is considered, that is, not including the rings. Here it is necessary to consider the *work* done by the deflecting and restraining forces, since that work is exerted on the deflection w_2, so that the higher the relative value of w_2, the more influence the forces have. In Case 2, the deflecting force D_2 acting upon an element of unit surface at the crest of a circumferential lobe can be expressed as $C\ p_2\ w_2$. Hence, also the restraining force R_2, that is in equilibrium with D_2, is equal to $C\ p_2\ w_2$. This may be considered as the total restraining force in the actual, combined case, since in Case 1 the deflecting forces are resisted primarily by the rings, so that the restraining force from the shell alone, as considered here, may be neglected. Hence, in the combined case, the negative work exerted by the restraining forces upon the longitudinal strip considered in Eq. (80) is

$$V_R = \int_{-(L/2)}^{L/2} R_2 w_2 dx = 2Cp_2 \int_0^{L/2} w_2^2 dx \quad (84)$$

The deflecting forces in the combined case are $D_1 = C\,p_{cr}\,w_1$ and $D_2 = C\,p_{cr}\,w_2$. Since the restraints $R = R_2$ against buckling of the shell panel (without the rings) are connected with the deflection w_2 only, the work done by the deflecting forces in the combined case is

$$V_D = \int_{-(L/2)}^{L/2} (D_1 + D_2) w_2 dx = 2Cp_{cr}\left[\int_0^{L/2} w_1 w_2 dx + \int_0^{L/2} w_2^2 dx\right] \quad (85)$$

Since $V_D = V_R$, from Eqs. (84) and (85)

$$p_{cr}(\gamma w_1 + w_{2m}) = p_2 w_{2m} \quad (86)$$

where

$$\gamma = w_{2m} \int_0^{L/2} w_2 dx \Big/ \int_0^{L/2} w_2^2 dx \quad (87)$$

Elimination of w_1 and w_{2m} from Eqs. (82) and (86) gives

$$p_{cr} = [1/2(1 - \gamma\varphi)]\{p_1 + p_2 - [(p_1 + p_2)^2 - 4(1 - \gamma\varphi)p_1 p_2]^{1/2}\} \quad (88)$$

If p_2 is much greater than p_1, this reduces conservatively to

$$p_{cr} = \{[p_2 + (1 - \gamma\varphi)p_1]/(p_2 + p_1)\}p_1 \quad (89)$$

analogous to Eq. (75) of reference 17. Inversely, if $p_1 \gg p_2$,

$$p_{cr} = \{[p_1 + (1 - \gamma\varphi)p_2]/(p_1 + p_2)\}p_2 \quad (90)$$

analogous to Eq. (74) of reference 17. Indeed, as shown in reference 1, with buckling in a number of lobes that makes p_1 minimum (say 4), p_2 is very high, so that Eq. (89) applies, from which p_{cr} is only slightly below p_1. On the other hand, for the number of lobes that makes p_2 minimum, p_1 is high, so that from Eq. (90), p_{cr} is only slightly smaller than p_2. The factor $(1 - \gamma\varphi)$ influences p_{cr}, but not very much, so that, as shown in reference 1, in computing $\gamma\varphi$ it is sufficiently accurate to assume

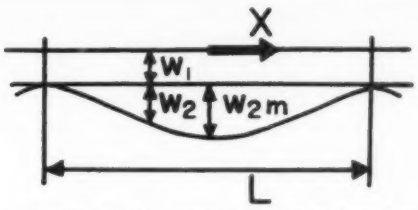

FIG. 10. Splitting of shell panel deflection w from buckling in general instability into deflections w_1 and w_2.

$$w_2 = w_{2m} \cos^2 (\pi x/L) \quad (91)$$

where w_2 is the deflection at the crest of the circumferential lobes. Eqs. (83) and (87) then give $\gamma\varphi = 2/3$, so that from Eqs. (89) and (90)

$$\left.\begin{aligned} &\text{for } p_2 \gg p_1\text{:}\quad p_{cr} = \{1 - (2/3)[p_1/(p_1 + p_2)]\}p_1 \\ &\text{for } p_1 \gg p_2\text{:}\quad p_{cr} = \{1 - (2/3)[p_2/(p_1 + p_2)]\}p_2 \end{aligned}\right\} \quad (92)$$

Here, p_1 and p_2 in each formula belong to the same number of lobes. Practically, p_{cr} becomes minimum if either p_1 or p_2 become minimum. As shown in reference 1, for a steel shell with $a = 25$ in., $L_t = 125$ in., $L = 31.25$ in., and $t = 0.073$ in., and with a moment of inertia I_y (Fig. 7) of the rings of 0.0120 in.^{4}, the minimum value of p_1 is 14.7 psi, occurring for $n = 4$. For this same number of lobes p_2 is 845 psi, since $n = 4$ is much smaller than the optimum number of waves for the shell panel, which is 13. Hence, from the first Eq. (92) p_{cr} for Mode B is only 1 per cent smaller than p_1. On the other hand, the shell thickness t was chosen such that also the minimum value of p_2, occurring with $n = 13$, is 14.7 psi. For this same n, the value of p_1 from Eq. (75) is 1040 psi, so that from the second Eq. (92), p_{cr} is less than 1 per cent smaller than $p_2 = 14.7$ psi. Hence, the interaction between p_1 and p_2 is negligible, due to the great difference between the number of lobes that makes p_1 or p_2 a minimum. As shown in reference 1, for these critical pressures and a total length not greater than $5a$, as were considered there, it is economical to place the rings as close as structurally possible, so that L/a should be smaller than assumed in this example. For smaller L/a ratios the difference between the optimum number of lobes for p_1 and p_2 becomes still greater, so that it may be assumed that p_{cr} for Mode B is equal to either p_1 or p_2, whichever is smallest. Since p_2 is always more than p_{cr} for Mode A, this means that the only value of p_{cr} for Mode B that can be governing is p_1.

PLASTIC REDUCTION FACTOR AND INFLUENCE OF OUT-OF-ROUNDNESS

From Fig. 13 of reference 19 for shells with small ratios L/t, for which the experimental buckling stresses σ_y are higher than about half the yield stress σ_{ys}, they are below the theoretical buckling stress from von Mises' equation [Eq. (287) of reference 10]. Besides

the limited applicability of small deflection theory, which is taken into account in Eq. (31), this is mainly due to two factors: (1) the decrease of the effective deformation modulus above the proportional limit, and (2) out-of-roundness. In view of the wide scatter of the experimental values, apparently due to varying out-of-roundness, it seems sufficiently accurate to take account of the decreased modulus by multiplying the elastic critical pressure, for panel as well as general instability, with the tangent modulus ratio E_t/E. This can be done for panel buckling without trial and error by calculating the slenderness $s_s = \pi\sqrt{E/\sigma_{ycr}}$ of a column with the same elastic buckling stress σ_{ycr}, where $\sigma_{ycr} = (a/t)p_{cr}$ and p_{cr} is given by Eq. (31), and finding the plastic buckling stress of the equivalent column and the shell panel from a slenderness-buckling stress diagram for columns of the same material. For general instability, the equivalent slenderness is $s_r = \pi\sqrt{E/\sigma_r}$, where σ_r is the compressive stress in the rings for the critical pressure that causes elastic general instability. From the preceding section, the latter is equal to p_1 from Eq. (75). σ_r is calculated from Eq. (247) of reference 14.

Out-of-roundness can be taken into account by determining the equivalent eccentricity of the equivalent column and multiplying its concentric buckling stress by a reduction factor μ for eccentricity that for various steels may be derived from data given in reference 20. The Fourier term of the initial deflection that has the greatest amplitude is probably that with the same number of lobes n as that in which the shell buckles, since this is the deformation that requires a minimum of work. Let the amplitude of the half waves be e. Assuming the stress-strain diagram to be straight up to the yield stress, as is assumed in deriving the secant formula as an approximation of the buckling stress of eccentrically loaded columns, with a direct stress σ_y the outer fiber stress practically reaches the yield stress σ_{ys} when the elastic bending stress is equal to $\sigma_{ys} - \sigma_y$. These bending stresses are sufficiently accurately given by $-(\partial^2 w_e/\partial y^2)(t/2)E$. As is well known, the elastic deflection $w_e = [\sigma_y/(\sigma_{ycr} - \sigma_y)]e \cos(\pi y/\lambda)$, where σ_{ycr} is the elastic circumferential buckling stress and $\lambda = \pi a/n$ is the half wave length of the lobes in which the shell buckles. Hence, in a panel, the yield stress is reached when

$$(\pi^2/\lambda^2)[\sigma_y/(\sigma_{ycr} - \sigma_y)]e(t/2)E = \sigma_{ys} - \sigma_y \quad (93)$$

For the equivalent column, with length $s_s r_s$, where $r_s = 0.289\,t$ is the radius of gyration of the shell wall, the same condition becomes

$$[\pi^2/(s_s r_s)^2][\sigma_y/(\sigma_{ycr} - \sigma_y)]e_e(t/2)E = \sigma_{ys} - \sigma_y \quad (94)$$

where e_e is the equivalent eccentricity of the column. Hence, in order to make the eccentric buckling stress of the column equal to that of the shell, its effective eccentricity should be assumed as

$$e_e = (s_s r_s/\lambda)^2 e \quad (95)$$

Similarly, for the rings

$$e_e = (s_r r_r/\lambda_r)^2 e_r \quad (96)$$

where the subscripts r refer to "ring" and e_r is the amplitude of the initial lobes with the same half wave length λ_r as that in which the shell buckles in general instability. The eccentricities e can be measured approximately as proposed in reference 21. The effective eccentricities e_e could be taken into account by multiplying the concentric buckling stresses with a reduction factor $\mu = 1/\gamma$, where for various steels γ is given in reference 20 as a function of slenderness, eccentricity and yield stress. However, from Table I of reference 22, for concentric buckling of a plate or shell with $\sigma_x = (1/2)\sigma_y$, the decrease with respect to the elastic region is only $(1 - 0.446)/(1 - 0.417) = 0.95$ times that for a column, so that the reduction factor μ for eccentricity may be assumed as

$$\mu = 1 - 0.95[1 - (1/\gamma)] \quad (97)$$

where γ is given by Eqs. (26) of reference 20. Hence, the eccentric buckling stress σ_y of the shell is

$$\sigma_{y\,ecc} = \mu(E_t/E)\sigma_{ycr} \quad (98)$$

where σ_{ycr} is the elastic circumferential buckling stress. A similar formula applies for the stress σ_r in the rings in the case of general instability. Here $\mu = 1/\gamma$.

A more accurate, but more laborious method for finding the buckling stress for general instability in the plastic range would be to multiply in Eq. (75) $C_1 + C_2\alpha$, due to the rigidity of the shell, with the plastic reduction factor η belonging to the ideal stress $(\sigma_x^2 + \sigma_y^2 - \sigma_x\sigma_y)^{1/2}$ in the shell,[22] and to multiply $C_3\alpha_1$ with the tangent modulus ratio E_t/E for the stress σ_r in the rings. To the concentric buckling stress found thus, the reduction factor μ for eccentricity is then applied. Theoretically, for minimum weight the buckling stresses for panel and general instability should be equal. However, since no test results are available for checking the calculation for general instability, especially in the plastic range, it is recommended that the dimensions be chosen such that p_{cr} for Mode B (general instability) is somewhat higher than p_{cr} for Mode A (panel buckling).

Example of Calculation and Comparison With Test

The only complete test data available to the writer are those of reference 19. The total length of the shell is $L_t = 33.75$ in., the ring spacing $L = 5.27$ in., $a = 13.375$ in., and $t = 0.062$ in. For the solid rings $b = 0.656$ in. and $t' = 0.1875$ in. The eccentricity e of the shell, determined according to reference 21, was $0.374\,t$. The yield stress of the material was 54,400 psi. Panel buckling occurred at $p = 80$ psi.

Panel Buckling (Mode A)

The heavy rings offer a high rotational restraint, so that as a first approximation the panel is assumed as

fully clamped. From reference 2 then, $l = 0.665L = 3.50$ in., and $l/a = 3.50/13.375 = 0.262$. From Eq. (29), $n = 16.7$, so that actually $n = 17$ and the circumferential half wave length $\lambda = \pi a/n = 2.47$ in. S^{III} in Eq. (38) depends on $\lambda/b = 2.47/0.656 = 3.76$ and $k = b^2t'\sigma_r/(\pi^2N_r)$. Assuming $\sigma_r = 10{,}000$ psi, one ends up with $p_{cr} = 80$ psi. Using now $p = 80$ psi, one obtains from page 404 of reference 14, with $\nu = 0.3$, $2\alpha = [3(1 - \nu^2)]^{1/4}L/(at)^{1/2} = 7.45$ and $\beta = 2\alpha/L = 7.45/5.27 = 1.413$. Then from Eq. (247) of reference 14, since all values χ are practically equal to one, $h = t = 0.062$ in., and $A = A_r = bt' = 0.123$ in., one obtains $P = P_r = 0.825\,p = 66$ lb./in., so that $\sigma_r = P_rA/A_r = 7{,}200$ psi. Further, $N_r = Et^3/[12(1 - \nu^2)] = 18{,}100$ lb.-in., so that $k = 0.00325$. With these values of λ/b and k, from reference 12, $S^{III} = 0.2203\,N_r/b = 6{,}080$ lb.in./in. Measuring b up to the middle plane of the shell, in Eq. (38), so that $b = 0.656 + 0.031 = 0.687$ in., it gives $\beta_r = 23{,}100$ lb.in./in. From Eqs. (39), (40), and (41), $\beta_t = -380$, $\beta_a = 23$, and $\beta_R = 22{,}743$ lb.in./in. Hence, in Eq. (7), $\beta = \beta_R/2 = 11{,}371$ lb.in./in., $c = L/2 = 2.635$ in., and $N = Et^3/[12(1 - \nu^2)] = 654$ lb.in., so that, by trial and error, $l = 3.57$ in. and $l/a = 0.267$. From Eq. (29) again, $n = 17$. From Eq. (27) now $(p_{cr})_{sh} = 181$ psi, so that for steel shells Eq. (18) yields $(l/a)_c = 2.23$. Then Eq. (31) gives $p_{cr} = 0.78\,(181) = 141$ psi, so that $\sigma_{ycr} = (a/t)p_{cr} = 30{,}400$ psi. This is in the elastic range, so that $E_t/E = 1$. The slenderness of the equivalent column is $s_s = \pi\sqrt{E/\sigma_{ycr}} = 98.7$; $r_s = 0.289 \times t = 0.018$ in.; $e = 0.374t = 0.0232$ in. From Eq. (95) $e_c = [98.7(0.018)/2.47]^2e = 0.519e = 0.0120$ in. From Eq. (27) of reference 20, with $\sigma_{ys} = 54{,}400$ psi, $(L/r)_c = 81$, so that γ has to be calculated from Eq. (26a) of reference 20, from which, with $k_c = t/6 = 0.0103$ in.,

$$\gamma = 1 + (21{,}000 - 0.235\sigma_{ys})(e/k_c)^{2/3}/s_s^2 = 1.97 \quad (99)$$

and from Eq. (97), $\mu = 0.5325$. Hence, the resulting buckling pressure is $\mu p_{cr} = 75$ psi. In reference 19, the panel length L was assumed as 4.92 in., in order to take account of the thickness of the rings and welds. From Eq. (8), the critical pressure is practically inversely proportional to l, and hence, to L. This brings the buckling pressure to $(5.27/4.92)75 = 80.3$ psi. The experimental buckling pressure was 80 psi.

General Instability (Mode B)

From the preceding, p_{cr} is equal to p_1 from Eq. (75). $L_t/a = 33.75/13.375 = 2.52$, so that, without rings, from Eq. (29), $n = 6.5$. With rings n will be smaller. Try $n = 5$. With the notations of reference 10, p. 480, $\lambda = \pi a/L_t = 1.245$, and $s = 1.25$. Hence, the C coefficients in Eq. (75) can be calculated from p. 480 of this reference. However, since s has little influence, they can be read directly from graphs in reference 23, where s is assumed as 1.2. This gives $C_1 = 2.9$; $C_2 = 64{,}000$; $C_4 = 500{,}000$; $C_4 = 20{,}000$; $C_5 = 1400$. Further, in Eq. (75), with the present notations, $\alpha = t^2/12a^2 = 1/558{,}000$ and $\alpha_1 = (1 - \nu^2)I_y/(Lta^2)$. To find I_y of the rings, the effective width b_e from Eq. (76) has to be calculated, giving $b_e = 0.685$ in. This leads to $I_y = 0.01142$ in.[4] and $\alpha_1 = 0.000178$. Hence, Eq. (75) yields $p_1 = 680$ psi. Repeating the calculation for $n = 4$ and $n = 3$ gives $p_1 = 464$ psi and 621 psi, respectively, so that $p_{cr} = p_1 = 464$ psi. This is much higher than p_{cr} for panel buckling, so that, also taking account of reductions for plasticity and eccentricity, general instability is not governing. This is in accordance with the test, since the shell failed by panel buckling.

References

[1] Bijlaard, P. P., *Buckling Under External Pressure of Cylindrical Shells Evenly Stiffened by Rings Only*, Bell Aircraft Corporation Report No. 02-941-002, May, 1952.

[2] Bijlaard, P. P., *Buckling Stress of Thin Cylindrical Clamped Shells Subject to Hydrostatic Pressure*, Journal of the Aeronautical Sciences, Vol. 21, No. 12, pp. 852–853, 1954.

[3] Flügge, W., *Statik und Dynamik der Schalen*, Edwards Brothers, Inc., 1943.

[4] Windenburg, D. F., and Trilling, C., *Collapse by Instability of Thin Cylindrical Shells Under External Pressure*, Transactions ASME, Vol. 56, pp. 819–825, 1934.

[5] Donnell, L. H., *Stability of Thin-Walled Tubes Under Torsion*, NACA Report No. 479, 1933.

[6] Lardy, P., *Sur une Methode Nouvelle de Résolution du Problème des Dalles Rectangulaires Encastrées*, Publ. Internat. Assoc. for Bridge and Struct. Engrg., Vol. 13, pp. 197–220, 1953.

[7] Sturm, R. G., *A Study of the Collapsing Pressure of Thin-Walled Cylinders*, University of Illinois, Eng. Exp. Sta., Bull. Ser. 329, 1941.

[8] Bijlaard, P. P., *Grundlegende Betrachtungen zum Ausbeulen der Platten und Schalen im plastischen Bereich*, Mitt. a.d. Institut für Baustatik, ETH, Zurich, No. 21, 1948.

[9] Niordson, F. I. N., *Buckling of Conical Shells, Subjected to Uniform External Lateral Pressure*, Acta Polytechnica, Civil Engineering and Building Construction Series, Vol. 1, No. 3, Stockholm, 1947.

[10] Timoshenko, S., *Theory of Elastic Stability*, McGraw-Hill Book Co., New York, 1936.

[11] Bijlaard, P. P., *Theory of the Plastic Stability of Thin Plates*, Publ. Internat. Assoc. for Bridge and Struct. Engrg., Vol. 6, 1940–41.

[12] Kroll, W. D., *Tables of Stiffness and Carry-Over Factor for Flat Rectangular Plates Under Compression*, NACA ARR 3K27, 1943.

[13] Timoshenko, S., *Strength of Materials, Part II*, van Nostrand Co., New York, 1946.

[14] Timoshenko, S., *Theory of Plates and Shells*, McGraw-Hill Book Co., New York, 1940.

[15] Bijlaard, P. P., *Computation of a Truss Bridge with Parallel Chords, Having Upper and Lower Lateral Bracings as Well as Cross Bracings, for Horizontal Load*, de Ingenieur (the Hague, Holland), No. 48, 1926 (in Dutch).

[16] Thürlimann, B., Béreuter, R. O., and Johnston, B. G., *The Effective Width of a Circular Cylindrical Shell Adjacent to a Circumferential Reinforcing Rib.*, Proc. First U. S. National Congress of Applied Mechanics, pp. 347–356, ASME, 1952.

[17] Bijlaard, P. P., and Fisher, G. P., *Interaction of Column and Local Buckling in Compression Members*, NACA TN 2640, 1952.

[18] Bijlaard, P. P., *The Method of Split Rigidities and its Application to Various Buckling Problems*, Report submitted to the NACA, June 1956; to be published as an NACA TN.

(Continued on page 455)

Newtonian Flow Theory for Slender Bodies

J. D. COLE*

The RAND Corporation and California Institute of Technology

SUMMARY

As an aid to the aerodynamicist in the design of air frames for hypersonic speeds (speeds faster than about Mach 5), Newtonian flow theory is examined from the point of view of gas dynamics and hypersonic small-disturbance theory. The usual theory is shown to result as the first approximation of an expansion valid for small $\lambda = (\gamma - 1)/(\gamma + 1)$. A basic similarity parameter $N = (\gamma + 1)/(\gamma - 1)M_\infty{}^2\delta^2$ is introduced. A general solution of the first approximation for the flow past slender bodies (bodies which cause only a small disturbance to the stream) at zero angle of attack is given. An important condition which limits the application of the theory is noted—namely, that the pressure coefficient on the surface not fall to zero. The theory is then applied to cones and to bodies whose shape is $r = x^n$.

SYMBOLS

a	= local speed of sound
C_D	= drag coefficient
C_p	= pressure coefficient
$F(x)$	= body shape, $= F(\bar{x})$
$G(x)$	= $0 \leq r^* \leq G(x) = S - F$
g	= λG
H	= hypersonic similarity parameter $= 1/M_\infty{}^2\delta^2$
k	= p/σ
L	= characteristic length
M_∞	= free-stream Mach Number, or flight Mach Number
m	= for axial symmetry = 1; for two-dimensional flow = 0
N	= Newtonian similarity parameter $= (\gamma + 1)/(\gamma - 1)M_\infty{}^2\delta^2$
P	= pressure
$\vec{q}$	= velocity vector
r	= distorted radius, $= \bar{r}/\delta$
$\bar{r}$	= dimensionless radius
r^*	= $r - F(x)$
$\tilde{r}$	= r^*/λ
$S(x)$	= shock shape, $= S(\bar{x})$
T	= temperature (absolute)
U	= free-stream velocity along $\bar{x}$-axis
x	= distorted coordinate, $= \bar{x}$
y	= distorted coordinate, $= \bar{y}/\delta$
z	= distorted coordinate, $= \bar{z}/\delta$
$\bar{x}, \bar{y}, \bar{z}$	= dimensionless space coordinates
γ	= C_p/C_v = ratio at specific heats, assumed constant
∇	= gradient in $\bar{x}, \bar{y}, \bar{z}$ system
δ	= flow deflection or thickness ratio; or flow deflection angle
θ	= temperature ratio, $= T/T_\infty$
θ_C	= semivertex angle of cone
ϵ_w	= shock-wave angle
λ	= $(\gamma - 1)/(\gamma + 1)$
ρ	= density
t	= maximum thickness
ψ	= stream function
$(\ )^{(1)}$	= conditions behind the bow shock wave
$(\ )_I$	= second Newtonian approximation
$(\ )_0$	= surface conditions
$(\ )_\infty$	= free-stream conditions

Received September 3, 1956.

* Consultant at RAND and Associate Professor of Aeronautics and Applied Mechanics, C.I.T.

(1) INTRODUCTION

THE CALCULATION of inviscid flow fields at high Mach Numbers is of increasing importance. However, even within the framework of classical perfect fluid theory the exact equations of motion are too difficult to solve with any generality. One class of approximations consists in studying only flows past slender bodies—that is, bodies which cause only a small disturbance to the stream. Hypersonic small-disturbance theory, as expounded by Van Dyke, is typical of this type of theory.

The basic idea of such an approximation for high Mach Numbers is that the flow perturbation transverse to the stream caused by the body is an order of magnitude larger than that along the stream. This fact may be determined from a study of shock-wave relations (or those for Prandtl-Meyer flow) provided that $M_\infty\delta$ is not much less than unity. (M_∞ = flight Mach Number, δ = flow deflection angle.) In these flows the entire region of interest lies very close to the body.

The mathematical formulation of hypersonic small-disturbance theory is presented in Section (2); however, two facts concerning the theory should be emphasized here. First, although the equations are very much simplified, they are still nonlinear and not capable of solution in any generality. A possible exception to this might be calculations based on the method of characteristics applied to the small-disturbance theory. Second, in the cases which have been calculated on small-disturbance theory, the results have been remarkably accurate when compared with more exact theory.[1]

An entirely different type of approximation is Newtonian flow theory.[2, 3] In this theory the flow is not analyzed in detail, but a hypothesis is made that the oncoming flow loses its normal component of momentum on striking the body. Calculations based on this idea are, of course, easy.

Various authors have pointed out that Newtonian flow is related to gas dynamic flow by a limiting process involving $\gamma \to 1$, $M \to \infty$.[1] In this memorandum a more detailed study of the relation of Newtonian flow to gas dynamic flow is made within the framework of hypersonic small-disturbance theory. In particular, the shock waves and flow field associated with Newtonian flow are investigated. This investigation is carried out by making the Newtonian approximation to the problem as the problem is simplified by hypersonic small-disturbance theory.

Section (2) is a mathematical formulation of the hypersonic small-disturbance theory. Section (3) discusses the mathematical expansion procedure associated

with Newtonian flow. In Section (4) the general solution to the first approximation equations is given for the case of zero angle of attack. Section (5) contains an estimate of the accuracy of Newtonian theory, based upon a comparison of the first and second approximations for flow past a cone with the small-disturbance solution. Section (6), the final section, studies flows past bodies whose shape is given by $r = x^n$. For these bodies, at infinite Mach Number the shock shape is similar to the body shape, and this is the only case in which such a similarity exists. Within this class of bodies a minimum drag body is found.

(2) Equations of Hypersonic Small-Disturbance Theory

Consider steady flow past a thin body in a set of dimensionless coordinates $(\bar{x}, \bar{y}, \bar{z})$. The coordinates are made dimensionless by a characteristic length L (which will drop out in the case of conical flow). Let δ = slope or thickness parameter characterizing a family of shapes. The flow at infinity is uniform and has velocity U along $\bar{x}$-axis, pressure P_∞, density ρ_∞. Then a hypersonic small-disturbance expansion is characterized by two parameters—M_∞ = Mach Number at infinity, and δ = slope or thickness parameter. For example, $\delta = t/L$, where t = maximum thickness of body. The dependence on other parameters is suppressed for the present.

In accordance with remarks of the previous section, the expansion is carried out in a distorted set of coordinates x, y, z,

$$x = \bar{x} \qquad y = \bar{y}/\delta \qquad z = \bar{z}/\delta \tag{2.1}$$

and has the form

$$\vec{q}(\bar{x}, \bar{y}, \bar{z};\ M_\infty, \delta)/U = \{1 + \delta^2 u_1(x, y, z; H) + \delta^4 u_2(x, y, z; H) + \ldots\}\vec{i} + \delta\vec{v}_1(x, y, z; H) + \delta^3\vec{v}_2(x, y, z; H) + \ldots \tag{2.2a}$$

where $\vec{v}_j \cdot \vec{i} = 0 \qquad j = 1, 2, \ldots$

$$(P - P_\infty)/\rho_\infty U^2 = \delta^2 p_1(x, y, z; H) + \delta^4 p_2 + \ldots \tag{2.2b}$$

$$\rho/\rho_\infty = \sigma_1(x, y, z; H) + \delta^2\sigma_2 + \ldots \tag{2.2c}$$

where

H = hypersonic similarity parameter = $1/M_\infty^2\delta^2$

The approximation is based on $\delta \to 0$ keeping H and (x, y, z) fixed. The expansion (2.2) is substituted into the equations of motion, shock relations, and boundary conditions to produce a sequence of approximation equations and boundary conditions.

It is first convenient to notice the existence of the invariant of the entire flow

$$a^2/U^2 = [(\gamma - 1)/2]\{1 - (q^2/U^2)\} + (1/M_\infty^2) \tag{2.3}$$

The first two terms of the expansion of the invariant according to Eq. (2.2) are

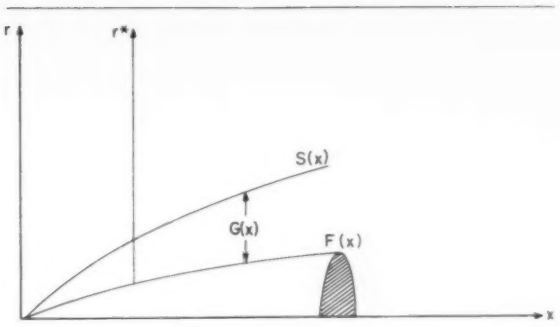

Fig. 1.

$$H - (\gamma - 1)[u_1 + (v_1^2/2)] = (H + p_1\gamma)/\sigma_1 \tag{2.4a}$$

$$-(\gamma - 1)\{u_2 + v_1v_2 + (u_1^2/2)\} = (1/\sigma_1^2)\{\gamma\sigma_1 p_2 - \gamma\sigma_2 p_1 - H\sigma_2\} \tag{2.4b}$$

In carrying out the expansion it is also convenient to use the notation

$\bar{\nabla}$ = gradient in x, y, z system

$\nabla_{(2)}$ = gradient in cross-section plane of (x, y, z); $\nabla_{(2)} = (\partial/\partial y, \partial/\partial z)$

so that $$\bar{\nabla} = \vec{i}(\partial/\partial x) + (1/\delta)\cdot\nabla_{(2)} \tag{2.5}$$

The derivative along a streamline is

$$(\vec{q}/U)\cdot\bar{\nabla} = [(\partial/\partial x) + \vec{v}_1\cdot\nabla_{(2)}] + \delta^2[u_1(\partial/\partial x) + \vec{v}_2\cdot\nabla_{(2)}] + \ldots \tag{2.6}$$

Now, applying the expansion procedure to the Euler equation,

$$(\vec{q}\cdot\bar{\nabla}\vec{q})/U^2 = -(1/\rho U^2)\bar{\nabla}P$$

The terms 0 (δ) are

$$[(\partial/\partial x) + \vec{v}_1\cdot\nabla_{(2)}]\vec{v}_1 = -(1/\sigma_1)\nabla_{(2)}p_1 \tag{2.7}$$

This is a momentum equation in the transverse plane. There are also higher order equations involving (v_2, p_2), etc., which are not written out here.

Applying the expansion procedure to the continuity equation,

$$\bar{\nabla}\cdot(\rho\vec{q}) = 0$$

yields $$(\partial\sigma_1/\partial x) + \nabla_{(2)}\cdot(\sigma_1\vec{v}_1) = 0 \tag{2.8}$$

and higher order equations. Applying the expansion to the entropy equation

$$\vec{q}\cdot\bar{\nabla}(P/\rho^\gamma) = 0$$

yields $$[(\partial/\partial x) + \vec{v}_1\cdot\nabla_{(2)}](P_1/\sigma_1^\gamma) = 0 \tag{2.9}$$

and higher order equations.

In summary, the first-approximation equations* of hypersonic small-disturbance theory can be written

* If, in Eqs. (2.10), x is identified with time, Hayes[10] has shown that the dynamic equations are exactly those of unsteady flow in the transverse plane.

$$
\left\{
\begin{aligned}
&\vec{q}/U = (1 + \delta^2 u_1 + \ldots)\vec{i} + \delta\vec{v}_1 + \ldots \\
&(P - P_\infty)/\rho_\infty U^2 = \delta^2 p_1 + \ldots \\
&\rho/\rho_\infty = \sigma_1 + \ldots \\
&\text{Continuity} \qquad (\partial\sigma_1/\partial x) + \nabla_{(2)}\cdot(\sigma_1\vec{v}_1) = 0 \\
&\text{Transverse Momentum} \qquad [(\partial/\partial x) + \vec{v}_1\cdot\nabla_{(2)}]\vec{v}_1 = -(1/\sigma_1)\nabla_{(2)}p_1 \\
&\text{Entropy} \qquad [(\partial/\partial x) + \vec{v}_1\cdot\nabla_{(2)}]\cdot(\gamma p_1 + H)/\sigma_1{}^\gamma = 0 \\
&\text{Invariant} \qquad H - (\gamma - 1)[u_1 + (v_1{}^2/2)] = (H + p_1\gamma)/\sigma_1
\end{aligned}
\right\} \tag{2.10}
$$

If the differential equations are solved for v_1, p_1, σ_1 then the invariant yields u_1 and the resultant velocity

$$q^2/U^2 = 1 + 2\delta^2[u_1 + (v_1{}^2/2)] + \ldots \tag{2.11}$$

The expansion procedure (2.2) can also be applied to the shock relations to obtain a sequence of approximate relations. In carrying this out it is useful also to determine the conditions at the shock front by an expansion about the shock front as determined in the first approximation. This will not be written out here as the equations for the second approximation are not considered seriously. The first approximation shock relations, for a shock in the undisturbed stream, read

$$
\left\{
\begin{aligned}
&p_1{}^{(1)} = -u^{(1)} \qquad \text{Shock Polar} \\
&\tan\theta_w = -\delta\,\frac{u_1{}^{(1)}}{|\vec{\nabla}v_1{}^{(1)}|} \qquad |\vec{v}_1{}^{(1)}| = -u_1{}^{(1)}\,\frac{1}{\sqrt{H - [(\gamma+1)/2]u_1{}^{(1)}}} \\
&\sigma^{(1)} = \frac{u_1{}^{(1)}}{u_1{}^{(1)} + v_1{}^{(1)2}}
\end{aligned}
\right\} \tag{2.12}
$$

A convenient form of Eqs. (2.12) can be found if the shock location in the case of two-dimensional or axially-symmetric flow is expressed as

$$\tan\theta_w = \delta S'(x) \qquad \text{or} \qquad \bar{r} = \delta S(\bar{x}) \tag{2.13}$$

Eqs. (2.12) may then be expressed

$$
\text{Shock Relations}\left\{
\begin{aligned}
p_1{}^{(1)} &= [2/(\gamma+1)](S'^2 - H) \\
\sigma_1{}^{(1)} &= \frac{S'^2}{[2/(\gamma+1)]H + [(\gamma-1)/(\gamma+1)]S'^2} \\
v_1{}^{(1)} &= [2/(\gamma+1)][S' - (H/S')]
\end{aligned}
\right. \tag{2.14}
$$

The approximate boundary conditions of tangent flow to the surface using Eqs. (2.2) can also be found. For the special cases of axially symmetric or two-dimensional flow at zero angle of attack we have

Body $r = \delta F(\bar{x})$ or $r = F(x)$;

$$
\left.
\begin{aligned}
r &= \sqrt{y^2 + z^2} \quad \text{axial symmetry} \\
r &= y \quad\quad\quad\;\; \text{two-dimensional}
\end{aligned}
\right\} \tag{2.15}
$$

and

$$v_1[x, F(x)] = F'(x) \tag{2.16}$$

In the domain of interest, $F(x) \leq r \leq S(x)$.

A slightly modified formulation of the equations for axial symmetry uses the distance measured from the body surface and the velocity difference taken from the value on the boundary. Let

$$
\begin{aligned}
&r^* = r - F(x) \\
&\text{then } v^*(x, r) = v_1(x, r) - F'(x) \\
&\text{where } 0 \geq r^* \geq G(x) = S - F \quad \text{(see Fig. 1)}
\end{aligned} \tag{2.17}
$$

In these variables the hypersonic Eqs. (2.10), for the cases of axial symmetry or two-dimensional flow, become

$$
\left\{
\begin{aligned}
&\text{Continuity} \qquad (\partial v^*/\partial r^*) + m[(v^* + F')/(r^* + F)] = (1/\sigma_1)[(\partial\sigma_1/\partial x) + v^*(\partial\sigma_1/\partial r^*)] \\
&\text{Transverse Momentum} \qquad [(\partial/\partial x) + v^*(\partial/\partial r^*)]v^* + F''(x) = -(1/\sigma_1)(\partial p_1/\partial r^*) \\
&\text{Entropy} \qquad [(\partial/\partial x) + v^*(\partial/\partial r^*)][(\gamma p_1 + H)/\sigma_1{}^\gamma] = 0 \\
&\text{Shock Relations} \qquad p_1{}^{(1)}(x, G) = [2/(\gamma+1)]\{F'^2 + 2F'G' + G'^2 - H\} \\
&\qquad\qquad \sigma_1{}^{(1)}(x, G) = \frac{F'^2 + 2F'G' + G'^2}{[2/(\gamma+1)]H + [(\gamma-1)/(\gamma+1)](F'^2 + 2F'G' + G'^2)} \\
&\qquad\qquad v^{*(1)} + F' = [2/(\gamma+1)]\{F' + G' - [H/(F' + G')]\}
\end{aligned}
\right. \tag{2.18}
$$

The number $m = 1$ for axial symmetry
$= 0$ for two-dimensional flow

(3) Newtonian Expansion Procedure

The usual Newtonian solution is obtained from the hypersonic Eqs. (2.18) by $\gamma \to 1$ and $H \to 0$. For the solution usually chosen $G = 0$ so that the shock is on the body surface, and $v^* = 0$, $\sigma_1 = \infty$, $p_1 \to F'^2$. No attempt is made to calculate the flow field. While it is possible to visualize this limiting flow with infinite density ratio as an approximation for a flat surface, its interpretation for a curved surface is questionable, and, in fact, previous papers[2,3] sometimes include a centrifugal force correction. In order to study the flow field in more detail, in particular to keep boundary conditions both on the shock and on the body, the limit $\gamma \to 1$, $H \to 0$ is carried out in a distorted coordinate system.

In the limit $H \to 0$, Eqs. (2.18) show that the density ratio $\sigma^{(1)} \to (\gamma + 1)/(\gamma - 1)$ so that

$$\lambda = (\gamma - 1)/(\gamma + 1), \qquad \gamma = 1 + 2\lambda + 2\lambda^2 + \ldots \tag{3.1}$$

The quantity λ is taken as a basic small parameter for the Newtonian limit. In order to conserve mass the shock must lie a distance $0(\lambda)$ off the surface. In order to carry out a limit in which the shock does not collapse to the surface, the distance from the surface must be measured relative to λ. The Newtonian limit mentioned above also shows $p = 0(1)$, $v^* = 0(\lambda)$. Therefore, the following expansion is assumed:

$$\left.\begin{aligned} p_1(x, r^*; H) &= p(x, \bar{r}; N) + \lambda p_I(x, \bar{r}; N) + \ldots \\ \sigma_1(x, r^*; H) &= (1/\lambda)\sigma(x, \bar{r}; N) + \sigma_I(x, \bar{r}; N) + \ldots \\ v^*(x, r^*; N) &= \lambda v(x, \bar{r}; N) + \lambda^2 v_I(x, \bar{r}; N) + \ldots \end{aligned}\right\} \tag{3.2}$$

where

N = Newtonian flow parameter $= H/\lambda = (\gamma + 1)/(\gamma - 1)M_\infty^2\delta^2$

$r = r^*/\lambda$

and shock location $\bar{r} = g(x) + \lambda g_1(x) + \ldots$. The Newtonian flow parameter N is fixed as $\lambda \to 0$, which corresponds to the fact that $H \to 0$ in the usual Newtonian limit.

Applying the expansion procedure (3.2) to the hypersonic small-disturbance Eqs. (2.18) and the boundary conditions produces a sequence of equations for (p, σ, v), (p_I, σ_I, v_I), etc. The variables (p, σ, v) should be related to the usual Newtonian flow approximation, while the higher terms represent corrections. The equations which result are

First Approximation Equations

$$\left.\begin{aligned} &\text{Continuity} && (F\sigma v)_{\bar{r}} + m\sigma F' + F\sigma_x = 0 \\ &\text{Transverse Momentum} && F'' = -(1/\sigma)p_{\bar{r}} \\ &\text{Entropy} && [\partial/\partial x) + v(\partial/\partial \bar{r})](p/\sigma) = 0 \end{aligned}\right\} \tag{3.3}$$

with the boundary conditions

$$\text{at body surface} \qquad v(x, 0) = 0 \tag{3.4}$$

$$\text{at the shock} \qquad \left.\begin{aligned} p(x, g) &= F'^2(x) \\ \sigma(x, g) &= F'^2/(N + F'^2) \\ v(x, g) &= g' - (N/F') - F' \end{aligned}\right\} \tag{3.5}$$

Second Approximation Equations

$$\left.\begin{aligned} &\text{Continuity} && v_{I\bar{r}} + m\frac{F'}{F}\left(\frac{v}{F'} - \frac{\bar{r}}{F}\right) = \left(\frac{\partial}{\partial x} + v\frac{\partial}{\partial \bar{r}}\right)\left(\frac{\sigma_I}{\sigma}\right) + v_I\frac{\partial}{\partial \bar{r}}(\log\sigma) \\ &\text{Transverse Momentum} && \left(\frac{\partial}{\partial x} + v\frac{\partial}{\partial \bar{r}}\right)v = \frac{\sigma_I}{\sigma^2}p_{\bar{r}} - \frac{1}{\sigma}p_{I\bar{r}} \\ &\text{Entropy} && \left(\frac{\partial}{\partial x} + v\frac{\partial}{\partial \bar{r}}\right)\left(\frac{p_I}{\sigma} - 2\frac{p}{\sigma}\log\sigma - \frac{p}{\sigma^2}\sigma_1\right) + v_I\frac{\partial}{\partial \bar{r}}\left(\frac{p}{\sigma}\right) = 0 \end{aligned}\right\} \tag{3.6}$$

with the boundary conditions

$$\text{at body surface} \qquad v_I(x, 0) = 0 \tag{3.7}$$

at the shock

$$\left.\begin{aligned} g_I(x)p_{\bar{r}}(x, g) + p_I(x, g) &= 2F'g' - F'g'^2 - N \\ g_I\sigma_{\bar{r}}(x, y) + \sigma_1(x, g) &= \frac{NF'(2g' + F')}{(N + F'^2)^2} \\ g_I v_{\bar{r}}(x, g) + v_I(x, g) &= g_I' + (Ng'/F'^2) \end{aligned}\right\} \tag{3.8}$$

In solving this system of equations the shock shape described by $g(x)$, $g_I(x)$, etc., must be found. The boundary conditions (3.8) are found by applying the shock relations at the shock as found in the first approximation. An expansion in terms of distance from the shock has been used.

It might be noted that the momentum equation of the first approximation indicates the existence of a pressure gradient normal to the x-axis which is proportional to the body surface curvature. The pressure immediately behind the shock is the Newtonian limit so that the surface pressure is lower if $F'' < 0$. It has been implicitly assumed that the body is smooth so that F', F'' etc., exist.

(4) General Solution of the First Approximation Equations

The pressure on the body surface can immediately be found by the introduction of a stream function ψ and the flow field can be found by integration.

ψ is defined in the conventional way as having the property of satisfying the continuity equation identically;

$$\psi(x, \bar{r}): \quad F^m\sigma v = -\psi_x \qquad F^m\sigma = \psi_{\bar{r}} \tag{4.1}$$

The momentum equation of Eqs. (3.3) thus reads

$$(1/F^m)F''\psi_{\tilde{r}} + p_{\tilde{r}} = 0 \tag{4.2}$$

Integration of Eqs. (4.2) from $\tilde{r} = 0$, the body surface, gives

$$(1/F^m)F''\psi + p = p_0(x) \tag{4.3}$$

using the fact that $\psi = 0$ at $\tilde{r} = 0$ and $p_0(x) = p(x, 0)$. The pressure distribution on the body $p_0(x)$ can be found from Eqs. (4.3) by evaluating the left-hand side on the shock. To do this ψ_{shock} can be found as follows:

$$(d\psi/dx)_{\text{shock}} = \psi_x(x, g) + g'(x)\psi_{\tilde{r}}(x, g) \tag{4.4}$$

and from the shock relations

$$(d\psi/dx)_{\text{shock}} = \psi_{\tilde{r}}[(N/F') + F']$$

Now, using Eq. (4.1) and the shock relations,

$$(d\psi/dx)_{\text{shock}} = F^m F'$$

Integration using $\psi_{\text{shock}} = 0$ at $x = 0$ gives ψ along the shock

$$\psi_{\text{shock}} = F^{m+1}(x)/(m + 1) = \psi[x, g(x)] \tag{4.5}$$

The result (4.5) is equivalent to finding ψ from mass flow ahead of the shock [Eq. (4.1)]. Now, using Eq. (4.5) and the value of p on the shock from the shock relations in Eq. (4.3) the pressure on the body surface is found:

$$p_0(x) = F'^2(x) + (1/2)F F'' \quad \text{axial symmetry} \tag{4.6a}$$

$$= F'^2(x) + F F'' \quad \text{two-dimensional} \tag{4.6b}$$

The formulas for the pressure on the surface agree with the Newtonian formulas usually given[2,4] which include centrifugal force corrections. According to the method used here, Eqs. (4.6a) and (4.6b) are the only correct Newtonian formulas. In terms of pressure coefficient, Eqs. (4.6) are

$$C_p(x) = 2\delta^2\{F'^2(x) + (1/2)F F''\} \quad \text{axial symmetry} \tag{4.7a}$$

$$= 2\delta^2\{F'^2(x) + F F''\} \quad \text{two-dimensional} \tag{4.7b}$$

It is quite important to note that the surface pressures just found are independent of the Newtonian parameter N, although the flow field and shock shape which will now be discussed depend on N. This means that as the Mach Number increases ($N \to 0$) the surface pressures reach their limiting value before the flow field, and that the surface pressures should be a good approximation over a wide range of Mach Number.

Now to find the flow field, Eq. (4.3) must be integrated with the right hand side $p_0(x)$ given by Eqs. (4.6). To do this, p is expressed in terms of ψ. First note that the entropy equation of Section (3) shows

$$p/\sigma = k(\psi) \tag{4.8}$$

or

$$p = 1/F^m\psi_{\tilde{r}}k(\psi) \tag{4.9}$$

Finally, $k(\psi)$ can be found by evaluating k along the shock and using ψ_{shock} of Eq. (4.5). This gives $k(\psi)$ parametrically. From the shock relations (3.5),

$$\text{on the shock } \begin{cases} k = F'^2(x) + N \\ \psi = \dfrac{F^{m+1}(x)}{m+1} \end{cases} \text{ gives } k(\psi) \text{ parametrically} \tag{4.10}$$

Thus, the equation for the stream function (4.3) becomes

$$k(\psi)\psi_{\tilde{r}} + F''(x)\psi = F^m p_0(x) \tag{4.11}$$

or

$$\partial\psi/\partial\tilde{r} = [F^m p_0(x) - F''(x)\psi]/k(\psi) \tag{4.12}$$

Coordinate x enters Eq. (4.12) only as a parameter so that the integration with respect to $\tilde{r}$ can be carried out keeping x fixed.

$$\tilde{r} = \int_0^{\psi} \frac{k(\phi)d\phi}{F^m(x)p_0(x) - F''(x)\phi} \tag{4.13}$$

The boundary condition $\psi = 0$ at $\tilde{r} = 0$ has been used. Carrying out the integration of Eq. (4.13) gives $\psi(x, \tilde{r})$ and the entire flow field.

It is important to note that if $p_0(x) = 0$ the integral diverges. That is, the solution fails whenever the pressure p_0 falls to zero on the body. The approximation is poor for some distance ahead of the point where $p_0 = 0$.

The shock shape is given by

$$g(x) = \int_0^{F^{m+1}(x)/(m+1)} \frac{k(\phi)}{F^m(x)p_0(x) - F''(x)\phi}\, d\phi \tag{4.14}$$

It is interesting to note that the surface distribution of density, temperature, and velocity, as well as the pressure, can be found without carrying out the integrations necessary to find the flow field off the surface. According to Eq. (4.10) at $x = 0$, $\psi = 0$ and

$$k(0) = F'^2(0) + N \tag{4.15}$$

so that

$$\sigma_0(x) = p_0(x)/[F'^2(0) + N] \tag{4.16}$$

that is, surface density is proportional to surface pressure. The surface temperature is found from the equation of state

$$T/T_\infty = \theta = (P/P_\infty)/(\rho/\rho_\infty) \tag{4.17}$$

Referring back to Eqs. (2.10),

$$P/P_\infty = 1 + \gamma M_\infty^2\delta^2 p_1 = [p_0(x)/N\lambda] + \ldots \tag{4.18}$$

so that the surface temperature is constant and equal to

$$\theta_0(x) = \{[F'^2(0)/N] + 1\} = k(0)/N + \ldots \tag{4.19}$$

The resultant velocity on the body surface can be found from Eq. (2.11) by applying the Newtonian expansion to the invariant of Eqs. (2.10).

$$u_1 + (v_1^2/2) = [1/(\gamma - 1)]\{H - [(H + p_1\gamma)/\sigma_1]\} = (1/2)\{N - (p/\sigma)\} + \ldots$$

or

$$u_1 + (v_1^2/2) = (1/2)\{N - k(\psi)\} \tag{4.20}$$

Thus the magnitude of resultant velocity at any point of the flow is

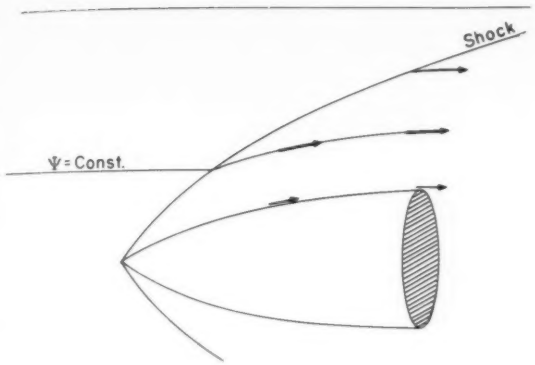

FIG. 2.

$$q^2/U^2 = 1 + \delta^2[N - k(\psi)] + \ldots \qquad (4.21)$$

Eq. (4.21) shows that in the first approximation the resultant velocity is constant along streamlines. The value of the velocity on the surface $\psi = 0$ is easily found since $k(0) = F'^2(0) + N$, so that

$$\text{on the surface} \quad q^2/U^2 = 1 - \delta^2 F'^2(0) + \ldots \qquad (4.22)$$

$k(\psi)$ is also known along the shock by (4.10) so that

$$\text{on the shock} \quad q^2/U^2 = 1 - \delta^2 F'^2(x) \qquad (4.23)$$

For a typical convex body the qualitative sketch of Fig. 2 describes the flow.

(5) First and Second Approximations for a Cone

The first and second approximations for the pressure on a cone are easily calculated. To find the second approximation to the pressure, some information about the flow field of the first approximation is needed. The first approximation is found directly as follows: for a cone

$$F(x) = x, \qquad \delta = \tan\theta_c, \qquad \theta_c = \text{semi-vertex angle} \qquad (5.1)$$

and the shock is

$$g(x) = Ax \qquad (5.2)$$

where A is an unknown positive constant fixing the first approximation to the shock angle. The shock conditions (3.5) become

$$\left.\begin{aligned} p(x, Ax) &= 1 \\ \sigma(x, Ax) &= 1/(1+N) \\ v(x, Ax) &= A - (N+1) \end{aligned}\right\} \qquad (5.3)$$

The transverse momentum equation of (3.3) is

$$p_{\bar{r}} = 0 \qquad \text{or} \qquad p = fn(x) \qquad (5.4)$$

From the shock conditions (5.3) it is seen that

$$p = 1 \qquad 0 \le \bar{r} \le Ax \qquad (5.5)$$

or that the pressure field is uniform everywhere. From the entropy equation of Eqs. (3.3) and the shock relation it follows that the density is constant

$$\sigma = 1/(1+N) \qquad (5.6)$$

The transverse component of velocity can be found from the continuity equation of Eqs. (3.3)

$$(xv)_{\bar{r}} = -1$$

or using the boundary condition $v = 0$ at $\bar{r} = 0$

$$v(x, \bar{r}) = -(\bar{r}/x) \qquad (5.7)$$

This represents a flow field whose streamlines are more inclined toward the cone surface as $\bar{r}$ increases. The shock angle can now be found from the boundary condition for v on the shock (5.3)

$$-A = A - (N+1) \qquad \text{or} \qquad A = (1+N)/2 \qquad (5.8)$$

The shock shape

$$g(x) = [(1+N)/2]x \qquad (5.9)$$

The formulas for wave angle θ_w and pressure coefficient C_p according to the first approximation are

$$\tan\theta_w/\tan\theta_c = 1 + \lambda[(1+N)/2] = [(3\gamma+1)/2(\gamma+1)] + (1/2M_\infty^2\delta^2) \qquad (5.10)$$

$$= 1.08 + (1/2M_\infty^2 \tan^2\theta_c) \quad \text{for } \gamma = 1.4 \qquad (5.11)$$

$$C_p = 2\delta^2 p = 2\tan^2\theta_c \qquad (5.12)$$

Some idea of the accuracy with which the external flow is found can be obtained from a comparison with the exact solution of Kopal's tables:

θ_c	M_∞	$M_\infty^2 \tan^2 \theta_c$	Newtonian θ_w	Kopal θ_w
15°	∞	∞	16.2	16.5
15°	3.63	0.95	23.4	22.8
10°	∞	∞	10.8	11.0
10°	9.10	2.58	12.6	12.6

These few results show the very good agreement of shock wave angle obtained by Newtonian theory with that obtained by exact theory over a wide range of conditions. However, it is to be expected that the theory will only give good results for $M_\infty \tan\theta_c > 1$, as this was assumed in the derivations. A comparison of the pressure coefficient with more exact theory is deferred until the second approximation is calculated.

The second approximation to the pressure is determined immediately by integration of the transverse momentum equation, using the known solution [Eqs. (5.5) and (5.7)] for $v(x, \bar{r})$ and p. Eq. (3.6) shows

$$2\bar{r}/x^2 = -(1-N)p_{I_{\bar{r}}} \qquad (5.13)$$

Integration gives

$$p_I(x, \bar{r}) = p_{I_0}(x) - [1/(1+N)](\bar{r}/x)^2 \qquad (5.14)$$

where $p_{I_0}(x)$ is the (of course constant) value of p_I on the surface. Evaluating (5.14) at the shock by (3.8) fixes p_{I_0}.

$$p_{I_0} - [1/(1+N)]A^2 = 2A - 1 - N = 0 \qquad (5.15)$$

$$\text{so} \qquad p_{I_0} = (1+N)/4 \qquad (5.16)$$

Combining first and second approximation, the formula for pressure coefficient on the cone surface is

$$C_p/\delta^2 = 2\{1 + \lambda[(1 + N)/4] + 0(\lambda^2)\} \quad (5.17)$$

This result is now compared with Van Dyke's numerical integration of the hypersonic small-disturbance equations. The solution expressed by (5.17) should be an approximation to Van Dyke's which is valid for $M_\infty \tan\theta_c \gg 1$.

$\gamma = 1.405$ $M_\infty \tan\theta_c$	1st Approx. C_p/δ^2	1st and 2nd Approx. C_p/δ^2	Van Dyke C_p/δ^2
0.6599	2.000	3.232	2.646
1.150	2.000	2.462	2.333
2.469	2.000	2.166	2.154
3.988	2.000	2.116	2.116
∞	2.000	2.084	2.091

It is seen that the first approximation predicts (C_p/δ^2) with a 16 per cent error for $M_\infty \tan\theta_c = 1.15$ while the error is decreased to 5 per cent by including the second approximation. From the point of view of Newtonian theory presented here, the dependence on the Newtonian flow parameter N is important. It is not to be expected that the expansion procedure based on $\lambda \to 0$ is uniformly valid with respect to N. It can be seen from Eq. (2.17) that in order for the error of the first approximation to be truly $0(\lambda)$ then N must be 0(1) or smaller. From a practical point of view we might expect the Newtonian expansion procedure to give useful results if

$$N = [(\gamma + 1)/(\gamma - 1)M_\infty^2\delta^2] < 2 \text{ or } 3 \quad (5.18)$$

(6) Body Shape $r = x^n$

An interesting question concerns the possibility of a flow field, other than a conical one, in which the shock shape is similar to the body shape. An examination of the equations of motion and boundary conditions (3.3), (3.4) and (3.5) shows that this is only possible for

$$F(x) = x^n \quad (6.1)$$

and $N = 0$.

This similarity solution of course exists also for the complete hypersonic small-disturbance equations, since an expansion in terms of λ cannot destroy similarity. The solution has been investigated in detail by L. Lees.[5] He has shown it to be a generalization of Taylor's and related solutions[6–8] for infinitely strong shock waves.

From the first approximation the pressure distribution and drag coefficient are easily found. Eq. (4.6) shows

$$p_0(x) = n(2n - 1)x^{2(n-1)} \quad \text{for two-dimensional flow} \quad (6.2)$$

$$= (n/2)(3n - 1)x^{2(n-1)} \quad \text{for axial symmetry} \quad (6.3)$$

The drag coefficient for a body of unit length can be found by

$$C_D = (1/\pi\delta^2)\int_0^1 C_p\, 2\pi\, \delta F\, \delta F'\, dx \quad \text{for axial symmetry} \quad (6.4a)$$

$$= (1/2\delta)\int_0^1 C_p \delta F' dx \quad \text{for two-dimensional flow} \quad (6.4b)$$

Although the body shapes have blunt noses, finite drag results for

$$1 > n > 2/3 \quad \text{two-dimensional} \quad (6.5a)$$

$$1 > n > 1/2 \quad \text{axial symmetry} \quad (6.5b)$$

The formulas for the drag coefficients are

$$C_D/\delta^2 = n^2[(2n - 1)/(3n - 2)] \quad \text{two-dimensional} \quad (6.6a)$$

$$C_D/\delta^2 = n^2[(3n - 1)/(2n - 1)] \quad \text{axial symmetry} \quad (6.6b)$$

From these formulas the existence of n for minimum drag is evident. It is found that for minimum drag

$$n = 0.866 \qquad (C_D/\delta^2)_{min} = 0.92 \quad \text{two-dimensional} \quad (6.7a)$$

$$n = 2/3 \qquad (C_D/\delta^2)_{min} = 4/3 \quad \text{axial symmetry} \quad (6.7b)$$

These are fore-bodies of minimum drag for a given thickness ratio δ. These formulas show a considerable reduction in drag when compared with wedge or cone $(n = 1)$:

$$(C_D/\delta^2)_{min}/(C_D/\delta^2)_{\text{wedge}} = 0.92 \quad (6.8a)$$

$$(C_D/\delta^2)_{min}/(C_D/\delta^2)_{\text{cone}} = 2/3 \quad (6.8b)$$

This result has to be taken seriously as it applies as the first approximation for all N, since the surface pressure is independent of N in the first approximation.

Eggers, *et al.*,[9] have considered minimum drag bodies according to Newtonian theory using the "exact" formula for pressure $C_p = 2\sin^2 d$ (d = local slope), but neglecting centrifugal force effects. The minimum drag shape corresponding to the one calculated here does not have a simple formula but turns out to be closely approximated by $r = x^{3/4}$ for axial symmetry. If centrifugal force is neglected in the present approximation it is found that (within the class of bodies x^n) $n = 3/4$ exactly. Thus, surprisingly, the use of an "exact" formula gives a result which agrees very closely with one based on small deflection angles. However, it should be emphasized that the results of reference 9 have no theoretical justification since centrifugal force effects must be included.

Certain anomalies of the flow field due to the singularity at the nose point should be mentioned. For example, Eq. (4.16) shows that the density on the surface $\sigma_1 = 0$, while Eq. (4.19) shows that the surface temperature is infinity. There is a corresponding difficulty with the surface velocity. These difficulties exist, as shown by Eq. (4.16), etc., even for $N \neq 0$. They are due to the violation of the assumptions of

hypersonic small-disturbance theory at a blunt nose. In this connection, the details of the actual flow near a blunt nose, with especial reference to its relation to the hypersonic small-disturbance theory, might comprise a topic for further study. The effect of a blunt nose would seem to form a sort of boundary layer along the surface within the similarity solution.

The physical interpretation of these flows for a given nose is clear. However, it should be noted that since this class of bodies has only one characteristic length, the parameter δ could have been eliminated by properly choosing the coordinates. The deeper significance of these flows in the large as an asymptotic approximation to the exact equations then has to be discussed. The same remark applies to the flow produced when there is no body but instead a concentrated energy source (and $M_\infty = \infty$). This flow due to a concentrated energy source can be interpreted as the effect of a blunt nose at very high speeds.[5]

References

[1] Van Dyke, M. D., *A Study of Hypersonic Small-Disturbance Theory*, NACA TN 3173, May, 1954.

[2] Busemann, A., *Flussigkeits und Gasbewegung*, "Handwortenbuch der Naturwissenschaften," Zweite Aurlage (Fischer, Jena), pp. 275–277, 1933.

[3] Grimminger, G., Williams, E. P., and Young, G. B. W., *Lift on Inclined Bodies of Revolvtion in Hypersonic Flow*, Journal of the Aeronautical Sciences, Vol. 17, No. 11, pp. 675–690, November, 1950.

[4] Ivey, H. R., Klunker, E. G., and Bowen, E. N., *A Method for Determining the Aerodynamic Characteristics of Two- and Three-Dimensional Shapes at Hypersonic Speeds*, NACA TN 1613, 1948.

[5] Lees, L., unpublished communication, December 1955, to appear in "Readers' Forum" of *Journal of the Aeronautical Sciences*.

[6] Courant and Friedrichs, *Supersonic Flow and Shock Waves*, Interscience Press, 1946.

[7] Lin, S. C., *Cylindrical Shock Waves Produced by Instantaneous Energy Release*, J. Appl. Phys., Vol. 25, No. 1, January, 1954.

[8] Latter, R., *Similarity Solutions for a Spherical Shock Wave*, J. Appl. Phys. Vol. 26, No. 8, pp. 954–960, August, 1955.

[9] Eggers, A. J., Dennis, D. H., and Resnikoff, M. M., *Bodies of Revolution for Minimum Drag at High Supersonic Airspeeds*, NACA RMA51K27, February, 1952.

[10] Hayes, W. D., *On Hypersonic Similitude*, Quarterly of Applied Math., Vol. 5, No. 1, April, 1947, pp. 105–106.

Laminar Boundary Layer on a Spinning Cone...

(*Continued from page 436*)

[7] Moore, F. K., *Three-Dimensional Compressible Laminar Boundary Layer Flow*, NACA TN 2279, March, 1951.

[8] Moore, F. K., *Three-Dimensional Laminar Boundary Layer Flow*, Journal of the Aeronautical Sciences, Vol. 20, No. 8, p. 525, August, 1953.

[9] Staff of the Computing Section, Center of Analysis (under direction of Kopal, Z.), *Tables of Supersonic Flow Around Yawing Cones*, M.I.T. Technical Report No. 3, 1947.

[10] Moore, F. K., *Displacement Effect of a Three-Dimensional Boundary Layer*, NACA TN 2722, June, 1952.

[11] Sedney, R., *Some Aspects of Three-Dimensional Boundary Layer Flows*, Quart. Appl. Math. (to be published).

[12] Ward, G. N., *Supersonic Flow Past Slender Pointed Bodies*, Quart. J. Mech. Appl. Math., Vol. 2, No. 1, p. 75, March, 1949.

[13] Schmidt, L. E., *The Dynamic Properties of Pure Cones and Cone Cylinders*, BRLM Report No. 759, January, 1954.

[14] Kelly, H. R., *An Analytical Method for Predicting the Magnus Forces and Moments on Spinning Projectiles*, U.S. NOTS, TM-1634, August, 1954.

Buckling Under External Pressure of Cylindrical Shells...

(*Continued from page 447*)

[19] Slankard, R. C., and Nash, W. A., *Tests on the Elastic Stability of a Ring-Stiffened Cylindrical Shell, Model BR-5* (λ = 1.705), *Subjected to Hydrostatic Pressure*, Report 822, David W. Taylor Model Basin, May, 1953.

[20] Bijlaard, P. P., Fisher, G. P., and Winter, G., *Eccentrically Loaded, End-Restrained Columns*, Trans. ASCE, Vol. 120, pp. 1070–1115, 1955.

[21] Holt, M., *A Procedure for Determining the Allowable Out-of-Roundness for Vessels Under External Pressure*, Trans. ASME, Vol. 74, No. 7, pp. 1225–1230, 1952.

[22] Bijlaard, P. P., *Theory and Tests on the Plastic Stability of Plates and Shells*, Journal of the Aeronautical Sciences, Vol. 16, pp. 529–541, 1949.

[23] Wong, R. E., *Design Charts for the Buckling of Cylindrical Shells Stiffened by Rings Under External Pressure*, Bell Aircraft Corporation Report No. 02-984-010, December 1953.

Readers' Forum

BRIEF REPORTS of investigations in the aeronautical sciences and discussions of papers published in the JOURNAL are presented in this special department. Entries must be restricted to a maximum of 1,300 words or the equivalent of one JOURNAL page including formulas and illustrations. Publication is completed as soon as possible after receipt of the material. The Editorial Committee does not hold itself responsible for the opinions expressed by the correspondents.

Contents

The Effect of Flexibility on the Drag Polar of an Aircraft.... W. P. RODDEN, T. E. SURBER, AND H. C. VETTER 456

Free Molecular Flow Forces and Heat Transfer for an Infinite Circular Cylinder at Angle of Attack... L. TALBOT 458

Boundary-Layer Stabilization by Distributed Damping.... MAX O. KRAMER 459

On Choosing Stress Functions in Rectangular Coordinates.... F. W. NIEDENFUHR 460

Normal Conduction Effects on Heat-Transfer Data During Transient Heating of Thin-Skin Models.... MORTON COOPER AND EDWARD E. MAYO 461

Calibration of Surface Tubes for Measurement of Surface Shear in Fluids.... J. N. HOOL 462

Induced Rolling Moments at Supersonic Speeds.... GEORGE S. CAMPBELL 463

A New Technique for Investigating Heat Transfer and Surface Phenomena Under Hypersonic Flow Conditions.... ANTONIO FERRI AND PAUL A. LIBBY 464

Geometric Stabilization.... A. LANGE 465

The Effect of a Simple Throat Distortion on the Flow in a Hypersonic Wind-Tunnel Nozzle.... ROBERT E. OLIVER AND BENJAMIN E. CUMMINGS 466

Polytropic Exponents for Air at High Temperatures.... J. G. LOGAN, JR., AND C. E. TREANOR 467

Note on the Turbulent Shear Stress Near a Wall.... H. G. ELROD, JR. 468

Wide-Angle Diffusers of High Performance and Diffuser Flow Mechanisms.... S. J. KLINE, C. A. MOORE, AND D. L. COCHRAN 469

Some New Conceptions of the Mechanism of Stall in Turbulent Boundary Layers.... STEPHEN J. KLINE 470

Note on the Boundary-Layer Instability on a Flat Plate Stopped Suddenly.... FRANCIS R. HAMA 471

The Effect of Flexibility on the Drag Polar of an Aircraft

W. P. Rodden, T. E. Surber, and H. C. Vetter
North American Aviation, Inc., Los Angeles

January 7, 1957

INTRODUCTION

IT HAS GENERALLY BEEN ASSUMED in aerodynamic analyses that aeroelasticity only affects the stability and control of an aircraft and that its effect on performance is negligible. It is the purpose of this note to show that this assumption is justified only for airplanes with slightly swept wings.

(1) EFFECTS OF FLEXIBILITY ON THE WING DRAG POLAR

The total induced drag C_{D_i} can be written as an integral of the spanwise drag:

$$C_{D_i} = (2/S_w)\int_0^{b/2} C_{d_i} c\, dy = \int_0^1 C_{l_i}(c/\bar{c})d\eta \qquad (1)$$

where η is the dimensionless spanwise coordinate. Using linearized strip theory, the local induced drag C_{d_i} of the twisted wing at supersonic speeds is given by

$$C_{d_i} = C_l\,(\alpha - \epsilon) \qquad (2)$$

where ϵ is the local angle of wing twist. The local lift coefficient is found from the rigid value and the increment due to twist

$$C_l = C_{l_0} + \Delta C_l \qquad (3)$$

as the angle of attack is also

$$\alpha = \alpha_0 + \Delta\alpha \qquad (4)$$

assuming a constant total lift.

Eqs. (1) through (4) can be combined into a form convenient for numerical integration:

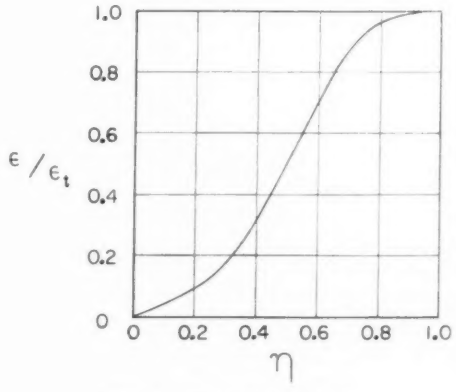

FIG. 1. Twist distribution.

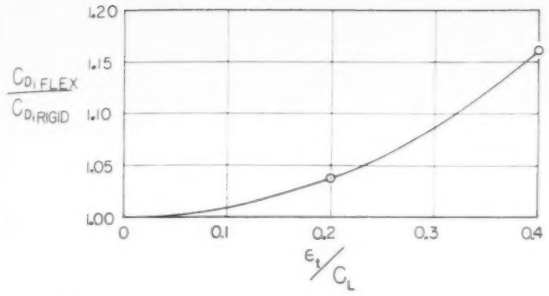

FIG. 2. Ratio of flexible to rigid induced drag.

TABLE I — COEFFICIENTS A & B

C. G.	dC_m/dC_L	A		B	
		$\frac{S_H}{S_W}=0.2$	$\frac{S_H}{S_W}=0.4$	$\frac{S_H}{S_W}=0.2$	$\frac{S_H}{S_W}=0.4$
Aft	-0.05	0	0	.566	1.131
$x/\bar{c}=0$	-0.10	0	0	.631	1.263
Fwd.	-0.15	.0655	.1235	.655	1.235
$x/c=0.1$	-0.20	.0714	.1343	.714	1.343

TABLE II — TYPICAL FLEXIBILITY PARAMETERS

	$\Lambda=10°$	$\Lambda=25°$	$\Lambda=45°$
$\Delta C_{L_{a_w}}/C_{L_{a_w}}$	-0.030	-0.075	-0.150
$\Delta x/\bar{c}$	-0.010	-0.025	-0.050

TABLE III — $\frac{\Delta C_{D_i}}{C_{D_{i_w}}}$, PERCENTAGE DRAG INCREMENT

C. G.	dC_m/dC_L	$\Lambda=10°$		$\Lambda=25°$		$\Lambda=45°$	
		$S_H/S_W=0.2$	0.4	0.2	0.4	0.2	0.4
Aft	-0.05	-.0113	-.0226	-.0283	-.0566	-.0566	-.1131
$x/\bar{c}=0$	-.010	-.0126	-.0253	-.0316	-.0631	-.0631	-.1263
Fwd.	-0.15	-.0170	-.0321	-.0426	-.0802	-.0851	-.1605
$x/\bar{c}=0.1$	-0.20	-0186	-.0349	-.0464	-.0873	-.0929	-.1746

$$C_{D_i} = C_L^2 \int_0^1 [(C_{l_0}c/C_L\bar{c}) + (\Delta C_l c/\epsilon_t \bar{c})(\epsilon_t/C_L)] \times \{(\alpha_0/C_L) + [(\Delta\alpha/\epsilon_t) - (\epsilon/\epsilon_t)](\epsilon_t/C_L)\}\, d\eta \quad (5)$$

where ϵ_t is the value of tip twist. The integral of Eq. (5) is evaluated with ϵ_t/C_L as a parameter using an elliptical additional lift distribution and a basic lift distribution computed from the additional lift by strip theory and the typical twist distribution of Fig. 1. The additional lift-curve slope is assumed to be $C_{L\alpha}$ = 0.05 per deg. = 2.865 per rad. The development of the basic lift also showed $\Delta\alpha/\epsilon_t = 0.4165$. The results are presented as the ratio of the flexible induced drag to the rigid induced drag in Fig. 2, and the corresponding lift distributions are shown in Fig. 3.

This analysis bears out the well-known fact that the total induced drag of the wing depends primarily on the magnitude of

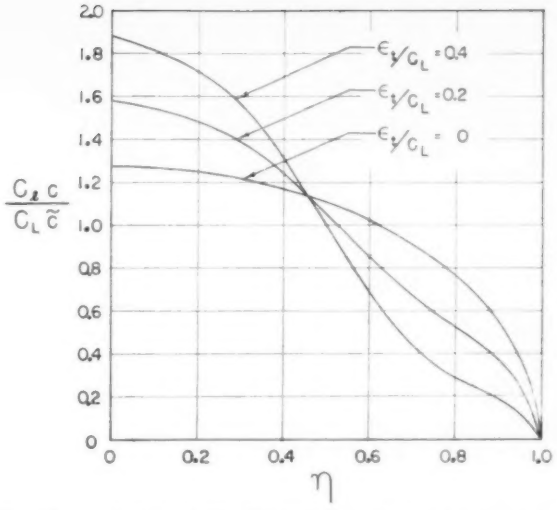

FIG. 3. Variation of lift distribution with twist parameter, ϵ_t/C_L.

the lift and only secondarily on its spanwise distribution. An extreme range of loading variation was investigated to demonstrate this point although a practical value of ϵ_t/C_L is less than 0.1. The parameter ϵ_t/C_L is given by aeroelastic calculations in the form $K_1q/(1 + K_2q)$, where K_1 and K_2 are parameters which vary slightly with Mach Number; the dependence of ϵ_t/C_L on speed is therefore apparent. The arguments presented are for a swept wing but should apply equally well to a straight wing. The modification to subsonic speeds would require that the induced angle of attack be added to Eq. (2), but the results should be approximately the same.

It is therefore seen that the approximation of neglecting aeroelastic effects on the drag polar of lifting surfaces and, hence, on the untrimmed airplane drag polar has less than 1 per cent error for present airplanes and that design speeds will have to increase considerably before any correction will be required. It remains now to consider aeroelastic effects on the trimmed airplane drag polar.

(2) Effects of Flexibility on the Trimmed Airplane Drag Polar

The total airplane-induced drag may be written as the sum of its components from wing, fuselage, and horizontal tail if interference is neglected:

$$C_{D_i} = K_w(C_{L\alpha_w}\alpha)^2 + K_H C_{LH}{}^2 + K_F(C_{L\alpha_F}\alpha)^2 \quad (6)$$

The trim condition is written as

$$\left.\begin{aligned} C_{L_{trim}} &= C_{L\alpha_w}\alpha + C_{LH} + C_{L\alpha_F}\alpha \\ C_m = 0 &= -(x/\bar{c})C_{L\alpha_w}\alpha - (l_H/\bar{c})C_{LH} + C_{m\alpha_F}\alpha \end{aligned}\right\} \quad (7)$$

From the conclusions of Section (1), the induced drag constants K_w and K_H can be considered to be unaffected by flexibility, and K_F is assumed independent of flexibility.

By taking differentials of Eqs. (6) and (7) and performing the necessary algebraic manipulations, we find the drag increment due to flexibility in terms of the change in lift-curve slope and center-of-pressure movement:

$$\Delta C_{D_i}/K_w C^2_{L_w} = 2A(\Delta C_{L\alpha_w}/C_{L\alpha_w}) + 2B(\Delta x/\bar{c}) \quad (8)$$

where

$$\left.\begin{aligned} B &= \frac{1 + (K_F/K_w)(C_{L\alpha_F}/C_{L\alpha_w})^2 - (K_H/K_w)(\bar{c}/l_H)[dC_m/dC_L]_{T.\,off}[1 + (C_{L\alpha_F}/C_{L\alpha_w})]^2}{[1 + (C_{L\alpha_F}/C_{L\alpha_w})]\{(l_H/\bar{c}) + [dC_m/dC_L]_{T.\,off}\}} \\ A &= 1 - (K_H/K_w)(\bar{c}/l_H)[dC_m/dC_L]_{T.\,off}[1 + (C_{L\alpha_F}/C_{L\alpha_w})] - B[(l_H/\bar{c}) - (x/\bar{c})] \end{aligned}\right\} \quad (9)$$

where $[dC_m/dC_L]_{T.\ off}$ is the tail-off static stability.

In order to get an insight into the magnitude of the drag variation and the important parameters involved, we will make the following assumptions:

$$K_H/K_w \sim S_w/S_H; \quad K_F/K_w \sim S_w/S_F; \quad C_{L\alpha_F}/C_{L\alpha_w} \sim S_F/S_w$$
$$l_H/c >> [dC_m/dC_L]_{T.\ off}$$

Following these assumptions, Eqs. (9) become

$$\left.\begin{aligned} B &= (c/l_H)\left\{1-(S_w/S_H)(c/l_H)[dC_m/dC_L]_{T.Off}[1+(S_F/S_w)]\right\}^{\frac{1}{2}} \\ A &= B(x/c) \end{aligned}\right\} \quad (10)$$

which shows the dependence on the tail-length ratio, static stability, and center-of-pressure location.

To investigate the range of variation of drag, we choose some typical parameters for airplanes at supersonic speeds (since flexibility effects are greatest at high speeds) as shown in Tables I, II, and III. Table I shows the variation of the coefficients A and B. The assumed variation with sweepback angle of the typical flexibility parameters at maximum speed is shown in Table II. The resulting drag variation is shown in Table III. It is immediately obvious upon examination of Table III that neglecting the effects of flexibility on the trimmed drag polar is justified for slightly swept wings, conservative for moderately swept wings, and overly conservative for highly swept wings.

Free Molecular Flow Forces and Heat Transfer for an Infinite Circular Cylinder at Angle of Attack*

L. Talbot
Assistant Professor of Mechanical Engineering, University of California, Berkeley, Calif.

February 4, 1957

STALDER *et al.*[1,2] have obtained expressions for the heat-transfer and force characteristics of an infinite circular cylinder transverse to a Maxwellian free molecule flow—that is, a flow in which the mean free path is large compared to the body dimension. They considered two cases: (a) perfectly specular reflection, wherein the molecules transfer zero energy and zero tangential momentum to the surface, and (b) perfectly diffuse reflection, wherein the molecules transfer all their tangential momentum to the surface and leave the surface in thermal equilibrium with it.

In this note, results are given for more general surface interactions and for the case of the cylinder at angle of attack. These results have some application in missile aerodynamics and in the interpretation of free molecule probes used in low-density wind-tunnel work.

The following surface interaction parameters are defined:[3, 4]

$$\alpha = (dE_i - dE_r)/(dE_i - dE_w) \quad \text{(accommodation coefficient)} \quad (1)$$

$$\sigma = (\tau_i - \tau_r)/\tau_i \quad \text{(specular reflection coefficient)} \quad (2)$$

$$\sigma' = (p_i - p_r)/(p_i - p_w) \quad (3)$$

Here E is the energy flux of the molecular flow, p the momentum flux normal to the surface (pressure), and τ the momentum flux parallel to the surface (shear stress). The subscripts i, r, and w, respectively, indicate the incident flux, the re-emitted flux, and the flux which would be re-emitted if the molecules were left in a Maxwellian stream at the surface temperature. The quantity E includes both energy of translation and energy contained in internal modes of motion of the molecules, assuming that all forms of molecular energy are accommodated to the surface in the same degree. It may be noted that the case of perfectly specular reflection corresponds to $\alpha = \sigma = \sigma' = 0$ and that perfectly diffuse reflection corresponds to $\alpha = \sigma = \sigma' = 1$. The data presently available for α and σ indicate values between about 0.7 and 1.0; no data are as yet available for σ', though it might be expected that σ' will be of the same order of magnitude as σ.

* This work was supported by the Office of Naval Research and Office of Scientific Research. Reproduction in whole or in part is permitted for any purpose of the United States Government.

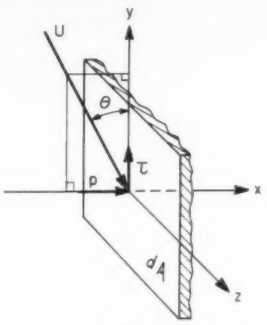

FIG. 1 (*Left*). Local coordinate system.

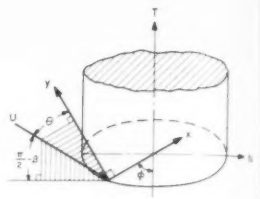

FIG. 2 (*Right*). Coordinate system on surface of cylinder.

In terms of the foregoing surface interaction parameters and in the nomenclature of Fig. 1, the shear stress, pressure, and heat transfer for a surface element dA aligned at angle θ with respect to the incident stream are

$$\tau = -(\sigma\rho U^2 \cos\theta/2s\sqrt{\pi})\left\{e^{-(s\sin\theta)^2} + \sqrt{\pi}(s\sin\theta)[1+\operatorname{erf}(s\sin\theta)]\right\} \quad (4)$$

$$p = \frac{\rho U^2}{2s^2}\left\{\left(\frac{2-\sigma'}{\sqrt{\pi}}\, s\sin\theta + \frac{\sigma'}{2}\sqrt{\frac{T_w}{T}}\right)e^{-(s\sin\theta)^2} + \left[(2-\sigma')\left(s^2\sin^2\theta + \frac{1}{2}\right) + \frac{\sigma'}{2}\sqrt{\frac{\pi T_w}{T}}(s\sin\theta)\right]\times\left[1+\operatorname{erf}(s\sin\theta)\right]\right\} \quad (5)$$

$$dQ = \alpha\rho RT\sqrt{\frac{RT}{2\pi}}\left\{\left(s^2 + \frac{\gamma}{\gamma-1} - \frac{(\gamma+1)}{2(\gamma-1)}\frac{T_w}{T}\right)\times\left(e^{-(s\sin\theta)^2} + \sqrt{\pi}(s\sin\theta)[1+\operatorname{erf}(s\sin\theta)]\right) - \frac{1}{2}e^{-(s\sin\theta)^2}\right\}dA \quad (6)$$

In these expressions ρ, U, and T are the density, velocity, and temperature of the incident stream; $s = U/\sqrt{2RT}$ is the molecular speed ratio; T_w is the temperature of the surface; and γ is the specific-heats ratio of the gas.

If it is assumed that the surface interaction parameters α, σ, and σ' and the body temperature T_w are all constant over the entire surface, the integration over a cylinder of the expressions given above may be carried out. The results of the integrations for the recovery factor and heat transfer are most conveniently expressed in terms of a modified recovery factor

$$r' = r\cdot[\gamma/(\gamma+1)] = [\gamma/(\gamma+1)]\cdot[(T_{aw}-T)/(T_0-T)] \quad (7)$$

where T_{aw} and T_0 are the adiabatic wall and stagnation temperatures; and a modified Stanton Number

$$St' = St\cdot[\gamma/\alpha(\gamma+1)] = [\gamma/\alpha(\gamma+1)]\cdot[Q/\pi d\rho UC_p(T_{aw}-T_w)] \quad (8)$$

where C_p is the specific heat of the gas at constant pressure, and d is the diameter of the cylinder. Likewise, the force calculation results are conveniently expressed in terms of a normal force coefficient

$$C_N = N/(1/2)\rho U^2 d \quad (9)$$

and a tangential force coefficient

$$C_T = T/(1/2)\rho U^2 d \quad (10)$$

where N and T are forces per unit length of cylinder.

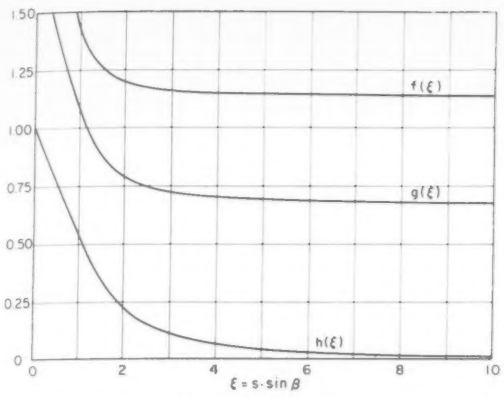

FIG. 3. Free molecular flow functions for cylinder at angle of attack.

The integrals are not difficult to set up and evaluate. For example,

$$C_T = (\sigma \cos\beta/\sqrt{\pi}s)\int_{-\pi/2}^{\pi/2} \{e^{-(\xi \sin\phi)^2} + \sqrt{\pi}\,\xi \sin\phi[1 + \text{erf}\,(\xi \sin\phi)]\}d\phi$$

One finds

$$St' = (\sin\beta/4\sqrt{\pi})g(\xi) \quad (11)$$

$$r' = 2 + (\sin^2\beta)h(\xi) \quad (12)$$

$$C_N = (\sigma' \sin\beta/4s)\pi^{3/2}\sqrt{T_w/T} + (4 + \sigma - 2\sigma')(\sin^2\beta)f(\xi) \quad (13)$$

$$C_T = (\sqrt{\pi}\,\sigma \cos\beta \sin\beta)g(\xi) \quad (14)$$

Here β is the angle of attack of the cylinder as shown in Fig. 2, $\xi = s \cdot \sin\beta$, and

$$f(\xi) = \{[(1/2\xi) + (1/3)\xi]I_0(\xi^2/2) + [(1/6\xi) + (1/3)\xi]I_1(\xi^2/2)\}e^{-\xi^2/2} \quad (15)$$

$$g(\xi) = \{[(1/\xi) + \xi]I_0(\xi^2/2) + \xi I_1(\xi^2/2)\}e^{-\xi^2/2} \quad (16)$$

$$h(\xi) = [I_0(\xi^2/2) + I_1(\xi^2/2)]/[(1 + \xi^2)I_0(\xi^2/2) + \xi^2 I_1(\xi^2/2)] \quad (17)$$

The above functions have been plotted in Fig. 3. If more accurate calculations are desired, they are easily accomplished through use of available tables[5,6] for the modified Bessel functions $I_0(x)$ and $I_1(x)$.

REFERENCES

[1] Stalder, J. R., Goodwin, G., and Creager, M. O., *A Comparison of Theory and Experiment for High Speed Free Molecule Flow*, NACA TN 2244, 1950.

[2] Stalder, J. R., and Zurick, V. J., *Theoretical Aerodynamic Characteristics of Bodies in a Free Molecule Flow Field*, NACA TN 2423, 1951.

[3] Bell, S., and Schaaf, S. A., *Heat Transfer to a Cylinder for the Free Molecule Flow of a Nonuniform Gas*, Jet Propulsion, Vol. 25, No. 4, pp. 168–169, April, 1955.

[4] Bell, S., and Schaaf, S. A., *Aerodynamic Forces on a Cylinder for the Free Molecule Flow of a Nonuniform Gas*, Jet Propulsion, Vol. 23, pp. 314–317, September-October, 1953.

[5] Watson, G. N., *A Treatise on the Theory of Bessel Functions*, 2nd Ed.; Cambridge University Press, 1944.

[6] Anding, E., *Sechsstelige Tafeln der Bessel'schen Funktionen Imaginaren Argumentes*; Leipzig, 1911.

Boundary-Layer Stabilization by Distributed Damping

Max O. Kramer
Coleman Engineering Company, Inc., Los Angeles

February 18, 1957

THE TRANSITION of the boundary layer from laminar to turbulent is a consequence of a dynamic instability that develops with increasing Reynolds Number. Thus it was felt that the introduction of artificial damping might increase the stability of the boundary layer. A systematic series of tests was conducted in order to study this novel approach to an artificial boundary-layer stabilization.

The tests utilized the spin test method which was specifically developed for a simple qualitative study of the effect of distributed damping on the transition Reynolds Number. The method was based on the wind-tunnel experience that qualitative transition studies can be made at slowly decreasing speed just as well as at slowly increasing speed. The method utilized a water-filled container of 20-in. inside diameter and 10-in. inside height. The container was spun up to 720 r.p.m. by an electric motor. After 10 min. at constant speed, required to eliminate turbulence, the container was suddenly stopped. A floating paddle inside the container, plus photoelectric recording equipment, permitted a reliable recording of the deceleration of the water speed in the Reynolds Number range from 10^7 to 10^4 (when referring the length and the speed to the inside circumference of the container). The transition Reynolds Number could be determined with an accuracy better than ±20 per cent by determining the break-away point of the measured speed-over-number-of-revolutions curve from the same calculated curve for fully laminar flow. By the application of short pieces of tripping wire in various places in the container, it could be proved that, for smooth metal walls, the transition starts in the center of the cylindrical area of the container at $R = 0.45 \times 10^6$ and reaches the top and the bottom of the container at $R = 4.5 \times 10^6$. The early beginning of the transition at $R = 0.45 \times 10^6$ was understandable when considering that theory and experiment agree on a drastic decrease of the transition Reynolds Number on concave surfaces as compared to flat surfaces.

The model of distributed damping tested covered the inside of the cylindrical wall of the container. A cross section of the lining is shown in Fig. 1. A thin natural rubber diaphragm was mounted on wires which ran on a cylindrical surface under an angle of 10° in reference to the general flow direction in order to make the damping effect more uniform. The wires in turn were mounted on the inside of a perforated cylindrical drum. Different mesh wire screens could be wrapped around the outside of the perforated drum in order to vary its hydraulic resistivity. An open space of 0.5-in. width was provided between the outside of the perforated drum and the inside of the spin test container in order to permit an oscillatory flow between various points of the

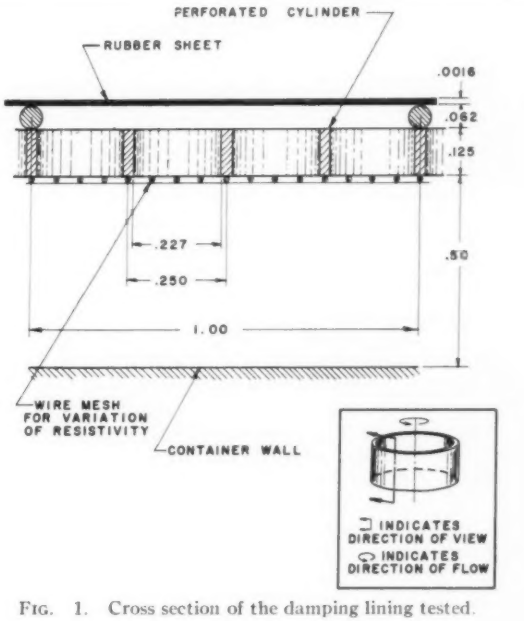

FIG. 1. Cross section of the damping lining tested.

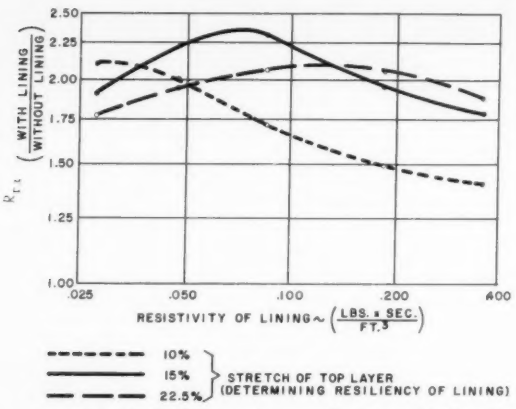

FIG. 2. The relative increase in transition Reynolds Number as a function of the resistivity and resiliency of the lining.

diaphragm. Small holes near the top and bottom made certain that the inside of the lining was automatically filled with water during the filling of the spin test container. The resiliency of the lining could be varied by a change in the stretch of the rubber diaphragm. The elasticity module of the rubber was 133 psi. The lining represented a damper which was to absorb oscillatory energy of the boundary-layer flow by a secondary oscillatory flow through the resistivity of the lining.

Fig. 2 shows the result of the investigation. The result is the relative increase of the transition Reynolds Number in the center of the cylindrical wall as a function of the two main parameters of the damping lining—the resistivity and the resiliency. The maximum relative increase in transition Reynolds Number measured equalled 2.4. The result means that the transition Reynolds Number of the properly tuned lining was 140 per cent greater than the transition Reynolds Number of the smooth rigid wall under equal conditions.

Since the preliminary study has shown promise, carefully controlled tests will be conducted under more normal conditions, such as increasing instead of decreasing speed, and zero pressure gradient in all three directions.

On Choosing Stress Functions in Rectangular Coordinates

F. W. Niedenfuhr
Instructor, Department of Engineering Mechanics, The Ohio State University, Columbus, Ohio
February 15, 1957

AS AN EXAMPLE of plane strain, most books on the theory of elasticity discuss the stresses in rectangular beams with distributed loading. The problem is conveniently handled by means of Airy's stress function. None of the standard books on the subject gives a general method of finding a polynomial stress function, to fit a particular problem, however. The purpose of this note is to present a general method which is especially useful when the load distribution is itself a polynomial.

In the absence of body forces, the stress function φ must satisfy the compatibility condition $\Delta^2\varphi = 0[\Delta = (\partial^2/\partial x^2) + (\partial^2/\partial y^2)]$ as well as certain boundary conditions. The boundary conditions are usually stated in terms of the stresses which are obtained from the stress function by the relations $\sigma_{xx} = \partial^2\varphi/\partial y^2$, $\sigma_{yy} = \partial^2\varphi/\partial x^2$, and $\sigma_{xy} = -\partial^2\varphi/\partial x\partial y$. It is easy to see that choosing these expressions for the stresses satisfies the equilibrium equations in two dimensions.

The most general polynomial in x and y is

$$\varphi = \sum_{i=0}^{N} p_i x^i \tag{1}$$

where

$$p_i = \sum_{j=0}^{P_i} a_{ij} y^j \tag{2}$$

and the a_{ij} are constants to be determined, as are N and the P_i. The appropriate derivatives of this polynomial are

$$\left.\begin{aligned} \partial^4\varphi/\partial x^4 &= \sum_{i=0}^{N} i(i-1)(i-2)(i-3)p_i x^{i-4} \\ \partial^4\varphi/\partial x^2\partial y^2 &= \sum_{i=0}^{N} i(i-1)p_i'' x^{i-2} \\ \partial^4\varphi/\partial y^4 &= \sum_{i=0}^{N} p_i^{IV} x^i \end{aligned}\right\} \tag{3}$$

where primes are used to indicate differentiation of the p_i.

With suitable shifts of indices, these partial derivatives can be substituted into the biharmonic equation and the coefficients of powers of x equated to zero. One obtains the recursion formula

$$p_{i-4}^{IV} + 2(i-2)(i-3)p_{i-2}'' + i(i-1)(i-2)(i-3)p_i = 0 \tag{4}$$

where $p_i \equiv 0$ for $i > N$. For $i = N+4, N+3, N+2, N+1$, the recursion formula yields

$$\left.\begin{aligned} p_N^{IV} = 0;\quad p_{N-2}^{IV} + 2N(N-1)p_N'' = 0 \\ p_{N-1}^{IV} = 0;\quad p_{N-3}^{IV} + 2(N-1)(N-2)p_{N-1}'' = 0 \end{aligned}\right\} \tag{5}$$

From this it can be seen that the P_i are determined as a function of N—i.e., in any given problem, if a starting place were known, all of the polynomials in y could be determined with just the right number of arbitrary constants to satisfy the biharmonic equation. Since the fourth derivative of p_N is zero, p_N is at most of third degree. The stress function is then of $(N+3)$rd degree in x and y and of Nth degree in x. The problem then is how large to make N, and this can be solved by considering the loading on the beam.

A theorem due to Weierstress states that any continuous function can be represented as closely as one likes by a function of the type $\sum_{k=0}^{n} q_k x^k$. There will be no loss of generality in assuming that the load on the beam is given in this form. In fact, since we deal with an elastic system in which superposition applies, we may consider the load on the beam to be simply qx^n, where q is a constant. In this case, it is clear that the bending moment on the beam is a polynomial of $(n+2)$nd degree. However, the bending moment must be resisted by internal stresses. In terms of stresses at a cross section of the beam, the bending moment per unit width is written as an integral of the form

$$\int_{y_1}^{y_2} y\sigma_{xx}dy = \int_{y_1}^{y_2} y \sum_{i=0}^{N} p_i'' x^i dy \tag{6}$$

This is by hypothesis a polynomial in x of degree no greater than N. Equating the expressions for moment obtained from stresses and loads, one obtains $N = n + 2$, where n is the degree of the polynomial which expresses the load.

When the load is expressed as a polynomial in x, then one generates a polynomial stress function containing only independent coefficients by repeated application of the recursion formula. Clearly this stress function satisfies the compatibility condition. The remaining undetermined coefficients a_{ij} are obtained from the boundary conditions.

The labor of calculating the remaining independent a_{ij} can be reduced by a good choice of axes. In particular, if the x axis is placed at the center of the beam so that the top (loaded) surface is $y = +c$ and the bottom (unloaded) surface is $y = -c$, certain simplifications arise. These are perhaps best illustrated by an example. Consider the cantilever beam loaded as shown in Fig. 1. The boundary conditions at the top and bottom surfaces are

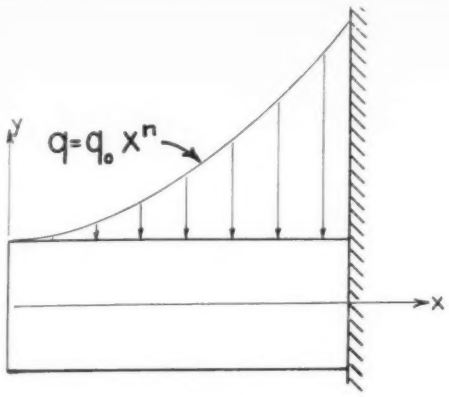

FIG. 1.

$$\left.\begin{aligned} -\sigma_{yy} &= q_0 x^n \quad \text{at} \quad y = +c \\ \sigma_{yy} &= 0 \quad \text{at} \quad y = -c \\ \sigma_{xy} &= 0 \quad \text{at} \quad y = \pm c \end{aligned}\right\} \tag{7}$$

In terms of the polynomials p_i these become the sets of equations:

$$-p_{n+2}(+c) = q_0 \tag{8}$$

$$p_i(+c) = 0 \qquad (i = 2, 3, \ldots n+1) \tag{9}$$

$$p_i(-c) = 0 \qquad (i = 2, 3, \ldots n+2) \tag{10}$$

$$p_i'(+c) = 0 \qquad (i = 1, 2, \ldots n+2) \tag{11}$$

$$p_i'(-c) = 0 \qquad (i = 1, 2, \ldots n+2) \tag{12}$$

The last two sets of equations [Eqs. (11) and (12)] written in summation form are

$$\sum_{j=1}^{N} j a_{i,j} c^{j-1} = 0 \tag{13}$$

$$\sum_{j=1}^{N} j(-1)^{j-1} a_{i,j} c^{j-1} = 0 \tag{14}$$

Adding these together one obtains

$$\sum_{k=0}^{[(P_i-1)/2]} (2k+1) a_{i,1k+1} c^{2k} = 0 \tag{15}$$

where $[(P_i - 1)/2]$ is the greatest integer in $(P_i - 1)/2$.

Similarly, on substracting Eq. (14) from Eq. (13),

$$\sum_{k=0}^{[(P_i-2)/2]} (2k+2) a_{i,\,2k+2} c^{2k} = 0 \tag{16}$$

The sets of equations (8), (9), (10), (15), and (16) are very nearly in triangular form and are quite easy to solve. Together with boundary conditions taken from the free end of the beam ($x = 0$) they form a complete set to solve for all the a_{ij}. The boundary conditions intended here are the approximate ones that the thrust, shear, and moment have prescribed values at the ends of the beam.

Normal Conduction Effects on Heat-Transfer Data During Transient Heating of Thin-Skin Models

Morton Cooper and Edward E. Mayo
Aeronautical Engineers, Langley Aeronautical Laboratory, NACA, Langley Field, Va.
February 20, 1957

ONE OF THE MOST commonly used methods to determine aerodynamic heat-transfer data is to expose a thin-skin model to a heated air stream. The heat-transfer coefficients are then evaluated by balancing the rate at which heat enters a unit volume of the skin with the rate at which heat is stored and leaves the skin. It is usual to minimize the skin thickness to keep the temperature difference across the skin negligible and the lateral conduction as small as possible. The use of a thin skin introduces structural problems, particularly for blunt noses, where the pressure may be sufficient to warp or fail the structure. To overcome this difficulty, it is common to use a fill material for added strength with the hope that only little heat may flow out the back face of the thin skin. It is the purpose of this note to establish the magnitude of the error involved by neglecting the presence of a fill material to show that, even for the best of fill materials, the errors might be quite significant.

If a thin skin backed by an insulating material is considered, then the aerodynamic heat input (q_{aero}) must equal the heat stored in the skin (q_{stored}) plus the heat removed by conduction through the rear face (q_{cond}). Lateral conduction may be neglected for simplicity inasmuch as its effects on the heat-transfer data can be superposed in the usual manner. The heat balance then becomes

$$q_{aero} = q_{stored} + q_{cond}$$

or

$$h(T_{adw} - T) = (\rho c_p \tau)_{skin}(dT/dt) + \left[\left(\sqrt{\rho c_p k}\right)_{ins}/\sqrt{\pi}\right]\int_0^t [T'(\lambda)/(t-\lambda)^{1/2}]d\lambda \tag{1}$$

where

h = aerodynamic heat-transfer coefficient
T_{adw} = adiabatic wall temperature
T = skin temperature
t = time
ρ = density
c_p = specific heat
k = thermal conductivity
τ = thickness

primes denote differentiation, and the subnotation *skin* and *ins* refer to the skin and insulating fill material, respectively. In order to express Eq. (1) in its present form, it has been assumed that there is no temperature variation across the skin, the interface of the skin and the insulating material are at the same temperature, the insulating material is of infinite extent normal to the skin, and the initial temperature distribution through the model is constant. The assumption of no temperature difference across the skin corresponds very well with reality when thin-skin metal models are used. Furthermore, for the illustrative case to be presented, it agrees very well with more exact calculations in which the heat-conduction equation in the skin was used.

If normal conduction through the rear face of the skin is important, then the heat-transfer coefficient depends upon the complete past history of the heating process, and Eq. (1) (or a form more suitable for numerical computation) must be used for the reduction of experimental data. To illustrate the magnitude of the heat flow into the insulating fill material, let us assume first that it is negligible and compute the temperature time history from the remaining terms as

$$T = T_{adw} - (T_{adw} - T_i)e^{-at} \tag{2}$$

where T_i is the initial skin temperature and

$$a = h/(\rho c_p \tau)_{skin}$$

If the conduction correction is not too large so that we can neglect the interaction between storage and conduction, we can estimate its magnitude by substituting Eq. (2) into the appropriate terms in Eq. (1) to obtain

$$q_{cond}/q_{stored} = (2/\sqrt{\pi})[(\sqrt{\rho c_p k})_{ins}/(\rho c_p \tau)_{skin}] \int_0^{t^{1/2}} e^{a\zeta^2} d\zeta \tag{3a}$$

$$= (2/\sqrt{\pi})[(\sqrt{\rho c_p k})_{ins}/(\rho c_p \tau)_{skin}] \sqrt{t} \times \sum_{n=0}^{\infty} [(at)^n/(2n+1)(n!)] \tag{3b}$$

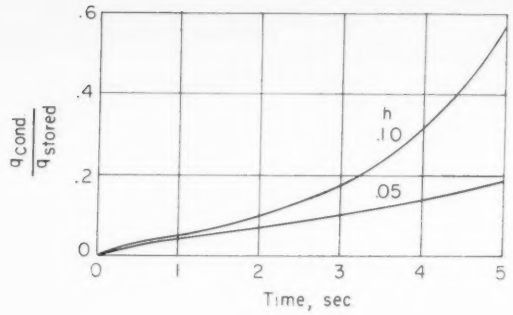

FIG. 1.

From Eq. (3) we note that the conduction term increases continuously relative to the heat stored in the skin. Furthermore, we observe, as is physically evident, that increasing the skin thickness reduces the normal conduction to the insulator. Also, the conduction effect increases with heat-transfer coefficient h and time t. Eq. (3) is plotted in Fig. 1 for a 0.030-in. skin steel model backed by balsa wood, a substance having a low value of $\rho c_p k$ and hence a good insulator. Heat-transfer coefficients of 0.05 and 0.10—values which might occur in supersonic flight—are assumed.

As can be seen from Fig. 1, the magnitude of the conduction term is quite significant. Hence, in the design of thin-skin models for aerodynamic heating studies, the simplicity of data reduction makes elimination of the insulating fill material far more preferable than attempting to account for its presence. It is of interest to note the similarity of the present problem with that encountered in shock-tube heat-transfer-data reduction.[1] In the shock tube one reverses the design criterion and minimizes the storage term relative to the conduction term in order to maximize the surface-temperature rise with time. Only recently[1] has the importance of the neglected term been established for the shock tube.

REFERENCE

[1] Vidal, Robert J., *A Resistance Thermometer for Transient Surface Temperature Measurements*, Paper presented at American Rocket Society Meeting, Buffalo, September 24–26, 1956.

Calibration of Surface Tubes for Measurement of Surface Shear in Fluids*

J. N. Hool
The New South Wales University of Technology, School of Mechanical Engineering, Sydney, N.S.W., Australia
February 18, 1957

THE DETERMINATION of the intensity of surface shear in a flowing fluid using the surface-tube technique depends upon a knowledge of the position of the effective center of the surface tube. If the distance of the effective center of the surface tube from the surface to which it is attached is y_1 and the velocity at this point found from the surface-tube pitot-static pressure is u_1, the intensity of surface shear τ_w is given by

$$\tau_w = \mu(u_1/y_1) \tag{1}$$

it being assumed that u_1/y_1 approximates closely $(\partial u/\partial y)_{y=0}$ for very small values of y_1.

Giedt,[1] using the Blasius-Hiemenz solution of the laminar layer, found for the surface tube used in his experiments that the surface-tube pitot-static pressure Δp is given by

$$\Delta p = 5.50 \times 10^{-3}(\partial u/\partial y)_{y=0}^{1.43} \tag{2}$$

where Δp is measured in lb.ft.$^{-2}$ and ∂u and ∂y are measured in ft.sec.$^{-1}$ and ft, respectively. This equation applies to surface tubes used in air at standard or near-standard temperature and pressure. Substitution of $(1/2)\rho u_1^2$ for Δp, u_1/y_1 for $(\partial u/\partial y)_{y=0}$ and using a value for ρ of 0.00233 slug-ft.$^{-3}$ yields

$$y_1 = 9.37 \times 10^{-4} u_1^{-0.4} \tag{3}$$

A number of surface tubes have been calibrated at Oxford University,[2] the surface tubes in this case being about 3/16 in. wide and having the form shown in Fig. 1. It was found that the effective center distance y_1 was represented by

$$y_1/y_d = 1.80(y_d^2 u_1/\nu y_1)^{-0.2} \tag{4}$$

between the limits of 0.75 and 2.25 for $\log_{10}(y_d^2 u_1/\nu y_1)$. Noting that $u_1/y_1 \approx u_d/y_d$, the dimensionless group $(y_d^2 u_1/\nu y_1)$ becomes $(y_d u_d/\nu)$, which is assumed to be the Reynolds Number for the surface tubes considered.

The height of the surface tube used by Giedt was approximately 0.0035 in. with an opening of 0.0030 in. The value of y_d for this tube using the notation of Fig. 1 is 3.25×10^{-3} in. or 2.71×10^{-4} ft. With this value of y_d and using the value of the kinematic viscosity ν for air at standard temperature and pressure, Eq. (4) becomes

$$y_1 = 4.97 \times 10^{-4} u_1^{-0.25} \tag{5}$$

The values of y_1 given in Eqs. (3) and (5) are shown plotted in Fig. 2. The intensity of surface shear found from Eq. (3) is given by

$$\tau_w = 4.05 \times 10^{-4} u_1^{1.4}$$

Using Eq. (4) in place of Eq. (3), the intensity of surface shear is given by

$$\tau_w = 7.64 \times 10^{-4} u_1^{1.25}$$

It is interesting to plot the ratio y_1/y_d obtained from Giedt's equation against the surface-tube Reynolds Number for air at standard temperature and pressure. This plot is compared with other results[2] in Fig. 3. It will be noted that Giedt's values of y_1/y_d are slightly greater than values represented by Eq. (4) and considerably greater than values obtained from the curve suggested by Taylor.[3]

Thom[4] produced a two-dimensional numerical solution for a surface tube in an ideal fluid. His solution indicates that adjacent

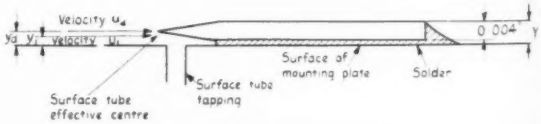

FIG. 1. Surface-tube nomenclature.

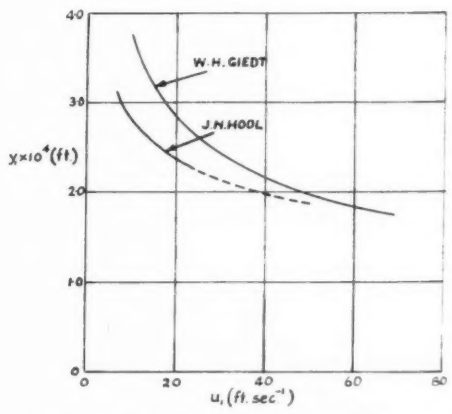

FIG. 2. Surface-tube effective center distances.

* Experimental values were obtained at the Engineering Laboratory, Oxford University.

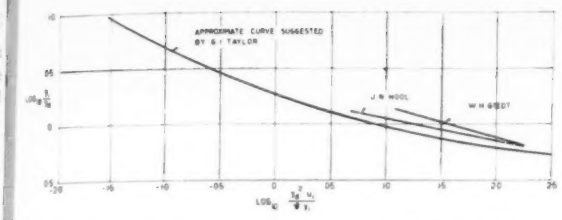

FIG. 3. Surface-tube results plotted nondimensionally.

to the leading edge of a surface tube the streamlines are at an angle of slightly less than 45° to the direction of motion.

The surface tubes used by various workers differ in outside shape and in the form of the leading edge. Surface tubes of reasonable width and with the upper inclined surfaces adjacent to the leading edges at angles of less than 45° to the direction of motion will have flow patterns adjacent to the surface-tube openings governed largely by the value of y_d. Surface tubes of this form should have comparable calibration curves when plotted as in Fig. 3. Surface tubes with the upper inclined surfaces adjacent to the leading edges at angles of greater than 45° will have the leading edges submerged in a standing eddy. In this case the flow pattern adjacent to the surface-tube opening will be governed very largely by the outside dimension Y of the surface tube.

REFERENCES

[1] Giedt, W. H., *Effect of Turbulence Level of Incident Air Stream on Local Heat Transfer and Skin Friction on a Cylinder*, Journal of the Aeronautical Sciences, Vol. 18, No. 11, pp. 725–730, November, 1951.

[2] Hool, J. N., *Measurement of Skin Friction Using Surface Tubes*, Aircraft Engineering, Vol. 28, No. 324, pp. 52–54, 1956.

[3] Taylor, G. I., *Measurements with a Half Pitot Tube*, Proceedings of the Royal Society, Series A, Vol. 166, pp. 476–481, 1938.

[4] Thom, A., *The Flow at the Mouth of a Stanton Pitot*, Aeronautical Research Council (Great Britain), Report No. 15228, 1952.

Induced Rolling Moments at Supersonic Speeds†

George S. Campbell*
Research Engineer, Weapon Systems Development Laboratories, Hughes Aircraft Company, Culver City, Calif.
February 21, 1957

INTRODUCTION

RECENT supersonic wind-tunnel tests of a missile have shown peculiar rolling-moment effects which were not expected on the basis of the usual slender-body theories. One of the problems encountered on a cruciform missile configuration may be described with the help of Fig. 1. It is desired to maneuver the missile in the vertical plane, but a disturbance of some kind results in deflection of the vertical control by an amount δ. Although linearized theory would not predict a rolling moment for this condition, the wind-tunnel results exhibited a strong induced rolling moment.

It is the purpose of this note to provide a quantitative explanation of this rolling moment and to compare the calculated results with available measurements. The explanation given relates the induced roll to a variation in dynamic pressure and local Mach Number above the main lifting surface, shown shaded in Fig. 1. Small disturbances and isentropic flow have been assumed for the calculation of this wing-interference effect. Any additional effects due to shock-wave losses from body or wing shock waves should be considered as soon as suitable methods become available.

† Funds for this study were provided by Wright Air Development Center.
* The writer wishes to acknowledge the contributions of W. M. Bleakney and R. H. Edwards in pointing out the basic causes of the induced rolling moments considered in the present note.

The present problem is intended as a simple illustration of strong dynamic pressure and Mach Number effects which may occur in supersonic flows. Other induced roll phenomena may be similarly explained, such as a reversal in the sign of the rolling moment of a banked missile at the higher Mach Numbers. The wing-interference field can also contribute to the variation of a missile's hinge moments with bank angle.

ANALYSIS

A simple strip theory may be used to calculate the rolling moment for the cruciform missile of Fig. 1. The rolling moment L is then given by the integral

$$L = \delta \int_{-s}^{s} (aq)\, cz\, dz \tag{1}$$

in which the section lift-curve slope is denoted by a and dynamic pressure by q. The induced rolling moment arises from small differences in the lift coefficient and the dynamic pressure from free-stream values, so that

$$L/\delta = a_0 \int_{-s}^{s} (\Delta q)\, cz\, dz + q_0 \int_{-s}^{s} (\Delta a)\, cz\, dz \tag{2}$$

The local lift-curve slope is given by the Ackeret value, $4 \div \sqrt{M^2 - 1}$, which may be expanded in powers of the Mach Number increment to give

$$\Delta a/a_0 = -\,[M_0^2/(M_0^2 - 1)]\,(\Delta M/M_0) \tag{3}$$

Within the framework of a small-disturbance theory, local Mach Number and dynamic pressure are linearly related to the perturbation velocity in the free-stream direction, ϕ_x. Use of the linearized Bernoulli equation and the isentropic flow relations lead to

$$\Delta M/M_0 = \{1 + [(\gamma - 1)/2]\, M_0^2\}\,(\phi_x/V) \tag{4}$$

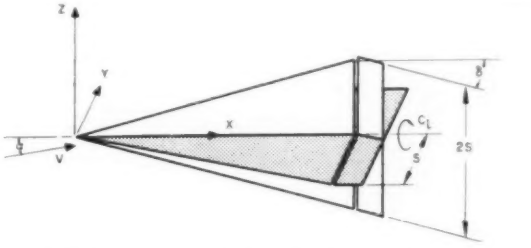

FIG. 1. Geometry of the induced-roll problem.

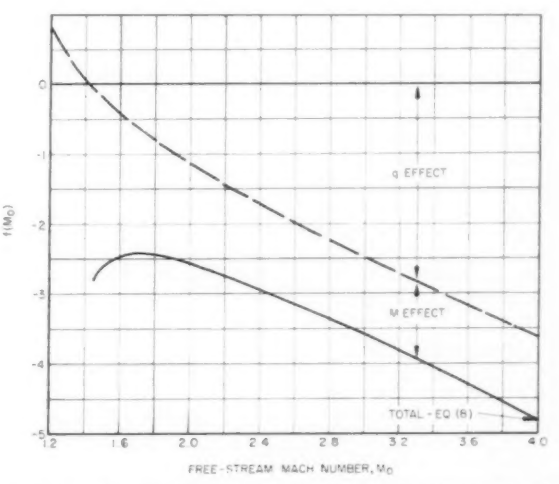

FIG. 2. Mach Number dependence of the induced rolling moment due to dynamic pressure and local Mach Number effects. $f(M_0)$ is proportional to C_l; see Eq. (7).

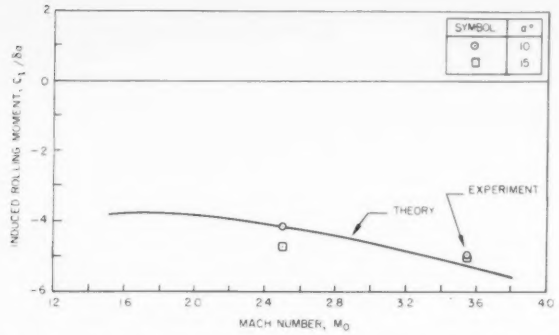

FIG. 3. Comparison of theoretical and experimental induced rolling moments for a cruciform missile.

$$\Delta q/q_0 = (2 - M_0^2)\,(\phi_x/V) \tag{5}$$

after dropping higher order terms. The velocity perturbation is required in the vertical plane above the centerline of the lifting wing, and slender-body theory provides this quantity in terms of the local semispan s.

$$\phi_x/V = (\alpha s/\sqrt{z^2 + s^2})\,(ds/dx) \tag{6}$$

The unknown quantities in the rolling-moment relation, Eq. (2), are now given in terms which permit a simple integration. The resulting rolling-moment coefficient may be written

$$C_l/\alpha\delta = K f(M_0)\,(ds/dx) \tag{7}$$

in which

$$f(M_0) = [(2 - M_0^2)/\sqrt{M_0^2 - 1}] - [M_0^2/(M_0^2 - 1)^{3/2}] \times \{1 + [(\gamma - 1)/2]\,M_0^2\} \tag{8}$$

$$K = 0.296 + 0.532\,\lambda \tag{9}$$

The rolling-moment coefficient of Eq. (7) is defined as $(L/q_0) \times b^2 c_r$, where b is the span and c_r is the root chord of the control surface. The taper ratio of the control is denoted by λ, the ratio of tip chord to root chord. If the main lifting surface were a delta wing, ds/dx would simply be the tangent of the wing's semiapex angle.

The Mach Number dependence of the induced rolling moment is determined by Eq. (8). The first term represents the effect of dynamic pressure variation, and the second term accounts for local Mach Number variation. The two terms are plotted for comparison in Fig. 2. q effect reverses sign at $M_0 = \sqrt{2}$ because of the maximum at this Mach Number in the isentropic relationship between q and M_0. Use of the Ackeret formula for two-dimensional lift results in the singularities in Eq. (8) as M_0 approaches unity.

Comparison With Experiment

The results of wind-tunnel measurements of the induced rolling moment for a cruciform missile configuration are given in Fig. 3, along with a theoretical estimate. In addition to the rolling moment from Eq. (7), a small additional moment contributed by the effective "sideslip" α of the vertical control surfaces has been included in the theoretical estimate. The linear theory of reference 1 is used for the latter calculation. The rolling-moment coefficients in Fig. 3 are based on body cross-sectional area and diameter, and the angles are expressed in radians. Presence of the body is neglected in the theory, and the planar surfaces are assumed to extend through the fuselage.

The theoretical estimate of the induced rolling moment is seen to be in very good agreement with the experimental results. It is expected that any refinements in the theory would generally reduce the estimated rolling moments. For example, tip effects are neglected in the strip theory. Nevertheless, the theory in its present simple form should be useful for preliminary estimates and for pointing out the design factors contributing to induced roll.

Reference

[1] Harmon, Sidney M., *Stability Derivatives at Supersonic Speeds of Thin Rectangular Wings With Diagonals Ahead of Tip Mach Lines*, NACA Rep. 925, 1949.

A New Technique for Investigating Heat Transfer and Surface Phenomena Under Hypersonic Flow Conditions*

Antonio Ferri and Paul A. Libby
Aerodynamics Laboratory, Polytechnic Institute of Brooklyn, Freeport, N.Y.
February 21, 1957

On the forebody of many practically interesting hypersonic vehicles, there is little interaction between the inviscid flow field and the boundary layer. Therefore, inviscid flow theory can be used to determine, independent of surface phenomena, the physically interesting quantities such as shock shape, shock detachment distance, sonic line shape, and pressure distribution. Furthermore, the pressure distribution so determined can then be used for the study of heat transfer, materials behavior, and other surface phenomena. Thus, for these bodies, the Prandtl boundary-layer concept can be utilized for the calculation of both the inviscid flow and the boundary-layer behavior.

It is the purpose of this note to point out that this concept can also be applied experimentally in order to provide, in conjunction with a conventional hypersonic wind-tunnel air supply, a means for investigating hypersonic heat transfer and surface phenomena under conditions of flight Reynolds Numbers.

Consider, for example, a blunt axisymmetric body at zero angle of attack; assume that the pressure distribution is known from a low Reynolds Number wind-tunnel test at the desired flight Mach Number or from an inviscid flow calculation or from a combination of theory and experiment. To study boundary-layer, surface, and heat-transfer phenomena on this body in a wind tunnel, it is not necessary to simulate the entire inviscid flow field but only that portion contiguous with the boundary layer. This suggests, then, that the model can be surrounded by a shroud which establishes the previously measured pressure distribution on the model. For a typical blunt body, the shroud must impose a mixed-subsonic and low-supersonic flow and leads to a configuration shown schematically in Fig. 1. For a given air supply, the model and shroud sizes are dictated by the requirement that under all test conditions the flow between the model and shroud should be far from a fully developed channel flow. The shroud can be designed to a first approximation from one-dimensional flow theory and then modified empirically so as to impose the desired pressure distribution.

This shrouded model technique can be used in connection with the air supply of existing hypersonic wind tunnels to provide data

* The technique reported here was developed in connection with contract AF 33(616)-17 sponsored by the Aeronautical Research Laboratory of Wright Air Development Center.

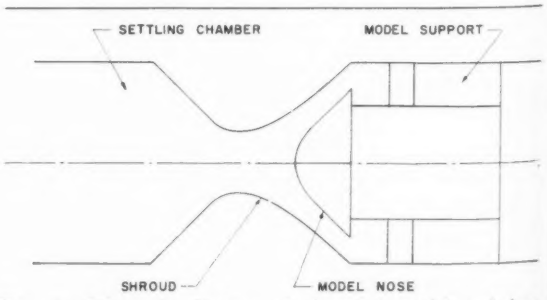

FIG. 1. Schematic diagram of shrouded model technique.

under high Reynolds Number, high heating conditions. There are two major advantages of this technique for the study of these phenomena:

(1) Because the mass flow from the heating system must be only one order of magnitude greater than that within the boundary layer at the aft end of the body, the model size can be enormously increased over that possible in the usual hypersonic test. As a result of increased model size, the study of many detailed phenomena is possible. For example, the study of the influence of surface roughness, local ablation, plastic flow, and cavities on transition and local heat transfer is practicable. Furthermore, thermal stresses can be investigated under close to flight thermal and mechanical loading conditions, thereby greatly reducing the problems of structural similitude. Moreover, the problem of installing model instrumentation is greatly reduced.

(2) The second advantage of this technique pertains to the realization of higher Reynolds Numbers and, consequently, larger rates of heating from a given heating system. Because there are no losses from the normal shock ahead of the model, the stagnation pressure on the model can be equal to the maximum heater pressure rather than to a few per cent thereof as is usual in hypersonic testing. Thus, with a stagnation pressure of 100–200 psia, flight Reynolds Numbers of practical interest can be obtained with existing air supplies.

Several comments concerning the applicability of this technique are pertinent. Although described above for axisymmetric flow about a blunt body, this technique can be applied to pointed and/or three-dimensional flows. In order to accomplish this extension, the desired pressure distribution and related shroud design must be established. For pointed bodies, the flow ahead of the apex must be sufficiently supersonic to permit the establishment of an attached shock. Furthermore, by combining this technique with that described in reference 1 for the simulation of the flow in the base region of hypersonic bodies, the entire viscous flow field can be studied with conventional hypersonic wind tunnels. Finally, by programing the stagnation pressure of the heater, it is possible to impose a time history of Reynolds Number. This permits a partial simulation of a missile heating cycle and the determination of transition from instantaneous and local heat-transfer data. Evidently, the influence of vehicle dynamics on boundary-layer behavior cannot be simulated by any fixed model technique.

It should be pointed out that the complete separation of inviscid and boundary-layer flows is required for the utilization of the testing technique described here; thus the effect on boundary-layer behavior of the entropy gradient due to bow shock curvature is not simulated.

The shrouded model technique described here has been employed in connection with the hypersonic facility of Polytechnic Institute of Brooklyn. The results of some preliminary tests are presented in reference 2.

References

[1] Ferri, Antonio, and Pallone, Adrian, *Note on the Flow Fields on the Rear Part of Blunt Bodies in Hypersonic Flow*, WADC TN 56-294, July, 1956.

[2] Ferri, Antonio, Cresci, Robert, and Libby, Paul A., *Preliminary Hypersonic Laminar and Turbulent Heat Transfer Data Obtained by a New Technique*, WADC TN 56-378 (Confidential), December, 1956.

Geometric Stabilization

A. Lange
Electromechanical Section, Raytheon Manufacturing Company, Wayland, Mass.
March 1, 1957

MR. GORCZYCKI is to be congratulated for his timely paper on geometric stabilization;[1] modern weapons systems abound with examples of this problem, and his paper is a welcome addition to a literature which appears to have large gaps between the theoretical and the detailed treatments. The writer shares Mr. Gorczycki's interest in the subject (cf. reference 2), and it seems fruitful to discuss certain of Mr. Gorczycki's concepts in detail. Most of the discussion which follows is essentially semantic in nature; however, it may be noted that the only difficulties involved in this basically simple application of Newton's second law are syntactical in nature. Consequently, concern with these details seem worth while.

It is the writer's belief that Mr. Gorczycki does not make it sufficiently clear that the concepts involved here apply to any device which is to be isolated from the motion of the base on which it is mounted; the device characterized by an axis always aligned with the direction of local gravity is one such system, but, as the author later points out, the platform can be oriented according to prescribed command signal data. Further, there seems to be some confusion regarding the role of the integrating rate gyros. In the first place, it is not the integrating nature of the stable platform but its synthetic inertness which satisfies the requirement of geometric stabilization. Useful as the integrating rate gyro is in such applications, it is but one of a number of devices which invoke Newton's second law to accomplish the same result.

Eq. (1) of reference 1 is not a statement of Newton's second law; it can more accurately be described as a statement of the law of Coriolis (reference 2; reference 4, pages 132–134). (Incidentally, this equation illustrates the hazard of using Newton's notation in that the dot over ω has inadvertently been omitted in the tangential acceleration term. The use of a differential operator symbol seems preferable.) Also, in a vector equation of this sort, it would be helpful to use a notation similar to that suggested by Weiss[3]—viz., $\boldsymbol{V} = \boldsymbol{V}_{ij}{}^{k}$, where $\boldsymbol{V}$ is any vector and the subscript ij indicates that the vector $\boldsymbol{V}$ is defined as some vector relationship between space i and space j (e.g., the position vector relating space j to space i, $\boldsymbol{R}_{ij}$). The superscript k indicates that the components of the vector $\boldsymbol{V}$ are evaluated in space k; the spaces i, j, and k may be represented, for example, by Cartesian sets, interrelated in some specified manner. The same statement is applicable to the components of Eq. (1)[1]—Eqs. (2), (3), and (4)—where it is not immediately clear, for example, that ω_x, ω_y, and ω_z are the components of the angular rate of the platform with respect to inertial space in inertial space coordinates, etc.

Further, under the assumptions used by Mr. Gorczycki, it is not clear to the writer why the translational form of Newton's second law is used. Since the platform is considered as a rigid body, the rotational form seems considerably more direct—viz.,

$$\boldsymbol{M}_p{}^{p} = \begin{vmatrix} M_x \\ M_y \\ M_z \end{vmatrix} = D_i\,(J_p \boldsymbol{W}_{ip}{}^{p})$$

where $\boldsymbol{M}_p$ = the vector sum of the moments applied to the platform, $D_i = (d/dt)\,(\ )_i$ = the rate of change of $(\ )$ with respect to inertial space, $J_p \equiv$ inertia tensor (reference 4, pages 146–156), and $\boldsymbol{W}_{ip}$ = the angular velocity of the platform (p) with respect to inertial space (i). The superscript p indicates, for example, that the components of the vectors are evaluated in platform coordinates. The three components of $\boldsymbol{M}_p$—M_x, M_y, and M_z—are supplied, in this case, by the inner gimbal-azimuth axis bearings and by the azimuth servo, respectively. If it is desired to introduce the effects of mass unbalance into the above expression, the following vector must be included in $\boldsymbol{M}_p$:

$$m_p \boldsymbol{A}_{ip}{}^{p} \times \boldsymbol{E}^{p}$$

where m_p is the mass of the platform, $\boldsymbol{A}_{ip}{}^{p}$ is the translational acceleration of the geometric center of the platform with respect to inertial space, and $\boldsymbol{E}^{p}$ is the eccentricity vector relating the center of mass to the geometric center. For the special case where only the acceleration due to gravity is desired,

$$\boldsymbol{A}_{ip}{}^{i} = g \begin{vmatrix} 0 \\ 0 \\ 1 \end{vmatrix} \qquad \boldsymbol{A}_{ip}{}^{p} = T_{pi}\,\boldsymbol{A}_{ip}{}^{i}$$

where g is the acceleration due to gravity and T_{pi} is the transformation matrix (see reference 2; reference 4, pp. 97–106) transforming $\boldsymbol{A}_{ip}$ from inertial space to platform space. It may be argued that introducing the latter term is, in effect, what Mr. Gorczycki introduces *ab initio*. However, in a practical design problem, a great deal of analysis and design may be completed before $\boldsymbol{E}$ can be specified. Then its effect can be introduced when more information is available.

It appears that Mr. Gorczycki's prime concern is to establish the torque requirements for the three servos of a particular gimbal configuration. The writer would like to suggest the following steps which are generally applicable to problems of this nature, and have been found to be quite useful:[2]

(1) Solve the kinematic equations

$$\boldsymbol{W}_{ip}{}^{p} = 0 \qquad \boldsymbol{U}_{ip}{}^{p} = 0$$

where $\boldsymbol{W}_{ip}$ = angular velocity of the platform with respect to inertial space, $\boldsymbol{U}_{ip}$ = angular acceleration of the platform with respect to inertial space, and p indicates that the components of the vectors are evaluated in platform space. The first equation is a function of W_x, W_y, and W_z—the components of the angular velocity of the base with respect to inertial space—as disturbances and the three gimbal servo angular rates as outputs. The second equation is a similar function, except that the Coriolis accelerations are also involved. The latter appear as twice the product of the gimbal rates and base rates. By setting the above vectors equal to zero and solving for gimbal angle rates, the gimbal rates necessary to isolate the platform from the motion of the base may be found. Reference 2 describes in detail the steps required to solve these equations, including the derivation of the transformation matrices. Several examples are given, and the servo rates required for all six of the nonredundant* three-axis gimbal systems are summarized in a table. Further, by restricting one of these angles to zero, each of the three-axis systems degenerates to a two-axis system so that, by implication, all of the two-axis systems are considered as well. Assuming sinusoidal disturbances, maximum servo rates, accelerations, and bandwidths may be determined.

(2) Using the values found above, solve the kinetic equations

$$\boldsymbol{M}_{p}{}^{p} = D_i J_p \boldsymbol{W}_{ip}{}^{p} \qquad \boldsymbol{M}_{ig}{}^{ig} = D_i J_{ig} \boldsymbol{W}_{iig}{}^{ig}$$

$$\boldsymbol{M}_{og}{}^{og} = D_i J_{og} \boldsymbol{W}_{iog}{}^{og}$$

where the subscripts *ig* and *og* refer to the inner and outer gimbals, respectively. These three vector equations represent nine scalar equations, of which three determine servo torques and the other six determine gimbal bearing couples. From the kinetic equations, torque and horsepower requirements can be found, and, from torque and angular velocity requirements, the necessary gear ratios can be selected.

The kinematic equations determine the quantities measured by the gyros; the kinetic equations determine the required torques so that a reasonable analysis of the servos may be performed. Depending on the location of the gyros, it is usually advisable to compensate for the fact that the gyro input axis and the gimbal axis are not always aligned. However, it should be observed that the resulting automatic gain control affects *only* the dynamic performance of the system and not its steady-state behavior.

Space does not permit an adequate discussion of the interesting problems posed by Mr. Gorczycki, but the interested reader is referred to the references where these and related problems are dealt with in detail.

References

[1] Gorczycki, Edmund, *Dynamic Considerations Relating to the Behavior of Inertial Space-Stabilized Platforms*, Journal of the Aeronautical Sciences, Vol. 24, No. 2, pp. 130–138, February, 1957.

[2] Lange, A., *Automatic Controls in Weapons Systems*, to be published in IRE Transactions on Automatic Control.

[3] Weiss, E., *Kinematic & Geometric Relations Associated with Motion of a Vehicle over the Earth*, Instrumentation Laboratory R-68, Massachusetts Institute of Technology, March, 1954.

[4] Goldstein, H., *Classical Mechanics;* The Addison-Wesley Publishing Company, Inc., Cambridge, Mass., 1953.

* A nonredundant gimbal system is designed so that, when all three gimbal angles are zero, the three axes are mutually orthogonal. A redundant gimbal system is designed so that, when the three angles are zero, two of the axes (usually the innermost and the outermost) are parallel.

The Effect of a Simple Throat Distortion on the Flow in a Hypersonic Wind-Tunnel Nozzle*

Robert E. Oliver and Benjamin E. Cummings

Guggenheim Aeronautical Laboratory, California Institute of Technology, Pasadena, Calif.

February 25, 1957

AN EXPERIMENTAL INVESTIGATION was conducted in the GALCIT $2^1/_2 \times 3$ in. supersonic wind tunnel to determine the effect of a known distortion of the throat section of a hypersonic nozzle on the flow in the region downstream from the throat. The flow in a nozzle with a rectangular throat section was compared with the flow in the same nozzle with the throat region distorted to produce a throat height which varied linearly across the throat section. The flow was investigated by means of pitot pressure surveys in the horizontal plane of symmetry of the undistorted nozzle.

The magnitude of the effect produced by this throat distortion was observed to be approximately that predicted by one-dimensional isentropic flow relations. However, the sign of the effect was reversed in about the distance required for a curved Mach line starting at the throat to cross the channel.

The nozzle used in this investigation is a full-scale section of the throat region of a proposed hypersonic nozzle to be constructed at the Jet Propulsion Laboratory. This section is 2.6 in. wide and covers the region from $5^1/_2$ in. upstream to $11^1/_2$ in. downstream from the throat. The nozzle channel is formed by two solid steel nozzle blocks and two parallel steel side plates.

Pitot pressures were measured in the horizontal plane of symmetry of the undistorted nozzle by means of a traversing nine-tube rake. The lower nozzle block was removed and distorted as indicated in Fig. 1 and was then reinstalled in its original position. Pitot pressures were again measured in the horizontal plane of symmetry of the undistorted nozzle.

Mach Numbers were determined from isentropic flow relations. The resulting constant Mach Number contours in the horizontal

* This investigation was a part of a broad hypersonic research program sponsored and supported jointly by Office, Chief of Ordnance, and the Office of Ordnance Research, U.S. Army, under Contract No. DA-04-495-Ord-19.

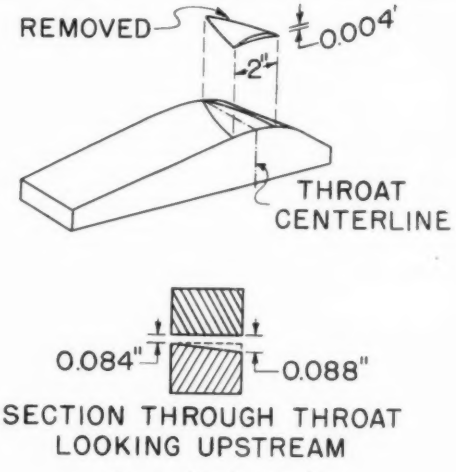

FIG. 1. Nozzle distortion.

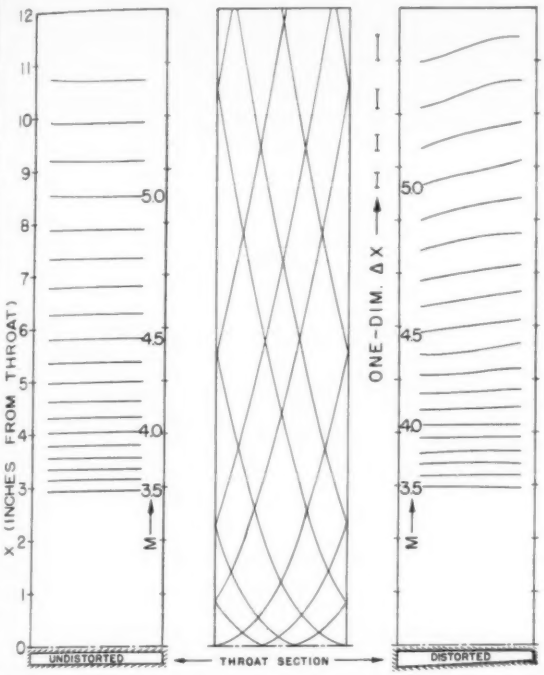

FIG. 2. Constant Mach Number contours and approximate characteristics.

plane of symmetry of the undistorted nozzle are shown in Fig. 2. Also shown in Fig. 2 are the approximate characteristics in this plane. The one-dimensional Δx's shown in Fig. 2 are the distortions of the constant Mach Number contours as predicted by one-dimensional isentropic flow relations. There was no apparent decay of the distortion effect within the region of this investigation.

Polytropic Exponents for Air at High Temperatures*

J. G. Logan, Jr., and C. E. Treanor
Head—Theoretical Flow Physics Section and Research Physicist, Respectively, Cornell Aeronautical Laboratory, Inc., Buffalo
March 4, 1957

IN ORDER to provide basic information for aerodynamic calculations pertaining to hypersonic flow, calculations of the thermodynamic properties of air in chemical equilibrium were recently carried out at 100° temperature intervals in the temperature range 3,000° to 10,000°K.[1] In analysis of these results, it was observed that for constant entropy the quantity log T/T_0 can be expressed, approximately, as a linear function of either log ρ/ρ_0 or P/P_0 in the temperature range 3,000° to 8,000°K. It therefore appears possible to relate to each value of the entropy in the real gas region a polytropic exponent from which the relationship between pressure, density, and temperature can be determined. Fig. 1 shows the variation of the log of the pressure with the log of temperature and the log of the density with the log of temperature for various values of the entropy. It can be observed that the relations are very nearly linear over a large entropy range and a large density and temperature range. These relationships have been pointed out by Moeckel.[2]

*This work was carried out under subcontract to the General Electric Company.

In a real gas, the molecular weight varies with the temperature, and the difference between specific heats is no longer equal to the gas constant R. Thus the specific-heat ratio, pressure, density, and temperature can no longer be related by the usual polytropic forms that are obtained for a constant entropy process in an ideal gas. However, using the plots of Fig. 1, an effective specific-heat ratio based on the average slope of the pressure and density curves can be obtained such that, for any constant entropy process,

$$T/T_1 = (P/P_1)^{(\gamma'-1)/\gamma'} = (\rho/\rho_1)^{\gamma''-1} \quad (1)$$

The subscript 1 refers to the initial conditions at the same entropy. The value of the polytropic exponent depends upon the entropy of the air and varies between 1.10 and 1.17 over the range of interest for hypersonic calculations (Fig. 2). In this same range, the actual value of the specific-heat ratio varies between 1.16 and 1.30.[1]

These values, shown in Fig. 2, represent average slopes in the temperature interval 3,000° to 9,000°K. As shown in Table 1, for a fixed entropy, the exponents for pressure (γ') and density (γ'') are almost equal and do not show large variations over large temperature intervals.

Similar results can be obtained for the relationship between temperature, enthalpy, and speed of sound—i.e.,

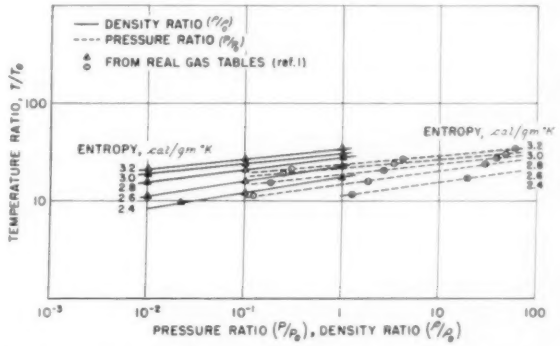

FIG. 1. Variation of temperature ratio with density and pressure ratios for constant values of entropy.

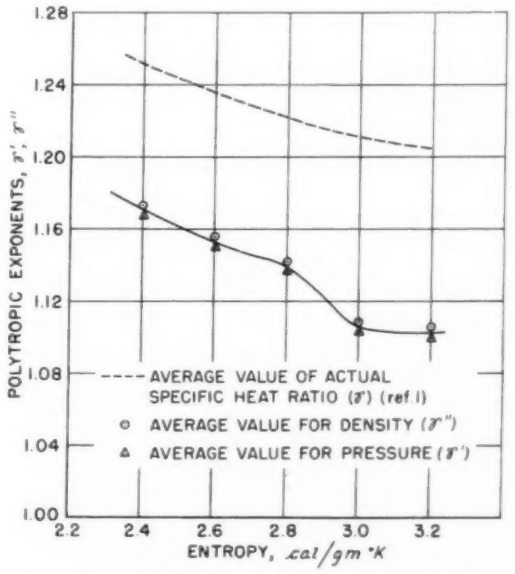
POLYTROPIC EXPONENTS, γ', γ''
AVERAGE VALUE OF ACTUAL SPECIFIC HEAT RATIO (γ) (ref.1)
AVERAGE VALUE FOR DENSITY (γ'')
AVERAGE VALUE FOR PRESSURE (γ')
ENTROPY, cal/gm °K

FIG. 2. Variation of the polytropic exponents, γ', γ'', with entropy for air.

TABLE 1
Polytropic Exponents (Entropy 3.0 cal./gm. °K.)

T_1, °K.	T_2, °K.	$\rho_1{}^*/\rho_0$	ρ_2/ρ_0	γ''	P_1/P_2	P_2/P_0	γ'
4220	5517	10^{-3}	10^{-2}	1.116	0.01787	0.2491	1.113
4220	6903	10^{-3}	10^{-1}	1.107	0.01787	3.397	1.104
4220	8869	10^{-3}	1	1.108	0.01787	48.21	1.104
5517	6903	10^{-2}	10^{-1}	1.097	0.2491	3.397	1.094
5517	8869	10^{-2}	1	1.103	0.2491	48.21	1.099
6903	8869	10^{-1}	1	1.109	3.397	48.21	1.104

*The subscript 0 refers to NACA standard reference conditions and the subscripts 1 and 2 values at constant entropy.

$$T/T_1 = (H/H_1)^{\alpha} = (a/a_1)^{\beta} \tag{2}$$

Values of α and β are shown in Fig. 3.

Comparisons between calculations using the average values of the polytropic exponents, Figs. 2 and 3, and real gas data[1] indicate that the maximum errors encountered in the use of these approximate forms is less than 15 per cent over the temperature range 3,000° to 8,000°K. Over this range the real gas pressure and density change by factors of 10^2.

Using relations (1) and (2), the Riemann characteristic for equilibrium isentropic flow,

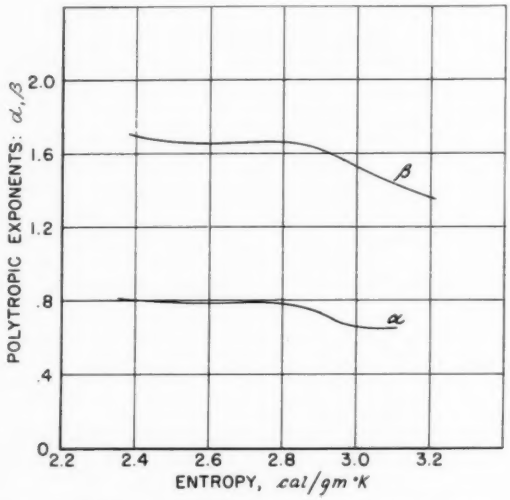

FIG. 3. Variation of the polytropic exponents for enthalpy (α) and speed of sound (β) with entropy.

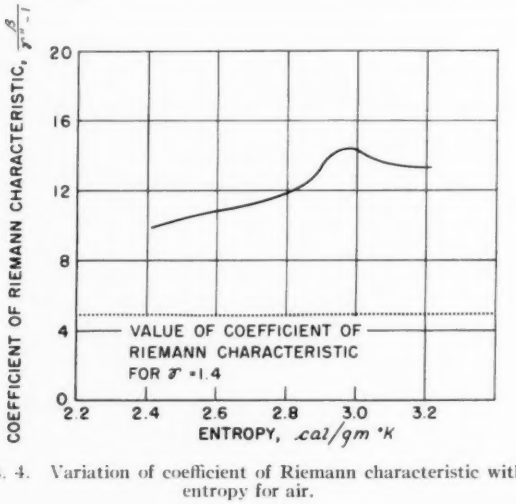

FIG. 4. Variation of coefficient of Riemann characteristic with entropy for air.

$$\sigma = \int^{\rho} (a/\rho)\, d\rho$$

evaluated at constant entropy, may be written

$$\sigma = [\beta/(\gamma''-1)]a \tag{3}$$

where the reference density is taken to be zero. The variation of the coefficient $\beta/(\gamma''-1)$ with entropy is shown in Fig. 4. As can be seen from this Figure, in one-dimensional nonsteady isentropic flow, the velocity change corresponding to a given change in sound speed Δa,

$$\Delta u = [\beta/(\gamma''-1)]\ \Delta a$$

may exceed the change in velocity for an ideal gas ($\gamma = 1.4$) by factors of 3.

REFERENCES

[1] Logan, J. G., Jr., and Treanor, C. E., *Tables of Thermodynamic Properties of Air from 3000° K to 10,000° K at Intervals of 100° K*, Cornell Aeronautical Laboratory Report BE-1007-A-3, January, 1957.

[2] Moeckel, W., *Oblique-Shock Relations at Hypersonic Speeds for Air in Chemical Equilibrium*, NACA TN 3895, January, 1957.

Note on the Turbulent Shear Stress Near a Wall

H. G. Elrod, Jr.
Associate Professor, Department of Mechanical Engineering, Columbia University, New York

March 7, 1957

THE PURPOSE of this note is to show the manner in which the turbulent contribution to shear stress vanishes in the neighborhood of a wall bounding the two-dimensional, established flow of an incompressible fluid.

Let x, y, z be the coordinates of a right-handed Cartesian system selected so that OX lies in the time-mean stream direction, OY is normal to the wall, and OZ is transverse to the time-mean stream. Let U, O, O be the time-mean velocity components and u, v, w the corresponding instantaneous velocity deviations therefrom.

Since the velocity vanishes at $y = 0$, the streamwise fluctuation $u(x, y, z, t)$ may be expanded in a Taylor series to give

$$u(x, y, z, t) = \alpha(x, z, t)y + \beta(x, z, t)y^2 + \ldots \tag{1}$$

Now the mass continuity equation gives

$$\partial v/\partial y = -[(\partial u/\partial x) + (\partial w/\partial z)] \tag{2}$$

or

$$v(x, y, z, t) = -(\partial\alpha/\partial x)\,(y^2/2) - (\partial\beta/\partial x)\,(y^3/3) \ldots - \int_0^y (\partial w/\partial z)dy \tag{3}$$

Therefore,

$$uv = -(\alpha y + \beta y^2 + \ldots)\,[(\partial\alpha/\partial x)\,(y^2/2) + (\partial\beta/\partial x)\,(y^3/3) \ldots] - u\int_0^y (\partial w/\partial z)dy \tag{4}$$

or

$$uv = -[(\partial\alpha^2/2)/\partial x]\,(y^3/2) - [(\partial\alpha\beta/\partial x)]\,(y^4/3) - [(\partial\beta^2/2)/\partial x]\,(y^5/3) - [\beta(\partial\alpha/\partial x)]\,(y^4/6) - u\int_0^y (\partial w/\partial z)dy \tag{5}$$

In an established flow the streamwise variation ($\partial/\partial x$) of the time-mean of all turbulent-velocity constructs is zero. Furthermore, by symmetry, u and w (and their derivatives) are uncorrelated. Hence,

$$\overline{uv} = -\beta\overline{(\partial\alpha/\partial x)}\,(y^4/6) = -\overline{(\partial^2 u/\partial y^2)\,(\partial^2 v/\partial y^2)}\,(y^4/6) \tag{6}$$

The foregoing demonstration establishes that $\overline{uv}$ vanishes near the wall with a power of y not less than four. This result is in contradiction to the formulations in references 1 and 2, although its possibility is mentioned in a footnote of reference 2. The result is in agreement with the hypothesis of Deissler[3] who was led to adopt the fourth power of y in order to correlate mass-transfer data taken at high Schmidt Numbers.

Combination of Eq. (6) with the wall-velocity "law" leads to

$$\overline{uv}/(\tau/\rho) = n^4(y\sqrt{\tau/\rho}/\nu)^4 \qquad (7)$$

where ρ is the fluid density, ν the fluid kinematic viscosity, and τ the wall shear stress. Deissler gives $n = 1/8$.

References

[1] Townsend, A. A., *The Structure of Turbulent Shear Flow*, p. 229; Cambridge University Press, 1956.

[2] Reichardt, H., *Complete Representation of the Turbulent Velocity Distribution in Smooth Pipes*, ZAMM, Vol. 31, No. 7, July, 1951.

[3] Deissler, R. G., *Analysis of Turbulent Heat Transfer, Mass Transfer, and Friction in Smooth Tubes at High Prandtl and Schmidt Numbers*, NACA Report 1210, 1955.

Wide-Angle Diffusers of High Performance and Diffuser Flow Mechanisms†

S. J. Kline,* C. A. Moore,** and D. L. Cochran***
Stanford University, Stanford, Calif.

March 21, 1957

In Professor Ralph Burton's Readers' Forum note,‡ certain speculations concerning the relation between the rate of jet spreading and the separation characteristics of diffusers are discussed. The problems of flow mechanisms in diffusers and performance of wide-angle diffusers have been under continuing investigation during the last 3 years at Stanford University under the sponsorship of the NACA. A considerable body of data is now available; a brief summary of some of the more pertinent and important results follows.

The results given below have been verified in several different units and are considered well established, except where noted otherwise, for the case of two-dimensional, plane-walled diffusers with thin inlet boundary layers, well-rounded entrances, and incompressible flow.

(1) The following parameters are known to be important in determining the flow regime for a fixed mean inlet velocity profile: (a) total divergence angle, (b) ratio of wall length to throat width (or area ratio), and (c) inlet free-stream turbulence.

Inlet boundary-layer momentum thickness is also believed to be of critical importance, but data are not yet available to substantiate completely this conclusion; tests on this point are in progress.

Tests of units of various sizes and at various velocities indicate that Reynolds Number plays only a minor role for all values in excess of that which gives a well-established turbulent boundary layer at the throat.

The tests also show that throat aspect ratio has little or no effect on the flow regime over the entire range of aspect ratio used in normal practice.

(2) As a function of the parameters listed above, there are four regimes of flow found in the diffuser. Holding all inlet conditions constant and holding the ratio of wall length to throat width constant, increasing angle from zero to 100 or more degrees causes these four regimes to appear in the following order: (a) no appreciable stall (small transitory stall), (b) large transitory stall, (c) fully-developed stall, and (d) jet flow. These regimes are sketched in Fig. 1 and are shown as a function of the parameters listed above in Fig. 2. The following comments are pertinent.

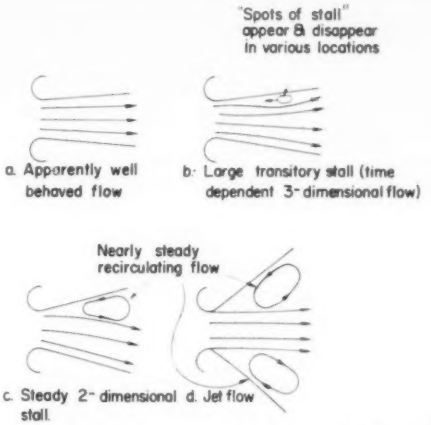
"Spots of stall" appear & disappear in various locations
a. Apparently well behaved flow
b. Large transitory stall (time dependent 3-dimensional flow)
Nearly steady recirculating flow
c. Steady 2-dimensional stall
d. Jet flow

Fig. 1. Schematic diagrams of the regimes of diffuser flow.

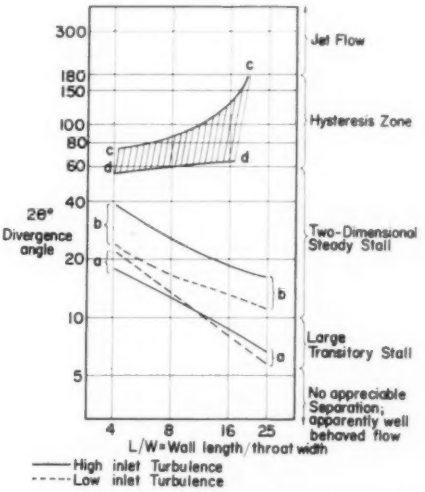

Fig. 2. Zones of diffuser flow in terms of governing parameters for fixed mean inlet velocity profile.

Transitory stall is not a two-dimensional flow; on the contrary, it is clearly a three-dimensional transient flow. Furthermore, it exists over a very wide range of conditions as can be seen in Fig. 2. Some important further details on this new mechanism are given in a separate brief note.

The regime of flow called fully developed stall on Fig. 2 corresponds to the classical picture of stall of a two-dimensional boundary layer. It has a recirculating flow region occupying most of the diffuser; the through flow follows down one wall or the other, and the performance is very poor. The fully developed stall regime is a relatively steady, stable, flow condition. The region of large fluctuations recorded by some observers is believed to be the region of large transitory stall and has been found to be so in every case checked to date. The distinction between the two regimes is simple: In the fully developed stall, one wall has a large area of backflow all the time; in transitory stall, any given wall area has forward flow part of the time and backward flow part of the time.

† The material summarized in this note and the associated note on the mechanisms of stall are covered in detail by contract reports to the NACA. The first of these reports should appear shortly as an NACA Technical Note.

* Associate Professor of Mechanical Engineering.

** Formerly Research Assistant. Now at Aerophysics Laboratory, North American Aviation, Inc., Downey, Calif.

*** Formerly Research Assistant. Now at Propulsion Research Corporation, Santa Monica, Calif.

‡ Burton, Ralph, *Discussion of the Influence of Confining Surfaces upon the Boundary Layer in a Channel*, Readers' Forum, Journal of the Aeronautical Sciences, Vol. 24, No. 2, pp. 149, 150, February, 1957.

The jet flow region occurs only at very high angles of divergence. It is characterized by a fully developed stall on both walls. It is less stable than the regime called fully developed stall, and thus one finds an overlap region on the flow mechanism chart of Fig. 2. If angle is increased, transition to jet flow occurs at the upper line; if angle is decreased, the transition is found at the lower line.

In connection with Burton's comments it is therefore clear that his remarks are in some respects pertinent to the zone of fully developed stall, but they cannot apply to the regime of transitory stall because the flow model is entirely dissimilar from that which he envisaged. Since the transitory stall regime is the region of stall inception, it is highly doubtful if the ideas suggested by Burton will be adequate to predict performance. This same comment, of course, applies to any wholly two-dimensional model of stall since the tests clearly show that stall does not normally begin in a two-dimensional manner.

(3) The flow mechanism chart of Fig. 2 can be used not only to explain the known data and performance of two-dimensional diffusers over the range of interest but also can be used very profitably as a basis for the design of wide-angle diffusers of high performance. In addition, the chart provides basic information about the nature of turbulent boundary-layer flows in adverse pressure gradients.

By the use of the chart of Fig. 2, vaned, two-dimensional diffusers have been designed and tested which give surprisingly good performance up to angles of divergence of at least 42°. In a typical case, a unit which would have an optimum recovery of approximately 0.76 at a total divergence angle of 15° for the unmodified case can, by use of simple flat vanes, give a recovery of 0.78 at 30° and a recovery of 0.71 at 42°. It is believed that still better results are possible at wide angles through further refinements. Design criteria for two-dimensional vaned units have been developed. Systems designed by these criteria appear to give good pressure recovery over a wide range of geometries and produce smooth stable flows with relatively good exit velocity profiles. The design of such systems is simple and relatively insensitive to minor changes provided that certain rules are followed. Tests on these systems are continuing.

Further details of the flow mechanisms and some of their implications are summarized in the following brief note.

Some New Conceptions of the Mechanism of Stall in Turbulent Boundary Layers*

Stephen J. Kline
Associate Professor of Mechanical Engineering, Stanford University, Stanford, Calif.
March 21, 1957

In the accompanying brief note by the author, Dr. C. A. Moore, and D. L. Cochran, a discussion of the governing parameters and flow regimes of two-dimensional diffusers with thin inlet boundary layers was presented together with an example of the performance of a wide-angle diffuser utilizing vanes. The data in that note together with the excellent results obtained from vaned diffusers and certain other known but inexplicable results have recently led the author to conduct further investigations into the nature of stall in diffusers. It is believed that the results of these studies shed considerable light on the problem of stall in general. A brief summary of some of the more important aspects of these studies follow.

In the work of C. A. Moore and the author, it was shown that a region of transitory stall was uniformly found in which the stalls were not two-dimensional but were, on the contrary, of a transient, three-dimensional nature. In this flow regime, transient "spots of stall" appear and disappear first in one location and then in another. The extent of this regime of flow was found to be strongly influenced by inlet free-stream turbulence as well as by diffuser divergence angle and area ratio. In the early work, the regimes of flow were mapped from water-table studies using dye injection of a conventional sort. Subsequently, as evidence accumulated, it began to be clear that transitory stall probably existed at much lower angles than those at which it already had been observed by Moore and Kline. And, finally, for a variety of reasons too lengthy to repeat here, the author recently reached the following tentative conclusions:

(a) Spots of transitory stall may exist down to at least very low values of adverse pressure gradient. (b) These spots originate very near the wall, probably in the laminar sublayer. (c) The spots grow in size, number, and time of duration as the adverse pressure gradient is increased in magnitude or in length of application. (d) The means by which the spots are carried back downstream is by leaving the wall and being caught up by the inertia of the mainstream.

Recent tests in a water table show that all of these ideas are true with the exception of the length of application of pressure gradient which has not yet been checked. These facts have now been verified repeatedly at low velocities using a dye persistence technique† that makes the laminar sublayer visible for several minutes. Careful observations of the wall layers using the dye persistence technique show that small local transient backflows do exist near the wall even for surprisingly mild adverse pressure gradients. For example, backflows, or spots of stall, have been clearly seen by several observers at a total divergence angle of 5° with a ratio of wall length to throat width of 6.7 and a thin inlet boundary layer. In some instances spots of stall have been observed at even lower angles. The actual minimum value of angle at which spots of stall can first be discerned apparently depends both on the number of observations made and on the free-stream turbulence level. Since the occurrence is statistical, exact information on these effects must await more detailed studies now in process.

When found at very small adverse pressure gradients the spots of stall are very small and appear for only short periods of time. Typically, on a 4-in. wall, one spot might appear in a matter of 2 min. at a given cross section and might be 1/16 in. in diameter. As the adverse pressure gradient is increased, the spots grow; several spots may appear at once at a given cross section, and they may extend through the boundary layer into the main flow. Finally, by a mechanism that is still under study, the spots coalesce and destabilize the entire flow pattern. A fully developed stall then ensues with flow moving upstream all along one wall. The growth of these spots of stall correlates with the increase in losses of the diffuser.

These facts together with certain other ideas about the mechanisms governing the flow in the various regimes can be used to explain many well-known but previously inexplicable facts. Among these are the large pressure pulsations which very frequently originate in diffusing passages, the large losses in diffusers which cannot be accounted for by wall friction and turbulence, the differing observations made by previous observers about the nature of stall, and the consistent failure of two-dimensional boundary-layer theory to predict stall of the turbulent boundary layer. All of the performance data found for the unvaned and vaned diffuser systems mentioned above can also be rationalized in terms of these mechanisms. In contradistinction, some of the known performance of both vaned and unvaned diffusers cannot be rationalized in terms of any known steady two-dimensional model of the flow.

It is now believed very likely that the inception of stall is usually a three-dimensional transient phenomenon which is called transitory stall. The transitory spots of stall are viewed as a mechanism that is adopted by the fluid to supply the energy needed by the very slow moving layers near the wall in order to negotiate an adverse pressure gradient. This conclusion is

* An NACA contract report covering this work in more detail is under preparation.

† This technique was largely developed by J. A. Miller, Research Assistant, Stanford University.

supported not only by the observations cited but also by the fact that careful analysis of the forces on a layer very near the wall in an adverse pressure gradient reveals certain cases in which it is impossible to satisfy the conditions of equilibrium by *any* steady, two-dimensional model. Apparently, the solution to this paradox is that the flow is not two dimensional but instead develops transitory spots of stall. These spots act both to reduce the adverse pressure gradient on the immediately adjacent unstalled areas and to add energy to the slow-moving layers by augmenting the mixing with the free stream.

Since the size and number of these spots grow with increasing adverse pressure gradient and since the spots may exist even for extremely low values of adverse pressure gradient, it must then follow that stall is not a single phenomenon as previously believed but is instead a spectrum of conditions. This spectrum extends from extremely small stall spots at one end to fully developed stall at the other. In the former case, the average fraction of the wall that is stalled over a period of time is very small; in the latter case, it is 100 per cent. Apparently, it is possible to obtain any value in between.

The preceding paragraph suggests that the production of stalled fluid in the layers very near the wall may be the inevitable accompaniment of large adverse pressure gradients at least for the turbulent boundary layer. If this is true, the relevant question regarding stall is not, as previously believed, is the wall stalled? On the contrary, the relevant questions are how fast is stall fluid produced by the action of the pressure forces on the fluid layers very near the wall? and how fast is this stalled fluid carried away by mixing with the faster moving layers of fluid? It would appear that the amount of stall actually present is determined by the balance between these two rates. The balance appears to be a relatively delicate one, and a small alteration in either of these rates will frequently cause a large change in the flow pattern over a period of time. These concepts have already been applied to the explanation of a number of known situations, and the results to date are most encouraging. Due to space limitations, only the application to vaned diffusers is covered here.

When applied to diffusers containing vanes or splitters, the mechanisms just discussed indicate that the action of the vanes or splitters is not that suggested by Burton‡ but is instead a type of stabilizing action. The mechanism suggested by Burton would imply that longer splitter vanes would always give less likelihood of flow separation, other things being equal, but this is not the case. The data now in hand show that there is an optimum length of vane as well as an optimum vane angle.

The actual action of vanes or splitters is believed to be dependent on their effect under transient conditions rather than on a steady-state effect. If the flow were truly steady, then a single splitter would produce no appreciable effect. However, if large transitory stalls are present, the action of a splitter is such that it tends to prevent breakdown of the overall flow pattern from transitory to fully developed stall. This can be seen by viewing a splitter as a cascade blade that only takes on loading under transient flow conditions or by examining the pressure distribution that would occur around the splitter vane if a fully developed stall were present. Either method shows that the splitter vane can supply the forces needed under transient conditions to stabilize the transitory stall regime. The effect of the splitter or vane is to direct the main-stream inertia in such a way that the rate at which stall fluid is swept off the walls cannot be reduced over one large area of a wall with a consequent destabilization of the overall flow pattern. Observations with tufts and dye in both the water table and the air unit verify that transitory stalls are indeed present even with vanes which produce the high performances cited in the above note. Thus, such vanes do not eliminate all stalls, but they do drastically reduce the total average area that is stalled over a given period of time.

The important conclusions to be drawn from the foregoing discussion are believed to be as follows:

(1) Inception of stall in a turbulent boundary layer cannot be described by a two-dimensional model for the cases observed.

(2) It is not sufficient to discuss merely stalled and unstalled flows. On the contrary, it is apparently necessary to recognize that stall is a spectrum of states. Stall may already be present at very low values of adverse pressure gradient, and the amount of stall produced then grows in a relatively continuous fashion with increased adverse pressure gradient until finally a fully developed stall corresponding to the classical picture occurs.

(3) In order to rationalize the behavior of stalls for all regimes found, it is necessary to compare the rate at which stalled fluid is produced to the steady rate at which it can be removed by the inertia forces of the main-stream flow and also to consider the stability of the entire flow pattern.

Work on several aspects of the flow mechanism and diffuser performance studies mentioned above is continuing. The author will welcome discussion or direct communications bearing on the points covered or empirical evidence concerning the mechanisms described.

‡ See footnote, p. 469.

Note on the Boundary-Layer Instability on a Flat Plate Stopped Suddenly*

Francis R. Hama
Assistant Research Professor, Institute for Fluid Dynamics and Applied Mathematics, University of Maryland, College Park, Md.
March 15, 1957

IN A RECENT PAPER[1] on transition from laminar to turbulent flow, the nature of a two-dimensional discrete vortex line imbedded in a shear flow was discussed briefly. The following theorem was brought forward: "In a shear flow, a two-dimensional vortex line with a positive vorticity, defined as that having the same direction as the background vorticity, is unstable under three-dimensional disturbances, whereas that with a negative vorticity is stable." The physical basis for this theorem is the interaction of the induction effect and mean-velocity gradient. When an originally straight vortex line is three-dimensionally disturbed, it will take on a wavy configuration along its axis. The plane of the wavy vortex line rotates, owing to self-induction effect, in a direction opposite to that of the vorticity. Mean-velocity distribution then interacts to intensify the waviness of a positive vortex line or to damp out the waviness of a negative vortex line.

Because of the first part of the theorem and of the experimental evidence that the formation of a three-dimensional vortex loop always precedes the creation of a turbulent spot, a positive vortex line can be regarded as a dangerous one which might lead the flow to transition. This appears to be the case for the amplified Tollmien-Schlichting wave in ordinary boundary layers. If the second part of the theorem is correct, a negative vortex line must have little to do with transition. Examination of the validity of the second part of the theorem, which has remained a conjecture without experimental evidence in reference 1, is the purpose of this note with special attention to the current interest in the stability problem on a decelerated flat plate.

Let us first consider the case when a smooth flat plate moving at a constant speed through a still fluid suddenly comes to a stop. In this case, the velocity distribution near the plate is dependent on time after the stoppage and has a separation-*type* profile as drawn in Fig. 1. This sort of velocity profile is theoretically unstable.[2] Fales[3] has experimentally demonstrated that the flow is indeed unstable and that a series of two-dimensional discrete vortices is soon produced. If the plate is kept still, the two-dimensional vortices are deformed into three-dimensional vortex loops which gradually entangle each other to form an irregular

* This research was supported by the U.S. Air Force through the Office of Scientific Research, ARDC, under Contract AF 18(600)-1014.

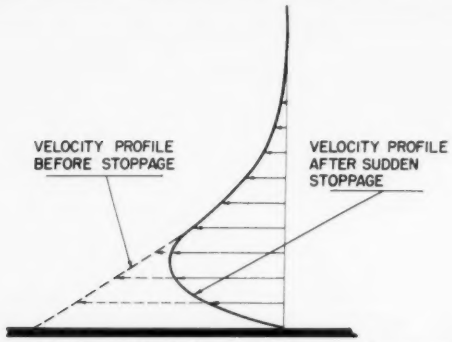

FIG. 1. Velocity profiles before and after a sudden stoppage of a flat plate.

pattern. This is possible in accordance with the first part of the theorem because the vortices are counterclockwise and have a positive sign with respect to the shear flow in the immediate vicinity of the plate surface. However, since the mean velocity gradually dies down, it cannot provide sufficient energy to maintain the irregular motion.

The case when the plate encounters a sudden stoppage followed by a sudden start shall be considered next. Such a case could be of more practical interest in connection with transition on an oscillating plate in a uniform flow or on a plate when the wind velocity fluctuates. After the stoppage counterclockwise discrete vortices are formed again. These vortices, however, become negative with respect to the velocity gradient near the plate after the succeeding start. Therefore, if the second part of the theorem is correct, the vortices should be stabilized and will not develop into a three-dimensional configuration.

Such an experiment is actually performed with a smooth flat plate (without a trip) horizontally submerged in a towing tank. A dye is injected into the flow field two-dimensionally through a narrow slit cut across the plate. When the plate is moving at a constant speed, a very thin film of the dye flows slowly over the plate surface toward the trailing edge. After the sudden stoppage the flow of dye changes the direction relative to the plate toward the leading edge (see Fig. 1). The film of dye gradually becomes concentrated to form a two-dimensional wave due to the instability. It is instructive to observe that the film eventually rolls up to create two-dimensional discrete vortices whose vorticity is counterclockwise and positive. This is additional evidence that, when a small-perturbation wave is amplified, it results in a series of concentrated positive discrete vortices. It is also noted that, especially when the initial plate speed is relatively high, the formation of the discrete vortices is very fast so that they appear to be created from nowhere.

As the discrete vortices are produced, they then begin to deform themselves into three-dimensional wavy configurations along their axes. If the plate starts again at this stage, the waviness is observed to develop no further and even often to recede. In other words, even though the original two-dimensional perturbation wave is sufficiently amplified, it does not originate turbulence. Needless to mention, if the plate starts before the formation of distinct discrete vortices, the boundary layer is stabilized again, and the discrete vortices do not appear.

From this experimental demonstration, it is evident that the second part of the theorem is also correct. Consequently, when a flat plate experiences deceleration and acceleration, the boundary layer is unstable in the deceleration stage, but the instability is harmless and will not result in transition. This may constitute an interesting example of nonlinear mechanics. In linear cases, the sign of vortices, or otherwise, is immaterial. On the contrary, the sign could become significant once the mechanics become nonlinear as in the present theorem.

Further remarks should be made on the stabilizing effect of the succeeding acceleration. If the plate is kept still for a long time after the sudden stoppage, the three-dimensional waviness is sufficiently intensified so that the stabilizing effect of the shear flow on a negative vortex will become no longer applicable. Furthermore, the succeeding acceleration even promotes a sudden appearance of a turbulent spot by stretching the three-dimensional vortex loop, even though the vorticity of the vortex loop is negative.

Finally, it may also be remarked that the present case, in which a plate itself is decelerated and accelerated, should be distinguished from the case when the velocity of oncoming flow to the plate fluctuates so as to create pressure gradients in the stream direction. In the latter, the boundary layer may indeed separate and produce dangerous positive discrete vortices, whereas the flow does not separate on an oscillating plate.

REFERENCES

[1] Hama, F. R., Long, J. D., and Hegarty, J. C., *On Transition from Laminar to Turbulent Flow*, J. Appl. Phys., Vol. 28, No. 4, pp. 388–394, 1957.

[2] von Kármán, Th., and Lin, C. C., *Theoretical Comments on the Paper of Mr. E. N. Fales*, J. Franklin Inst., Vol. 259, No. 6, pp. 517, 518, 1955.

[3] Fales, E. N., *A New Laboratory Technique for Investigation of the Origin of Fluid Turbulence*, J. Franklin Inst., Vol. 259, No. 6, pp. 491–515, 1955.

IAS Twenty-Sixth Annual Meeting

Hotel Sheraton-Astor, New York City, January 27–30, 1958

The Meetings Committee plans to schedule sessions on Aerodynamics, Aeroelasticity, Design, Electronics, Flight Propulsion, Instruments, Rotating Wing Aircraft, Safety in Flight, Structures, Air Transportation, etc.

Members or organizations wishing to have papers considered for presentation at this meeting should submit outlines or short abstracts to the Meetings Committee, 2 East 64th St., New York 21, N.Y., no later than August 1, 1957.

NACA Wind Tunnel Panel Hypersonics Meeting

The Wind Tunnel and Model Testing Panel of the Advisory Group for Aeronautical Research and Development is sponsoring a meeting on hypersonic aerodynamics and testing facilities, which will be held at Scheveningen, Holland, July 8–11, 1957. The general subjects to be covered by the meeting will be theoretical work on hypersonic fluid mechanics, devices for hypersonic research such as wind tunnels, gun-launched and rocket models. One day will be devoted to a discussion on shock tubes and their uses.